

Polish Academy of Sciences
Institute of Physics

PH.D. DISSERTATION

SPIN WAVES AND THE ANOMALOUS
HALL EFFECT IN FERROMAGNETIC
(Ga,Mn)As

Agnieszka M. Werpachowska

Supervisor:
Professor Tomasz Dietl

Warsaw 2011

*for Tintin
the greatest lil' ferret that ever lived*

Acknowledgements

I would like to thank my advisor, Professor Tomasz Dietl, for providing me with the opportunity to work on many interesting topics and encouraging me to aim high in academic life. Working under the direction of such a successful and dedicated scientist taught me to trust my skills, accept responsibility and work hard to achieve set goals, the things I will certainly benefit from in the future.

One of the greatest aspects of my research work has been the cooperation with the group of Professor Hideo Ohno from Tohoku University, whose groundbreaking experiments have been an inspiration also for my work. I will ever remain grateful to Professor Ohno for his kind attitude.

It was nice to meet the people of our Institute, especially the fellow members of the SL2 group. My work would not proceed smoothly without the help of our group's computing cluster, which was kept running by the expertise of Czarek Sliwa—thank you for this, and your patient tolerance of my numerous attempts to bring the cores down. I regret that I did not pursue research together with you and Lukasz. I have always felt a bit of envy towards the experimentalists in our group, who fight at the frontline of physics, but my only visit in the lab ended up triggering the fire alarm (thank you, Krzys!).

I would like to thank Professor Jacek Majewski and Rafał Oszwałdowski for providing me with C. Strahberger's tight-binding code, which made my work easier.

There is also a group of people, whom I could always ask for advice and words of encouragement, especially Arek Wójs, Jacek Majewski and Professor Witold Dobrowolski. Their friendship and support are invaluable and helped me a lot during the darkest moments of my PhD journey.

Outside of the institute, Maria and Alex, my partners in crime, you are always welcome to our home no matter how many kitchen appliances you destroy. Seb, thank you for polishing my Englirz. Now that I have more time, I can go back to making my culinary experiments with strange cuisines and crazy cakes on you and Roman. Halina, big thanks for managing everything for us in Poland. To all my mates from physics forums and blogs, thank you for fascinating discussions on physics and maths, and all your interest in my poor fate ;-)

It was my grandma, who taught me the respect for knowledge and education from my early days, as the indestructible key to my personal independence and freedom. Remembering in what tough conditions you pursued your goals is the source of my determination. You are my heroine. (ps. Out of caution I am not taking philosophy on my exams.) My grandpa, you have always remained the man of truth and justice, showing me the way I can go through my life with peace of mind.

Scientists want to find out the global topology of the Universe to give the firm foundation to what we believe in. Roman, you defined the global topology of my life and gave sense to all the things, recognised only locally, unstable or without connection.

My research was supported by the Scholarship of the President of Polish Academy of Sciences, the EC NANOSPIN (FP6-IST-015728) and EC Network SemiSpinNet (PITN-GA-2008-215368) grants.

Preface

The following thesis presents my research on III–V diluted magnetic semiconductors (DMS) that I have conducted at the Institute of Physics, Polish Academy of Sciences under the supervision of Professor Tomasz Dietl. It covers a wide spectrum of topics related to magnetic and transport phenomena in these materials, which are crucial for their future spintronics applications.

To begin with, I give the background for my research and describe the employed theoretical and computational models. Then, I investigate and extend the theory of III–V DMS as described by the model of hole-mediated ferromagnetism by Dietl *et al.*, focusing on (Ga,Mn)As. I start with the atomic quantum-mechanical description of the analysed systems, using the proposed variation-perturbational Löwdin calculus, and then turn to the emerging macroscopic picture employing phenomenological constants. Within this framework I study the Curie temperature, magnetocrystalline anisotropies, spin waves and the exchange stiffness. Analysing the anisotropic part of the exchange interaction, I find that the Dzyaloshinskii-Moriya exchange may lead to a cycloidal spin arrangement and uniaxial in-plane anisotropy in thin layers, and define the relativistic counterpart of the exchange stiffness tensor. I also derive and discuss the spin-wave contribution to magnetization and the Curie temperature. Next, I analyse the intrinsic part of the anomalous Hall effect (AHE), believed to dominate in ferromagnetic (Ga,Mn)As, and reveal the spectacular sensitivity of the Berry curvature and related conductivity to the bulk inversion asymmetry of the zincblende structure. Finally, I attempt to explain the new and unanticipated AHE features in thin layers observed in the experiments performed by the group of Professor Hideo Ohno at Tohoku University. I provide a thorough comparison of my results to the available experimental data. My observations prompt me to distinguish between the static and dynamic properties of DMS. The simplest analysed $k \cdot p$ approaches are sufficient to describe the first, but the other require advanced multiband models (like 40-band $spds^*$ and 20-band sps^* tight-binding approximations).

The presented results have been published in peer-reviewed articles and presented on multiple conferences, listed in the included curriculum vitae.

CURRICULUM VITAE

EDUCATION AND TRAINING

10/2005–4/2009 **PhD studies**, Laboratory of Cryogenic and Spintronic Research, IP PAS

Thesis Topic: *Spin waves and the anomalous Hall effect in (Ga,Mn)As*

Advisor: Professor Tomasz Dietl

(10/2005–10/2006) Division of Solid State Spectroscopy, IP PAS

Research Area: Spin waves and anisotropies in (Ga,Mn)As

Advisor: Professor Zbysław Wilamowski

10/2003–10/2005 **MSc**, College of Science at PAS

Thesis Topic: *Magnetic Anisotropies in (Ga,Mn)As*

Advisor: Professor Zbysław Wilamowski

2/2004–6/2004 Laboratory of Cryogenic and Spintronic Research, IP PAS

Research Area: Ferromagnetism in (Ga,Mn)As

Advisor: Dr Maciek Sawicki

7/2004–9/2004 DESY Summer Student Programme, Hamburg, Germany

Project: *Theory of FEL laser induced heating of electron gas in metals*

Advisor: Professor Jacek Krzywiński

10/2000–9/2003 **BSc** in mathematics, physics and chemistry (speciality: computational physics), College of Science at PAS

Thesis 1 Topic: *Simulations of chaotic electron transport in antidot lattices subject to in-plane magnetic field*

Advisor: Dr Zbigniew Tkaczyk

Thesis 2 Topic: *Analysis of luminescence kinetics measurements*

Advisor: Professor Marek Godlewski

AWARDS

Scholarship of the President of Polish Academy of Sciences for doctoral students, 2007-2009

IUPAP Young Author Best Paper Award, International Conference on the Physics of Semiconductors, Rio de Janeiro, Brazil, 2008

CONFERENCE PRESENTATIONS

grant reports:

Nanospin Meeting, Paris, France, 2008, *Spin waves and anomalous Hall effect in thin layers and bulk crystals of (Ga,Mn)As*

Nanospin Meeting, Prague, Czech Republic, 2007, *Magnetic stiffness and anomalous Hall effect in ferromagnetic (Ga,Mn)As*

conference talks:

14th International Conference on Modulated Semiconductor structures (MSS-14), Kobe, Japan, 2009, *Effect of inversion asymmetry on anomalous Hall effect in ferromagnetic (Ga,Mn)As*

XXXVII International School on the Physics of Semiconducting Compounds, Jaszowiec, Poland, 2008, *Anomalous Hall effect in (Ga,Mn)As*

29th International Conference on the Physics of Semiconductors, Rio de Janeiro, Brazil, 2008, *Anomalous Hall effect in (Ga,Mn)As*

XII Workshop on Semimagnetic Semiconductors, Obory, Poland, 2007, *Magnetic Stiffness in (Ga,Mn)As Ferromagnetic Semiconductors*

MAG-EL-MAT Network *New materials for magnetoelectronics*, Bedlewo, Poland, 2005, *RKKY model with Zeeman splitting*

conference posters:

30th International Conference on the Physics of Semiconductors, Seoul, Korea, 2010, *Spin waves in (Ga,Mn)As*

5th International School and Conference on Spintronics and Quantum Information Technology, Cracow, Poland, 2009, *Effect of inversion asymmetry on anomalous Hall effect in ferromagnetic (Ga,Mn)As*

XXXVIII International School on the Physics of Semiconducting Compounds, Krynica, Poland, 2009, *Effect of inversion asymmetry on anomalous Hall effect in ferromagnetic (Ga,Mn)As*

Polish-Japanese Join Meeting, Leszno, Poland, 2007, *Magnetic stiffness and anomalous Hall effect in ferromagnets*

1st WUN Worldwide University Network International Conference on Spintronic Materials and Technology, York, Great Britain, 2007, *Anomalous Hall Effect in Ferromagnetic (Ga,Mn)As*

XXXVI International School on the Physics of Semiconducting Compounds, Jaszowiec, Poland, 2007, *Magnetic Stiffness and Anomalous Hall Effect in (Ga,Mn)As*

XXXV International School on the Physics of Semiconducting Compounds, Jaszowiec, Poland, 2006, *High Order Anisotropy Terms in (Ga,Mn)As*

XXXIV International School on the Physics of Semiconducting Compounds,

Jaszowiec, Poland, 2005, *RKKY and Zener contributions to magnetic stiffness in (Ga,Mn)As*

XXXIII International School on Physics of Semiconducting Compounds, Jaszowiec, Poland, 2004, *Beyond the Stoner-Wolfarth approach to magnetic properties of as grown (Ga,Mn)As*

seminars:

Theory and modelling of nanostructures, Faculty of Physics, University of Warsaw, 2008 *Anomalous Hall effect in dilute magnetic semiconductors*

Theory and modelling of nanostructures, Faculty of Physics, University of Warsaw, 2007 *Spin waves in dilute magnetic semiconductors*

Seminar on microwave spectroscopy, IP PAS, 2005, *Analytical solutions for RKKY coupling in dilute magnetic semiconductors*

OTHER ACTIVITIES

Help in the organisation of the Spintech conference in Cracow, Poland, 2009; Taking part in the Science Picnic in Warsaw representing the College of Science; Voluntarily tutoring young students

PUBLICATIONS

Werpachowska, A., *Exact and approximate methods of calculating the sum of states for classical non-interacting particles occupying a finite number of modes*, Phys. Rev. E **84**, 041125 (10/2011)

Werpachowska, A. and T. Dietl, *Theory of spin waves in ferromagnetic (Ga,Mn)As*, Phys. Rev. B **82**, 085204 (8/2010)
plus online supplement *Löwdin calculus for multiband Hamiltonians*, arXiv:1101.5775 (1/2011)

Werpachowska, A. and T. Dietl, *Theory of spin waves in ferromagnetic (Ga,Mn)As*, ICPS30 Proceedings (subm. 7/2010, accepted for publication)

Werpachowska, A. and T. Dietl, *Effect of inversion asymmetry on the anomalous Hall effect in ferromagnetic (Ga,Mn)As*, Phys. Rev. B **81**, 155205 (4/2010)

Chiba, D., A. Werpachowska, M. Endo, Y. Nishitani, F. Matsukura, T. Dietl, and H. Ohno, *Anomalous Hall Effect in Field-Effect Structures of (Ga,Mn)As*, Phys. Rev. Lett. **104**, 106601 (3/2010)

Werpachowska, A. and Z. Wilamowski, *The RKKY coupling in diluted magnetic semiconductors*, Mater. Sci.-Poland **24**, 675 (2006)

Wilamowski, Z. and A. Werpachowska, *Spintronics in semiconductors*, Mater. Sci.-Poland **24**, 803 (2006)

Werpachowska, A., *Electron billiards* in the Polish popular scientific magazine *Delta* (4/2004).

Contents

Preface	4
1 Introduction	13
2 Motivation and outline	19
3 (Ga,Mn)As as a dilute magnetic semiconductor	23
3.1 Brief history	23
3.2 Crystal structure	26
3.3 Mn impurities	29
3.4 Lattice strain	30
4 Origin of magnetism in (Ga,Mn)As	33
4.1 Exchange interaction	33
4.2 Mechanisms of magnetic ordering	35
4.2.1 Superexchange	36
4.2.2 Bloembergen–Rowland mechanism	37
4.2.3 Double exchange	37
4.2.4 RKKY interaction	38
4.2.5 The p – d Zener model	39
4.2.6 Bound magnetic polarons	41
4.3 Magnetic regimes in (Ga,Mn)As	42
5 Band structure of (Ga,Mn)As	45
5.1 Reciprocal space	46
5.2 Band structure	48
5.3 Spin-orbit coupling	52
5.4 Inversion symmetry breaking	53
5.4.1 Bulk inversion asymmetry	54
5.4.2 Structure inversion asymmetry	55
5.5 The effect of strain	56
5.6 The effect of sp – d exchange coupling	56

6	Band structure methods	59
6.1	The $k \cdot p$ method	59
6.1.1	Strain	61
6.1.2	Exchange interaction	62
6.1.3	Parametrisations	62
6.2	Tight-binding approximation	70
6.2.1	Strain	73
6.2.2	Exchange interaction	74
6.3	Comparison of the $k \cdot p$ and tight-binding approximations . .	74
7	Ferromagnetism in (Ga,Mn)As	79
7.1	Basic statistical picture	82
7.1.1	Free energy of Mn spins	83
7.1.2	Free energy of ion-carrier system	86
7.1.3	Average magnetisation and critical temperature	89
7.2	Self-consistent Löwdin calculus	93
7.3	Interpretation of the effective Hamiltonian	97
7.4	Small oscillations approximation	98
7.5	Summary	101
8	Curie temperature and uniaxial anisotropy in (Ga,Mn)As	103
8.1	Mean-field Curie temperature	103
8.2	Uniaxial anisotropy field	105
8.3	Summary	107
9	Spin waves and exchange stiffness in (Ga,Mn)As	109
9.1	Microscopic picture of spin waves	111
9.2	Micromagnetic theory	116
9.3	Bulk (Ga,Mn)As	118
9.4	Thin (Ga,Mn)As layers	121
9.4.1	Cycloidal spin structure in (Ga,Mn)As layers	121
9.4.2	Stiffness tensors in layers	127
9.5	Normalised spin-wave stiffness	128
9.6	Spin waves' contribution to magnetisation	131
9.7	Comparison to experiment	135
9.8	Summary	141
10	Anomalous Hall effect in ferromagnetic (Ga,Mn)As	143
10.1	Theoretical approach	147
10.2	Berry curvature	148
10.3	Anomalous Hall conductivity	150
10.4	Comparison to experiment	154
10.4.1	Bulk (Ga,Mn)As	154
10.4.2	Thin layers of (Ga,Mn)As	155

10.5 Summary	158
11 Summary and outlook	161
11.1 Summary of thesis work	161
11.2 Open problems	163
A Numerical implementation	165
A.1 Code structure	165
A.2 Computational problems	166
B Acronyms and symbols	169
C Odpowiedzi dla Recenzentów	173
Bibliography	177

Chapter 1

Introduction

Another decade is probably straightforward. . . There is certainly no end to creativity. Gordon Moore, Intel co-founder and chairman emeritus of the board, speaking of extending the Moore's Law at the International Solid-State Circuits Conference, February 2003.

Spintronics is an already well-established field of science and technology—the distinction is only in the eye of the beholder, as the whole research effort in this field is fuelled by various ideas on how spin phenomena in solids can be rolled out for use in next-gen practical devices. For example, the electron spin with its two possible “up” and “down” orientations can represent 0's and 1's of binary programming, in analogy to current “on” and “off” states in conventional silicon chips. The basic computational model is thus unchanged. However, the advantages of spin over the charge current are numerous.

Every overclocker¹ knows that the temperature of a standard CPU can reach above 100°C. The heat is produced by a swarm of electrons being pushed through integrated circuits, and it takes a lot of extra power to cool them. Above this temperature, circuit boards, designed by fancy algorithms to minimise their size and avoid overheating, simply refuse to work. Even when cooling with liquid nitrogen, we get stuck at a mere 7.3 GHz clock frequency [1]. The power bills form a major part of the costs of running computer farms or data centres.² Even a single modern gaming rig can eat up to 600–800 W when you are playing your Crysis or Fallout. I do not have

¹Overclocking is the process of running a computer component at a higher clock rate (more clock cycles per second) than it was designed for or was specified by the manufacturer, usually practised by enthusiasts seeking an increase in the performance of their computers. (source: wikipedia.org)

²In 2009 it was estimated that Internet data centres worldwide consume about 2% of global electricity production or ca 30 billion US dollars. Most of this electricity undoubtedly comes from non-green sources and is mainly needed to keep the servers from overheating. To give a rough idea, performing two Google searches we generate about the same amount of CO₂ as boiling a kettle for a cup of tea [2]. In the era when global warming is no longer a controversy but rather a fact we are facing, it is worth keeping

to look far to find another example of the energy inefficiency of modern computers: last summer, I had to suspend my numerical simulations on the institute cluster because it was overheating. Things would be so much easier if instead of accelerating the charges, one could flip the spins of electrons. The latter requires less energy and produces hardly any heat at all [5].

The quantum nature of spins has even more to offer. Traditional MOS (metal-oxide-semiconductor) technology operates on classical bits collected in words of usually 64-bit size. Each word can represent numbers from 0 to $2^{64} - 1$, associated with different bits' configurations. Quantum bits, or qubits, can be in a superposition of all the bit states, effectively allowing to perform (via unitary evolution) up to 2^{64} classical computations in parallel! [6] The idea of quantum computations came from Feynman, who envisaged a machine capable of simulating generic quantum mechanical systems, a task intractable for classical computers. It would allow to solve one of the most nagging problems in physics, concerning the simulation of many-body quantum systems in condensed matter, chemistry, and high energies [7, 8]. The first quantum computer presented by D-Wave Systems in 2007 [9] did not convince the audience neither about its performance (it solved a Sudoku puzzle) nor its purely quantum nature [10], but—as its creators responded—at least it worked.

Last but not least, spin-based data storage is nonvolatile—unlike electric charge, spin polarisation does not disappear when the current stops. Hence, data can be accessed nearly instantly when a computer is switched on (without a lengthy boot-up), and stored permanently even when it is switched off. This feature opens a possibility of unifying data storage and processing. On the performance side, it will remove the main bottleneck faced by the modern CPUs, which often waste cycles waiting for the input data to be processed by their arithmetic units. Current numerical libraries are often optimised simply to provide the data to the algorithm at a maximum rate (for example, this is a major problem in matrix multiplication routines). With spintronics, data access would cost less and the optimisation criteria would change drastically, forcing a reimplementaion of practically every important numerical algorithm, from FFT to linear algebra. An area of economic activity which makes particularly heavy use of fast, low latency data access and processing is the oft-maligned algorithmic trading. It is certain that the top players in this field, such as Goldman Sachs and other Tier 1 banks, will use the spintronics devices in algo trading, increasing the trading volumes, market liquidity and the speed of price discovery.

Although all this might seem futuristic, spintronics has already bloomed with applications in daily life. The GMR (giant magnetoresistance) was

that in mind when we carelessly tap into Google [3]. Aware of these problems, IBM is developing a method to capture this heat and use it to generate electricity or warm our houses [4].

discovered independently in 1988 by future Nobel Prize laureates, Peter Grünberg of the KFA research institute in Jülich and Albert Fert of the University of Paris-Sud [11, 12]. Shortly after, the spin valve (Fig. 1.1a) exploiting this effect was put into mass production in read heads of magnetic hard disk drives by the spintronics guru Stuart Parkin and his colleagues at Almaden Laboratory of IBM.³ These first simple spin-based devices allowed to increase the data storage capacity about 10 000 times, whilst the manufacturing cost has dropped by 100. Ironically, the now venerable electromechanical disk drives are being supplanted by faster, nonvolatile and more reliable solid-state disks, which are not the spintronics' achievement. Then, one may think that spintronics has already reached its full potential in this field. Nothing of the kind—it quests after what is called the holy grail of memory technology, MRAM (magnetoresistive random access memory) (Fig. 1.1c) [14, 15]. It combines the advantages of all memory types used in our computers (the density of DRAM, the speed of SRAM and the nonvolatility of flash or hard disk) with none of their shortcomings, and in the future it will replace them with a combo memory chip.⁴ MRAM, initially employing the GMR and later its close cousin exhibiting higher magnetoresistance at room temperature, the TMR effect (tunnelling magnetoresistance) [16], competes with other types of novel memories at the stage of development, like the racetrack memory invented by Parkin (Fig. 1.1b) [17] or Spin Torque Transfer RAM [18, 19]. The described devices employ a spin-polarised current in metals, obtained by passing the electrons through a ferromagnetic material. The metal-based spintronics devices, together with various types of magnetic sensors, utilise the spin in a passive way—for detecting and reading tiny magnetic fields associated with magnetically stored data. They are certainly one of the most successful technologies of the past decade.

However, spintronics is projected to go beyond passive spin usage, and introduce new applications (or even new technologies) based on the active control of spins. In such devices, spins can either play a peripheral role in storing, processing and transmitting information by electric charges or handle these functions themselves, without involving charge at all. Their quintessential examples are the spin-FET (spin field-effect transistor) and spin logic [20]. The theoretical proposal of spin-FET by Datta and Das in

³GMR sandwich structures in read heads of magnetic hard disk drives were commercialised within ten years from the discovery of the fundamental physical effect, while a typical timeline from discovery to the marketplace is 20–30 years [13].

⁴In 2006 Freescale started selling the first commercial MRAM modules with 4 Mbit of memory for 25 US dollars a piece. Although still of low density and quite expensive, more than a million chips were sold. They already proved themselves in critical programs and data storage in extreme environments, and soon will be put to use in flight control computers on the next-generation Airbus aeroplanes. Various companies working on MRAM estimate a realistic timeframe for a cellphone, PDA or a Disk-On-Key with MRAM as 2011, while for a personal computer as 2015.

1990 was a watershed event in the field of spintronics [21]. However—despite long-running efforts—it has turned out to be its pratfall in the experimental field. In this dispirited atmosphere the advantages of such a device over traditional MOS transistors become increasingly questioned [22, 23].⁵ However, if the obstacles (lying mainly in the quality of spintronic materials) are overcome, spin-FETs will certainly play an important role as a complementary part of spintronic integrated circuits.

These and many other spintronics dreams shared by computer geeks, scientists and engineers, have the potential to revolutionise the IT industry as did the development of the MOS field-effect transistor 50 years ago [25]. Transition from electronics to spintronics will change drastically the IT landscape—not without introducing a number of new pitfalls. The unification of data storage with operating memory will radically simplify software systems design, bringing new challenges at the same time—notably, the greater potential for data corruption by running processes. The implications for information security are particularly interesting. On one hand, nonvolatile memory can be examined after the computer has been turned off, potentially revealing sensitive information.⁶ On the other, even partially eliminating the need for the caching of data simplifies the problem of securing the access to it. Furthermore, nonvolatile memory requires less energy to operate, which makes the system harder to eavesdrop on. It could also memorise internally read accesses performed on it, enabling easy creation of an audit trail [27]. Spintronic devices will interface naturally with quantum cryptography systems, greatly improving the security of data transmissions.

Although we cannot wait the new spintronics era to begin, we are aware that a new technology never comes as an immediate total replacement for the old. After all, we cannot shut down the world for a year and spend all our effort on upgrading our computers and other electronic devices to spin-based technologies. Spintronics and electronics will have to still coexist for some time, possibly decades. Also, in some cases the transition will never be made. (Mostly thanks to audiophiles' ears, transistors never fully replaced vacuum lamp devices. It is hard to imagine music lovers saying that jazz sounds better on silicon than on DMS, but I am sure somebody will eventually make such a statement.) Scientists predict that spintronic materials will only find widespread use in technology if they are similar to the conventional

⁵It is worth mentioning that there have been proposed many solutions for a spin transistor alternative to that originally proposed by Datta and Das. Recently the group of researchers employed the spin Hall effect to realise a device which actually works [24].

⁶With the advent of the cold boot attacks, one could say that this problem is with us already, despite the fact that we use a nominally volatile operating memory. Contrary to popular assumption, DRAMs used in most modern computers retain their contents for seconds to minutes after power is lost, even at operating temperatures and even if removed from a motherboard (this time prolongs to hours at liquid nitrogen temperatures), which is sufficiently long for malicious (or forensic) acquisition of usable full-system memory images [26].

semiconductors. For this reason, dilute magnetic semiconductors are a major focus of spintronics research. In particular, manganese-doped gallium arsenide, (Ga,Mn)As, is based on gallium arsenide, a direct gap semiconductor that hit the market back in the 1970s and nowadays is commonly used in various electronic and optoelectronic devices. Enhanced with magnetic properties, the material can realise the full potential of spintronics as it offers the integration of magnetic and semiconductor properties, allowing the combination of data processing and storage in one chip.

However, there is a serious obstacle on the way to the commercialisation of DMS-based spintronic devices—their operation temperature. The magnetic order in these materials occurs below the Curie temperature, which—despite long years of research effort—does not exceed 200 K in (Ga,Mn)As and other III–V DMS [28]. Theoretical and experimental quest toward room-temperature ferromagnetism in these systems is being pursued by many laboratories, from different points of view and often shaping new research directions. For its purposes, (Ga,Mn)As is identified as a prototypical DMS and used as a test bed for various spintronic device concepts and functionalities. In this context, my dissertation work can be seen as a contribution to this application-oriented struggle. For example, the theory of spin waves it explores is a basis of the mechanism of current-induced domain wall motion employed in racetrack memories, while the anomalous Hall effect is an important tool for probing spintronic properties as well as spin generation and manipulation in DMS. Sceptics have raised doubts whether we will ever succeed [29]. Even if they are right, research in the solid-state physics has value of its own as the obstacles we encounter are often catalysts for fundamental investigations. For example, the exclusion of magnetic flux from a superconductor was interpreted by Anderson as generation of mass for a gauge boson [30]—the effect popularised by Higgs himself plays a central role in the electroweak theory [31]. Statistical Chern-Simons gauge fields in field theory are now commonly used to describe the quantum Hall effect [32], which also started the experimental search for a related phenomenon of the parity anomaly in (2+1)-dimensional electrodynamics in solid bodies [33]. The significant development of quantum physics over the 20th century have resulted from efforts to theoretically describe ensembles of atoms and their interaction, leading to fundamental theoretical and numerical methods, like the Metropolis algorithm for solving of the many-body Schrödinger equation [34]. To these I added two penn’orth predicting the cycloidal spin structure on the surface of the zincblende DMS structures or formulating mathematical methods, like the Löwdin variation-perturbational calculus generalising the RKKY theory to more complex, realistic energy bands, an exact formula for the sum of states of classical spins, and a general method used for modelling spin-wave excitations (enforcing the correct constraint on their number). The detailed outline of my work will be provided in the next chapter.

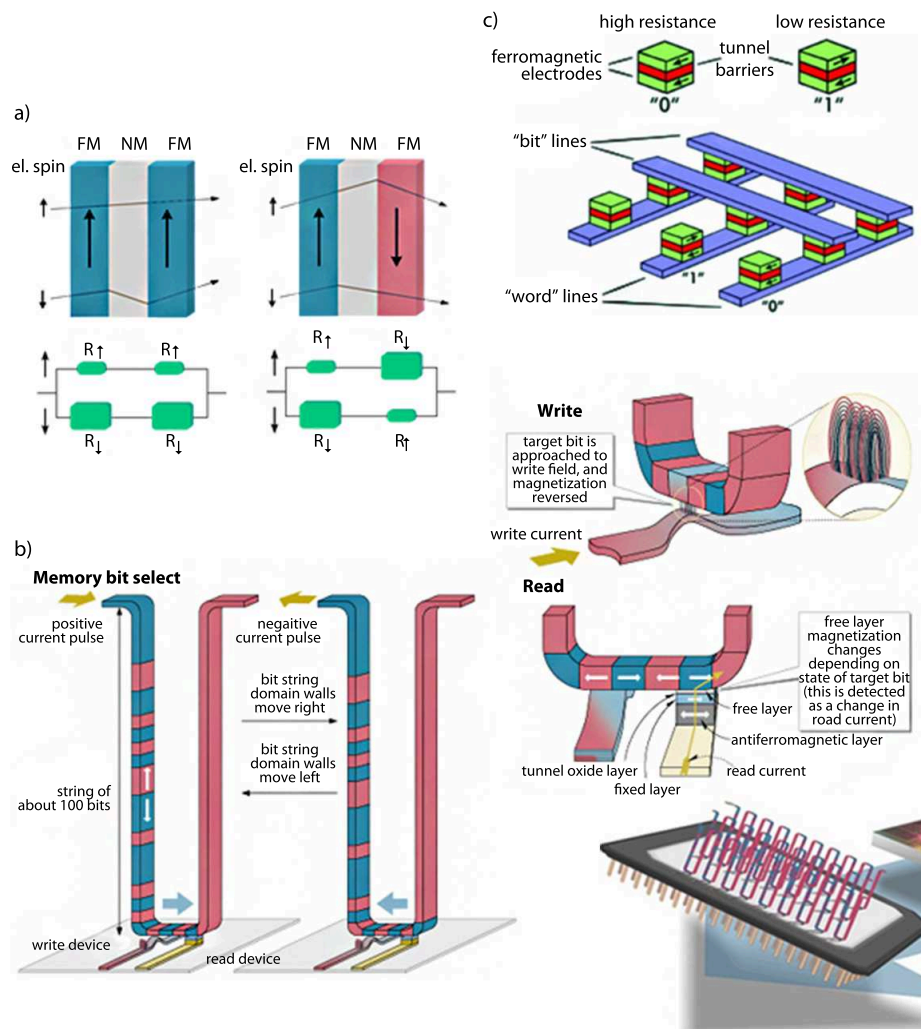


Figure 1.1: Examples of spintronic devices. In the GMR spin-valve (a) the current flowing through ferromagnetic (FM) layers separated by a nonmagnetic (NM) spacer depends on the relative magnetisation of the two FM layers. The effect results from the electron scattering at the interfaces of the structure, which depends on whether the electron spin (\uparrow or \downarrow) is parallel or antiparallel to the layer magnetic moment. It can be interpreted as a parallel coupling of resistances that grow when the electron spin is opposing the magnetisation of the layer. S. Parkin's racetrack memory (b) uses a spin-coherent electric current to move magnetic domains along a nanoscopic permalloy wire. The domains pass by a GMR read head positioned near the wire, which can retrieve bit patterns that have been encoded by a magnetising write head. MRAM (c) combines a magnetic device with standard silicon-based microelectronics. The magnetic tunnel junctions it employs as storage cells rely on TMR. The cells have two stable magnetic states corresponding to high or low resistance and retain their values without any applied power. They can be read by sensing the resistance, while writing is carried out by the magnetic fields generated from the current flowing in the bit and word lines. Images by Wikipedia and IBM Corporation.

Chapter 2

Motivation and outline

The motivation for my dissertation work has been the experimental research conducted by Professor Hideo Ohno and his group at Tohoku University. They investigated the magnetic-field and current-induced domain-wall motion [35] and achieved the magnetic state control in the field-effect transistor structures utilising a thin-film ferromagnetic (III,Mn)V channel [36, 37]. Their results are crucial for novel spintronic applications, including race-track memories [17], domain-wall logic circuits [38], spin-polarised current control and magnetisation characterisation.

The above problems are linked to two fundamental physical effects: spin waves and magnetic stiffness, which determine the magnetic domains' parameters, and the anomalous Hall effect, which enables the control of magnetisation through electric current. These and other important characteristics of (Ga,Mn)As, such as the Curie temperature and magnetocrystalline anisotropies, have been the focal point of my thesis work.

The thesis is organised as follows.

To begin with, I describe (Ga,Mn)As as a dilute magnetic semiconductor, its crystal structure, the origin of ferromagnetism in this system and the details of the interactions shaping its band structure, in Chs. 3–5. The different band structure computational schemes that I have used in my investigations are reviewed in Ch. 6.

In Chapter 7, I analyse the hole-mediated magnetic order in dilute magnetic semiconductors [39, 40]. The presented basic statistical model gives an intuitive overall picture of ferromagnetism in these systems. To derive it, I have used the proposed exact formula for the sum of states of classical spins. I also provide a physically transparent perturbation-variational method of treating the systems of localised magnetic moments coupled by spin carriers, based on the Löwdin calculus [41]. It is an extension of the RKKY theory [42], which—contrary to the original—is self-consistent (takes into account the dynamics of free carriers) and can accommodate any band structure (of any number of bands, with the spin-orbit coupling and the

values of spin-splitting up to those encountered in (III,Mn)V ferromagnets). Employing this method, I obtain the effective Hamiltonian for the lattice spins in a dilute magnetic semiconductor—the starting point for my further investigations.

Chapter 8 contains the application of the obtained Hamiltonian to the calculations of the Curie temperature and uniaxial anisotropy, using the different band structure computational schemes described in Ch. 6. In particular, I compare the known results of the 6-band $k \cdot p$ method [40] with the new approaches utilising the 8-band $k \cdot p$ and two tight-binding (20-orbital sps^* and 40-orbital $spds^*$) models. I obtained good agreement between all of them.

To model spin waves in Ch. 9, I diagonalise the effective Hamiltonian using the Bogoliubov transform adapted to systems with broken inversion symmetry, thus extending the symmetric case solved by König *et al.* [43]. Then I turn to the macroscopic theory of these systems and describe their micro-magnetic exchange and anisotropy constants. I find a relativistic correction to the exchange stiffness constant resulting from the spin-orbit coupling, the anisotropic exchange stiffness constant T , and suggest new physical effects it may induce. In thin layers of (Ga,Mn)As I show that the spins in the ground-state form a cycloid which accounts for the surface anisotropy of the diagonal in-plane directions. Next, I discuss the spin-wave contribution to magnetisation and propose its self-consistent theory which amends the flaws of the previous approach [44]. Finally, I introduce a normalised spin-wave stiffness parameter D_{nor} , which may be a convenient tool for the experimentalists to estimate the spin-wave stiffness value D given the Curie temperature and the magnetisation of the sample, and use it to reconstruct the experimental data.

Moving on to the second major theme of my dissertation, Chapter 10 deals with the anomalous Hall effect. I begin by reviewing the theory of the AHE. Next, I compare the results for the Berry curvature and the AHE conductivity obtained using different band structure computational schemes, discussing the differences between the 8-band $k \cdot p$ and two tight-binding parametrisations and the previously employed 6-band $k \cdot p$ approach [45]. The anomalous Hall effect is shown to exhibit qualitative dependence on the details of the band structure beyond the six hole bands. In particular, the inversion asymmetry of the zincblende lattice is shown to lead to the negative anomalous conductivity sign. This contrast between the previously revealed robustness of the 6-band model when applied to the Curie temperature, magnetocrystalline anisotropy field and spin waves will prompt me to distinguish between *static* and *dynamic* properties of DMS, the simplest $k \cdot p$ approaches being sufficient for the first but not for the other. To conclude, I compare the obtained theoretical results with the experimental data for bulk and thin samples, and discuss possible origins of the observed discrepancies, including the additional mechanisms occurring in thin layers. The

AHE simulations in the latter were the most laborious part of my thesis work, which unfortunately was not finalised due to the lack of time.

The work presented in this dissertation is summarised in Ch. 11, which also provides suggestions for future research. To model (Ga,Mn)As numerically, I developed a modularised, object-oriented library employing the different computational schemes (Ch. 6). The details of its implementation are listed in Appendix A.

Significant part of the results has been already published in Refs. [46], [37] and [47]. The first paper contains the comparison of the various band structure calculation methods with respect to the mean-field Curie temperature and uniaxial anisotropy (Ch. 8) and the results from Ch. 10 for the AHE in bulk samples. The second one, published in *Physical Review Letters* together with the group of Professor Hideo Ohno at Tohoku University, contains the analysis of the experimental measurements for the AHE in thin layers supported by my theoretical results (Sec. 10.4.2). Finally, Ref. [47] includes the exposition of the proposed self-consistent Löwdin calculus, the derivation of the effective Hamiltonian for lattice spins and its application to the spin waves in (Ga,Mn)As, gathering the results for the exchange stiffness and anisotropy constants (including the comparison with experiment), cycloidal ground-state spin structure, and the spin waves' contribution to magnetisation, as described in Chs. 7 and 9.

Chapter 3

(Ga,Mn)As as a dilute magnetic semiconductor

3.1 Brief history

The first ferromagnetic semiconductor, CrBr₃, was discovered by Tsubokawa in 1960 [48]. Shortly after, the identification of magnetic properties in concentrated rare-earth chalcogenide compounds, like Eu-chalcogenides and Cr-chalcogenide spinels, dispelled any doubts about the possible existence of ferromagnetic semiconductors [49–51]. Studies of these materials revealed that their fascinating properties arise from magnetic moments stemming from the partially filled $4f$ (or $3d$) shells of the involved rare-earth ions on each lattice site. A certain type of indirect exchange coupling these moments leads to full spin polarisation, and spectacular magnetic and magneto-optical properties, like the drastic redshift of the optical absorption edge [52]. Moreover, the properties of these materials strongly depend on the concentration of free charge carriers, created by doping with suitable impurities [53, 54]. Based on these findings, the first ferromagnetic semiconductors were described by the s – f (or s – d) model of localised spins coupled by conduction band electrons [55], demonstrating the relevance of an interplay between semiconducting and magnetic properties. Despite these interesting results, extreme difficulties in growing such crystals and their low Curie temperatures (even for optimum doping and processing) hindered their further studies till date [56].

The idea of combining magnetism with semiconductor physics was brought back to a new ground in the late 1970s. Professor Robert Gałazka and his colleagues from the Institute of Physics of Polish Academy of Sciences in Warsaw, inspired by their friend Professor Jacek Furdyna of Purdue University in Indiana, cast crystals which were ordinary II–VI or IV–VI semiconductors diluted with a small amount of transition-metal atoms [57, 58]. Initially dubbed semimagnetic semiconductors and later renamed to

dilute magnetic semiconductors, they were such alloys as $\text{Cd}_{1-x}\text{Mn}_x\text{Te}$, $\text{Cd}_{1-x}\text{Mn}_x\text{Se}$ and $\text{Hg}_{1-x}\text{Mn}_x\text{Te}$ (for II–VI-based DMS) or $\text{Pb}_{1-x}\text{Mn}_x\text{Te}$, $\text{Sn}_{1-x}\text{Mn}_x\text{Te}$ and $\text{Ge}_{1-x}\text{Mn}_x\text{Te}$ (IV–VI-based). In these materials the valency of cations matches that of Mn, which indicates its high chemical solubility on the cation lattice sites. Its relatively small concentration x does not compromise the quality of the host, meaning that the semiconducting properties (optical and transport effects) can be probed. At the same time, the presence of Mn in the form of magnetic Mn^{2+} ions [59] accounts for the dramatic modification of the material properties upon application of magnetic fields—the band gap energy can be significantly shifted [57]. The ground state of Mn^{2+} in a tetrahedral environment of the semiconductor crystals is an orbital singlet, hence the crystal field has negligible effects on the magnetic properties of the ion. This, together with the simplicity of the host crystal structure, makes the materials readily tractable to theoretical studies. The model proposed explained their physics with the strong exchange coupling between s and p band electrons and $3d$ electrons on the Mn ions. The resulting Mn spin ordering in II–VI-based DMS is mainly antiferromagnetic, which produces paramagnetic, antiferromagnetic or spin glass behaviour, while ferromagnetism in these systems has been reported much later and below the very low temperature of 2 K [60]. Despite the low Curie temperatures, the alloys attracted much interest for several reasons. Their ternary nature gives the possibility of tuning the lattice constant and band parameters by varying the composition of the material, thus making it possible to engineer the band gap [57]. The substitutional Mn atoms display highly efficient electroluminescence, which has already found applications in flat panel displays. Finally, the interplay between the magnetism and semiconductor physics results in various interesting phenomena, which are not present in conventional nonmagnetic semiconductors, like the giant Faraday rotation, semiconductor-metal transition induced by magnetic field or magnetic polaron effects [57]. On the other hand, because the high solubility is concomitant with an isovalent doping process, the transition metals in the II–VI compounds do not generally contribute band carriers on their own. The resulting difficulties to dope II–VI compounds to p- and n-type, together with the presence of instabilities inherent in these materials, hampered the study of the transport properties and plans for potential applications in traditional electronics devices. This was not the case of IV–VI-based DMS, which can be grown with high concentrations of free band carriers through the control of native defects, and thus achieve higher Curie temperatures, as it was first demonstrated by Professor Tomasz Story and colleagues in PbSnMnTe [61]. Recently reported Curie temperatures reach 100 K (in Fe doped GeTe films [62]), however they are limited by the effect of diamagnetism of the host crystal.

A younger class of related materials is based on III–V semiconductors, such as GaAs and InAs [63]. These direct gap semiconductors hit the market

in the 1970s and became commonly used in electronics and optoelectronics in the form of efficient infra-red light-emitting diodes (IR LED), magnetic sensors, microwave transistors (e.g. in cellular phones), semiconductor lasers (in compact disk players) or solar cells. This provided additional motivation to introduce magnetism to these systems. A major obstacle was the low solubility of magnetic elements in the compounds under equilibrium conditions. The transition metals are more similar chemically to the group II than the group III atoms, which had enabled the straightforward doping of high Mn concentrations into II–VI materials. Their dissimilarity to gallium results in rather low solubility on the gallium sites, namely well below 1% [64]. When the concentration of magnetic elements exceeds the solubility limit, formation of the extremely stable second phase (MnAs, GaMn₃) occurs. Since the magnetic effects are roughly proportional to the concentration of the magnetic ions, one did not expect a major change in the materials' properties within the solubility limits of the order of 10^{18} cm⁻³ or less. The breakthrough came with the advent of low-temperature molecular-beam epitaxy (MBE), which enables to grow crystal films under conditions that are far from thermal equilibrium. At low temperature MBE growth, there is not enough thermal energy available to form the second phase, and yet there still exists a local potential landscape that allows epitaxial growth of uniform layers, one after another, forming a monocrystal. The first such III–V DMS was reported in 1989 with paramagnetic n-type (In,Mn)As thin layers prepared on GaAs(001) substrates by Professor Hiro Munekata and colleagues (including Professor Leo Esaki himself) at IBM Thomas J. Watson Research Centre [64]. By setting the substrate temperature ($\approx 200^\circ\text{C}$) during epitaxial growth far below the previously used values ($\approx 400\text{--}450^\circ\text{C}$), they avoided the formation of the second phase in the regime beyond the equilibrium solubility limit. In this way, the incorporation of Mn ions up to $x = 0.2$ in the form of In_{1-x}Mn_xAs was realised. In 1991 the activation of holes from incorporated Mn ions was realised for the (In,Mn)As layers prepared at the temperature of 300°C [65]. The magnetotransport measurements (in particular, of the anomalous Hall effect) established the hole-mediated ferromagnetism in p-(In,Mn)As in 1992 [66, 67] and in the strained p-(In,Mn)As/(Al,Ga)Sb heterostructure in 1993 [68]. The studied ferromagnetic, electronic and optical properties of these materials revealed their mutual correlations and possibilities to control them by changing the material composition and strain. However, it was the discovery of ferromagnetic (initially at temperatures up to 60–110 K) p-type (Ga,Mn)As [69], born after the study of GaAs:MnAs [70] in 1996, which envisaged the potential of dilute magnetic semiconductors for technology. In 2001, Professor Tomasz Dietl and colleagues [40] presented the *p-d* Zener model of the hole-mediated ferromagnetism in these systems.

The same paper has drawn attention to wide band gap semiconductors, predicting room temperature ferromagnetism in GaN and ZnO containing

5% Mn and a high hole concentration of 0.35 nm^{-3} . The compounds with smaller anions have smaller lattice constants, which leads to greater p - d hybridisation, and smaller spin-orbit coupling, which scales with the atomic number as Z^4 and (in the simple picture) has a detrimental effect on the Curie temperature. The p-type carriers are chosen for their much stronger exchange coupling with the magnetic centres than that of the s electrons. However, their high concentrations are unlikely in the nitrides and oxides. Although the hole-mediated ferromagnetism in these systems has been observed [71], it is still unclear whether it comes from substitutional Mn ions in the semiconductor lattice or unwanted precipitates. The nature of ferromagnetism in these systems has been studied extensively by *ab initio* methods [29, 72], also at our Institute [73, 74].

Nowadays, ferromagnetism in semiconductor-based materials remains the subject of intense interest in solid state physics. Theoretical treatments of carrier-mediated ferromagnetism and experimental investigations toward room-temperature III-V-based DMS have been pursued by many laboratories, from various points of view and shaping new research directions. They identified (Ga,Mn)As as a prototypical DMS. Although the progress in synthesizing and controlling magnetic properties has been astounding, the highest reported Curie temperatures in this material are around 190 K (and lower in (In,Mn)As) [28]. Until the ferromagnetic phase is achieved at room temperatures, dilute magnetic semiconductors will not realise their full potential in practical applications.

3.2 Crystal structure

As already mentioned, isomorphic crystals of manganese-doped gallium arsenide, (Ga,Mn)As, are fabricated by randomly substituting a small amount of Mn, typically 2% to 6%, for cation sites of the GaAs semiconductor host lattice. Hence, they have a zincblende structure similar to that of GaAs, as depicted in Fig. 3.1. It is typical of the III-V compounds (except for nitrides, which are stable in the wurzite structure), as well as II-VI compounds and group IV elements.

In GaAs, the outermost s - and p -like atomic orbitals from the neighbouring Ga and As atoms (three from the $4s^24p^1$ orbital configuration of Ga and five from the $4s^24p^3$ configuration of As) hybridise in the crystal to form covalent bonds. This type of bonds is responsible for the semiconducting properties of the compound. Additionally, the two shared As electrons forming each Ga-As bond are more attracted toward the atom with largest nucleus, As. This gives some ionic character to the bond, which may result—for instance—in piezoelectric properties of the GaAs crystal [75].

The crystal structure of GaAs is determined by the spatial arrangement of hybridised sp^3 tetrahedral orbitals around atoms. Each orbital lobe con-

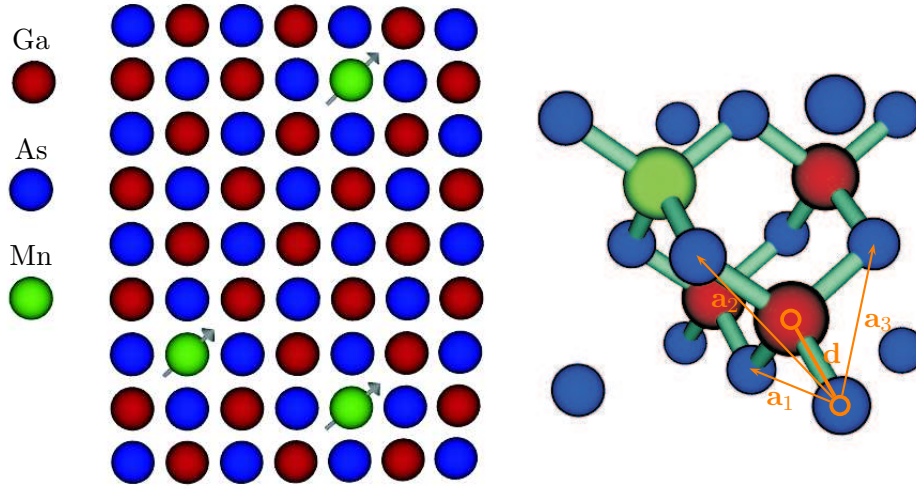


Figure 3.1: (Ga,Mn)As lattice and its zincblende unit cell with the two-atom primitive cell marked in thick orange lines, its translation vectors (\mathbf{a}_1 , \mathbf{a}_2 , \mathbf{a}_3) and nonprimitive translation vector \mathbf{d} .

tains an electron pair shared with the neighbouring atoms. Accordingly, every atom is surrounded by four such nearest neighbours of the other sort located at the corners of a regular tetrahedron.¹ Its local symmetry is isomorphic to T_d , the point group containing 24 symmetry operations representing the proper and improper rotations of a methane molecule [76]:

- E : identity;
- eight C_3 operations: clockwise and counter-clockwise rotations of 120° about the $[111]$, $[\bar{1}11]$, $[1\bar{1}1]$ and $[11\bar{1}]$ axes, respectively;
- three C_2 operations: rotations of 180° about the $[100]$, $[010]$ and $[001]$ axes, respectively;
- six S_4 operations: clockwise and counter-clockwise improper rotations of 90° about the $[100]$, $[010]$ and $[001]$ axes, respectively;
- six σ operations: reflections with respect to the (110) , $(1\bar{1}0)$, (101) , $(10\bar{1})$, (011) and $(01\bar{1})$ planes, respectively.

The above symmetry operations do not include inversion, as the inversion symmetry at the midpoint of each Ga–As bond is broken. If the atoms of the compound were identical, the symmetry would be restored, resulting in

¹It is a reasonable approximation that the orbitals of each atom in the crystal overlap with those of its nearest neighbours only. I will assume it in numerical modelling of the semiconductor lattice by the tight-binding methods described in Section 6.2.

point group O_h (of a cube) with twice as many symmetry operations. Hence T_d is a subgroup of O_h .

The whole GaAs lattice can be generated by translating the primitive cell containing two atoms: Ga and As, which are marked by orange circles in Fig. 3.1b. For the sake of convenience in numerical modelling, I choose the origin at the As site. The three primitive vectors $\mathbf{a}_1 = \frac{a}{2}(1, 1, 0)$, $\mathbf{a}_2 = \frac{a}{2}(1, 0, 1)$ and $\mathbf{a}_3 = \frac{a}{2}(0, 1, 1)$ (orange arrows), turn from this point toward the centres of the faces of the cube adjacent to this site. The primitive translations constitute an invariant symmetry group. They generate a crystal structure characterised by a face centred cubic Bravais lattice with the basis given by the blue As atom at the origin plus the red Ga atom at the centre of the tetrahedron. It can be thought of as two chemically distinct interlocking fcc sublattices, displaced from each other by one-quarter of the unit cube main diagonal, $\mathbf{d} = \frac{a}{4}(1, 1, 1)$.

The combinations of the primitive translations with the rotations of the T_d point group form the space group of zincblende, T_d^2 (or $F\bar{4}3m$ in the international notation, which can be deciphered as the cubic lattice with a four-fold rotation-inversion axis, a three-fold rotation axis, and mirror planes perpendicular to it). The space group is symmorphic. However, if again the two atoms in the primitive cell were identical, the group would contain elements combining the operations of the O_h point group, the primitive translation group and, additionally, a nonprimitive translation by vector \mathbf{d} . Together they form the nonsymmorphic space group O_h^7 ($Fd\bar{3}m$), which generates the diamond lattice. The group contains the inversion operation, which consists in the inversion about the origin point plus a translation by \mathbf{d} . The lack of this particular symmetry operation in the crystal lattice may result in many interesting phenomena, such as the parity anomaly, current- and strain-induced spin polarisation, spin dependent scattering or various electric and optical effects [77, 78]—I would venture to say, all phenomena produced by polar-vector perturbations. The so-called bulk inversion asymmetry will be addressed in the further course of this thesis and its effect on magnetotransport properties in ferromagnetic (Ga,Mn)As will be demonstrated in Ch. 10.

The (Ga,Mn)As samples are usually grown epitaxially on a buffer, forming layers of controlled thickness with abrupt interfaces. These lower the symmetry of the samples to D_{2d} or C_{2v} , as will be explained further in Sec. 5.4.2. Thicker layers are usually satisfactorily modelled as bulk crystals of the T_d^2 or O_h^7 symmetry (the latter neglecting the bulk inversion asymmetry). However, in thinner samples (up to few tens of nanometres thick), the effects brought about by the presence of the interfaces may become very important, like in the case of spin waves in Sec. 9.4.1 and the anomalous Hall effect in Sec. 10.4.2.

3.3 Mn impurities

The (Ga,Mn)As crystal consists of a GaAs host with Mn ions randomly replacing Ga at the cation sites, as shown in Fig. 3.1. The preferred Mn position results from the nominal electronic structure of the atoms involved: $[\text{Ar}]3d^{10}4s^24p^1$ for Ga, $[\text{Ar}]3d^{10}4s^24p^3$ for As and $[\text{Ar}]3d^54s^2$ for Mn; Mn is most similar to Ga. Its two $4s$ electrons participate in crystal bonding in place of the Ga $4s$ electrons. Its half-filled d shell forms a local moment with zero angular momentum L and spin $S = \frac{5}{2}$, according to the Hund rules. Due to the missing $4p$ valence electron, the impurity acts as an acceptor—it can attract a hole from the As valence shell. If the hole binds on the acceptor, they form together a neutral complex $A^0(d^5 + \text{hole})$, which is most probably encountered in bulk crystals grown under equilibrium conditions of low Mn contents and free of unintentional defects, as confirmed with various experimental techniques [79–82]. Its five d electrons occupy a triplet of bonding orbitals of t_{2g} symmetry, $3d_{xy}$, $3d_{yz}$ and $3d_{xz}$, and two antibonding states of e_g symmetry, $3d_{x^2-y^2}$ and $3d_{z^2}$, into which the $sp-d$ orbitals are split by the tetrahedral crystal field. The hole bound on this centre occupies one of the antibonding states of the dominant As $4p$ character. Quite differently, in MBE-grown epilayers the high hole concentrations increase the screening of Coulomb potentials of $3d^5$ cores, resulting in a low binding energy of the holes [83, 84]. Then, the substitutional Mn forms an ionised $A^-(d^5)$ state ($S = \frac{5}{2}$, $L = 0$, Landé factor $g = 2$), Mn^{2+} , while the hole is delocalised and contributes to the p-type conductivity in these materials [85, 86]. The conversion from the first situation to the other [79] is called the Mott insulator-metal transition [87].

Only a part x_{sub} of the total Mn content x_{tot} , quoted in experimental works as x in $\text{Ga}_{1-x}\text{Mn}_x\text{As}$, forms substitutional defects. The low-temperature MBE-grown material has a tendency toward self-compensation, which becomes apparent at higher Mn concentrations [88]. In effect, the remaining part x_i of Mn integrates into the lattice in the form of interstitial ions, while a part of As atoms x_a substitutes cation sites forming antisite defects. In this sense, instead of the $1-x$ and x subscripts in $\text{Ga}_{1-x}\text{Mn}_x\text{As}$ relating to the total Mn content x_{tot} , one should put $1-x_{\text{sub}}-x_a$ and $x_{\text{sub}} = x_{\text{tot}} - x_i$, respectively. Still, not the whole x_{sub} has to contribute to the magnetic moment.

Both interstitials and antisites can have a severe impact on the electric and magnetic properties of (Ga,Mn)As epilayers. First, the Mn interstitials tend to form pairs with substitutional Mn acceptors with approximately zero net magnetic moment of the pair, reducing the effective local-moment doping to $x_{\text{eff}} = x_{\text{sub}} - x_i$, e.g. for $x_{\text{tot}} > 1.5\%$, $x_i/x_{\text{tot}} = 0.2$ [89, 90]. Furthermore, both Mn interstitials and As antisites are double-donors—they compensate the hole density as $p = \frac{4}{a_0^3}[x_{\text{sub}} - 2(x_i + x_a)] = \frac{4}{a_0^3}[\frac{3}{2}x_{\text{eff}} - \frac{1}{2}x_{\text{tot}} + 2x_a]$. (To make the system of the above equations solvable, I will have to set x_a to

zero in further considerations.) The unintentional defects can be partially removed by post-growth annealing [91]. During this process, the interstitial Mn, characterised by relatively high mobility in GaAs lattice, migrates to the surface where it is passivated and can be removed by chemical etching. Usually both x_{eff} and p will rise, but still remain smaller than it would result from the nominal Mn doping [92].

Before I can move on to the next chapter treating about the electronic structure of (Ga,Mn)As, one thing needs to be made clear. At the beginning, I have assumed that the concentration of impurities in the material is small enough to safely say that the host crystal structure remains unaffected. Thus, it can be modelled as that of pure GaAs. In fact, the GaAs lattice diluted by Mn atoms is not even crystalline (for the point of view of its electronic structure): the potential felt by the electrons has no exact translational symmetry due to the random distribution of Mn at its sites. However, the random perturbation of the periodicity averages out, which allows us to use the virtual crystal approximation [93]. It restores the crystalline structure of the alloy by treating it as an ideal crystal of an effective material that produces the same periodic potential felt on the average by the electrons in the alloy. In the course of this work, this approximation will justify e.g. performing the Fourier transform in the spin-wave calculations.

3.4 Lattice strain

The Mn impurities in the GaAs lattice do not affect its crystalline structure, as assumed in previous sections. In spite of that, other aspects of Mn doping become important when we proceed to describe realistic heterostructures of (Ga,Mn)As grown on different substrates. They concern the lattice constant and its mismatch between the two layers, which leads to biaxial strain in the sample plane.

Considering the values of the atomic radii of Mn (1.17 Å) and Ga (1.25 Å), simple intuition suggests that replacing Ga with Mn may lead to a very small reduction of the lattice constant of a pure GaAs, a_0 . The latter can be calculated from the Vegard law, which says that for the Mn content x the lattice constant of $\text{Ga}_{1-x}\text{Mn}_x\text{As}$ equals $a = a_0 + x(a' - a_0)$, where a' is the lattice constant of a hypothetical MnAs crystal [94]. Such results were observed experimentally for very small x_{tot} [95]. However, in the majority of samples the lattice constant—quite surprisingly—increases with increasing concentration of Mn [96–98]. This effect is primarily due to antisite defects found in large numbers in low-temperature GaAs, and increasing with Mn doping [99]. Then a can be further increased by emerging Mn interstitials. These two types of defects lead to significant expansion of the lattice, which can overcome the minor effect of substitutional Mn. Still, there exist a wealth of experimental data yielding the lattice constant

values too large to be explained by the unintentional defects only [95, 97]. That being said, the common statement that the (Ga,Mn)As lattice expands with respect to pure GaAs is just an experimental observation, while its explanation is shrouded in mystery so far.²

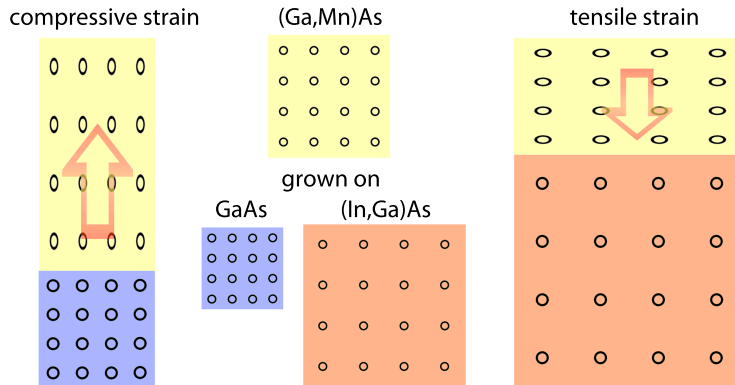


Figure 3.2: Epitaxial growth of (Ga,Mn)As on GaAs (left) or (In,Ga)As (right) produces either compressive or tensile strain in the plane of the layer, respectively.

The realistic (Ga,Mn)As samples are pseudomorphically grown on different substrates. The lattice mismatch between the substrate and the epilayer leads to the biaxial strain in the sample plane. Indeed, growing (Ga,Mn)As on a GaAs substrate, which has a smaller lattice constant (as described in the previous paragraph), leads to compressive strain in the plane of the layer [100]. In this case, sample annealing, which removes Mn interstitials, leads to the decrease of the growth strain [89]. On the other hand, epilayers grown on a substrate with a larger lattice constant, e.g. InP or thick relaxed (In,Ga)As buffers, are subject to tensile strain [69]. Both situations are presented in Fig. 3.2.

The strain energy is accumulated as more and more material is deposited on the surface, until some mismatch-dependent critical layer thickness is reached. Then strain relaxation begins with the formation of lattice defects and degradation and roughening of the growth front, as the lattice constant subsequently approaches the unstrained value. The strain tensor is defined as the relative difference between the strained, a_{str} , and unstrained, a , lattice

²Even in (Ga,Mn)As with Mn only substituting Ga atoms, the interstitial manganese having been removed by low-temperature annealing (which can be verified e.g. by SQUID measurements), the observed lattice constant is still much higher as compared to the reference sample (low-temperature MBE-grown GaAs). This increase might stem from e.g. defects of some sort, electrically neutral or compensated, which have not been identified heretofore. (The above considerations are based on the valuable and thorough comments I received from Dr J. Sadowski, *MAX-Lab, Lund University, Sweden.*)

constants' values with respect to the crystallographic directions:

$$\epsilon_{xx} = \epsilon_{yy} = \frac{a_{\text{str}} - a}{a}, \quad \epsilon_{zz} = -2\epsilon_{xx}c_{12}/c_{11},$$

where $c_{12}/c_{11} = 0.453$ is the ratio of moduli of elasticity, as defined by the Hooke's law [101, 102].

The lattice strain yields qualitative effects on the electronic band structure and is one of the driving forces behind the complex, anisotropic magnetic behaviour of (Ga,Mn)As [40, 103, 104]. These problems will be elaborated in Ch 8.

Chapter 4

Origin of magnetism in (Ga,Mn)As

4.1 Exchange interaction

The local Mn moments described in Sec. 3.3 are the most obvious source of magnetism in (Ga,Mn)As. The question about the mechanism of the magnetic ordering, however, is more complex and recondite. To give a generic answer I shall start by looking at the spins of electrons in an outer $3d^5$ atomic shell of the substitutional Mn. The Pauli exclusion principle prohibits any two of them to have identical properties: no two electrons can be in the same location at the same time and have spins in the same direction.¹ Thus, the electrons follow the Fermi–Dirac statistics

$$f = \frac{1}{\exp\left(\frac{E-E_F}{k_B T}\right) + 1},$$

they occupy energy levels E from the lowest available to the uppermost called the Fermi level, E_F . The Fermi-level states spread with the growth of the temperature T . Putting this together with an ordinary Coulomb repulsion of negative electron charges, one obtains what is commonly called the exchange interaction. It governs the behaviour of electrons with respect

¹Why does it happen? The answer lies somewhere at the core of best currently known theory explaining the subatomic world—the relativistic quantum mechanics. It was founded in 1928 by Dirac who combined quantum mechanics with special relativity to explain the behaviour of the electron—he gave the electron a spin. Ten years later Fierz and Pauli, on the ground of the postulated spin-statistics theorem, divided all fundamental particles into bosons with integer spin, occupying symmetric quantum states, and fermions with half-integer spin, occupying antisymmetric states, meaning that no other values of spin can exist. From this distinction the Pauli principle follows. Greats like Feynman, Schwinger, Streater and Berry racked their brains looking for the foundation of this one of the most important pillars of the modern understanding of Nature. The last proposed

to their spin; it is practically enough to derive such paradigms of physics as the Ising, Heisenberg or Hubbard model.

Similarly to spin, the exchange interaction is a purely quantum phenomenon, which has no analogy in the classical world.² It arises from the Coulomb interaction and is characterised by an electrostatic potential integral. It competes with the spin-orbit interaction, which couples the spin and orbital momenta of the electron (described in Sec. 5.3 in more detail). In this context, the two interactions are often respectively referred to as non-relativistic and relativistic. This seems to be at odds with the fact that the exchange interaction arises from the spin statistics, which results from the Lorentz invariance of the spinor field operators in the relativistic quantum field theory. Actually, the latter being the epistemically fundamental theory, gives a tint of the relativistic character to every physical phenomenon. On the other hand, the relativistic character of the spin-orbit interaction results from the Lorentz invariance of the electromagnetic field.

Since on the atomic scale the strength of the spin-orbit interaction is much lower than that of the exchange energy, ca $1 Kk_B$ vs. up to $1000 Kk_B$, one is tempted to think that the former has no chance to make its mark. In fact, comparing the Bohr radius, $a^* \approx 0.053$ nm, representing the nonrelativistic scale, and the fine structure constant, $\alpha = 1/137$, representing the relativistic scale, one can see that the two types of exchange become comparable at the length scales considered in solid bodies, $a^*/\alpha \approx 7$ nm [107]. Thus, one can expect to observe the veritable cornucopia of physical effects resulting from the interplay of these two mechanisms, many of which are discussed in this thesis: magnetic anisotropies (Sec. 8.2) and formation of domain walls, effective magnetic fields of Bychkov–Rashba and Dresselhaus (Sec. 5.4) and Dzyaloshinskii–Moriya interaction, as well as their important consequences on physics of spin waves (Ch. 9) and the anomalous Hall effect (Ch. 10).

Underlying the microscopic origin of the first Hund rule, the exchange interaction maximises the total moment within the half-filled Mn d shell to the value of $S = \frac{5}{2}$, already mentioned in Sec. 3.3. Similarly, it couples the s and d electrons on the same Mn site. On the other hand, the phenomena of magnetic order require interaction between Mn moments, and thus the exchange coupling acting between electrons residing at different sites. Such is the coupling between the d electrons of the Mn substituting Ga sites and delocalised p holes which are more heavily weighted on As sites of the (Ga,Mn)As lattice. The last two interactions result from the sp – d hybridisation of atomic orbitals, and are called the s – d and p – d exchange coupling.

an exceptionally beautiful topological explanation (though not a proof) [105].

²Spin has no classical analogue. The commonly shown picture of a spinning sphere is just an understanding aid, as the electron's size is so small that it would need to spin with equatorial speeds faster than the speed of light to have the required value of the angular momentum, a.k.a. spin [106].

They lead to dramatic spin-dependent properties in DMS, like the formation of magnetic polarons [108], the coherent transfer of spin polarisation from carriers to magnetic ions [109] and carrier-mediated ferromagnetism [40], on which my thesis centres.

The necessary condition for the exchange interaction is that the wavefunctions of the involved holes or electrons overlap to allow them to hop between the sites.² Furthermore, the energy gain from arranging the spins has to be greater than the cost of electron hopping. In other words, the exchange energy has to compete with the kinetic energy for the magnetic state to occur (which becomes more and more obvious with the growth of temperature, as will be shown in Sec. 9.6). This, despite its unambiguous origin, comes in different forms and realisations depending on the analysed system and often even on the specific sample, as in the case of (Ga,Mn)As. The different mechanisms through which the exchange interaction can realise the magnetic ordering will be discussed in the next section.

4.2 Mechanisms of magnetic ordering

Magnetism in (Ga,Mn)As and some other (III,Mn)V compounds is believed, based on the broad experimental data, to originate from the interactions between Mn local moments [28]. For any two Mn spins the interaction can be well expressed as $-J\mathbf{S}_i \cdot \mathbf{S}_j$. Depending on the respective positive or negative sign of J , the interaction favours the parallel or antiparallel alignment of the spins, which usually translates into ferromagnetic or antiferromagnetic order. In addition, there exist noncollinear spin structures due to the relativistic interactions.

It is also known that the direct dipole-dipole interaction of the classical electrodynamics is too weak to explain these data (its strength for two discrete moments separated by a lattice constant in a typical solid is only $1\text{ K}k_B$ [88]). The ultimate origin of magnetism is simply the quantum exchange, which, however, manifests itself in many different ways, depending on the system chemical composition, size and geometry. For this reason, investigating magnetic order in dilute magnetic semiconductors is one of the most challenging problems of the field. Different instances of the exchange interaction are usually identified as separate mechanisms, which facilitates understanding of the material's physics, as well as its theoretical and numerical modelling. The relative importance of these mechanisms, regarding different phenomena and potential applications, depends on the sample parameters and preparation procedure.

The simplest mechanism of magnetic order is the direct exchange, where

²This also implies that the exchange coupling depends on the lattice constant (and thus on strain) [110]—the effect usually omitted in theoretical considerations, including my thesis.

the electrons localised on neighbouring magnetic atoms are coupled by the exchange interaction. As its name suggests, it proceeds directly without the need for an intermediary. It is caused by the Coulomb energy difference between the singlet and triplet states of two $\frac{1}{2}$ spins. However, there is usually not enough direct overlapping between electronic orbitals of the distant spins to make the direct exchange the dominant mechanism in controlling the magnetic properties; this is also the case in (Ga,Mn)As. This forces us to consider some kind of indirect exchange interactions, which can couple magnetic moments over large distances. They come in many complicated variants, some of them being the Ruderman–Kittel–Kasuya–Yosida (RKKY) exchange, Stoner itinerant exchange, superexchange, double exchange or Zener kinetic exchange and anisotropic exchange. In the following sections, I will describe the types of indirect exchange most commonly associated with (Ga,Mn)As.

4.2.1 Superexchange

Kramer’s superexchange occurs between magnetic ions separated by a nonmagnetic atom [111]. In a crystal environment, an electron of the nonmagnetic atom can be transferred to the empty shell of a magnetic ion and interact, through the direct exchange interaction, with electrons forming its local moment. During this process, the nonmagnetic atom becomes polarised and couples in the same way also with its other magnetic neighbours.

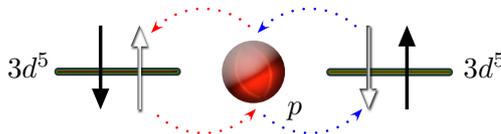


Figure 4.1: Two Mn moments in Ga positions coupled by superexchange interaction via the nonmagnetic As anion shell. The indirect interaction is a result of the exchange interaction between the electrons from the $3d^5$ levels of both Mn ions and the p electrons of a fully filled As shell. The virtual interatomic transitions of the electrons (enhanced by the $sp-d$ hybridisation) are marked by dotted lines.

Figure 4.1 illustrates this situation in the (Ga,Mn)As lattice. The magnetic Mn ions, which substitute cation sites, are separated by nonmagnetic As anions. The spin-up electron from the As p orbital can jump to the Mn d orbital on the left. In this process the first Hund rule has to be fulfilled, which in the case of singly occupied Mn orbitals means that the electron has to have the opposite spin to that of the d spins. At the same time the remaining p electron with the opposite spin can jump to the right d orbital only if the Mn ion is oppositely polarised, i.e. anti-parallel to the left Mn moment. As a result, the superexchange favours antiferromagnetic

alignment of the Mn moments. The electron hopping between the singly occupied Mn $3d^5$ orbitals and fully occupied p orbitals is enhanced by their covalent mixing [112].

This type of indirect d - d coupling dominates the interaction between substitutional Mn moments in strongly compensated (Ga,Mn)As systems (with hole densities significantly lowered by acceptor defects), i.e. in insulating crystals with completely filled valence bands [88]. The antiferromagnetic superexchange is also responsible for the compensation of substitutional Mn moments by the interstitial Mn spins mentioned in Sec. 3.3 [113]. In other materials, it can lead either to ferromagnetic or antiferromagnetic coupling, depending on the relative sign of the involved direct coupling interactions [114, 115].

4.2.2 Bloembergen–Rowland mechanism

The mechanism which differs from the superexchange only by the selection of intermediate states (it allows for virtual transitions between different atomic shells) is called the Bloembergen–Rowland interaction (Fig. 4.2) [116, 117]. It can lead to ferromagnetic d - d coupling.

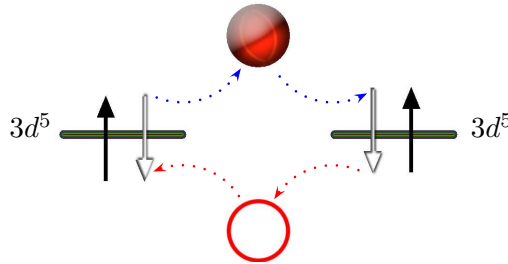


Figure 4.2: Two Mn moments in Ga positions coupled by the Bloembergen–Rowland mechanism via the nonmagnetic As anion shell. As opposed to superexchange, the virtual interatomic transitions of the electrons involve two different shells of intermediate atoms.

4.2.3 Double exchange

Zener’s double exchange [118, 119] occurs when two ions separated by a nonmagnetic atom have a different number of electrons in their magnetic shells. The electrons can more easily hop through the intermediate nonmagnetic atom between the magnetic shells. To fulfil the Hund rule and in this way increase the probability of hopping, the electrons in magnetic shells of both ions need to have the same spin. Then the wavefunction of the hopping electron extends in the space between the two ions, and thus the kinetic energy of the system drops.

The (Ga,Mn)As systems near the insulator-metal transition, where the magnetic order starts to set in, are sometimes regarded as an example of the double-exchange ferromagnetism in the (III,Mn)V literature [88]. In this regime, the Mn acceptor states form an impurity band with mixed $sp-d$ character. Hopping with the impurity band allows the electric conduction and the exchange coupling of Mn ions.

4.2.4 RKKY interaction

Indirect exchange interaction can act over large distances when mediated by free carriers. The interactions of local moments embedded into the carrier gas are then described by the Ruderman–Kittel–Kasuya–Yosida (RKKY) theory [42]. It considers the perturbation of the carriers by the magnetic moments and treats the system by second-order perturbation theory. The local moments create wave-like perturbations, similar to a body dropped into water (Fig. 4.3), leading to an interaction oscillating with the distance between them.

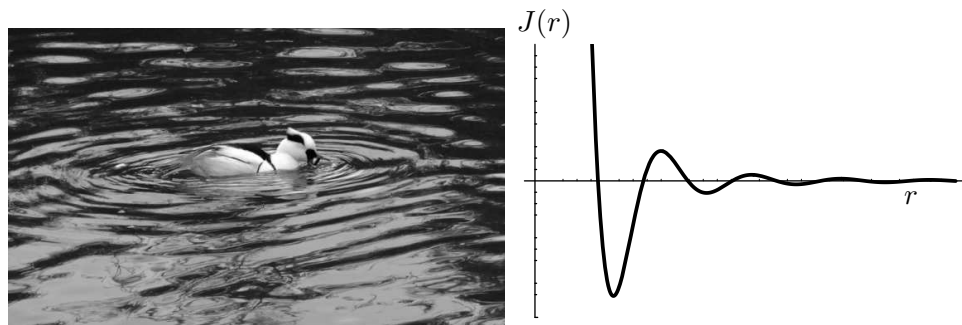


Figure 4.3: The RKKY interaction: mechanical analogy (a diving duck making a circular wave on the water) and distance dependence [107].

In the simplest case of magnetic ions in metals coupled by conduction electrons, the strength of the RKKY interaction can be expressed as

$$J(r) = -\frac{\rho(E_F)k_F^3 J_0^2}{2\pi} \frac{\sin(2k_F r) - 2k_F r \cos(2k_F r)}{(2k_F r)^4}, \quad (4.1)$$

where $\rho(E_F)$ and k_F are the density of states at the Fermi level and the Fermi wavevector of the carriers, J_0 is the exchange coupling between the carriers' and ions' spins and r is the average distance between the magnetic ions. As follows from the above equation, the RKKY coupling can be either ferromagnetic or antiferromagnetic, depending on the separation between the magnetic moments, and tends to vary in space on the length scale of the carriers' Fermi wavelength (Fig. 4.3) [107].

Although $J(r)$ describes exchange interactions mediated by free carriers, the underlying theory can fairly well approximate arbitrary electron systems, such as tight-binding electrons in metals [120] and electron clusters in dilute magnetic semiconductors [121]. This is because its essence is only the perturbative treatment of the interactions mediated between the magnetic moments, and the free-electron gas may well be replaced by any more complicated system.

In metallic ferromagnets, like optimally annealed (Ga,Mn)As with highest Mn concentrations and hole concentrations (grown by the MBE techniques), the holes on impurity centres are delocalised (see Sec. 3.3). For typical estimated Mn and hole concentrations ($\sim 1 \text{ nm}^{-3}$ and $0.01\text{--}1 \text{ nm}^{-3}$, respectively), the value of $k_F r$ is essentially smaller than that of the first root of $J(r)$ function (4.1). Thus, the long-range RKKY interaction leads to ferromagnetic order in metallic (Ga,Mn)As. In this limit the RKKY theory becomes equivalent to a simplified model of the carrier-mediated ferromagnetism proposed by Zener [118].

The RKKY picture has been questioned in the context of (III,Mn)V ferromagnets, as it does not take into account the spin-splitting Δ of the carrier band due to the average effective field induced by the Mn ions [88]. Hence, it only applies as long as the perturbation induced by the Mn spins on the itinerant carriers is very small, i.e. $\Delta \ll E_F$. This condition is fulfilled only in the case of strongly metallic systems. In Chapter 7 I will show how to overcome this limitation using the proposed perturbation-variational Löwdin calculus. It can be seen as an extension of the RKKY theory, which is self-consistent (takes into account the dynamics of free carriers) and can accommodate any band structure (of any number of bands, with the spin-orbit coupling and the values of spin-splitting up to those encountered in (III,Mn)V ferromagnets). In Ref. [122], I have derived the analytical solution of this model for two spin-split energy bands.

4.2.5 The p - d Zener model

As mentioned in the previous section, the effective RKKY coupling for Mn spins in metallic (Ga,Mn)As is ferromagnetic and long-range. In this limit the RKKY theory becomes equivalent to a model of the carrier-mediated ferromagnetism proposed by C. Zener [118, 123]. It neglects the oscillatory character of the magnetic interactions, but allows to include the effect of the spin-orbit interaction and the details of the electronic structure in a transparent and easy way.

A mean-field approach based on the Zener model was developed by Dietl *et al.* [39, 40]. It explains ferromagnetism in III-V and II-VI magnetic semiconductors with the presence of delocalised band-carriers mediating (via the p - d exchange interaction) ferromagnetic ordering between localised spins, which—in return—produce the spin-splitting of the valence

band, lowering the carriers' energy. The delocalisation length and density of the carriers should be sufficient to enable each of them to interact with a few localised spins, so that they can mediate the magnetic order between them.

The celebrated p - d Zener model [39, 40] describes the valence band structure of the zincblende and wurzite semiconductors with the 6×6 Kohn-Luttinger $k \cdot p$ matrix [124]. It includes the p - d exchange coupling between the valence band holes' spins and the local Mn moments ($S = \frac{5}{2}$ and $g = 2$) within two approximations: the already mentioned virtual crystal approximation, which replaces the random distribution of Mn with their average density per each lattice site, and the mean field approximation, which neglects the fluctuations of their spins.

The Mn magnetisation M dependence on the magnetic field H and temperature T is given (in the absence of carriers) by the Brillouin function

$$M = g\mu_B x_{\text{eff}} N_0 S B_S \left[\frac{g\mu_B H}{k_B(T + T_{AF})} \right].$$

The effective Mn concentration x_{eff} reflects the effect of compensation due to unintentional defects (Sec. 3.3), while the empirical parameter T_{AF} accounts for the short range antiferromagnetic superexchange between the Mn ions mediated by the p - d exchange coupling with the occupied electron bands (Sec. 4.2.1). It can be safely neglected in (Ga,Mn)As with the dominant long-range ferromagnetic interactions.

The mean-field approach is based on the minimisation of the Ginzburg-Landau free-energy functional $F(M)$. It can be split into the hole dependent contribution $F_c(M)$, calculated from the Kohn-Luttinger $k \cdot p$ matrix and p - d exchange energy, and the local ions contribution $F_S(M)$. The latter is expressed as

$$F_S(M) = \int_0^M dM' H(M')$$

The minimisation of the total free-energy $F(M) = F_c(M) + F_S(M)$ leads to the solution of the mean-field equation

$$M = g\mu_B x_{\text{eff}} N_0 S B_S \left[\frac{g\mu_B (-\partial F_c[M]/\partial M + H)}{k_B(T + T_{AF})} \right].$$

Near the Curie temperature, where the magnetisation M is small, it can be expected that $F_c(M) - F_c(0) \sim M^2$. This can be related to the carrier magnetic susceptibility $\chi_s = A_F (g\mu_B)^2 \rho_s$, where ρ_s is the spin density of states and A_F accounts for the carrier-carrier interactions, as

$$F_c(M) = F_c(0) - \frac{A_F \rho_s M^2 \beta^2}{8(g\mu_B)^2}.$$

Taking into account the above equations, the series expansion of the Brillouin function with respect to M yields the mean-field expression for the Curie temperature in the following form:

$$T_C = \frac{x_{\text{eff}} S(S+1) \beta^2 A_F \rho_s(T_C)}{12 N_0 k_B} - T_{AF}. \quad (4.2)$$

The above formula reflects the nature of the carrier-mediated ferromagnetism in (Ga,Mn)As—the Curie temperature is proportional both to the concentration and spin of the magnetic ions, as well as to the density of states of the mediating holes and to the square (due to the indirect exchange process) of the local coupling constant. It should be noted, however, that the obtained mean-field Curie temperature increases without limit, while in reality this should be stopped by such effects as localisation induced by strong exchange interactions or spin-frustration due to high carrier concentrations. Furthermore, a large density of states at the Fermi energy may also result in a variation of the sign of the RKKY interaction, which may lead outside of the mean-field limit.

Although the mean-field model overestimates the T_C values as compared to experiment [28], it highlights the requirements toward room temperature ferromagnetic semiconductors (see e.g. [65] and references therein). It also explains the anomalous magnetic circular dichroism observed in (Ga,Mn)As [125], as well as the strain dependence of the magnetic easy axis [126].

On approaching the metal-insulator transition, the extended carrier states mediating ferromagnetism become localised [39]. According to the universal scaling theory of this transition [127], the localisation radius decreases gradually from infinity at the transition point toward the Bohr radius deep in the insulator phase. Within this radius the carrier wavefunction retains an extended character, and hence can mediate the long-range interactions between localised spins according to the mechanism of the p - d Zener model.

4.2.6 Bound magnetic polarons

In the insulating regime, an alternative, bound magnetic polaron (BMP) model is sometimes invoked, in which the carriers are quasi-localised states in an impurity band [128]. According to its theory, a localised hole in (Ga,Mn)As is coupled by antiferromagnetic exchange mechanism with a number of magnetic impurities within its localisation radius, which leads to the creation of a BMP, as shown in Fig. 4.4. Such quasiparticles, in turn, interact ferromagnetically with each other, in contrast to the antiferromagnetic interactions which led to their formation. The effective radius of the polaron increases with the ratio of the exchange and thermal energy, causing

BMPs to overlap at sufficiently low temperatures and giving rise to a ferromagnetic exchange interaction between percolated polarons (Fig. 4.4). If the hole localisation radius is significantly lower than the distance between them, disorder effects are of crucial importance for the magnetic properties of the material [129].

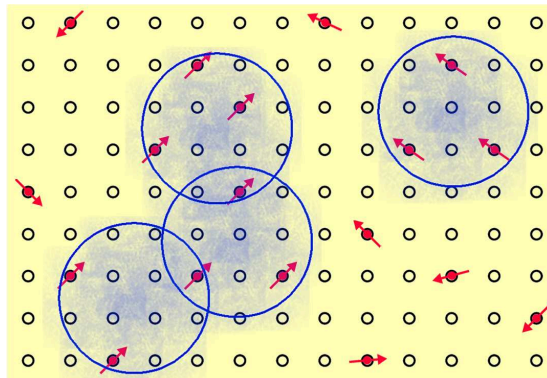


Figure 4.4: Bound magnetic polaron. Holes hop among Mn centres (red arrows) and align their d shell spins via the exchange interaction. The percolated BMPs (blue circles) can connect into ferromagnetic clusters.

Some theoretical works, like the donor impurity band model, tried to apply this picture to the regime where the density of localised holes is much smaller than the density of Mn ions [130]. To the best of my knowledge, this model did not find unequivocal confirmation by the experimental data.

4.3 Magnetic regimes in (Ga,Mn)As

The character of long-range magnetic order in (Ga,Mn)As depends strongly on the interplay of all the types of direct and indirect exchange interactions distinguished in the previous section. As it has been already mentioned, their relative prominence depends on such crucial sample parameters as the carrier and magnetic moment concentrations. Additionally, the number of Mn moments and (or) holes participating in the ordered state may change significantly in presence of charge and moment-compensating defects.

The following qualitative picture of different magnetic regimes in the (Ga,Mn)As dilute magnetic semiconductor emerges from the experimental data and their theoretical interpretations discussed above:

- At very low doping levels, the average distance r between Mn impurities (or between holes bound to Mn ions) is much larger than the size of the bound hole approximately given by the impurity effective

Bohr radius a^* . One can expect that in this regime, holes remain localised around isolated Mn ions, as confirmed by the measured value of $g = 2.77$, which corresponds to the neutral $A^0(d^5 + \text{hole})$ Mn complex. The theoretical model of exchange interactions mediated by thermally activated carriers, proposed to describe this very dilute insulating limit [131], did not find its confirmation in experiments, though, as the material turned out to be a paramagnet [80].

- When Mn doping reaches 1%, ferromagnetism sets in [132, 133]. The system is close to the Mott insulator-metal transition—the localisation length of holes’ states bound on Mn impurities starts to extend to a degree that allows them to mediate the exchange interaction between neighbouring moments. Several approaches have been used to describe ferromagnetism in this regime, including the interacting BMPs or holes hopping within the impurity band. Due to the hopping nature of conduction and the mixed $sp-d$ character of states in the impurity band, this semi-insulating regime is often regarded as an example of double-exchange ferromagnetism [88].
- At highest Mn concentrations, the holes become delocalised—the desired end product, where (Ga,Mn)As becomes a ferromagnetic semiconductor, with the magnetic degrees of freedom strongly coupled to the electronic ones. They can mediate the coupling between Mn local moments over large distances. Thus, the dominant mechanism of magnetic order in this metallic limit can be described by the RKKY theory or the $p-d$ Zener model. On the other hand, in strongly compensated systems, where the overall magnitude of the hole-mediated exchange is weaker, antiferromagnetic superexchange can have a significant effect.

Although the nature of ferromagnetism in (Ga,Mn)As and related DMS is still debated [134, 135], the above list presents what is usually done when modelling the physics of these materials. I will concentrate on the last case—the metallic regime, including some compensation effects.

At first glance, it seems that substitutional Mn spins are necessary for creating magnetic order in (Ga,Mn)As. But, as the discoveries of recent years show [136–139], there exist other mechanisms which can produce effective magnetic fields in crystals. They result from the spin-orbit interaction in the presence of symmetry-breaking factors such as interfaces, electric fields, strain,³ and crystalline directions [136]. What is more, the combined crystal symmetry and relativistic effects can lead to a more complicated non-collinear magnetic ordering of spins, like the spin canting caused by the Dzyaloshinskii–Moriya interaction. Some of these effects will be addressed in the further part of my thesis.

³In one of the fascinating experiments on graphene, the application of strain allowed to create an enormous effective magnetic field of 300 T [140].

Until now I have been discussing the building blocks of (Ga,Mn)As, its lattice structure, strain, the integration of Mn dopants and the *sp-d* hybridisation which leads to the magnetic ordering in this material, focusing on single atoms. In the next chapter, based on this picture, I will show how to model a large system of these atoms making up realistic (Ga,Mn)As samples, and its physical properties.

Chapter 5

Band structure of (Ga,Mn)As

In materials science, all crystal properties can be explained by quantum mechanics, when one takes into account Coulomb interactions among the nuclei and the electrons. The gravitational, strong, and electroweak interactions are safely far away from the eV energy scales that we deal with in solid bodies. The first step to finding these properties is to calculate the cohesive energy of a given crystal structure, namely the difference in energy between the crystalline body and the isolated atoms. For this purpose, we have to solve the Schrödinger (or Dirac) equation for the electronic states of each free atom and for the periodic crystalline structure, like the one described in the previous chapter. This problem is impossible to solve exactly (for more than two particles, and even numerically for more than a few hundred), since all $N_A \approx 10^{23}$ electrons interact dynamically with themselves and with atomic nuclei. Hence, drastic simplifications are required.

First, we notice that the nuclei are much more massive than the electrons, so they move much more slowly. Hence, we can assume that they are stationary and occupy fixed lattice positions. We decouple these two subsystems and focus on the problem of electrons interacting with the field of fixed nuclei and with all other electrons. The diagonalisation of the resulting many-particle Hamiltonian in the Born-Oppenheimer approximation is still quite a computational task. Here, one usually uses the mean-field approximation, i.e. one assumes that every electron experiences the same average potential $V(\mathbf{r})$. As a result, the many-electron problem reduces to that of a single electron moving in the background potential generated by positively charged nuclei and the charge density of other electrons. Its Hamiltonian has the following form:

$$\hat{H} = \frac{\hat{p}^2}{2m_0} + V(\mathbf{r}) . \quad (5.1)$$

The next step is to describe the nature of the $V(\mathbf{r})$ potential. This can

be done from first principles, where the only input parameters are atomic numbers and positions, and the band structure is obtained using a variational calculation of the ground state of a many-body system. The methods falling in this category, such as the density functional theory, Hartree, or the Hartree-Fock approximation, require onerous iterative procedures to achieve self-consistency. That is why we often prefer the so-called semi-empirical approaches, which assume a certain form of the potential based on our knowledge about the crystal. Among these methods are:

- the simplest one, nearly-free electron approximation, which assumes that the lattice potential $V(\mathbf{r})$ is vanishingly small and therefore its influence on the band structure shows only in the form of the symmetries of the Brillouin zone,
- the pseudopotential method, which solves the one-electron equation in the plane-wave basis, assuming a given form of the Fourier transform of the lattice potential,
- the $k \cdot p$ method,
- the tight-binding (TB) approximation.

The last two methods usually express $V(\mathbf{r})$ in terms of parameters determined from fitting experimental results, allowing the quantitative description of the electron energy in a crystal (though there exist empirical pseudopotential methods, as well as—growing in popularity—*ab initio* tight-binding approach [141]).

The above procedures require that we turn the formal expression (5.1) into a quantum-mechanical operator acting on a well-defined Hilbert space, and perform numerical calculations in a concrete finite-dimensional basis. To this end, I will now analyse the general form of the electronic eigenstates in the crystal, building upon the discussion of its symmetries from Ch. 3.

5.1 Reciprocal space

In Chapter 3, I have described a dilute magnetic semiconductor crystal and defined its space group according to its symmetries. Mathematically, the abstract (real crystals are not infinite) periodic potential of the crystal lattice does not differ much from a plane wave spreading from $-\infty$ to ∞ . According to the Heisenberg uncertainty principle such a wave can be characterised by a well-defined wavevector and momentum. Similarly, our model corresponds to precise values of a wavevector \mathbf{G} , the set of which constitute a reciprocal lattice Λ^* dual to the real one. This important structure enables the application of analytic geometry of linear forms to coordinate systems with non-orthonormal bases, like those of crystals of lower symmetry. Therefore,

I know how to decompose the potential $V(\mathbf{r})$ of the lattice into a Fourier series (as opposed to a Fourier integral):

$$V(\mathbf{r}) = \sum_{\mathbf{G} \in \Lambda^*} V_{\mathbf{G}} e^{i\mathbf{G} \cdot \mathbf{r}} . \quad (5.2)$$

Consequently, the Hamiltonian of delocalised electrons in the lattice can be written as

$$\mathcal{H} = \int d^3k \sum_{\mathbf{G} \in \Lambda^*} \left(\frac{\hbar^2 k^2}{2m} \delta_{\mathbf{G},0} + V_{\mathbf{G}} \right) |\mathbf{k}\rangle \langle \mathbf{k} + \mathbf{G}| . \quad (5.3)$$

One can see that the allowed transitions between their plane-wave states $|\mathbf{k}\rangle$, caused by the scattering on the potential $V(\mathbf{r})$, may only involve momentum changes equal to $\hbar\mathbf{G}$. The eigenstates of the Hamiltonian, conserved in the scattering process, can thus be written in the form

$$\psi(\mathbf{r}) = \sum_{\mathbf{G} \in \Lambda^*} \psi_{\mathbf{G}} e^{i(\mathbf{G}+\mathbf{k}) \cdot \mathbf{r}} ,$$

where \mathbf{k} does not have to belong to Λ^* .

The above result is simply the Bloch theorem, which I have derived using a language slightly non-standard, but nevertheless better adapted to the problems discussed in my thesis, because of the emphasis it places on disorder and scattering processes. Indeed, it is easy to recognise that $\psi(\mathbf{r})$ is a Bloch function, as for any $\mathbf{a} \in \Lambda$

$$\psi(\mathbf{r} + \mathbf{a}) = \sum_{\mathbf{G} \in \Lambda^*} \psi_{\mathbf{G}} e^{i(\mathbf{G}+\mathbf{k}) \cdot (\mathbf{r}+\mathbf{a})} = e^{i\mathbf{k} \cdot \mathbf{a}} \sum_{\mathbf{G} \in \Lambda^*} \psi_{\mathbf{G}} e^{i(\mathbf{G}+\mathbf{k}) \cdot \mathbf{r}} = e^{i\mathbf{k} \cdot \mathbf{a}} \psi(\mathbf{r}) .$$

Hence, to cover all possible states, it suffices to consider \mathbf{k} vectors belonging to the first Brillouin zone \mathcal{B} , as all others are equal to a vector from \mathcal{B} plus a vector from Λ^* . In this sense, the first Brillouin zone is a Wigner-Seitz primitive cell in the reciprocal space.

Invoking the analogy to the Heisenberg principle again, introducing the disorder and scattering to this picture mixes various \mathbf{k} -vectors from \mathcal{B} and broadens the eigenstates of the Hamiltonian in the reciprocal space. Then, the potential $V(\mathbf{r})$ is no longer periodic and the series (5.2) acquires additional terms. (These two statements are actually equivalent, which reflects the fact that the uncertainty principle is firmly grounded in Fourier analysis.) Within this spirit, I will phenomenologically model the anomalous Hall effect in a disordered (Ga,Mn)As in Ch. 10.

Any Bloch wavefunction $\psi(\mathbf{r})$ with wavevector \mathbf{k} can be written in the form

$$\psi(\mathbf{r}) = e^{i\mathbf{k} \cdot \mathbf{r}} u(\mathbf{r}) ,$$

where $u(\mathbf{r})$ has the periodicity of the lattice potential and is called the periodic part of ψ . I adopt the normalisation convention in which

$$\int_V d\mathbf{r}^3 |\psi(\mathbf{r})|^2 = V ,$$

where V is the crystal volume. The matrix element of any quantum operator is defined for the Bloch wavefunctions as

$$\langle \psi | \hat{O} | \phi \rangle = \frac{1}{V} \int_V d\mathbf{r}^3 \psi(\mathbf{r})^* \hat{O} \phi(\mathbf{r}) .$$

The periodic parts' normalisation follows from the Bloch wavefunctions' normalisation,

$$\int_{\Omega} d\mathbf{r}^3 |u(\mathbf{r})|^2 = \Omega .$$

Since the Bravais lattice underlying the zincblende structure of (Ga,Mn)As (as I assumed it to be similar to GaAs within the virtual-crystal approximation) is the fcc lattice, its reciprocal lattice Λ^* is body centred cubic with primitive vectors $\mathbf{b}_1 = \frac{2\pi}{a}(1, 1, \bar{1})$, $\mathbf{b}_2 = \frac{2\pi}{a}(\bar{1}, 1, 1)$ and $\mathbf{b}_3 = \frac{2\pi}{a}(1, \bar{1}, 1)$ (the same as for diamond). The first Brillouin zone \mathcal{B} is obtained by bisecting these vectors with perpendicular planes (which is a very simple example of the construction known to mathematics as the Voronoi tessellation—interestingly, it also underlies the spinodal decomposition in dilute magnetic semiconductors and many other phenomena in various fields of science). It is shaped as a truncated octahedron, as illustrated in Fig. 5.1 where several special points and lines are displayed. As will be explained in the next section, they are reminiscent of the fact that Hamiltonian \mathcal{H} (5.3) in the reciprocal space carries (through the potential term) the symmetries of the point group of the crystal characterised in Section 3.2. Thanks to these symmetries, the band structure calculations can be limited to the irreducible wedge of the \mathcal{B} , which is a fraction of only $\frac{1}{48}$ of \mathcal{B} (marked in red in Fig. 5.1). I make use of this fact in all numerical procedures prepared for this thesis. (The \mathcal{B} of the diamond space group has the same geometry, but the point group symmetries associated with the same high symmetry points can differ.)

5.2 Band structure

Consider an eigenstate ψ of the crystal Hamiltonian \mathcal{H} (5.3) with eigenvalue E , $\mathcal{H}\psi = E\psi$. The Hamiltonian \mathcal{H} commutes with the symmetry operations t of the point group T_d , hence

$$\mathcal{H}t\psi = t\mathcal{H}\psi = tE\psi = Et\psi .$$

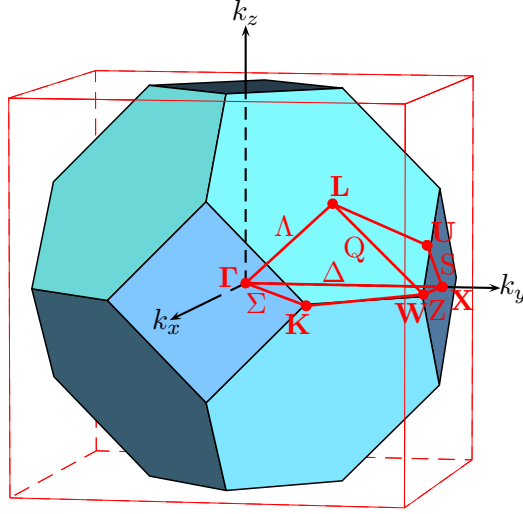


Figure 5.1: The First Brillouin zone \mathcal{B} of a fcc lattice, with high symmetry \mathbf{k} points marked, which is also the Wigner-Seitz cell of a bcc Bravais lattice. The irreducible wedge of the fcc lattice (marked in red) is spanned on the high symmetry points (Γ , \mathbf{X} , \mathbf{L} , \mathbf{W} , \mathbf{K} and \mathbf{U}) connected by symmetry lines (Λ , Δ , Σ , \mathbf{Q} , \mathbf{S} and \mathbf{Z}).

This means that $t\psi$ is also an eigenstate of \mathcal{H} with the same eigenvalue E . The eigenspace V_E corresponding to E (a subspace spanned by the eigenstates of \mathcal{H} with energy E) is therefore conserved under the action of all symmetry operations from T_d . It carries a representation of T_d (operations t truncated to V_E), whose basis is any complete orthonormal set of all eigenvectors with energy E . Conversely, to each eigenvalue of \mathcal{H} corresponds a representation of T_d ; barring accidental degeneracies, these representations turn out to be irreducible.

The action of point group symmetry operation $p \in T_d$ on the Bloch function $\psi(\mathbf{r}) = e^{i\mathbf{k}\cdot\mathbf{r}}u_{\mathbf{r}}$ is defined as

$$[p\psi](\mathbf{r}) := \psi(p^{-1}\mathbf{r}) = e^{i\mathbf{k}\cdot p^{-1}\mathbf{r}}u(p^{-1}\mathbf{r}) .$$

Operation p cannot change the lengths of vectors nor the angles between them, so $\mathbf{a} \cdot \mathbf{b} = p\mathbf{a} \cdot p\mathbf{b}$ and

$$\mathbf{k} \cdot p^{-1}\mathbf{r} = p\mathbf{k} \cdot pp^{-1}\mathbf{r} = p\mathbf{k} \cdot \mathbf{r} .$$

On the other hand, we have for $\mathbf{a} \in \Lambda$

$$u[p^{-1}(\mathbf{r} + \mathbf{a})] = u(p^{-1}\mathbf{r} + p^{-1}\mathbf{a}) = u(p^{-1}\mathbf{r}) ,$$

since $p^{-1}\mathbf{a} \in \Lambda$. Thus, applying p to a Bloch function with wavevector \mathbf{k} turns it into another Bloch function, but with wavevector $p\mathbf{k}$, which may be different from \mathbf{k} . This means that the Bloch states belonging to a single \mathbf{k}

may not always be able to carry the representation of the full point group T_d , but of a subgroup $T_{\mathbf{k}} \subset T_d$, defined as

$$T_{\mathbf{k}} := \{t \in T_d | t\mathbf{k} = \mathbf{k} + \mathbf{G}\} ,$$

where $\mathbf{G} \in \Lambda^*$. As $t = 0$ in the $\mathbf{k} = 0$ point, $T_{\mathbf{k}=0} = T_d$. For this reason, the centre of the Brillouin zone, denoted as Γ , is the highest symmetry point. For other \mathbf{k} wavevectors, those of highest symmetry being marked in Fig. 5.1 by Roman letters, Bloch states are split into representations of the group $T_{\mathbf{k}}$. The analysis of their properties requires the study of the periodic parts u of Bloch functions ψ , to which I now turn.

I define a \mathbf{k} -dependent Hamiltonian $\mathcal{H}(\mathbf{k})$ acting solely on the periodic parts of Bloch functions via the formula

$$\langle u | \mathcal{H}(\mathbf{k}) | u' \rangle = \langle e^{i\mathbf{k}\mathbf{r}} u | \mathcal{H} | e^{i\mathbf{k}\mathbf{r}} u' \rangle .$$

Since T_d group may change the \mathbf{k} vector, $\mathcal{H}(\mathbf{k})$ does not commute with all $p \in T_d$, but it does commute with all $q \in T_{\mathbf{k}}$. Eigenstates of $\mathcal{H}(\mathbf{k})$ and their energies form the bands at \mathbf{k} . The irreducible representations of $T_{\mathbf{k}}$ permit a classification of the electronic states. In all the models of the band structure I have used, $\mathcal{H}(\mathbf{k})$ was described by a finite matrix in a fixed basis. Because $\mathcal{H}(\mathbf{k})$ commutes with operations from $T_{\mathbf{k}}$, which is a subgroup of T_d , it is beneficial to build this basis from functions whose symmetry properties are as close to T_d as possible, as this will give the Hamiltonian matrix a block structure. In my case, the basis functions have s , p and d orbital symmetries. This is also directly related to the symmetry properties of the atomic orbitals which the periodic functions arise from.

The basis functions of different symmetries span subspaces invariant with respect to the operators from irreducible representations of group $T_{\mathbf{k}}$. The eigenstates of $\mathcal{H}(\mathbf{k})$, which belong to these subspaces, are s -like, p -like or d -like, meaning that in the limit of separate non-interacting atoms they would become the respective atomic orbitals. They transform under irreducible representations listed in the character table of $T_{\mathbf{k}}$ [76]. Indeed, the s -like orbitals in the group of the Γ point form states that belong to the irreducible representation Γ_1 (singly degenerate, i.e. neglecting spin, and totally symmetric under all operations). The three p orbitals (p_x, p_y, p_z) belong to the same triply degenerate representation Γ_{15} . Finally, two of the d -like states transform as Γ_{12} and the remaining three as Γ_{25} .¹

Since the unit cell contains two atoms, their atomic orbitals can overlap one another in two different ways, yielding states which are either bonding

¹There are many notations for the irreducible representations of the T_d group used in literature. The correspondence between them and the BSW (Bouckaert, Smoluchowski and Wigner) notation used herein can be found e.g. in [76] (Table 2.3). What is more, the Γ_3 and Γ_4 (Koster notation) are sometimes reversed, like in [142, 143].

or antibonding. In semiconductors like GaAs, the bonding orbitals are usually filled with electrons and form the valence bands, while the antibonding orbitals give rise to the conduction bands. The electrons come from the outermost partially filled atomic shells, which usually determine the properties of semiconductors. The remaining, core electrons reside in the completely filled inner atomic shells and are strongly localised around the nuclei. Thus we can neglect those shells electrons. The schematic plot of a part of the energy levels in the vicinity of the Γ point is shown in Fig. 5.2a.

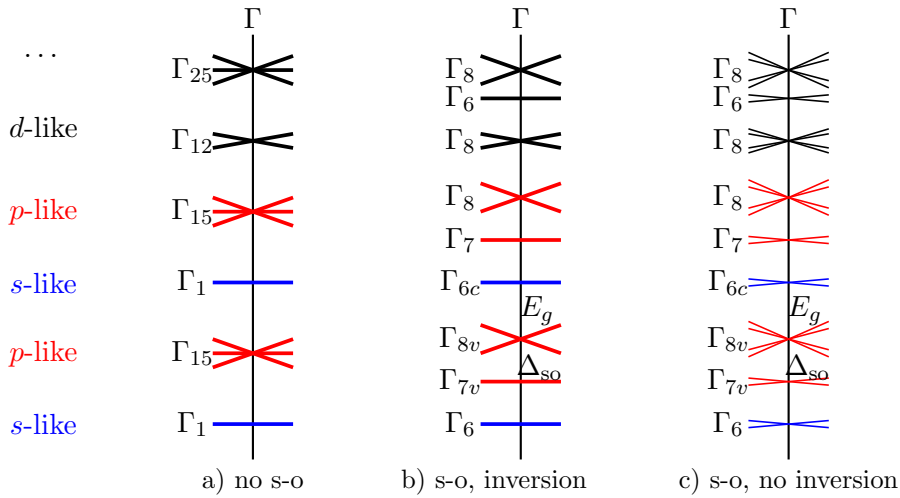


Figure 5.2: Simplified diagram of the energy levels in zincblende structure at the centre of the Brillouin zone, demonstrating the influence of spin-orbit interaction and inversion asymmetry: (a) without the spin-orbit coupling, all energy levels are degenerate at the Γ point; (b) spin-orbit coupling leads to the splitting of the p -like bands (e.g. those transforming under Γ_{8v} split into heavy and light hole levels) but leaves the spin degeneracy in lattices with inversion symmetry; (c) in a lattice without inversion symmetry, the spin degeneracy is fully removed, except for the Γ point.

Outside the Γ point, $\mathcal{H}(\mathbf{k})$ contains non-zero terms linear in the momentum operator \hat{p} (like the $\mathbf{k} \cdot \mathbf{p}$ term in the Kohn–Luttinger $k \cdot p$ Hamiltonian), which couple orbitals with different angular momentum. Since these terms do not commute with the symmetry operators, the symmetry of the Hamiltonian (and the periodic parts of its eigenstates) decreases. As a result, the degenerate energy bands can split, depending on the \mathbf{k} value and direction, though the spin degeneracy always remains unaltered.

A realistic picture of zincblende semiconductor bands requires taking into account the relativistic spin-orbit coupling interaction and the spin property of the wavefunctions. I will move to it in the next section.

5.3 Spin-orbit coupling

According to the special relativity theory the motion of an electron in a lattice potential results in a kinematic effect, in which the electromagnetic tensor acquires a magnetic field component in the electron's rest frame. The interaction of the electron spin with this magnetic field results in the so-called spin-orbit coupling, which is described by the following general expression:

$$\mathcal{H}_{\text{so}} = \frac{\hbar}{4m_0^2c^2} \nabla V \times \mathbf{p} \cdot \boldsymbol{\sigma} , \quad (5.4)$$

where m_0 is the free electron mass, c is the speed of light and $\boldsymbol{\sigma}$ is the vector of Pauli matrices [144]. It couples the spins to the orbital motion which is influenced by the crystal fields, and thereby provides a mechanism through which the spins feel the crystal symmetry. Although, due to the large Dirac gap ($2m_0c^2 \approx 1 \text{ MeV}$) in the denominator, the term is very small for electrons moving slowly in the vacuum, it may have a significant influence on electrons propagating in a crystal lattice, where it is enhanced by the fast electron motion in the strong electric field of the lattice nuclei.

The spin-orbit interaction couples the spatial and spin part of the wavefunctions, which means that the spin is not an orthogonal degree of freedom any more. Due to the spin transformation properties, a rotation by 2π is no longer equivalent to identity but changes the sign of the wavefunction. It has to be added as a new operation to the group $T_{\mathbf{k}}$, which gives a double group $\tilde{T}_{\mathbf{k}}$. This (which in other words means adding a perturbation to the Hamiltonian) results in the splitting of some band states. The emerging band structure can be derived from the irreducible representations of $\tilde{T}_{\mathbf{k}}$, which are the product of the irreducible representations of $T_{\mathbf{k}}$ and the representation of the spin functions $D^{1/2}$ [142]. The previous Γ_{15} bands in a scalar-relativistic representation now split into p -like four-fold degenerate states $|j = \frac{3}{2}, m_j\rangle$ and doubly degenerate states $|j = \frac{1}{2}, m_j\rangle$ (where j is the total angular momentum and m_j is its projection on the z axis). They transform under Γ_{8v} and Γ_{7v} irreducible representations, respectively, and form the valence band. The topmost one, Γ_{8v} , splits up in a heavy- ($m_j = \pm\frac{3}{2}$) and a light-hole ($m_j = \pm\frac{1}{2}$) band outside of $\mathbf{k} = 0$, named according to their curvature (i.e. effective mass). The spin-orbit split-off valence bands, which belong to Γ_{7v} , are lower in energy opening the gap Δ_{so} to the Γ_{8v} bands. The s -like Γ_6 bands do not belong to the valence band as they are formed of orbitals most deeply bound on the atoms. Now, the lowest s -like conduction band transforms according to Γ_{6c} . Since GaAs is a direct band-gap semiconductor, the extrema of the conduction band Γ_{6c} and the valence band Γ_{8v} lie at the centre of the Brillouin zone, and their energy difference defines the band gap E_g . The remaining antibonding bands, which belong to the irreducible representations Γ_6 , Γ_7 and Γ_8 , lay at higher energies. The resulting energy levels in the vicinity of the energy band-gap at the centre

of the Brillouin zone are illustrated in Fig. 5.2b.

5.4 Inversion symmetry breaking

The form of the spin-orbit interaction term \mathcal{H}_{so} (5.4) suggests that it can lift the spin-degeneracy of an energy level by splitting it into levels with spin parallel and antiparallel to the orbital angular momentum vector.² This is what happens in a free atom with degenerate states which have the same spatial wavefunction but opposite spins. In crystals, however, such a splitting may be forbidden due to the lattice symmetry. This situation occurs in elemental semiconductors like silicon, whose lattice structure preserves the spatial inversion symmetry.

In the absence of magnetic fields, $E_{\mathbf{k}\uparrow} = E_{-\mathbf{k}\downarrow}$, which is often called the Kramers degeneracy between a wavefunction and its complex conjugate.³ The equality describes quite an intuitive fact that an electron moving to the left has the same energy as an electron moving to the right. It remains unaffected when including the \mathcal{H}_{so} term in the Hamiltonian of the crystal: $E_{\mathbf{k},m_j} = E_{-\mathbf{k},-m_j}$. If the crystal lattice has inversion symmetry (i.e. the inversion operation $\mathbf{r} \rightarrow -\mathbf{r}$ belongs to its space group), it holds that $E_{\mathbf{k},m_j} = E_{-\mathbf{k},m_j}$ and $E_{\mathbf{k},-m_j} = E_{-\mathbf{k},-m_j}$. Collecting all these facts, one obtains that $E_{\mathbf{k},m_j} = E_{\mathbf{k},-m_j}$, which means that the energy of the crystal does not depend on the spin. Consequently, the spin splitting is forbidden. This situation is presented in Fig. 5.2b.

As described above the combined spatial and time inversion symmetries in centrosymmetric semiconductors produce the spin degeneracy of states. There are two obvious ways of lifting this degeneracy: to break time reversal symmetry with the magnetic field, as will be discussed in Sec. 5.6, or to break inversion symmetry by applying an external electric field or strain in a proper crystallographic direction. The latter can be alternatively achieved by a more subtle mechanism in structures which intrinsically lack the spatial inversion symmetry. The spin-orbit interaction (5.4) in their lattice potentials produces terms which break the spin degeneracy. One of such terms is the Dresselhaus spin-orbit interaction resulting from the bulk inversion asymmetry of the constituent non-centrosymmetric semiconductors, such as zincblende crystals of GaAs [142, 147, 148]. The other is the Bychkov–

²It is simplest to show for the case of a centrally symmetric potential, for which \mathcal{H}_{so} equals $\frac{1}{2m^2c^2} \frac{1}{r} \frac{dV}{dr} \mathbf{s} \cdot \mathbf{l}$.

³In 1930, in his study of the Schrödinger equation of an electron with spin in the absence of a magnetic field, H. A. Kramers defined an operator \hat{K} that given a solution Ψ with energy E produces another solution $\hat{K}\Psi$ with the same energy [145]. For systems with an odd number of electrons these states are orthogonal, and thus they have to be degenerate—the so-called Kramers degeneracy. Shortly thereafter Wigner pointed out that \hat{K} is simply the time reversal operator and that the degeneracy is a manifestation of the preserved time reversal symmetry of the system [146].

Rashba spin-orbit interaction, originating from the inversion asymmetry of the confining potential in quantum wells and heterostructures [149, 150].

5.4.1 Bulk inversion asymmetry

Treating the spin-orbit interaction term (5.4) as a perturbation, one can expect that close to the Γ point the lowest order terms that couple to the spin can be described as the lowest-order expansion in \mathbf{k} of the following expression:

$$\mathcal{H}_{\text{so}} = \mathbf{B}(\mathbf{k})\boldsymbol{\sigma} .$$

When the system preserves both time-reversal symmetry: $\mathbf{B}(-\mathbf{k}) = -\mathbf{B}(\mathbf{k})$, and spatial inversion symmetry: $\mathbf{B}(-\mathbf{k}) = \mathbf{B}(\mathbf{k})$, the only possible solution is $\mathbf{B}(\mathbf{k}) = 0$ and the above interaction term has to vanish. Otherwise, when the spatial inversion symmetry is broken, an effective \mathbf{k} -dependent internal magnetic field $\mathbf{B}(\mathbf{k})$ appears—clearly, it has to be always odd in \mathbf{k} . As a consequence, the energy bands lose the $\pm\mathbf{k}$ symmetry and split. The spin splitting can be described as $\hbar\boldsymbol{\Omega}(\mathbf{k}) \cdot \boldsymbol{\sigma}$ where $\boldsymbol{\Omega}(\mathbf{k})$ is the precession vector specifying the magnitude and the direction (quantisation axis) of the splitting.

The zincblende lattice of GaAs does not have inversion symmetry—the property included by the T_d^2 but not by the O_h^7 space group, as discussed in Sec. 3.2. This is called the bulk inversion asymmetry. Its effect on the electron spin via the \mathcal{H}_{so} term is the spin splitting of energy levels, as presented in Fig. 5.2c. The Γ_8 bands mix with each other away from $\mathbf{k} = 0$ and split by small amounts. Since the splitting is proportional to k , the extrema of the bands in question are displaced from the centre of the Brillouin zone. The Γ_7 bands split as k^3 in all but the [111] and [100] directions, where they remain degenerate. Finally, the Γ_6 band split also as k^3 in the [110] direction.

The enlisted \mathbf{k} -dependent spin-orbit splittings in zincblende-type semiconductors were investigated theoretically with various calculation techniques [142, 147, 148]. Although they have not been directly observed experimentally because of the small magnitude of k and their small energies [151], their influence on various phenomena in solids can be crucial. Of significant importance is the result obtained by Dresselhaus for the s -like Γ_6 conduction band [142]:

$$\boldsymbol{\Omega}_D(\mathbf{k}) = [k_x(k_y^2 - kz^2), k_y(k_z^2 - kx^2), k_z(k_x^2 - ky^2)] ,$$

which accounts for the so-called Dresselhaus spin splitting. In Chapter 10, I will investigate its impact on the magnetotransport properties of (Ga,Mn)As by comparing various models of the band structure with and without the bulk inversion asymmetry.

5.4.2 Structure inversion asymmetry

In heterostructures integrating layers of (Ga,Mn)As, termination of the crystal by a surface breaks the three-dimensional inversion symmetry, as already mentioned in Sec. 3.2. Consequently, the symmetry of the lattice reduces from T_d^2 to D_{2d} or C_{2v} , depending on the atomic structure of the layer, as explained by Fig. 5.3.

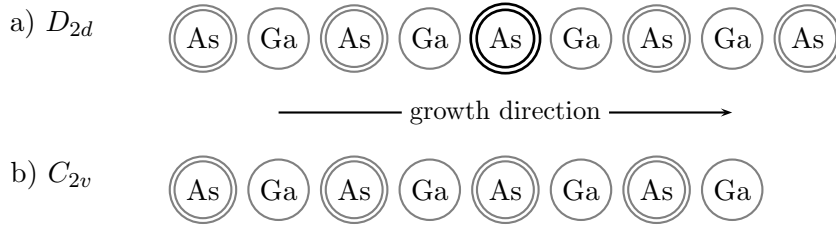


Figure 5.3: a) A layer of GaAs consisting of four monolayers of Ga and five monolayers of As atoms, characterised by the point group D_{2d} . (The middle atom lying on the inversion axis is marked.) b) A layer of GaAs consisting of four monolayers of Ga and As atoms each, characterised by the point group C_{2v} . The first structure is probably less common, according to sample growers.

In this way, the symmetry of the structure permits the surface states with the same parallel wavevector \mathbf{k}_{\parallel} but opposite spins to have different energies: $E(\mathbf{k}_{\parallel}, m_j) \neq E(\mathbf{k}_{\parallel}, -m_j)$. A similar reasoning to the one in the previous subsection leads to the Bychkov–Rashba spin splitting [149, 150, 152]:

$$\boldsymbol{\Omega}_R(\mathbf{k}) \cdot \boldsymbol{\sigma} \sim \sigma_x k_x - \sigma_y k_y ,$$

for a layer grown along the [001] direction (the z axis). The magnitude of $\boldsymbol{\Omega}_R(\mathbf{k})$ depends on the parameters of the heterostructure integrating the layer and is linear in k in the vicinity of the Γ point. This is only the case of C_{2v} -symmetric layers (Fig. 5.3a), as for D_{2d} -symmetric ones (Fig. 5.3b), the inversion axis is restituted and the Bychkov–Rashba spin-orbit splitting vanishes [153].

The Bychkov–Rashba effect is of an intense research interest because of its crucial role in potential spintronics applications (current spin manipulation) [154]. It is a driving mechanism of the Datta and Das' spin transistor [21], which heralded the advent of spintronics, or the asymmetric resonant tunnelling diode spin filter [155]—to mention a few. The interference of the Bychkov–Rashba and Dresselhaus terms (the latter of which acquires a k -linear part arising from the surface inversion asymmetry in layers) is a subject of fascinating theoretical and experimental studies [156]. In Section 9.4, I will make use of the fact that the layers of (Ga,Mn)As have

their symmetry reduced to C_{2v} . This basic feature of the studied materials accounts for one of the most interesting results described in this thesis, which is the cycloidal ground-state spin structure and the resulting surface anisotropy of the diagonal in-plane directions in (Ga,Mn)As. Its derivation can certainly be translated into the language of Bychkov–Rashba and Dresselhaus spin-orbit couplings. A similar Bychkov–Rashba term, resulting from the presence of the sample interfaces, will be invoked in Sec. 10.4.2 as a possible explanation of the experimental results on the anomalous Hall effect in thin layers of (Ga,Mn)As.

5.5 The effect of strain

As mentioned in Section 3.4, the lattice strain yields qualitative effect on the electronic band structure. The tetragonal deformation of the lattice induced by the difference of the substrate and the film lattice parameters lifts the degeneracy of the light and heavy hole bands. It creates a splitting $2bQ_\epsilon$, where b is the deformation parameter (1.7 for GaAs) and Q_ϵ is a function of the strain tensor components

$$Q_\epsilon = \epsilon_{zz} - \frac{\epsilon_{xx} + \epsilon_{yy}}{2} .$$

Consequently, the sign of the growth strain dictates the relative position of the heavy and light holes in the Γ point. Under compressive strain the heavy hole band becomes the topmost valence band, whereas under tensile strain it is the light hole band. A direct consequence of the strain is the orientation of the easy and hard axes of magnetisation in (Ga,Mn)As layers [40], which will be analysed in Ch. 10.

5.6 The effect of sp - d exchange coupling

As described in Chapter 4, the spin of partially filled electronic shells of substitutional Mn atoms can couple to the spin of mobile band electrons via the sp - d exchange coupling, altering the band structure. This can be represented by the Heisenberg Hamiltonian

$$\mathcal{H}_{sp-d} = \sum_{i=1}^P \sum_{j=1}^N \mathbf{s}_i \cdot \mathbf{S}_j I(\mathbf{r}_i - \mathbf{R}_j) , \quad (5.5)$$

where \mathbf{s}_i and \mathbf{S}_j are the i -th carrier's and j -th ion's spin operators, while \mathbf{r}_i and \mathbf{R}_j are their respective positions. The strength of the sp - d exchange interaction between these two spins is described by a smooth, quickly vanishing function $I(\mathbf{r}_i - \mathbf{R}_j)$, localised around the j -th magnetic ion.

Behind (5.5) lie several physical assumptions about the magnetic ions. Firstly, that the magnitude of the localised spin is constant, as the number

of electrons on the ion's electronic shell is fixed. Secondly, that the localised moment can be described using the spin eigenstates, rather than the total angular momentum. These simplifications are justified by the agreement of the resulting model with a wide range of experimental data on III-V semiconductors.

The wavefunctions of band electrons extend through the whole crystal, and interact with all magnetic ions. In this way, they are subject to an average spin value of the localised moments, which allows to simplify the Hamiltonian (5.5) by making the mean-field approximation, i.e. replacing \mathbf{S}_j by their average $\langle \mathbf{S} \rangle$. It can now be written as

$$\mathcal{H}_{sp-d} = \sum_{i=1}^P \mathbf{s}_i \cdot \langle \mathbf{S} \rangle \sum_{j=1}^N I(\mathbf{r}_i - \mathbf{R}_j) .$$

Additionally, I recall the virtual crystal approximation from Sec. 3.3 and assume that the sum $\sum_{j=1}^N$ runs over all lattice sites in the crystal, with an average spin $x\langle \mathbf{S} \rangle$ occupying each of them, where x is the fraction of magnetic ions in the system. Assuming a given value of $\langle \mathbf{S} \rangle$, the exchange interaction is thus a Zeeman-type spin-splitting term acting on all electrons in the same way. I assume that the z coordinate axis is aligned with the average ion spin $\langle \mathbf{S} \rangle$, hence $\mathbf{s}_i \cdot \langle \mathbf{S} \rangle = s_i^z \langle S^z \rangle$.

The effect of the $sp-d$ coupling on the band structure of (Ga,Mn)As can be analytically derived for the case of the two-fold degenerate s -like conduction band ($l = 0$, $s^z = +1/2, -1/2$) and the six-fold degenerate p -like valence bands ($l = 1$, $l^z = -1, 0, 1$, $s^z = +1/2, -1/2$), which is often sufficient for e.g. optical experiments. The spin-orbit interaction splits the eigenstates of the total angular momentum $j = 1/2$ from those of the $j = 3/2$ state in the valence band by a relatively large value of Δ_{so} , which causes the $j = 1/2$ eigenstates to be negligible when dealing with processes taking place in the vicinity of the band gap.

The spin is a good quantum number for the s -type conduction band electrons, which makes the effect of exchange coupling easy to calculate for these states: the change in the band energy at the Γ point is equal

$$E(s^z) = x\langle S^z \rangle N_0 \alpha s^z , \quad \text{where } s^z = \pm \frac{1}{2} , \quad (5.6)$$

where N_0 is the number of crystal sites per volume,

$$\alpha = \int_V d^3r S(\mathbf{r})^* I(\mathbf{r} - \mathbf{R}) S(\mathbf{r}) = V \langle S|I|S \rangle$$

is the $s-d$ exchange integral over the crystal volume V and $|S\rangle$ is the periodic part of the s -type band wavefunction at $\mathbf{k} = 0$.

For the p -type valence bands, which are not eigenstates of spin, we can define a $p-d$ exchange integral as

$$\beta = V \langle X|I|X \rangle = V \langle Y|I|Y \rangle = V \langle Z|I|Z \rangle ,$$

where $|X\rangle$, $|Y\rangle$ and $|Z\rangle$ are the p -type periodic wavefunctions from the Γ point of the valence band. The p - d exchange interaction for these bands is described by the operator

$$E(j^z) = \frac{1}{3}x\langle S^z\rangle N_0\beta j^z, \text{ where } j^z = \pm\frac{1}{2}, \pm\frac{3}{2}. \quad (5.7)$$

As indicated by Eqs. (5.6) and (5.7), the s - d and p - d exchange couplings lead to effective magnetic fields $\langle S^z\rangle$ in the system. Unlike the effective spin-orbit fields (Sec. 5.4), they always break the time reversal symmetry, as they result from Zeeman-type spin-splitting of the bands, which—by itself—breaks this symmetry [153]. It removes the spin degeneracy and induces a nonequilibrium spin polarisation.

There are two processes contributing to the sp - d exchange interaction: the direct exchange interaction between the band states and the localised electrons and the hybridisation of $3d^5$ levels with the s and p band electrons. The first mechanism tends to align the electron spins parallel to each other, and thus leads to ferromagnetic interaction. It gives a positive contribution to the α and β exchange constants. However, at the Γ point, the s - d hybridisation is forbidden by symmetry, and this contribution vanishes. Therefore α arises only from the direct exchange and is always positive. On the other hand, the β exchange constant contains both contributions, from the p - d hybridisation (which is always allowed) and the direct exchange (though in much smaller part). The dominant effect of hybridisation on the character of the p - d exchange makes it strongly dependent on the electronic configuration of the Mn ions (discussed in Sec. 3.3). The sign of β depends on the character of the impurity centre: in the presence of a loosely bound hole in A^0 , it opens a ferromagnetic exchange path whereas the A^- acceptor has only antiferromagnetic channels.⁴ What is more, the direct measurement of the exchange constants in (Ga,Mn)As is precluded by high concentration of growth defects, and their values can be based only on estimations [158–162]. The problem of the estimation of the coupling constants falls outside the scope of my thesis. I have used the values which were previously employed in calculation made in our group within the tight-binding model [163–165]; they will be listed in Ch. 6.

Before I demonstrate how the exchange interaction leads to ferromagnetic coupling of the ensemble of Mn ions in Ch. 7, I will describe the band structure methods that I have used in my calculations based on the above considerations.

⁴Such a dependence on the nature of the Mn acceptor core is often suggested as an explanation for the apparent sign change of the p - d term when the Mn concentration is increased from the very dilute paramagnetic limit to the high doping ferromagnetic regime [157].

Chapter 6

Band structure methods

In this chapter I discuss the $k \cdot p$ and tight-binding computational schemes, which will be employed in the calculations of the band structure of (Ga,Mn)As. I provide the theoretical underpinning and the modelling parameters of these methods. They are based on the $k \cdot p$ (6- and 8-band) and tight-binding (sps^* 20- and $spds^*$ 40-orbital) band structure approximations of the GaAs host lattice. The presence of Mn substitutional atoms is taken into account within the mean-field and virtual crystal approximations, and modelled as the Zeeman-type spin-splitting of the bands induced by the $sp-d$ exchange interaction. Additionally, the effects of the growth-induced biaxial strain are included.

Throughout the text, I will refer to different computational schemes by the names of the GaAs band structure calculation methods they employ.

6.1 The $k \cdot p$ method

Bir and Pikus [166] observed, since the physics of a semiconductor is largely governed by the carriers in the extreme points of energy bands, that only the neighbourhoods of the band extrema should be important and that the qualitative properties of these materials should be governed by the shape of these energy surfaces. Although not always correct, the first observation is what has historically driven the development of the $k \cdot p$ method as a perturbative approach [142, 167, 168]. On the other hand, the power of symmetry analysis manifested itself in the non-perturbative $k \cdot p$ analysis of semiconductor band structure by Kohn and Luttinger [124] and led to the development of full-zone $k \cdot p$ calculations such as demonstrated by [169].

Bloch functions $\varphi_{n\mathbf{k}} = e^{i\mathbf{k}\cdot\mathbf{r}}u_{n\mathbf{k}}$ form a complete orthonormal basis. Kohn and Luttinger have shown that a different set of functions,

$$\chi_{n\mathbf{k}} := e^{i\mathbf{k}\cdot\mathbf{r}}u_{n\mathbf{k}_0}, \quad \mathbf{k}_0 \in \mathcal{B}, \quad (6.1)$$

is also a complete orthonormal basis, in which the eigenstates $\varphi_{n\mathbf{k}}$ can be

expanded:

$$\varphi_{n\mathbf{k}} = \sum_{n'} b_{nn'}(\mathbf{k}) \chi_{n'\mathbf{k}}, \quad b_{nn'}(\mathbf{k}_0) = \delta_{nn'}. \quad (6.2)$$

The coefficients $b_{nn'}(\mathbf{k})$ can be found by solving the Schrödinger equation

$$\left(\frac{\hat{\mathbf{p}}^2}{2m_0} + V(\mathbf{r}) \right) \varphi_{n\mathbf{k}} = E_{n\mathbf{k}} \varphi_{n\mathbf{k}}.$$

Using (6.1) and (6.2), we obtain a set of equations for $b_{nn'}(\mathbf{k})$

$$\sum_{n'} b_{nn'}(\mathbf{k}) \left\langle u_{n''\mathbf{k}_0} \left| \frac{\hat{\mathbf{p}}^2}{2m_0} + V(\mathbf{r}) + \frac{\hat{\pi}}{m_0} \cdot \hbar \mathbf{k} + \frac{\hbar^2 \mathbf{k}^2}{2m_0} \right| u_{n'\mathbf{k}_0} \right\rangle = E_{n\mathbf{k}} b_{nn''}(\mathbf{k}), \quad (6.3)$$

where

$$\hat{\pi} = \hat{\mathbf{p}} + \frac{1}{4m_0c^2} \sigma \times \nabla V$$

accounts for both momentum and spin-orbit operators. Assuming that we know the matrix elements

$$\begin{aligned} H_{nn'}(\mathbf{k}) &= \left\langle u_{n\mathbf{k}_0} \left| \frac{\hat{\mathbf{p}}^2}{2m_0} + V(\mathbf{r}) + \frac{\hat{\pi}}{m_0} \cdot \hbar \mathbf{k} + \frac{\hbar^2 \mathbf{k}^2}{2m_0} \right| u_{n'\mathbf{k}_0} \right\rangle \\ &= E_{n\mathbf{k}_0} \delta_{nn'} + \left\langle u_{n\mathbf{k}_0} \left| \frac{\hat{\pi}}{m_0} \cdot \hbar (\mathbf{k} - \mathbf{k}_0) + \frac{\hbar^2 (\mathbf{k}^2 - \mathbf{k}_0^2)}{2m_0} \right| u_{n'\mathbf{k}_0} \right\rangle \end{aligned}$$

we have reduced the problem of calculating the full electron structure to diagonalising a \mathbf{k} -dependent matrix $H(\mathbf{k})$. Choosing \mathbf{k}_0 to be a point with high symmetry simplifies the task of calculating the elements of this matrix, as the group theory tells us which of them are zero and which of them are equal to others because of symmetry properties [124] (for simplicity and because it is the most common case, I set $\mathbf{k}_0 = 0$ in the remaining part of this chapter). The remaining ones have to be calculated using *ab initio* methods or determined by fitting to experimental data. For this purpose, we can make use of the optical measurements, which provide information about the matrix elements of the momentum operator.

To describe the band structure across the full Brillouin zone, the $k \cdot p$ method requires the use of a large number of basis functions. Recently, basis sizes as high as 30 were used for GaAs [170]. However, this increases the computational cost and requires the fitting of many parameters to experimental measurements, which is a non-trivial problem already for small basis sizes (see e.g. [171]). Another approach is to use multiple expansion points for different parts of the Brillouin zone [172], or to extrapolate the more precise self-consistent pseudopotential energy band calculations [173].

When only a small number of Γ point eigenstates are used as a basis for the $k \cdot p$ Hamiltonian, the method becomes perturbational and loses its accuracy as the distance $|\mathbf{k}|$ increases. The coupling of the first N bands to

the higher-lying ones can be taken into account using the Loewdin perturbation calculus [41, 174]. Namely, we can replace $H_{nn'}(\mathbf{k})$, $n, n' \leq N$, with the following expression

$$H'_{nn'}(\mathbf{k}) = H_{nn'}(\mathbf{k}) + \sum_{k>N} \frac{H_{nk}(\mathbf{k})H_{kn'}(\mathbf{k})}{E_{n0} - E_{k0}} .$$

For an example of such procedure applied to GaAs, see [175]. The bases of the $k \cdot p$ Hamiltonians I have used are composed of either six (Kohn–Luttinger) or eight (Kane) states, and thus are both perturbational. Finally, the simplest application of the perturbational $k \cdot p$ method is the calculation of the effective mass tensor for the n -th band at $\mathbf{k} = 0$, performed by treating the term $\frac{\hbar}{m_0} \cdot \hbar \mathbf{k} + \hbar^2 \mathbf{k}^2 / 2m_0$ as a perturbation of the u_{n0} eigenstate.

6.1.1 Strain

The term which needs to be added to the $k \cdot p$ Hamiltonian to account for the strain was derived by Bir and Pikus [166]. We consider a uniformly deformed crystal, in which the lattice coordinates are subject to the transformation

$$\mathbf{r}' = (1 + \epsilon) \mathbf{r} ,$$

where ϵ is the constant strain tensor. The corresponding transformation for the momentum operator is

$$\hat{\mathbf{p}}' = \hat{\mathbf{p}}(1 - \epsilon) ,$$

which leads to, in the limit of small ϵ ,

$$(\hat{\mathbf{p}}')^2 \approx \hat{\mathbf{p}}^2 - 2 \sum_{i,j} \hat{p}_i \epsilon_{ij} \hat{p}_j .$$

Also in this limit, the lattice potential is transformed to

$$V(\mathbf{r}') \approx V(\mathbf{r}) + \sum_{i,j} V_{ij}(\mathbf{r}) \epsilon_{ij} .$$

where

$$V_{ij}(\mathbf{r}) := \left. \frac{\partial V((1 + \epsilon)\mathbf{r})}{\partial \epsilon_{ij}} \right|_{\epsilon=0}$$

We thus arrive at the equation for the band eigenstates in the presence of strain:

$$\left[\hat{H}(\mathbf{r}) + \hat{H}_\epsilon(\mathbf{r}) \right] \varphi_{n\mathbf{k}'} [(1 + \epsilon)\mathbf{r}] = E_{n\mathbf{k}'} \varphi_{n\mathbf{k}'} [(1 + \epsilon)\mathbf{r}] ,$$

where

$$\hat{H}_\epsilon(\mathbf{r}) = \sum_{i,j} \hat{D}^{ij} \epsilon_{ij} = \sum_{ij} \left(-\frac{1}{m_0} \hat{p}_i \hat{p}_j + V_{ij}(\mathbf{r}) \right) \epsilon_{ij}$$

is the strain perturbation term. Using the $k \cdot p$ Hamiltonian basis and leaving only the terms linear in ϵ , we obtain the strained Hamiltonian matrix

$$(H_{\text{BS}}(\epsilon))_{kl} = \sum_{ij} \hat{D}_{kl}^{ij} \epsilon_{ij} ,$$

where \hat{D}_{kl}^{ij} are the matrix elements of operators \hat{D}^{ij} . Using the symmetry properties of the Γ point eigenstates, they are decomposed into linear combinations of a lower number of parameters, called the deformation potentials. Although theoretically it is possible to calculate them via the pseudopotential or *ab initio* methods, it is more convenient to fit the deformation potentials to experimental results.

6.1.2 Exchange interaction

The presence of Mn ions is introduced using the mean-field and virtual-crystal approximations. The exchange spin splitting of the heavy hole bands in the Γ point, $\Delta = xN_0\beta S$, which for typical $x = 5\%$ Mn concentration gives -0.15 eV. The value of the p - d exchange integral is taken to be $\beta = -0.054$ eV nm³ (assuming the lattice constant $a_0 = 0.565$ nm) [40]. The s - d exchange integral, responsible for the Γ_6 band spin splitting, is taken to be $\alpha = 0.009$ eV nm³ [176]. Defining P_p and P_s as the projection operators on the p - and s -type basis functions, respectively, the total exchange interaction Hamiltonian can be written as

$$H_{\text{ex}} = xN_0S (\beta P_p + \alpha P_s) s^z = \Delta P_{\text{ex}} s^z , \quad (6.4)$$

where $N_0 = 4/a_0^3$ and $P_{\text{ex}} = P_p + \frac{\alpha}{\beta} P_s$ commutes with the spin operator.¹ As the s - d exchange integral α is much smaller than β , the latter determines the strength of the ion-carrier coupling. In the case of Kohn–Luttinger Hamiltonian, which describes only the p -type bands, operator (6.4) is simplified to

$$H_{p-d} = \Delta s^z .$$

6.1.3 Parametrisations

In my thesis I have used the 6-band Kohn–Luttinger $k \cdot p$ Hamiltonian for GaAs, after Dietl *et al.* [40], and 8-band Kane, in the parameterisation by Ostromek that takes into account the inversion asymmetry of GaAs [171]. Ostromek defines two optimised sets of parameters for the Kane Hamiltonian, which give very similar results. The values of Luttinger parameters for each Hamiltonian are given in Table 6.1, while the additional parameters of the Kane Hamiltonian are given in Table 6.2. The spin-orbit splitting of the Γ_8 and Γ_7 bands, Δ_{SO} , equals 0.341 eV in both parametrisations.

¹In general, P_{ex} is not a projection operator, as $(P_p + \frac{\alpha}{\beta} P_s)^2 = P_p^2 + \frac{\alpha}{\beta} (P_p P_s + P_s P_p) + \frac{\alpha^2}{\beta^2} P_s^2 = P_p + \frac{\alpha^2}{\beta^2} P_s \neq P_{\text{ex}}$ for $\alpha \neq \beta$. However, it maps its image onto itself.

Parameter	Kohn–Luttinger	Kane (set 1)	Kane (set 2)
γ_1^l	6.85	6.672	6.669
γ_2^l	2.10	1.866	1.864
γ_3^l	2.90	2.669	2.668

Table 6.1: Luttinger parameters for $k \cdot p$ Hamiltonians

Parameter	Set 1	Set 2
$E_c \equiv E(\Gamma_6)$ [eV]	1.1519	1.1519
$E_v \equiv E(\Gamma_8)$ [eV]	0	0
A' [eV \AA^2]	0	-14.70
E_p [eV]	22.827	29.112
C_0 [eV \AA^2]	0.1257	0.1564
B [eV \AA^2]	41.90	39.11

Table 6.2: Additional parameters of the Kane 8x8 Hamiltonian.

Kohn–Luttinger Hamiltonian

The Hamiltonian matrix is calculated in the following basis:

$$\begin{aligned}
u_1 &= \frac{1}{\sqrt{2}}(X + iY)|\uparrow\rangle, & u_2 &= \frac{i}{\sqrt{6}}[(X + iY)|\downarrow\rangle - 2Z|\uparrow\rangle], \\
u_3 &= \frac{1}{\sqrt{6}}[(X - iY)|\uparrow\rangle + 2Z|\downarrow\rangle], & u_4 &= \frac{i}{\sqrt{2}}(X - iY)|\downarrow\rangle, \\
u_5 &= \frac{1}{\sqrt{3}}[(X + iY)|\downarrow\rangle + Z|\uparrow\rangle], & u_6 &= \frac{i}{\sqrt{3}}[-(X - iY)|\uparrow\rangle + Z|\downarrow\rangle],
\end{aligned}$$

where X , Y and Z are the Kohn–Luttinger wavefunctions which transform under the symmetry operations of the crystal point group as p_x , p_y and p_z orbitals, respectively.

The $k \cdot p$ Hamiltonian matrix in the above basis is given by

$$H_{k \cdot p}(\mathbf{k}) = -\frac{\hbar^2}{2m_0} \times
\begin{pmatrix}
P + Q & L & M & 0 & iL/\sqrt{2} & -i\sqrt{2}M \\
L^* & P - Q & 0 & M & -i\sqrt{2}Q & i\sqrt{3/2}L \\
M^* & 0 & P - Q & -L & -i\sqrt{3/2}L^* & -i\sqrt{2}Q \\
0 & M^* & -L^* & P + Q & -i\sqrt{2}M^* & -iL^*/\sqrt{2} \\
-iL^*/\sqrt{2} & i\sqrt{2}Q & i\sqrt{3/2}L & i\sqrt{2}M & P + \Delta & 0 \\
i\sqrt{2}M^* & -i\sqrt{3/2}L^* & i\sqrt{2}Q & iL/\sqrt{2} & 0 & P + \Delta
\end{pmatrix},$$

where

$$\begin{aligned}
P &= \gamma_1^l k^2, & Q &= \gamma_2^l (k_x^2 + k_y^2 - 2k_z^2), \\
\Delta &= 2m_0 \Delta_{\text{SO}} / \hbar^2, & M &= \sqrt{3} \left[\gamma_2^l (k_x^2 - k_y^2) - i2\gamma_3^l k_x k_y \right], \\
L &= -i2\sqrt{3}\gamma_3^l (k_x - ik_y)k_z,
\end{aligned}$$

and the negative sign in front of the Hamiltonian indicates that the bands are of the hole type. The spin operator matrices are equal

$$s^x = \begin{pmatrix} 0 & \frac{i}{2\sqrt{3}} & 0 & 0 & \frac{1}{\sqrt{6}} & 0 \\ -\frac{i}{2\sqrt{3}} & 0 & \frac{i}{3} & 0 & 0 & -\frac{1}{\sqrt{23}} \\ 0 & -\frac{i}{3} & 0 & \frac{1}{2\sqrt{3}} & \frac{1}{\sqrt{23}} & 0 \\ 0 & 0 & -\frac{i}{2\sqrt{3}} & 0 & 0 & -\frac{1}{\sqrt{23}} \\ \frac{1}{\sqrt{6}} & 0 & \frac{1}{\sqrt{23}} & 0 & 0 & \frac{i}{6} \\ 0 & -\frac{1}{\sqrt{23}} & 0 & -\frac{1}{\sqrt{23}} & -\frac{i}{6} & 0 \end{pmatrix},$$

$$s^y = \begin{pmatrix} 0 & \frac{1}{2\sqrt{3}} & 0 & 0 & -\frac{i}{\sqrt{6}} & 0 \\ \frac{1}{2\sqrt{3}} & 0 & \frac{1}{3} & 0 & 0 & \frac{i}{\sqrt{23}} \\ 0 & \frac{1}{3} & 0 & \frac{1}{2\sqrt{3}} & \frac{i}{\sqrt{23}} & 0 \\ 0 & 0 & \frac{1}{2\sqrt{3}} & 0 & 0 & -\frac{i}{\sqrt{23}} \\ \frac{i}{\sqrt{6}} & 0 & -\frac{i}{\sqrt{23}} & 0 & 0 & \frac{1}{6} \\ 0 & -\frac{i}{\sqrt{23}} & 0 & \frac{i}{\sqrt{23}} & \frac{1}{6} & 0 \end{pmatrix},$$

and

$$s^z = \begin{pmatrix} \frac{1}{2} & 0 & 0 & 0 & 0 & 0 \\ 0 & \frac{1}{6} & 0 & 0 & \frac{\sqrt{2}}{3}i & 0 \\ 0 & 0 & -\frac{1}{6} & 0 & 0 & -\frac{\sqrt{2}}{3}i \\ 0 & 0 & 0 & -\frac{1}{2} & 0 & 0 \\ 0 & -\frac{\sqrt{2}}{3}i & 0 & 0 & -\frac{1}{6} & 0 \\ 0 & 0 & \frac{\sqrt{2}}{3}i & 0 & 0 & \frac{1}{6} \end{pmatrix},$$

while the Bir-Pikus strain operator matrix is

$$H_{\text{BS}}(\epsilon) = b \begin{pmatrix} -Q_\epsilon & 0 & R_\epsilon & 0 & 0 & -i\sqrt{2}R_\epsilon \\ 0 & Q_\epsilon & 0 & R_\epsilon & i\sqrt{2}Q_\epsilon & 0 \\ R_\epsilon & 0 & Q_\epsilon & 0 & 0 & i\sqrt{2}Q_\epsilon \\ 0 & R_\epsilon & 0 & -Q_\epsilon & -i\sqrt{2}R_\epsilon & 0 \\ 0 & -i\sqrt{2}Q_\epsilon & 0 & i\sqrt{2}R_\epsilon & 0 & 0 \\ i\sqrt{2}R_\epsilon & 0 & -i\sqrt{2}Q_\epsilon & 0 & 0 & 0 \end{pmatrix},$$

where b is the uniaxial deformation potential taken to be $b = -1.7$ eV [40],

and Q_ϵ and R_ϵ are the following functions of the strain tensor ϵ :

$$\begin{aligned} Q_\epsilon &= \epsilon_{zz} - (\epsilon_{xx} + \epsilon_{yy})/2 , \\ R_\epsilon &= \sqrt{3}(\epsilon_{xx} - \epsilon_{yy})/2 , \end{aligned}$$

neglecting the hydrostatic strain. Additionally, since I consider the growth-induced biaxial strain only, $\epsilon_{xx} = \epsilon_{yy}$ and $R_\epsilon = 0$.

The complete Hamiltonian matrix for wavevector \mathbf{k} , spin splitting Δ and strain tensor ϵ is $H_{k,p}(\mathbf{k}) + H_{\text{BS}}(\epsilon) + \Delta s^z$. As $H_{k,p}(\mathbf{k}) = H_{k,p}(-\mathbf{k})$, the Kohn–Luttinger does not account for the inversion symmetry breaking of the zincblende lattice structure.

Kane Hamiltonian

The Kane model describes the s - and p -type bands in a basis composed of eight s - and p -like states, expanding the Hamiltonian around the $\mathbf{k} = 0$ point. The coupling to other states is taken into account using the Löwdin calculus [171].

As in the case of the Kohn–Luttinger Hamiltonian, I express $H(\mathbf{k})$ as $H_{k,p}(\mathbf{k}) + H_{\text{BS}}(\epsilon) + \Delta s^z$. Below I provide the definitions of the Hamiltonian basis

$$\begin{aligned} u_1 &= S|\downarrow\rangle , & u_2 &= S|\uparrow\rangle , \\ u_3 &= -\frac{i}{\sqrt{6}}(X + iY)|\downarrow\rangle + i\sqrt{\frac{2}{3}}Z|\uparrow\rangle , & u_4 &= \frac{i}{\sqrt{2}}(X + iY)|\uparrow\rangle , \\ u_5 &= -\frac{i}{\sqrt{2}}(X - iY)|\downarrow\rangle , & u_6 &= \frac{i}{\sqrt{6}}(X - iY)|\uparrow\rangle + i\sqrt{\frac{2}{3}}Z|\downarrow\rangle , \\ u_7 &= -\frac{i}{\sqrt{3}}(X - iY)|\uparrow\rangle + \frac{i}{\sqrt{3}}Z|\downarrow\rangle , & u_8 &= -\frac{i}{\sqrt{3}}(X + iY)|\downarrow\rangle - \frac{i}{\sqrt{3}}Z|\uparrow\rangle , \end{aligned}$$

where S , X , Y and Z are the Kohn–Luttinger wavefunctions transforming under the crystal point group symmetry operations as s , p_x , p_y and p_z

orbitals, respectively. The $k \cdot p$ Hamiltonian matrix in this basis is given by

$$\begin{aligned}
H_{k \cdot p}(\mathbf{k}) = & \\
& \left(\begin{array}{cccc}
A & 0 & T^* + V^* & 0 \\
0 & A & \sqrt{2}(W - U) & -\sqrt{3}(T^* + V^*) \\
T + V & \sqrt{2}(W^* - U) & -P + Q & -S^* \\
0 & -\sqrt{3}(T + V) & -S & -P - Q \\
-\sqrt{3}(T^* - V^*) & 0 & R^* & 0 \\
\sqrt{2}(W^* - U) & T^* - V^* & 0 & R^* \\
W^* - U & -\sqrt{2}(T^* - V^*) & \sqrt{\frac{3}{2}}S^* & -\sqrt{2}R^* \\
\sqrt{2}(T + V) & W + U & -\sqrt{2}Q & \sqrt{\frac{1}{2}}S^* \\
-\sqrt{3}(T - V) & \sqrt{2}(W - U) & W - U & \sqrt{2}(T^* + V^*) \\
0 & T - V & -\sqrt{2}(T - V) & W^* + U \\
R & 0 & \sqrt{\frac{3}{2}}S & -\sqrt{2}Q \\
0 & R & -\sqrt{2}R & \sqrt{\frac{1}{2}}S \\
\cdots & -P - Q & \sqrt{\frac{1}{2}}S^* & \sqrt{2}R^* \\
S & -P + Q & \sqrt{2}Q & \sqrt{\frac{3}{2}}S^* \\
\sqrt{\frac{1}{2}}S & \sqrt{2}Q & Z & 0 \\
\sqrt{2}R & \sqrt{\frac{3}{2}}S & 0 & Z
\end{array} \right) + M_{\text{kso}} ,
\end{aligned} \tag{6.5}$$

where

$$\begin{aligned}
A &= E_c + \left[A' + \frac{\hbar^2}{2m_0} \right] k^2 , & U &= \frac{1}{\sqrt{3}} P_0 k_z , \\
V &= \frac{1}{\sqrt{6}} P_0 (k_x - ik_y) , & W &= \frac{i}{\sqrt{3}} B k_x k_y , \\
T &= \frac{1}{\sqrt{6}} B k_z (k_x + ik_y) , & P &= -E_v + \gamma_1 \frac{\hbar^2}{2m_0} k^2 , \\
Q &= \gamma_2 \frac{\hbar^2}{2m_0} (k^2 - 3k_z^2) , & R &= -\sqrt{3} \frac{\hbar^2}{2m_0} [\gamma_2 (k_x^2 - k_y^2) - 2i\gamma_3 k_x k_y] , \\
S &= \sqrt{3} \gamma_3 \frac{\hbar^2}{m_0} k_z (k_x - ik_y) , & Z &= E_v - \Delta_{\text{SO}} - \gamma_1 \frac{\hbar^2}{2m_0} k^2 ,
\end{aligned}$$

$E_p = \frac{2m_0}{\hbar^2} P_0^2$, and

$$\begin{aligned}
\gamma_1 &= \gamma_1^l - \frac{E_p}{3E_g + \Delta_{\text{SO}}} , & \gamma_2 &= \gamma_2^l - \frac{1}{2} \frac{E_p}{3E_g + \Delta_{\text{SO}}} , \\
\gamma_3 &= \gamma_3^l - \frac{1}{2} \frac{E_p}{3E_g + \Delta_{\text{SO}}} , & E_g &= E_c - E_v .
\end{aligned}$$

The matrix M_{kso} describes the \mathbf{k} -dependent part of the spin-orbit interaction and is of the form

$$M_{\text{kso}} = \begin{pmatrix} 0 & M_1 & M_2 \\ M_1^\dagger & 0 & 0 \\ M_2^\dagger & 0 & 0 \end{pmatrix},$$

where

$$M_1 = \frac{C_0}{\sqrt{2}} \begin{pmatrix} -(k_x + ik_y) & 0 & -\sqrt{3}(k_x - ik_y) & 2k_z \\ 2k_z & \sqrt{3}(k_x + ik_y) & 0 & k_x - ik_y \end{pmatrix}$$

and

$$M_2 = 2C_0 \begin{pmatrix} -k_z & k_x + ik_y \\ k_x - ik_y & k_z \end{pmatrix}.$$

The spin operator matrices in this basis have the form

$$s^x = \begin{pmatrix} 0 & \frac{1}{2} & 0 & 0 & 0 & 0 & 0 & 0 \\ \frac{1}{2} & 0 & 0 & 0 & 0 & 0 & 0 & 0 \\ 0 & 0 & 0 & -\frac{1}{2\sqrt{3}} & 0 & \frac{1}{3} & \frac{1}{\sqrt{23}} & 0 \\ 0 & 0 & -\frac{1}{2\sqrt{3}} & 0 & 0 & 0 & 0 & -\frac{1}{\sqrt{6}} \\ 0 & 0 & 0 & 0 & 0 & -\frac{1}{2\sqrt{3}} & \frac{1}{\sqrt{6}} & 0 \\ 0 & 0 & \frac{1}{3} & 0 & -\frac{1}{2\sqrt{3}} & 0 & 0 & -\frac{1}{\sqrt{23}} \\ 0 & 0 & \frac{1}{\sqrt{23}} & 0 & \frac{1}{\sqrt{6}} & 0 & 0 & -\frac{1}{6} \\ 0 & 0 & 0 & -\frac{1}{\sqrt{6}} & 0 & -\frac{1}{\sqrt{23}} & -\frac{1}{6} & 0 \end{pmatrix},$$

$$s^y = \begin{pmatrix} 0 & \frac{i}{2} & 0 & 0 & 0 & 0 & 0 & 0 \\ -\frac{i}{2} & 0 & 0 & 0 & 0 & 0 & 0 & 0 \\ 0 & 0 & 0 & -\frac{i}{2\sqrt{3}} & 0 & -\frac{i}{3} & -\frac{i}{\sqrt{23}} & 0 \\ 0 & 0 & \frac{i}{2\sqrt{3}} & 0 & 0 & 0 & 0 & \frac{i}{\sqrt{6}} \\ 0 & 0 & 0 & 0 & 0 & -\frac{i}{2\sqrt{3}} & \frac{i}{\sqrt{6}} & 0 \\ 0 & 0 & \frac{i}{3} & 0 & \frac{i}{2\sqrt{3}} & 0 & 0 & -\frac{i}{\sqrt{23}} \\ 0 & 0 & \frac{i}{\sqrt{23}} & 0 & -\frac{i}{\sqrt{6}} & 0 & 0 & -\frac{i}{6} \\ 0 & 0 & 0 & -\frac{i}{\sqrt{6}} & 0 & \frac{i}{\sqrt{23}} & \frac{i}{6} & 0 \end{pmatrix}$$

and

$$s^z = \begin{pmatrix} -\frac{1}{2} & 0 & 0 & 0 & 0 & 0 & 0 & 0 \\ 0 & \frac{1}{2} & 0 & 0 & 0 & 0 & 0 & 0 \\ 0 & 0 & \frac{1}{6} & 0 & 0 & 0 & 0 & -\frac{\sqrt{2}}{3} \\ 0 & 0 & 0 & \frac{1}{2} & 0 & 0 & 0 & 0 \\ 0 & 0 & 0 & 0 & -\frac{1}{2} & 0 & 0 & 0 \\ 0 & 0 & 0 & 0 & 0 & -\frac{1}{6} & -\frac{\sqrt{2}}{3} & 0 \\ 0 & 0 & 0 & 0 & 0 & -\frac{\sqrt{2}}{3} & \frac{1}{6} & 0 \\ 0 & 0 & -\frac{\sqrt{2}}{3} & 0 & 0 & 0 & 0 & -\frac{1}{6} \end{pmatrix}.$$

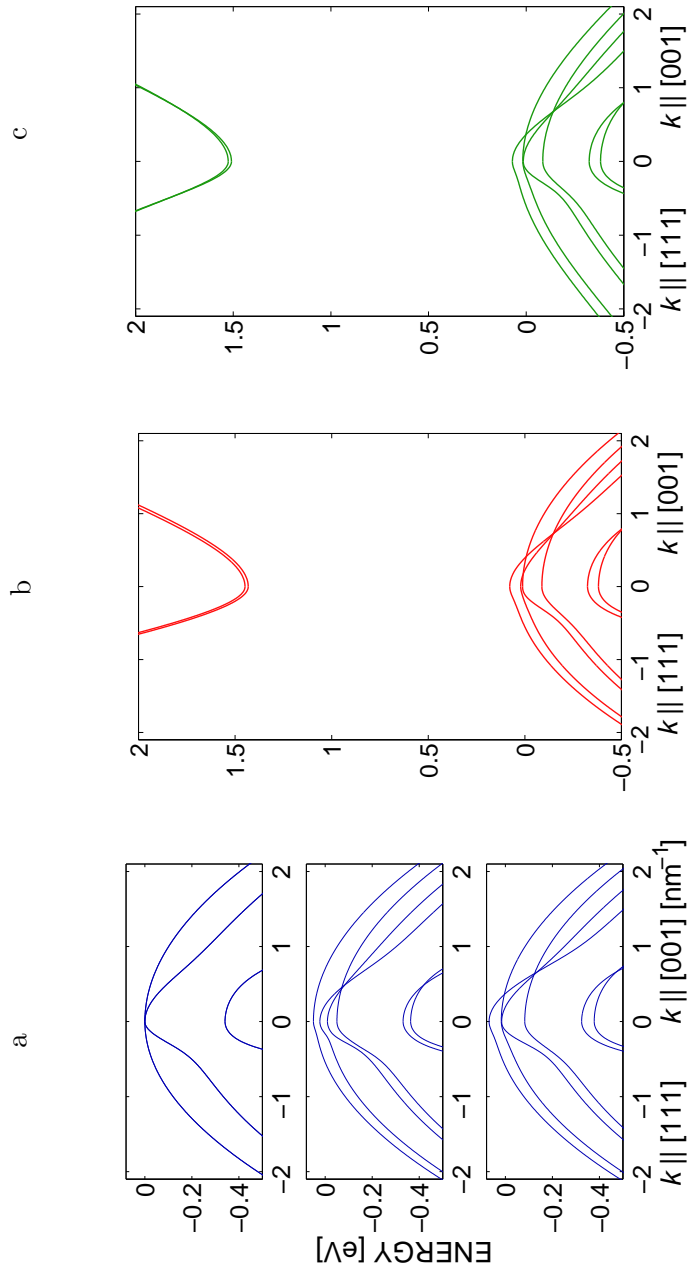


Figure 6.1: The vicinity of the band gap in (Ga,Mn)As. a) The 6-band $k \cdot p$ model: (top) pure GaAs, (middle) unstrained (Ga,Mn)As taking into account the p - d exchange interaction resulting in spin-splitting $\Delta = -0.1$ eV in the valence band, (bottom) biaxially tensile strained (Ga,Mn)As with $\Delta = -0.1$ eV and $\epsilon_{xx} = 1\%$. The last case is also calculated using the 8-band $k \cdot p$ (b) and 40-orbital $spds^*$ tight-binding model (c – analysed in the next section), additionally including the s - d exchange coupling resulting in the spin-splitting of the conduction band.

6.2 Tight-binding approximation

The significance of the original paper, by Slater and Koster (1954), can perhaps be best demonstrated by anecdotal evidence—in the shelves of the Radcliffe Science Library, Oxford, volume 94 of Physical Review stands out from its shelf for its broken spine, and falls open at table 1 on page 1503. [178]

The tight-binding method describes the electrons in a periodic crystal using a basis set composed of Bloch functions built from localised, atomic-like wavefunctions, which share the angular momentum components of the atomic orbitals and like them are easily split into radial and angular parts. In this sense it is the opposite of the pseudopotential method, which uses a plane-wave basis. Although both bases are complete, and therefore theoretically equivalent, in numerical calculations we must use a finite subset of the infinite number of basis vectors.

For each wavevector \mathbf{k} we obtain a set of Bloch functions, their number equal to the number of atomic orbitals in a unit cell used to construct the basis. The exact many-body Hamiltonian operator is replaced by a parametrised Hamiltonian matrix with \mathbf{k} -dependent elements. The parameters of the matrix are fitted to experimental data or more accurate band structure calculations in selected points of the reciprocal space (*empirical tight-binding*, invented by Slater and Koster in 1954 [179]); alternatively, they are calculated by *ab-initio* methods (*first principles tight-binding*).

Within the tight-binding method, we construct the crystal lattice by translating the minimum unit cell along the primitive lattice vectors [179]. In the present case, it is composed of one Ga and one As atom, as described in Sec. 3.2. The localised wavefunction $\varphi_{i\alpha}$ corresponds to the i -th atom in the unit cell and its α -th orbital. For each (i, α) , one constructs the corresponding Bloch wavefunction (following the normalisation convention from Sec. 5.1),

$$\Phi_{\mathbf{k},i\alpha}(\mathbf{r}) = \sqrt{\Omega} \sum_n e^{i\mathbf{k}\cdot\mathbf{R}_{ni}} \varphi_{ni\alpha}(\mathbf{r}) ,$$

where Ω is the unit cell volume,

$$\varphi_{ni\alpha}(\mathbf{r}) := \varphi_{i\alpha}(\mathbf{r} - \mathbf{R}_{ni})$$

and \mathbf{R}_{ni} is the position of i -th intracell atom in n -th (out of N) unit cell. If $\{\varphi_{i\alpha}\}$ were equal to atomic orbitals $\{\phi_{i\alpha}\}$, then $\{\varphi_{ni\alpha}\}$ would not be orthonormal due to non-diagonal overlap integrals. We construct an orthonormal basis from translated atomic orbitals $\phi_{ni\alpha}(\mathbf{r}) := \phi_{i\alpha}(\mathbf{r} - \mathbf{R}_{ni})$ using a method by Löwdin [180]. Let Δ be the matrix of overlap integrals for $\{\phi_{ni\alpha}\}$, $\Delta_{ni\alpha n'i'\alpha'} = \langle \phi_{ni\alpha} | \phi_{n'i'\alpha'} \rangle$. Then an orthonormal basis $\{\varphi_{ni\alpha}\}$ is given by

$$\varphi_{ni\alpha} = \sum_{n'i'\alpha'} \phi_{n'i'\alpha'} (\Delta^{-1/2})_{n'i'\alpha' ni\alpha} .$$

It is easy to see that the basis states $\Phi_{\mathbf{k},i\alpha}$ are orthonormal as well, which means that band energy eigenstates and eigenvalues can be obtained by diagonalising the \mathbf{k} -dependent Hamiltonian matrix $H(\mathbf{k})$,

$$\begin{aligned} H(\mathbf{k})_{i\alpha i'\alpha'} &= \frac{1}{N} \sum_{n,n'} e^{i\mathbf{k}\cdot(\mathbf{R}_{n'i'}-\mathbf{R}_{ni})} H_{ni\alpha n'i'\alpha'} , \\ &= \sum_{n'} e^{i\mathbf{k}\cdot(\mathbf{R}_{n'i'}-\mathbf{R}_{ni})} H_{ni\alpha n'i'\alpha'} \end{aligned} \quad (6.6)$$

where $H_{ni\alpha n'i'\alpha'} = \int d^3r \varphi_{ni\alpha}^* \hat{H} \varphi_{n'i'\alpha'}$. (As they are non-periodic and square-integrable, Löwdin orbitals $\varphi_{ni\alpha}$ are normalized so that $\int d^3r |\varphi_{ni\alpha}(\mathbf{r})|^2 = 1$.)

Due to the translational invariance of the crystal lattice, the overlap integrals $H_{ni\alpha n'i'\alpha'}$ depend on n and n' only via the relative position vector $\mathbf{R}_{ni} - \mathbf{R}_{n'i'}$. Functions $\{\varphi_{ni\alpha}\}$ have the same symmetries as $\{\phi_{ni\alpha}\}$, which helps to decrease the number of $H_{ni\alpha n'i'\alpha'}$ values needed to be evaluated [179]. Also, due to the exponential decay of localised wavefunctions, we can assume that $H_{ni\alpha n'i'\alpha'} = 0$ for $|\mathbf{R}_{ni} - \mathbf{R}_{n'i'}|$ larger than some cutoff value. This leaves us with a finite number of unknown parameters.

A straightforward calculation of the Hamiltonian matrix elements $H_{ni\alpha n'i'\alpha'}$ would require the evaluation of the matrix elements of $\Delta^{-1/2}$. As the boundary conditions are periodic, Δ has infinite size. Neglecting all overlap integrals apart from the ones for atoms lying close to each other (nearest neighbours or possibly also second-nearest neighbours) makes it sparse. There are approximations which allow to calculate $(\Delta^{-1/2})_{n'i'\alpha'ni\alpha}$ in this case, but it still remains a difficult task [181]. The crucial insight of Slater and Koster was that by treating the tight-binding Hamiltonian matrix $H(\mathbf{k})$ as, in their words, an “interpolator” and fitting the unknown parameters to more accurate (but also much more time-consuming) band structure calculations for particular points in reciprocal space (e.g. Γ , X or L), one avoids the orthogonalisation problem altogether, because the explicit form of basis states is not needed anywhere. This approach is called an empirical tight-binding method, and has been used successfully already decades ago, when the computational power at physicists’ disposal was only a fraction of what we have available today. Its main drawback is that the physical nature of fitted parameters is unclear, and the parameters themselves are not guaranteed to be transferable between different phases of the same material [178].

Depending on how many aspects of the band structure one wants to capture, one uses a different number of atomic orbitals to build the basis set or even adds artificial ones, for example an additional s orbital (denoted s^*) to account for the influence of excited d states [182]. In my calculations, I have used the empirical GaAs parametrisations by Jancu *et al.* [143], which uses $sp^3d^5s^*$ orbitals, and by Di Carlo [183], which uses sp^3s^* orbitals and therefore has lower accuracy than the first one. In particular, d orbitals are

important for the description of conduction bands. The spin-orbit interaction is taken into account following Ref. [184], where it couples p orbitals (the corresponding splitting of d orbitals is much smaller and can be neglected) on the same atom and is described by one constant per atom, e.g.

$$\langle \Phi_{\mathbf{k},As,p_x, \uparrow} | \hat{H}_{SO} | \Phi_{\mathbf{k},As,p_z, \downarrow} \rangle = \frac{1}{3} \Delta_{SO,As} .$$

All parameters are given in Table 6.4 where $E_{i\alpha} := H_{ni\alpha ni\alpha}$, and symbols of

Parameter	Jancu	Di Carlo	Parameter	Jancu	Di Carlo
$E_{Ga,s}$	-0.4028	-2.7788	$ss\sigma$	-1.6178	-1.612825
$E_{Ga,p}$	6.3853	3.5547	$s^*s^*\sigma$	-3.6761	0.0000
$E_{Ga,d}$	13.1023		$ss^*\sigma$	-1.9927	0.0000
E_{Ga,s^*}	19.4220	6.6247	$s^*s\sigma$	-1.5648	0.0000
$E_{As,s}$	-5.9819	-8.4570	$ps\sigma$	2.4912	1.9400
$E_{As,p}$	3.5820	0.9275	$sp\sigma$	2.9382	3.3991
$E_{As,d}$	13.1023		$ps^*\sigma$	2.1835	2.0967
E_{As,s^*}	19.4220	8.4775	$s^*p\sigma$	2.2086	3.0311
$\Delta_{SO,Ga}$	0.0408	0.0580	$ds\sigma$	-2.7333	
$\Delta_{SO,As}$	0.1824	0.1300	$sd\sigma$	-2.4095	
Δ_{Ga}	0.0274	0.0178	$ds^*\sigma$	-0.9606	
Δ_{As}	0.1382	0.0970	$s^*d\sigma$	-0.6486	
			$pp\sigma$	4.4094	2.87365
			$pp\pi$	-1.4572	-0.70385
			$dp\sigma$	-1.7811	
			$pd\sigma$	-1.8002	
			$dp\pi$	1.7821	
			$pd\pi$	2.0709	
			$dd\sigma$	-1.1409	
			$dd\pi$	2.2030	
			$dd\delta$	-1.9770	

Table 6.4: Jancu and Di Carlo parametrisations of GaAs. All values in eV.

the form $\mu\nu\gamma$ (where $\mu, \nu = s, p, d, s^*$) denote two-centre (involving only the potential originating from the two atoms on which the overlapping orbitals reside) nearest-neighbour overlap parameters between μ -type orbital of Ga and ν -type orbital of As. The third symbol γ denotes the common value of the angular momentum projection on the vector between the atoms: σ for 0, π for 1 and δ for 2. Overlap parameters of orbitals with different angular momentum projections vanish due to the symmetry of the two-centre potential. All overlap integrals $\{H_{ni\alpha n'i'\alpha'}\}$ can be calculated as linear combinations of parameters $\{\mu\nu\gamma\}$, using geometric transformations of spherical harmonics. The overlap integrals depend on the angles between the atoms just through the angle-dependent coefficients of these combinations, while the

dependence on the interatomic distance is via the $\{\mu\nu\gamma\}$ parameters only. This parametrisation is the same as the one used in the LCAO method for diatomic molecules.

The lack of transferability of empirical tight-binding method parameters is highlighted by the fact that the diagonal integrals $\{H_{n\alpha n\alpha}\}$, the so-called *on-site energies*, differ between two parametrisations for the same orbitals (i.e. $E_{As,s}^{\text{Jancu}} \neq E_{As,s}^{\text{Di Carlo}}$); also the spin-orbit splittings are different.

The tight-binding method has been proposed as a means of calculating electronic band structures, but its uses, especially of the first-principles tight-binding method, reach much further than that, and include the modelling of defects and dislocations, amorphous and liquid semiconductors, fullerenes and calculation of atomic forces [178]. They require the relaxation of assumptions underlying the empirical tight-binding, and therefore are much more computationally demanding, for example the Hamiltonian matrix increases its size dramatically for non-periodic systems. On the other hand, using a single parametrisation, even the empirical TB is able to describe systems with widely differing symmetries and heterogeneous composition: from periodic bulk to layers and interfaces. I made use of its versatility while investigating the spin waves in layers of (Ga,Mn)As.

6.2.1 Strain

The parameters listed in Table 6.4 have been fitted for particular positions of atoms in the unit cell. To include strain in the model, it is necessary to change the lattice and overlap integrals so that they match the atomic positions in a strained lattice. The distortion of interatomic bond angles is taken care of by recalculating $\{H_{n\alpha n'\alpha'}\}$ for new directional cosines from old $\{\mu\nu\gamma\}$ values. However, the distortion of distances requires the change of the latter set. In empirical tight-binding, it is done by assuming that the overlap parameters follow power scaling laws [143, 185] as functions of the strained and unstrained interatomic distances d and d_0 ,

$$\mu\nu\gamma(d) = \mu\nu\gamma \left(\frac{d_0}{d} \right)^{\eta_{\mu\nu\gamma}} .$$

In the free electron approximation [185], we have $\eta_{\mu\nu\gamma} = 2$, while Jancu *et al.* [143] give the scaling laws for the parameters used in my calculations by calibrating some of the exponents to additional first-principles calculations and experimental data. Except for the d bands, the diagonal elements of the Hamiltonian are assumed to be independent of strain. As the electrons in s^* and d bands (the so-called “high bands”) are much more delocalised than the ones in s and p bands, the influence of strain on interaction terms between s^* and d states is either set to zero in [143] or assumed to be equal to the free-electron model. The interaction terms between high- (s^* and d) and low-lying (s and p) states, or among the s and p states themselves, were

fitted to detailed deformation potential calculations in several points of the Brillouin zone. In my calculations, I only took into account the dependence of d -orbital on-site energies on strain, and recalculated the $\{H_{ni\alpha n'i'\alpha'}\}$ for the new directional cosines without changing the $\{\mu\nu\gamma\}$ parameters. Thus, my $k \cdot p$ calculations can be considered to describe the effects of strain on the s and p bands more accurately than the tight-binding method.

6.2.2 Exchange interaction

The exchange interaction is introduced to the TB Hamiltonian using the virtual-crystal and mean-field approximations, as described by Eq. (6.4), but it is implemented differently than in the $k \cdot p$ method, because of the different basis functions used in these two methods. The $k \cdot p$ basis is composed of the Bloch wavefunctions from the Γ point, while the tight-binding approximation uses atomic-like orbitals. The Mn ions are coupled to p -type orbitals of As and s -type orbitals of Ga. The spin splittings applied to these orbitals must take into account their weights in the s - and p -type band wavefunctions close to the centre of the Brillouin zone. The operator P_{ex} in (6.4) is therefore redefined to

$$P_{\text{ex}} = \Delta_{5\%}^{-1} (e_p P_p^{As} + e_s P_s^{Ga}) ,$$

where $\Delta_{5\%} = -0.15$ eV is the Γ_8 valence band spin splitting for 5% Mn concentration, P_p^{As} and P_s^{Ga} are projection operators on the respective orbitals, and the effective orbital spin-splittings for 5% Mn concentration are

Parametrisation	e_p [eV]	e_s [eV]
Jancu	-0.2764	0.0548
Di Carlo	-0.1940	0.0356

The values of the above constants were chosen so that the band spin splittings agree with the $k \cdot p$ method. The weights of the projection operators are almost the same in both methods,

$$\frac{e_{p, \text{Jancu}}}{e_{s, \text{Jancu}}} \approx \frac{e_{p, \text{Di Carlo}}}{e_{s, \text{Di Carlo}}} \approx \frac{\beta}{\alpha} .$$

To obtain the band splittings for different Mn concentrations, I scaled linearly the Δ parameter in Eq. (6.4) as it has been done for the $k \cdot p$ method.

The band structure of (Ga,Mn)As calculated by the tight-binding method is presented in Fig. 6.2.

6.3 Comparison of the $k \cdot p$ and tight-binding approximations

The presented $k \cdot p$ computational schemes are one of the most economical descriptions of the energy bands in DMS. By means of a perturbative approach, they reduce the basis size to six or eight bands, ensuring very good

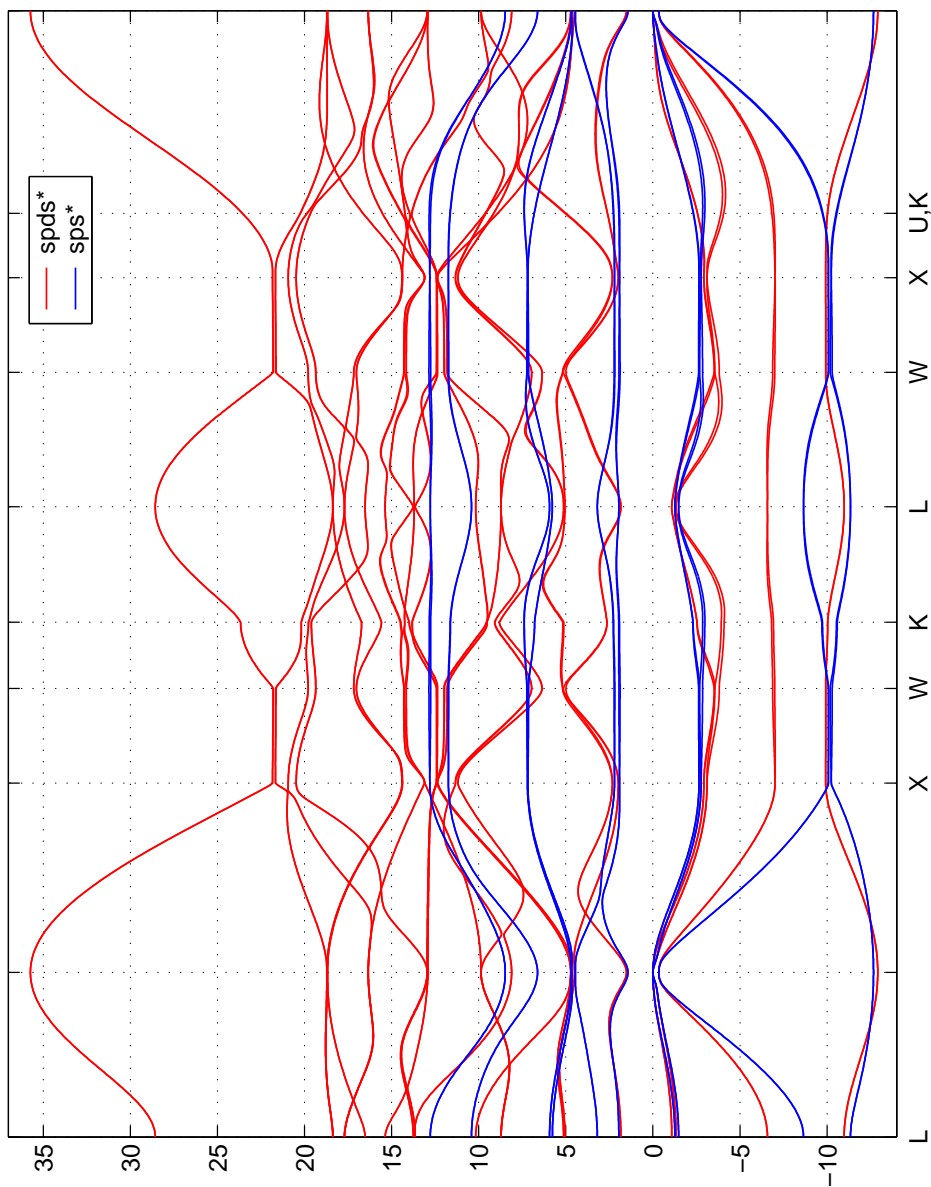


Figure 6.2: The band structure of (Ga,Mn)As according to the tight-binding method $sp^3d^5s^*$ Jancu and sp^3s^* di Carlo parametrisations, plotted in the entire Brillouin zone along the traditional symmetry directions for the fcc lattice.

numerical performance. Although their bases contain only s - and p -type (or just p -type) states, their Hamiltonians reproduce very well the respective bands in the vicinity of the band gap, as they depend on an optimised set of parameters which are determined empirically from experiments. The $k \cdot p$ methods also allow to easily capture the effect of moderate strain on the band structure.

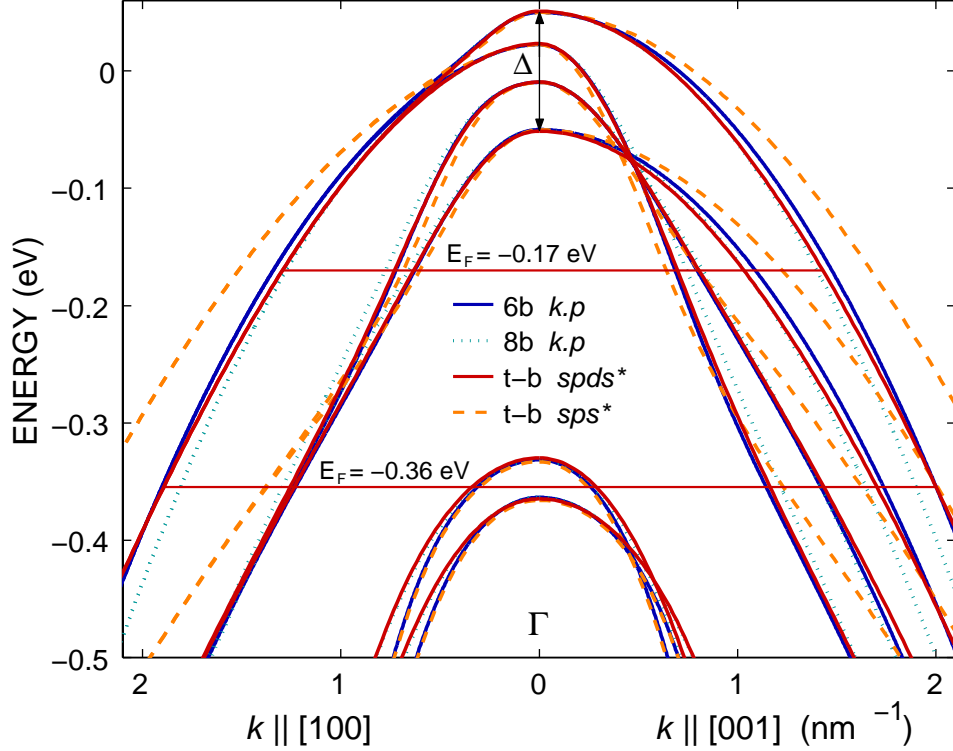


Figure 6.3: The top of the (Ga,Mn)As valence band in the Γ point with spin splitting $\Delta = -0.1$ eV calculated by different computational schemes. Horizontal lines denote the positions of the Fermi level E_F for the hole densities 0.3 and 1.2 nm^{-3} in the $spds^*$ tight-binding model.

The 8-band $k \cdot p$ model reflects the T_d^2 symmetry of the zincblende lattice, while the 6-band version neglects the bulk inversion asymmetry, artificially increasing the symmetry group to O_h^7 . This allows to include the s - d exchange interaction (Sec. 6.1.2) and the Dresselhaus spin splitting of the conduction band [142] in the first method. However, it happens at the cost of introducing additional Hamiltonian parameters, which leads to a cumbersome parametrisation procedure giving two alternative optimised sets of empirical parameters. Therefore, neither of them can be considered the “best fit” and they should be used with caution [171]. Both employed $k \cdot p$ methods apply only to bulk systems, which are treated as infinite crystals.

The more complex of the employed methods, the 20-orbital sps^* and

40-orbital $spds^*$ tight-binding approximations recover accurately also other energy bands, at the cost of an increased basis size and, consequently, lower computational efficiency. As presented in Fig. 6.2, they work in the full Brillouin zone (though, the sps^* method does not work very well away from the Γ point [143]). Similarly to the 8-band $k \cdot p$ model, the methods describe the full $sp-d$ exchange interaction and capture the inversion asymmetry of the zincblende lattice. Additionally, they can be easily applied to model thin layers, which allows to include the structure inversion asymmetry inducing the Bychkov–Rashba spin splitting (Sec. 5.4.2). Bulk systems are obtained by applying periodic boundary conditions.

The lack of a transparent relation between the input parameters and experimentally determined quantities is considered to be the greatest disadvantage of the tight-binding approach. Including the strain in the tight-binding Hamiltonian requires nonlinear rescaling of the parameters, which I omitted for simplicity, thus lowering the accuracy of strain-dependent calculations in the TB method as compared to the $k \cdot p$ method.

Figure 6.3 compares the energy bands at the top of the valence band calculated by four different computational schemes. There is almost complete agreement between the 6-band $k \cdot p$ and $spds^*$ tight-binding methods, while the 8-band $k \cdot p$ and sps^* TB methods differ from the first two, the last one most visibly. The details of the numerical implementation of the above models are described in Appendix A.

Chapter 7

Ferromagnetism in (Ga,Mn)As

The magnetic behaviour of systems belongs to the fundamental properties in solid state physics and is the basis of our research on dilute magnetic semiconductors. The presence of magnetic order in these systems can be revealed by magnetisation measurements using a superconducting quantum interference device (SQUID), as presented in Fig. 7.1a for (Ga,Mn)As. Square hysteresis loops in the magnetisation vs. magnetic field curves indicate a well-ordered magnetic state of the Mn ions. The spontaneous magnetisation appears below the Curie temperature specific to every sample. Recording the magnetisation with increasing temperature allows to observe the critical behaviour of the system, which undergoes a second-order phase transition at the Curie point and becomes paramagnetic. The theoretical predictions show that the Curie temperature for (Ga,Mn)As increases with the free hole concentration (Sec. 4.2.5 and Ref. [40]), which has been repeatedly confirmed by experiment. However, the process can be impeded e.g. by the accompanying increase in number of compensating defects (see Sec. 3.3).

These facts can be also observed in magnetotransport studies. Additionally, as demonstrated in Fig. 7.1b, the measurements of conductivity (or resistivity) and Hall effects in (Ga,Mn)As can reveal whether the sample is in the insulating or metallic regime of Mn concentrations (Sec. 4.3). In addition to the magnetisation, some other parameters are often investigated to phenomenologically describe the properties of ferromagnetic semiconductors. One critical parameter is the magnetic anisotropy, which determines the magnetisation direction in the crystal (easy axis) and is usually the effect of spin-orbit coupling. In (Ga,Mn)As we distinguish the cubic magnetocrystalline term resulting from the symmetry of the crystal, the uniaxial term induced by strain due to the lattice mismatch (Sec. 3.4), and the in-plane uniaxial anisotropy of unknown origin. Together with the spin-wave or exchange stiffness, which determines the rigidity of the coupling between

adjacent magnetic moments and their excitations, they govern the properties of magnetic domains.

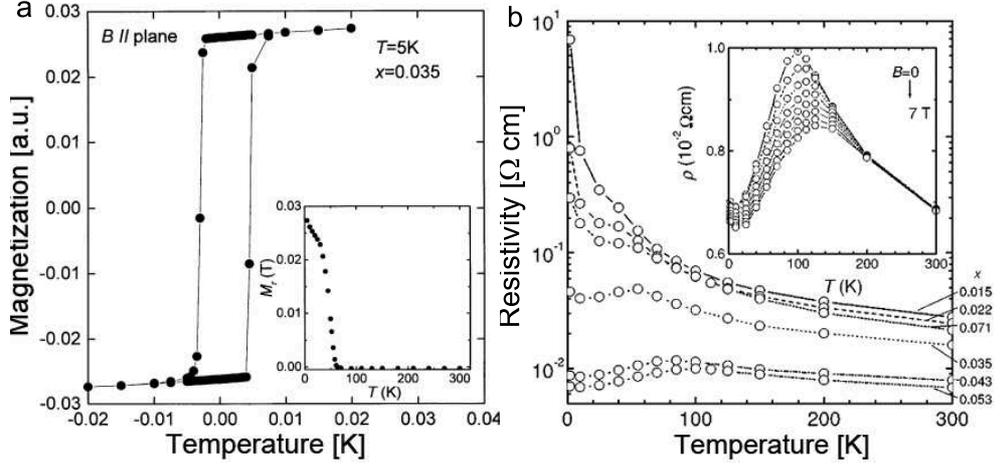


Figure 7.1: a) Magnetic hysteresis loop in Ga_{0.965}Mn_{0.035}As at 5 K with the magnetic field applied parallel to the sample surface, indicating the magnetic order along the parallel easy axis. It vanishes at the Curie temperature of about 50 K, as presented in the inset (after Ohno *et al.* [97]). b) Temperature dependence of resistivity at zero field for varying Mn concentrations x . Samples with intermediate composition $x = 3.5\%$ – 5.3% exhibit metallic behaviour. The inset shows the expanded view of the sample with $x = 5.3\%$ at around the Curie temperature of about 110 K with the magnetic-field dependence (after Matsukura *et al.* [186]).

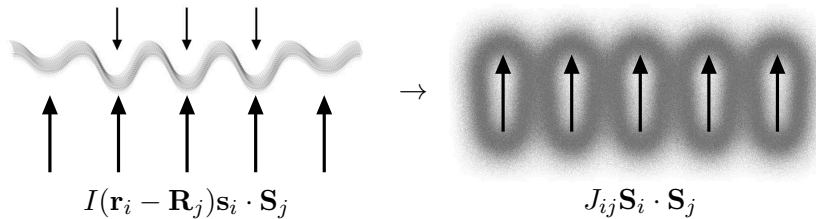
In this chapter I use mathematical tools to build the theoretical model of ferromagnetism in dilute magnetic semiconductors. It will be the basis for further considerations on the phenomena mentioned above.

The statistical analysis of modern models of phase transitions is based on the Ginzburg–Landau theory [187]. In particular, this meta-theory served to describe the carrier-mediated ferromagnetism in dilute magnetic semiconductors in the seminal paper by Dietl *et al.*, which fuelled the intense worldwide research in this field (Sec. 4.2.5). The Ginzburg–Landau theory introduces the general concept of an order parameter, a thermodynamic quantity that acquires non-zero values in one phase (the ordered phase) and vanishes in the other (the disordered phase). The order parameter in the considered ferromagnetic systems is simply the total magnetisation.

In Section 7.1, I will use the basic statistical theory to describe the behaviour of magnetic lattice moments coupled to delocalised spin carriers. The main challenge when solving such problems is the large number of available spin configurations, which increases exponentially with the size of the system. To rise to it, I will use the proposed combinatorial formula for the number of states of classical spins realising the same magnetisation value. (I will also demonstrate the corresponding recursive algorithm, derive the

version of the formula for bosons and provide convenient analytical approximations. These results can find applications in many other fields of physics, from nuclear spins, quantum dots, microwave cavities to Bose-Einstein condensate and even thermodynamics of black holes [188].)

For a quantitative analysis of ferromagnetism in (Ga,Mn)As dilute magnetic semiconductor, I will turn to its detailed image emerging from the previous chapters. It consist in the system of manganese lattice ions coupled to the carriers due to the $sp-d$ hybridisation. The interaction between the localised $3d^5$ electron spins from different ions is mediated by delocalised holes residing in the p -type valence band, as illustrated in the left part of the below picture. The holes lower the energy of the system by aligning their spins antiparallel to the ion spins. This antiferromagnetic $p-d$ exchange interaction produces Zeeman-type spin splitting of the hole bands analogously to the $s-d$ exchange acting on the conduction bands, as outlined in Sec. 5.6. Similar effects can arise from the spin-orbit interaction in the presence of the inversion symmetry breaking in the zincblende lattice of (Ga,Mn)As, as described in Sec. 5.4. The detailed description of the band structure of the system incorporating all these effects within the $k \cdot p$ and tight-binding computational schemes has been provided in Ch. 6.



Due to the spatial extent of the holes' wavefunctions, a single hole interacts with many localised magnetic moments, which leads to their effective ferromagnetic coupling, as illustrated in the right part of the above picture. This can be well described by the oscillatory long-range Heisenberg interaction J_{ij} . This type of interaction was originally calculated for a single carrier band without the spin splitting by Ruderman and Kittel [42] in what is known as the RKKY model, outlined in Sec. 4.2.4. In my master's thesis I extended it to the case of two spin-split bands, obtaining an analytical expression for the $J(r)$ range function, and applied it to interpret the spin-wave resonance data on (Ga,Mn)As [122]. These approaches do not take into account fully the nature of the interaction between holes and ions. Indeed, both subsystems have their own degrees of freedom which interact with each other, holes polarising the Mn spins and manganese ions polarising the hole spins. This necessitates a self-consistent description.

In Section 7.2, I will demonstrate a physically transparent perturbation-variational method of treating the systems of localised magnetic moments coupled by spin carriers, based on the Löwdin calculus [41]. It is self-

consistent and can accommodate any band structure. I will use it to construct the effective Hamiltonian for Mn ions in (Ga,Mn)As. While the above RKKY methods assume the form of Mn–Mn interaction, I will derive it explicitly from a generic Hamiltonian of holes coupled by the exchange interaction to free localised spins. In this way, I will obtain the full effective Hamiltonian of the system including other terms, which will allow me to make some important observations. This full description of the analysed system will be the starting point for further considerations contained in this thesis.

7.1 Basic statistical picture

A simple phenomenological free-energy model of the emergence of magnetic order in the analysed systems can be based on the foundation of Landau theory [189, 190]. In (Ga,Mn)As and other systems with carrier-mediated ferromagnetism, it describes a gas of carriers coupled to a mean-field arising from the exchange interaction with localised magnetic moments [40].

At zero temperature T , the system reaches an equilibrium by minimising its total energy E , which includes interactions with external forces. At non-zero temperatures, this trend towards minimal energy is countered by the thermal disorder, and an equilibrium is realised by minimising the free energy $F = E - TS$, where S is the entropy. The inclusion of S with a negative sign means that the randomness of thermal excitations favours disordered states—the entropy can actually be considered a measure of disorder. To give a mechanical analogy, the zero temperature equilibrium is that of a tiny steel ball rolling towards the bottom of a bowl ($E = 0$) and coming to a full stop there after losing its kinetic energy. At non-zero temperatures the thermal excitations cause the ball to move randomly around the sides of the bowl, creating a state which is more expensive energetically ($E > 0$) but is entropically favourable due to thermal disorder.

Let us consider a system of N localised (hence, obeying classical statistics) moments with spin $S = \frac{5}{2}$ each and P carriers with spin $1/2$. I will derive the formula for the free energy of localised, non-interacting spins as a function of M , $F_S(M)$, and then calculate the free energy functional $F_c(M)$ of the carriers interacting with the mean-field proportional to M . The sum $F(M) = F_S(M) + F_c(M)$, minimised over M , characterises the temperature dependence of the average lattice spins' magnetisation $\langle M \rangle$ in the ion-carrier system. This leads to the expression for critical temperature T_C , at which $\langle M \rangle = 0$. Choosing the temperature T and ion magnetisation M as my control parameters, over which the free energy is varied, is easier than using the canonical ensemble for the total system and calculating $\langle M \rangle$ as an ensemble average.

7.1.1 Free energy of Mn spins

The lattice spins' energy is independent of their configuration, hence their free energy F_S depends on magnetisation M only via the entropy \mathcal{S} . This in turn is equal to $k_B \ln \Omega$, where $\Omega = \Omega(N, M, S)$ is the number of states of N spins, each of length S , realising the magnetisation $M = \sum_j S_j$.

Exact expression for Ω

Let $M' = M + NS \geq 0$ denote the difference between the current magnetisation and its minimal value (which I call “shifted magnetisation”), and $S'_j = S_j + S/2 \geq 0$ the difference between the j -th ion's spin and its minimal value (which I call “shifted spin”). For given N and S , the maximum achievable M' is NS' , where $S' = 2S$ is the maximum shifted spin.

For given M' , the number n of spins with $S'_j = s$, $s = 0, 1, \dots, 2S$ cannot be higher than $[M'/s]$, where $[x]$ is the integer part of x (otherwise the shifted magnetisation would exceed M'). On the other hand, the maximum M' that $N - n$ ions with $S'_j \leq s - 1$ can realise is $(N - n)(s - 1)$, which leads to the inequality

$$M' \leq ns + (N - n)(s - 1) = n + N(s - 1) .$$

Thus, n is bounded from below and above,

$$\max(M' - N(s - 1), 0) \leq n \leq [M'/s] .$$

Once we fix the number n of ions with shifted spin equal to S' , the other ions can only have their shifted spins between 0 and $S' - 1$, and *their* shifted magnetisation must be equal to $M' - nS'$. This leads to a recursive formula for $\Omega'(N, M', S') \equiv \Omega(N, M' - NS'/2, S'/2)$:

$$\Omega'(N, M', S') = \sum_{n=\max(M'-N(S'-1),0)}^{[M'/S']} \binom{N}{n} \Omega'(N-n, M'-nS', S'-1) , \quad (7.1)$$

where the factor $\binom{N}{n} = \frac{N!}{(N-n)!n!}$ accounts for the fact that the localised lattice ions are classical, distinguishable particles. In terms of the original function Ω , the above relation reads

$$\Omega(N, M, S) = \sum_{n=\max(M-N(S-1),0)}^{[(M+NS)/(2S)]} \binom{N}{n} \Omega(N-n, M-nS, S-1) .$$

The boundary condition for Ω' is

$$\Omega'(N, M', 0) = \begin{cases} 1 & M' = 0 \\ 0 & M' > 0 \end{cases} ,$$

which gives for $M' \leq N$

$$\Omega'(N, M', 1) = \binom{N}{M'} .$$

The recursive formula (7.1) can be converted to an explicit expression for $\Omega(N, M, S)$:

$$\Omega(N, M, S) = \sum_{n_{2S}=Q_{2S}}^{P_{2S}} \cdots \sum_{n_2=Q_2}^{P_2} \frac{N!}{n_{2S}! \cdots n_2! n_1! n_0!} \quad (7.2)$$

where for $s = 2, \dots, 2S$

$$Q_s = \max \left(M + NS - \sum_{t=s+1}^{2S} (t-s+1)n_t - N(s-1), 0 \right) ,$$

$$P_s = \left[\left(M + NS - \sum_{t=s+1}^{2S} t n_t \right) / s \right]$$

and

$$n_1 = M + NS - \sum_{t=2}^{S'} t n_t ,$$

$$n_0 = N(1-S) - M + \sum_{t=2}^{S'} (t-1)n_t .$$

The indices n_s are the numbers of spins with a given value of S'_j , $\sum_{s=0}^{2S} n_s = N$, such that

$$\sum_{s=0}^{2S} n_s s = M' . \quad (7.3)$$

The fraction with factorials in (7.2) is the number of spin states realising a given combination $\{n_s\}$. Essentially, this formula presents a simple way to sum over all allowed combinations, subject to the constraint (7.3), and as such can be used also for spins with Bose statistics, where it has the form

$$\Omega_{\text{boson}}(N, M, S) = \sum_{n_{2S}=Q_{2S}}^{P_{2S}} \cdots \sum_{n_2=Q_2}^{P_2} 1$$

due to the indistinguishability of quantum particles.

As $2S = 5$ for Mn ions in (Ga,Mn)As lattice, Eq. (7.2) is relatively easy to use in numerical calculations: it is iterative, the number of nested loops is low and has small memory footprint. It can be used to check the correctness of approximate analytical expressions for $\Omega(N, M, S)$ even in the

case $N = 50$, for which the total number of states reaches an astronomical number 6^{50} .

Another procedure for the exact computation of $\Omega(N, M, S)$ is based on recursion in the number of lattice spins, not maximum spin value. Let us consider what happens when I add a new spin S_N to the system of $N - 1$ spins. The new spin takes values between $-S$ and S . For each of them, denoted by s , magnetisation M can be realised by $\Omega(N - 1, M - s, S)$ configurations of the remaining $N - 1$ spins. Hence,

$$\Omega(N, M, S) = \sum_{s=-S}^S \Omega(N - 1, M - s, S) , \quad (7.4)$$

or using the shifted quantities

$$\Omega'(N, M', S') = \sum_{s=0}^{S'} \Omega'(N - 1, M' - s, S') . \quad (7.5)$$

The starting condition for relation (7.4) is

$$\Omega(0, M, S) = \begin{cases} 0 & M \neq 0 \\ 1 & M = 0 \end{cases} ,$$

and for relation (7.5)

$$\Omega'(0, M', S) = \begin{cases} 0 & M' \neq 0 \\ 1 & M' = 0 \end{cases} .$$

They are identical because for $N = 0$, $M' = M$.

The numerical advantage of the second approach is that, using a relatively small amount of memory, three nested loops (over N , M and s) one can calculate the whole dependence of Ω on M in an iterative manner, using a single array updated in-place.¹ It can be evaluated much faster than (7.2), but can only be used for distinguishable spins. To avoid arithmetic overflow, it is more practical for large N or S to calculate iteratively a rescaled function

$$\omega(N, M, S) = \frac{\Omega(N, M, S)}{(2S + 1)^N} . \quad (7.6)$$

Gaussian approximation for Ω

The formulae (7.2) and (7.4), though accurate, are not convenient for analytical calculations. I will now derive a Gaussian approximation for Ω .

¹This is because $\Omega'(N, M', S)$ depends on $\Omega'(N - 1, m, S)$ only for $m \leq M'$.

One can associate each lattice spin S_j with an independent, uniformly distributed random variable with values $-S, -S+1, \dots, S-1, S$, each having a probability $1/(2S+1)$, so that its expected value $E[S_j] = 0$ and variance

$$\text{Var}[S_j] = E[S_j^2] = \frac{1}{2S+1} \sum_{s=0}^{2S} (s-S)^2 = \frac{1}{3}S(S+1) .$$

The total magnetisation M is a sum of these variables,

$$M = \sum_{j=1}^N S_j$$

and the probability that $M = m$ is equal to $\omega(N, m, S)$, defined in (7.6). On the other hand, the central limit theorem states that the distribution of M is well approximated for large N by a Gaussian distribution with mean zero and variance $\frac{N}{3}S(S+1)$. Hence,

$$\frac{\Omega(N, M, S)}{(2S+1)^N} \approx \frac{1}{\sqrt{2\pi\frac{N}{3}S(S+1)}} \exp\left(-\frac{3M^2}{2NS(S+1)}\right)$$

which can be also expressed as

$$\Omega(N, M, S) = \Omega(N, 0, S) \exp\left(-\frac{3M^2}{2NS(S+1)}\right) . \quad (7.7)$$

In Fig. 7.2, I compare the exact and approximate expressions for $\Omega(N, M, S)$ for $N = 50$, plotting the logarithm of $\omega(N, M, S)$ to highlight the discrepancies for high magnitudes of M . Taking the logarithm of (7.7), I obtain the free energy of the lattice spins as

$$F_S(M) = -k_B T \ln \Omega(N, 0, S) + k_B T \frac{3M^2}{2NS(S+1)} , \quad (7.8)$$

which in the absence of the lattice spins and carriers coupling leads to the minimum of $F_S(M)$ lying at $M = 0$, hence $\langle M \rangle = 0$ at all temperatures (no magnetic order).

7.1.2 Free energy of ion-carrier system

I will now use the canonical ensemble to calculate the free energy of the carriers as a function of the ions' magnetisation M . This will allow me to obtain the average magnetisation $\langle M \rangle$ of the whole system and solve it for the Curie temperature T_C , in which $\langle M \rangle = 0$.

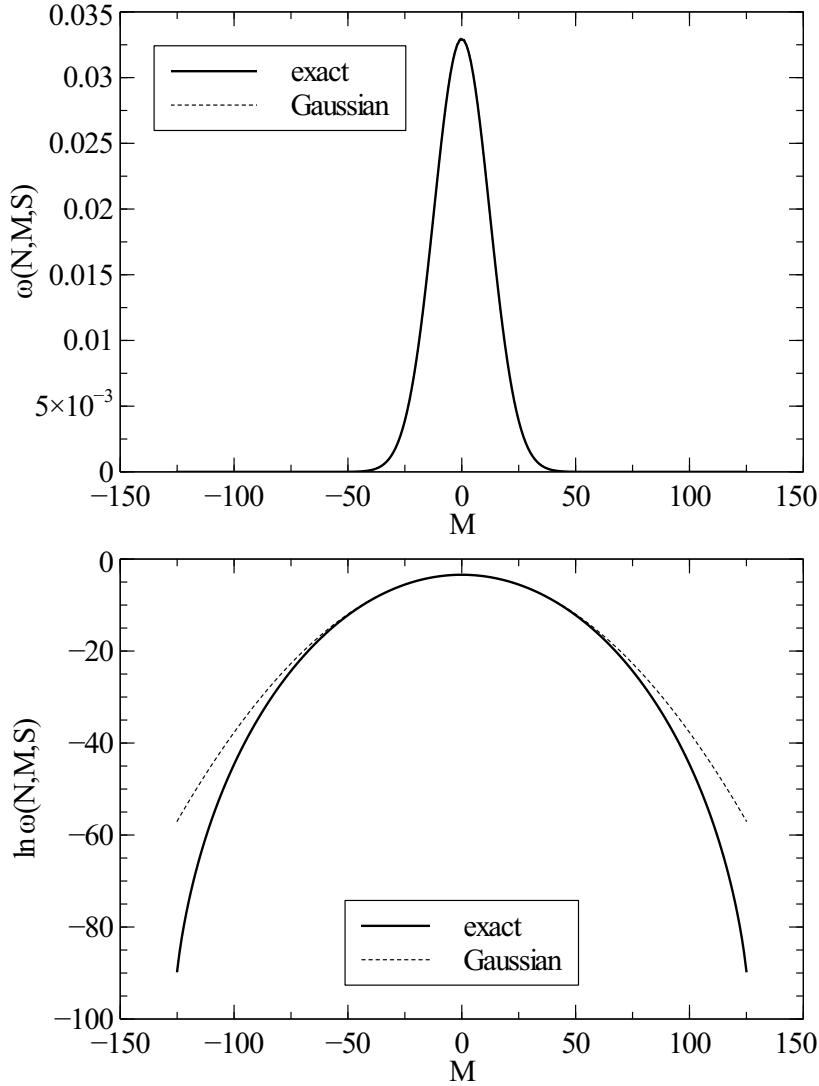


Figure 7.2: Exact and approximate values of $\omega(N, M, S)$ (upper panel) and their logarithms (lower panel) for $N = 50$ and $S = \frac{5}{2}$. The $\ln \omega$ plot reveals the inaccuracy of the approximation at higher N , which is damped by the strong exponential term in ω .

The total system is composed of N Mn ions with the free energy F_S given by (7.8) and P carriers coupled to ions by the exchange interaction. The energy of a carrier with momentum \mathbf{p} and spin $s = \pm 1/2$ is given by

$$E_{\mathbf{p}} = \frac{p^2}{2m^*} + JM s ,$$

where m^* is the carrier effective mass, M is the ions' magnetisation and $J = \frac{\beta}{V}$, where $\beta < 0$ is the p - d exchange integral and V is the crystal

volume. For P carriers, the Fermi energy E_F is equal to

$$E_F(P) = \left(\frac{3\pi^2 P}{V} \right)^{2/3} \frac{\hbar^2}{2m^*} = E_F(1)P^{2/3},$$

where V is the crystal volume.

In the canonical ensemble, the partition function of P carriers is given by

$$Z(P) = \sum_{\{n_{\mathbf{p}}^+\}, \{n_{\mathbf{p}}^-\}} \exp \left[-\frac{1}{k_B T} \left(\sum_{\mathbf{p}} (n_{\mathbf{p}}^+ + n_{\mathbf{p}}^-) \frac{p^2}{2m^*} + \frac{J}{2} M \sum_{\mathbf{p}} (n_{\mathbf{p}}^+ - n_{\mathbf{p}}^-) \right) \right].$$

It can be expressed using the partition functions $Z_0(P)$ for free *spinless* fermions (perfect Fermi gas) [191],

$$Z(P) = e^{\frac{JMP}{2k_B T}} \sum_{P^+=0}^P Z_0(P^+) Z_0(P - P^+) e^{-\frac{JMP^+}{k_B T}},$$

where $P^+ = \sum_{\mathbf{p}} n_{\mathbf{p}}^+$ is the sum of the carriers with spins up. Since, in the canonical ensemble, the free energy $F = -k_B T \ln Z$, one can write for the coupled carriers

$$F_c(M) = JM(P^+ - P/2) + F_0(P^+) + F_0(P - P^+) + O(\ln P), \quad (7.9)$$

where $F_0(P)$ is the free energy of perfect Fermi gas. Assuming that $k_B T \ll E_F(P)$ (which holds in (Ga,Mn)As) even at room temperatures), the free energy F_0 of perfect Fermi gas is given by [191]

$$\begin{aligned} F_0(P) &\approx P \left[\frac{3}{5} E_F(2P) - \frac{1}{4} \frac{\pi^2 k_B^2 T^2}{E_F(2P)} \right] \\ &= \left[\frac{3}{5} 2^{2/3} E_F(1) P^{5/3} - \frac{2^{-2/3}}{4} \frac{\pi^2 k_B^2 T^2}{E_F(1)} P^{1/3} \right], \end{aligned}$$

where the factor 2 in $E_F(2P)$ accounts for the difference in the Fermi energy of spinless and spin-1/2 fermions. Inserting this into (7.9) and minimising over P^+ , one finds the average number of spin-up carriers [191],

$$\langle P^+ \rangle = \frac{P}{2} + \frac{3JMP}{8E_F(P)} \left[1 - \frac{\pi^2}{12} \left(\frac{k_B T}{E_F(P)} \right)^2 \right] + O \left[\left(\frac{k_B T}{E_F(P)} \right)^3 \right].$$

Inserting this again into (7.9), I obtain the free energy of carriers as a func-

tion of M only,

$$\begin{aligned}
F_c(M) = & -\frac{3J^2M^2P}{8E_F(P)} \left[1 - \frac{\pi^2}{12} \left(\frac{k_B T}{E_F(P)} \right)^2 \right] \\
& + \frac{3}{5} 2^{2/3} E_F(1) \left(\frac{P}{2} - \frac{3JMP}{8E_F(P)} \left[1 - \frac{\pi^2}{12} \left(\frac{k_B T}{E_F(P)} \right)^2 \right] \right)^{5/3} \\
& - \frac{2^{-2/3}}{4} \frac{\pi^2 k_B^2 T^2}{E_F(1)} \left(\frac{P}{2} - \frac{3JMP}{8E_F(P)} \left[1 - \frac{\pi^2}{12} \left(\frac{k_B T}{E_F(P)} \right)^2 \right] \right)^{1/3} \\
& + \frac{3}{5} 2^{2/3} E_F(1) \left(\frac{P}{2} + \frac{3JMP}{8E_F(P)} \left[1 - \frac{\pi^2}{12} \left(\frac{k_B T}{E_F(P)} \right)^2 \right] \right)^{5/3} \\
& - \frac{2^{-2/3}}{4} \frac{\pi^2 k_B^2 T^2}{E_F(1)} \left(\frac{P}{2} + \frac{3JMP}{8E_F(P)} \left[1 - \frac{\pi^2}{12} \left(\frac{k_B T}{E_F(P)} \right)^2 \right] \right)^{1/3}.
\end{aligned} \tag{7.10}$$

The sum of (7.8) and (7.10) gives the total free energy of the ion-carrier system,

$$\begin{aligned}
F(M) = & k_B T \frac{3M^2}{2NS(S+1)} - \frac{3J^2M^2P}{8E_F(P)} \left[1 - \frac{\pi^2}{12} \left(\frac{k_B T}{E_F(P)} \right)^2 \right] \\
& + \frac{3P}{5} 2^{2/3} E_F(P) \left(\frac{1}{2} - \frac{3JM}{8E_F(P)} \left[1 - \frac{\pi^2}{12} \left(\frac{k_B T}{E_F(P)} \right)^2 \right] \right)^{5/3} \\
& - \frac{2^{-2/3}P}{4} \frac{\pi^2 k_B^2 T^2}{E_F(P)} \left(\frac{1}{2} - \frac{3JM}{8E_F(P)} \left[1 - \frac{\pi^2}{12} \left(\frac{k_B T}{E_F(P)} \right)^2 \right] \right)^{1/3} \\
& + \frac{3P}{5} 2^{2/3} E_F(P) \left(\frac{1}{2} + \frac{3JM}{8E_F(P)} \left[1 - \frac{\pi^2}{12} \left(\frac{k_B T}{E_F(P)} \right)^2 \right] \right)^{5/3} \\
& - \frac{2^{-2/3}P}{4} \frac{\pi^2 k_B^2 T^2}{E_F(P)} \left(\frac{1}{2} + \frac{3JM}{8E_F(P)} \left[1 - \frac{\pi^2}{12} \left(\frac{k_B T}{E_F(P)} \right)^2 \right] \right)^{1/3},
\end{aligned} \tag{7.11}$$

where I have omitted the M -independent term. The above expression will be used to derive the critical temperature at which $\langle M \rangle = 0$, therefore the quadratic approximation (7.8) can be used safely despite its inaccuracies for high magnitudes of M .

7.1.3 Average magnetisation and critical temperature

The equilibrium state of the system of lattice spins and carriers is found by minimising the Mn magnetisation M over the range $[-NS, NS]$. At low but non-zero temperatures, the $F(M)$ function is approximately an inverted

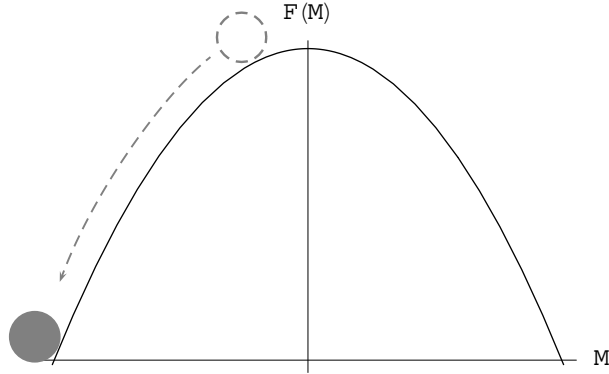


Figure 7.3: Free energy F of the system of Mn ions and band carriers in (Ga,Mn)As as a function of ion magnetisation $M \in [-NS, NS]$ for low temperature $T = 2$ K. The Mn concentration $x = 0.05$ and carrier concentration $p = P/V = 0.65 \text{ nm}^{-3}$, while the p - d exchange integral $\beta = -0.054 \text{ eV nm}^{-3}$. The carrier mass $m = 0.6m_0$, where m_0 is free electron mass. The minima of the free energy coincide here with the groundstate of the system.

parabola, as shown in Fig. 7.3. The free energy has two minima at $M = \pm NS$, corresponding to saturation magnetisation. Magnetic order exists in this system in finite temperatures, i.e. the crystal is a ferromagnet. Coming back to my mechanical analogy, the steel ball is lying safely at the very centre of the bowl and thermal excitations are unable to move it at all.

Conversely, for high temperatures $F(M)$ is an upwards pointing parabola with a minimum at $M = 0$ (Fig. 7.4). This indicates that there is no magnetic order in the system. The thermal excitations have blown the tiny ball out of the bowl.

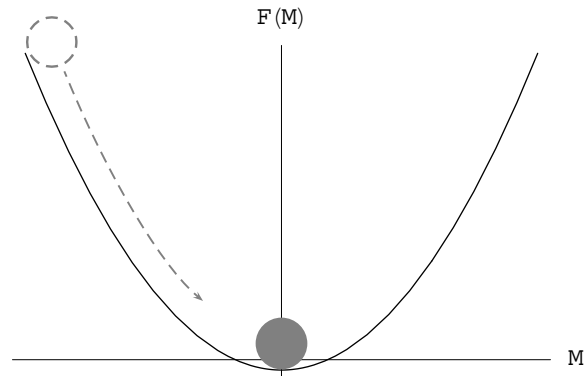


Figure 7.4: Free energy F of the system of Mn ions and band carriers in (Ga,Mn)As as a function of ion magnetisation $M \in [-NS, NS]$ for high temperature $T = 15$ K.

The intermediate situation close to the disappearance of magnetic order is shown on Fig. 7.5. The free energy (7.11) has two minima for non-zero M .

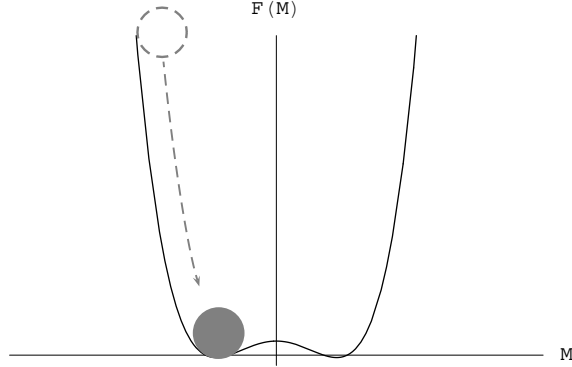


Figure 7.5: Free energy F of the system of Mn ions and band carriers in (Ga,Mn)As as a function of ion magnetisation $M \in [-NS, NS]$ for temperature $T = 4.46$ K close to the destruction of the magnetic order.

As the system is close to a critical transition, I can use the Ginzburg-Landau mean field theory. It is based on the crucial assumption that $F(M)$ is an analytic function of the order parameter M and can thus be expanded in a power series. Up to fourth-order terms I obtain

$$F(M) = f_0(T) + f_2(T)M^2 + f_4(T)M^4 . \quad (7.12)$$

Indeed, the M and M^3 terms in the Taylor series of $F(M)$ are zero, and the shape of the curve on Fig. 7.5 agrees with the formula (7.12). The physical value of M is the one that minimises $F(M)$. When $f_2(T) < 0$, the equation $F'(M) = 0$ has two solutions, one trivial at $M = 0$ and two at $\pm \sqrt{-\frac{f_2(T)}{2f_4(T)}}$. Otherwise, only the $M = 0$ solution remains. The second derivative of F is

$$F''(M) = 2f_2(T) + 12f_4(T)M^2 ,$$

hence for $f_2(T) < 0$ the trivial solution is a maximum, but the ones at $M \neq 0$ lead to

$$F'' \left(\pm \sqrt{-\frac{f_2(T)}{2f_4(T)}} \right) = -10f_2(T) > 0 ,$$

hence they are minima and correspond to equilibrium magnetisation values. Using the language of bowls and balls, the thermal excitations have caused the ball to bounce about the bowl's sides, pushing it away from the lowest position at the centre.

Because the $F(M)$ dependence is practically parabolic even much below the critical transition, I can use the expansion (7.12) to solve for $\langle M \rangle$ as a function of T across the whole temperature range. The results for the same material parameters as in previous plots are presented in Fig. 7.6. The

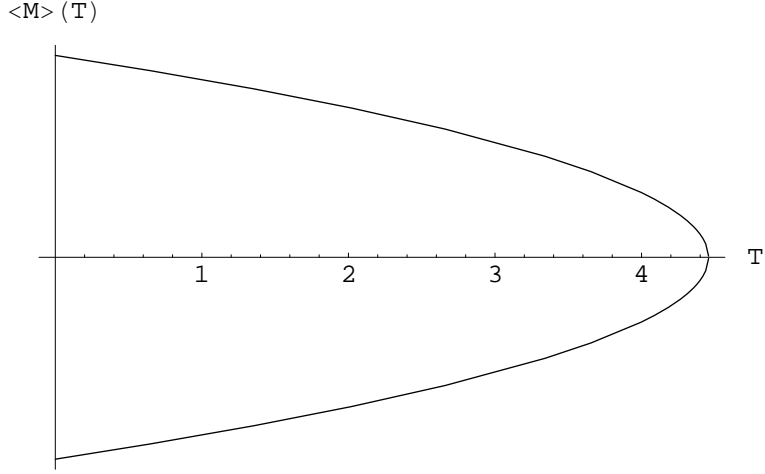


Figure 7.6: Average magnetisation $\langle M \rangle$ of the system of Mn ions and valence band carriers in (Ga,Mn)As as a function of temperature T [K]. The Mn concentration $x = 0.05$ and carrier concentration $p = P/V = 0.65 \text{ nm}^{-3}$, while the p - d exchange integral $\beta = -0.054 \text{ eV nm}^{-3}$.

critical temperature is so low in my numerical examples, because the band model I used is a very simplified one.

The condition for the critical temperature T_C is $f_2(T_C) = 0$. Expanding $f_2(T)$ in a power series in T and keeping only linear terms (for typical material parameters this is enough) yields

$$f_2(T) = \frac{3k_B T}{2NS(S+1)} - \frac{3J^2 P}{16E_F(P)},$$

which leads to the critical temperature

$$T_C = \frac{J^2 N P S(S+1)}{8E_F(P)k_B}.$$

Using the density of states formula $\rho(E_F(P)) = \frac{1}{2\pi^2} \left(\frac{2m^*}{\hbar^2}\right)^{3/2} \sqrt{E_F(P)}$ and the definition of $J = \beta/V$, I obtain

$$T_C = \frac{(N/V)\rho(E_F(P))S(S+1)\beta^2}{12k_B},$$

where N/V is the Mn ion density. The final expression for T_C recovers the celebrated formula (4.2) for the Curie temperature in the p - d Zener model, up to the phenomenological constants A_F and T_{AF} [40].

The above formula shows that the Curie temperature is, essentially, equal to the exchange energy between the localised spins. Indeed, the ferromagnetic order in the analysed systems arises from interatomic exchange mediated by the carriers, whose nature is reflected in the appearance of the

squared β constant. It occurs below T_C , where the mean-field equations have two ferromagnetic solutions $\pm NS(T)$, and vanishes above this value due to the thermal disorder. The observed critical behaviour is purely classical and always takes place at a non-zero critical temperature (which is in contrary to quantum phase transitions, like the metal-insulator transition, which belong to a different universality class [192]).

The discussed model captures the physical origin of magnetic order and provides transparent predictions of its thermodynamic properties. It employs a simple two-parabolic band model for the carriers' band structure. Based on the mean-field approximation, it gives a reasonable overall description of the magnetisation but breaks down at low temperatures and close to the Curie transition. In the first limit, the system magnetisation is reduced by spin waves, in the other the long-range critical fluctuations interfere.

In the next section, I will provide the detailed description of ferromagnetism in the analysed systems. It will be the basis for the quantitative analysis of their physical properties in the further part of this thesis—it takes into account the dynamics of free carriers and can accommodate any band structure, including the $k.p$ and tight-binding approximations outlined in Ch. 6. In Chapter 8, I will estimate realistic Curie temperatures in these models. Then, I will move to Ch. 9 to derive the dispersion spectrum of spin waves, investigate their physics and take them into account to correctly model the low-temperature magnetisation behaviour.

7.2 Self-consistent Löwdin calculus

I consider the ferromagnetic phase of a system consisting of P carriers and N magnetic lattice ions, described by the Hamiltonian \mathcal{H}_0 and coupled by the sp - d exchange interaction \mathcal{H}' described in Sec. 5.6,

$$\mathcal{H} = \mathcal{H}_0 + \mathcal{H}' = \mathcal{H}_0 + \sum_{i=1}^P \sum_{j=1}^N \mathbf{s}_i \cdot \mathbf{S}_j I(\mathbf{r}_i - \mathbf{R}_j), \quad (7.13)$$

where \mathbf{s}_i and \mathbf{S}_j are the i -th carrier's and j -th ion's spin operators, while \mathbf{r}_i and \mathbf{R}_j are their respective positions. The exchange interaction between these two spins is described by a smooth, quickly vanishing and positive function $I(\mathbf{r}_i - \mathbf{R}_j)$, localised around the j -th magnetic ion. As described in Sec. 5.6, the matrix elements of I between the p - and s -type basis functions (β and α , respectively) determine the strength of the p - d and s - d exchange interaction, respectively. They are defined in Ch. 6, where it is shown that the exact nature of these functions depends on the band structure model used. In the absence of external fields, \mathcal{H}_0 depends on the carriers' degrees of freedom only.

The dynamics of magnetic ions coupled to the system of carriers require a self-consistent description, which takes into account how the carriers react to

the ions' magnetisation changes. Therefore, I use the Löwdin perturbation method specifically adapted for multiparticle Hamiltonians [41, 122, 193, 194], to derive an effective Hamiltonian \mathcal{H}^{eff} for ions only. The perturbation in question is the sp - d interaction between carriers and ions.

I choose the multiparticle basis states of \mathcal{H} as $M \otimes \Gamma$. The ion part M has spins quantised along the z direction, while the carrier part Γ is a Slater determinant of P one-particle eigenstates $\psi_{\mathbf{k}m}$ of the one-particle carrier Hamiltonian, derived under the mean-field and virtual crystal assumptions:

$$h = h_0 + \Delta s^z P_{\text{ex}} , \quad (7.14)$$

where h_0 describes the host band structure. Subscripts \mathbf{k} and m denote the wavevector and the band number, respectively. The operator P_{ex} , defined in Sec. 6.1.2 for the $k \cdot p$ method and in Sec. 6.2.2 for the tight-binding method, ensures that I apply the correct spin-splittings to conduction and valence bands. For the 6-band $k \cdot p$ method, $P_{\text{ex}} = 1$.

The Löwdin calculus consists in dividing the multiparticle basis states into two subsets, A and B ,

$$\mathcal{H} = \begin{pmatrix} \mathcal{H}_{AA} & \mathcal{H}_{AB} \\ \mathcal{H}_{BA} & \mathcal{H}_{BB} \end{pmatrix} .$$

Set A contains all states $M \otimes \Gamma_0$, where Γ_0 is a Slater determinant of the P lowest eigenstates of h . Set B contains all the remaining states, in which at least one carrier is excited above the Fermi level. I construct the effective Hamiltonian for the states from set A only, adding their coupling with set B as a second order perturbation,

$$\mathcal{H}_{nn'}^{\text{eff}} = (\mathcal{H}_0)_{nn'} + \mathcal{H}'_{nn'} + \sum_{n'' \in B} \frac{\mathcal{H}_{nn''} \mathcal{H}_{n''n'}}{E - \mathcal{H}_{n''n''}} , \quad (7.15)$$

where $\mathcal{H}_{nn'} = \langle n | \mathcal{H} | n' \rangle$ (similarly for $(\mathcal{H}_0)_{nn'}$ and $\mathcal{H}'_{nn'}$) and $n, n' \in A$. The term $(\mathcal{H}_0)_{nn'}$ is independent of the ion configurations, so I set it to zero for simplicity. Thus, the effective Hamiltonian \mathcal{H}^{eff} depends only on the ion degrees of freedom but, thanks to the Löwdin method, takes carrier excitations into account and can be used to calculate the spin-wave dispersion in a self-consistent manner.

The variational part of the presented method consists in searching for the energy E somewhere in the region for which we want accurate results, which in my case are the lowest eigenenergies of \mathcal{H} , in particular the groundstate. For a known average spin splitting Δ , I can set E to the total energy of the carrier multiparticle state Γ_0 , $E_{\Gamma_0} = \sum_{(\mathbf{k}, m) \in \Gamma_0} E_{\mathbf{k}m}$, where $E_{\mathbf{k}m}$ is the eigenenergy of $\psi_{\mathbf{k}m}$, and the sum goes over all occupied eigenstates in Γ_0 . The states n'' are of the form $M'' \otimes \Gamma''$, $\Gamma'' \neq \Gamma_0$. To simplify the sum over n'' , I approximate the diagonal matrix element $\mathcal{H}_{n''n''}$, which depends on

both M'' and Γ'' , by the total energy of the multiparticle carrier state Γ'' , $E_{\Gamma''} = \sum_{(\mathbf{k}, m) \in \Gamma''} E_{\mathbf{k}m}$. It describes the interaction of Γ'' with the average configuration of the ions' spins corresponding to the spin splitting Δ . I can thus write the Hamiltonian (7.15) in the following form:

$$\mathcal{H}_{nn'}^{\text{eff}} = \mathcal{H}'_{nn'} + \sum_{M''} \sum_{\Gamma'' \neq \Gamma_0} \frac{\mathcal{H}_{nn''} \mathcal{H}_{n''n'}}{E_{\Gamma_0} - E_{\Gamma''}}, \quad n, n' \in A. \quad (7.16)$$

The factor $\mathcal{H}_{nn''} \mathcal{H}_{n''n'}$ under the sum can be written as $\langle M \otimes \Gamma_0 | \mathcal{H} | \Gamma'' \otimes M'' \rangle \langle M'' \otimes \Gamma'' | \mathcal{H} | \Gamma_0 \otimes M' \rangle$, where $n = M \otimes \Gamma_0$ and $n' = M' \otimes \Gamma_0$. Since the denominator in Eq. (7.16) is independent of M'' , summing over M'' is equivalent to inserting an identity operator in the ion Hilbert space, which allows me to write the last term as

$$\sum_{\Gamma'' \neq \Gamma_0} \frac{\langle M \otimes \Gamma_0 | \mathcal{H} | \Gamma'' \rangle \langle \Gamma'' | \mathcal{H} | \Gamma_0 \otimes M' \rangle}{E_{\Gamma_0} - E_{\Gamma''}}.$$

I can thus treat \mathcal{H}^{eff} as a Hamiltonian acting on ion states only,

$$\begin{aligned} \mathcal{H}_{MM'}^{\text{eff}} &= \langle M | \mathcal{H}^{\text{eff}} | M' \rangle \\ &= \langle M \otimes \Gamma_0 | \mathcal{H}' | \Gamma_0 \otimes M' \rangle + \sum_{\Gamma'' \neq \Gamma_0} \frac{\langle M \otimes \Gamma_0 | \mathcal{H} | \Gamma'' \rangle \langle \Gamma'' | \mathcal{H} | \Gamma_0 \otimes M' \rangle}{E_{\Gamma_0} - E_{\Gamma''}}. \end{aligned} \quad (7.17)$$

Since the sp - d exchange term in \mathcal{H} , which produces the non-diagonal matrix element $\langle M \otimes \Gamma_0 | \mathcal{H} | \Gamma'' \otimes M'' \rangle$, is the interaction of a single carrier with an ion, the only Γ'' states which have a non-zero contribution to the sum over Γ'' in Eq. (7.17) are those which are created from Γ_0 by just one excitation, $\psi_{\mathbf{k}m} \rightarrow \psi_{\mathbf{k}'m'}$ from below to above the Fermi level; I denote such states by $\Gamma_{\mathbf{k}m\mathbf{k}'m'}$. Hence, I have $E_{\Gamma_0} - E_{\Gamma_{\mathbf{k}m\mathbf{k}'m'}} = E_{\mathbf{k}m} - E_{\mathbf{k}'m'}$ and Hamiltonian (7.17) can be written as

$$\begin{aligned} \mathcal{H}_{MM'}^{\text{eff}} &= \langle M \otimes \Gamma_0 | \mathcal{H}' | \Gamma_0 \otimes M' \rangle + \\ &\sum_{\mathbf{k}\mathbf{k}'} \sum_{mm'} \frac{f_{\mathbf{k}m}(1 - f_{\mathbf{k}'m'})}{E_{\mathbf{k}m} - E_{\mathbf{k}'m'}} \langle M \otimes \Gamma_0 | \mathcal{H} | \Gamma_{\mathbf{k}m\mathbf{k}'m'} \rangle \langle \Gamma_{\mathbf{k}m\mathbf{k}'m'} | \mathcal{H} | \Gamma_0 \otimes M' \rangle, \end{aligned} \quad (7.18)$$

where $f_{\mathbf{k}m}$ is the Fermi-Dirac distribution (this generalises the calculation to finite temperatures).

To integrate out the carrier degrees of freedom in (7.18), I need to calculate the matrix elements $\langle \psi_{\mathbf{k}m} | s^\sigma I(\mathbf{r} - \mathbf{R}_j) | \psi_{\mathbf{k}'m'} \rangle$, where $\sigma = +, -, z$ and $[\hat{s}^+, \hat{s}^-] = \hat{s}^z$ by convention. Assuming that the function $I(\mathbf{r} - \mathbf{R}_j)$ vanishes quickly outside the unit cell and that $e^{i\mathbf{k}\cdot\mathbf{r}}$ and $e^{i\mathbf{k}'\cdot\mathbf{r}}$ vary slowly over the same range, I obtain

$$\langle \psi_{\mathbf{k}m} | s^\sigma I(\mathbf{r} - \mathbf{R}_j) | \psi_{\mathbf{k}'m'} \rangle = e^{i(\mathbf{k}' - \mathbf{k}) \cdot \mathbf{R}_j} \langle u_{\mathbf{k}m} | s^\sigma I(\mathbf{r} - \mathbf{R}_j) | u_{\mathbf{k}'m'} \rangle,$$

Because of the spin-orbit coupling I cannot separate $\langle u_{\mathbf{k}m} | s^\sigma I(\mathbf{r} - \mathbf{R}_j) | u_{\mathbf{k}'m'} \rangle$ into a product of the spin and spatial matrix elements. To overcome this problem, I write $u_{\mathbf{k}m}$ as $\sum_s u_{\mathbf{k}m}^s \psi_s$ using the spinor basis $\psi_s = |\uparrow\rangle, |\downarrow\rangle$, where $u_{\mathbf{k}m}^s$ is a purely spatial wavefunction, and

$$\langle u_{\mathbf{k}m} | s^\sigma I(\mathbf{r} - \mathbf{R}_j) | u_{\mathbf{k}'m'} \rangle = \sum_{ss'} \langle \psi_s | s^\sigma | \psi_{s'} \rangle \langle u_{\mathbf{k}m}^s | I(\mathbf{r} - \mathbf{R}_j) | u_{\mathbf{k}'m'}^{s'} \rangle .$$

The operator P_{ex} projects the wavefunctions on the basis functions which are coupled to the magnetic ion via the exchange interaction described by the function I (cf. Secs. 6.1.2 and 6.2.2). Hence, I can write that

$$\langle u_{\mathbf{k}m}^s | I(\mathbf{r} - \mathbf{R}_j) | u_{\mathbf{k}'m'}^{s'} \rangle = c \langle u_{\mathbf{k}m}^s | P_{\text{ex}} | u_{\mathbf{k}'m'}^{s'} \rangle ,$$

which leads to

$$\begin{aligned} \langle u_{\mathbf{k}m} | s^\sigma I(\mathbf{r} - \mathbf{R}_j) | u_{\mathbf{k}'m'} \rangle &= c \sum_{ss'} \langle \psi_s | s^\sigma | \psi_{s'} \rangle \langle u_{\mathbf{k}m}^s | P_{\text{ex}} | u_{\mathbf{k}'m'}^{s'} \rangle \\ &= c \langle u_{\mathbf{k}m} | s^\sigma P_{\text{ex}} | u_{\mathbf{k}'m'} \rangle , \end{aligned} \quad (7.19)$$

as P_{ex} commutes with the spin operator. The scaling factor c can be derived from the condition that in for the system fully polarised along the z axis and in the mean-field and virtual-crystal approximation, I have

$$S \sum_{j=1}^N \langle u_{\mathbf{k}m} | s^z I(\mathbf{r} - \mathbf{R}_j) | u_{\mathbf{k}'m'} \rangle = \Delta \langle u_{\mathbf{k}m} | s^z P_{\text{ex}} | u_{\mathbf{k}'m'} \rangle$$

where S is total ion spin (this can be simply generalised to arbitrary temperature by replacing Δ and S by their temperature-dependent versions). Inserting (7.19), I obtain

$$NSc \langle u_{\mathbf{k}m} | s^z P_{\text{ex}} | u_{\mathbf{k}'m'} \rangle = \Delta \langle u_{\mathbf{k}m} | s^z P_{\text{ex}} | u_{\mathbf{k}'m'} \rangle .$$

But $\Delta = NS\beta/V$, where β is the p - d exchange integral defined in Sec. 5.6, so $c = \Delta/(NS) = \beta/V$ and

$$\langle \psi_{\mathbf{k}m} | s^\sigma I(\mathbf{r} - \mathbf{R}_j) | \psi_{\mathbf{k}'m'} \rangle = \frac{\beta}{V} e^{i(\mathbf{k}' - \mathbf{k}) \cdot \mathbf{R}_j} s_{\mathbf{k}m\mathbf{k}'m'}^\sigma .$$

where $s_{\mathbf{k}m\mathbf{k}'m'}^\sigma = \langle u_{\mathbf{k}m} | s^\sigma P_{\text{ex}} | u_{\mathbf{k}'m'} \rangle$. The above expression is proportional to β , but the operator P_{ex} inside the matrix element takes into account the difference between p - d and s - d exchange integrals.

I can now write Hamiltonian (7.17) using ion spin operators,

$$\mathcal{H}^{\text{eff}} = \sum_{\sigma} \sum_{j=1}^N H_j^\sigma S_j^\sigma + \sum_{\sigma\sigma'} \sum_{j=1}^N \sum_{j'=1}^N H_{jj'}^{\sigma\sigma'} S_j^\sigma S_{j'}^{\sigma'} . \quad (7.20)$$

The coefficients H_j^σ and $H_{jj'}^{\sigma\sigma'}$ are given by

$$H_{jj'}^{\sigma\sigma'} = \frac{\beta^2}{V^2} \sum_{\mathbf{k}\mathbf{k}'} \sum_{mm'} \frac{f_{\mathbf{k}m}(1-f_{\mathbf{k}'m'})}{E_{\mathbf{k}'m'} - E_{\mathbf{k}m}} e^{i(\mathbf{k}'-\mathbf{k})\cdot(\mathbf{R}_j-\mathbf{R}_{j'})} s_{\mathbf{k}m\mathbf{k}'m'}^\sigma s_{\mathbf{k}'m'\mathbf{k}m}^{\sigma'}, \quad (7.21)$$

where due to the condition $\Gamma'' \neq \Gamma_0$ in Eq. (7.16), for $\mathbf{k} = \mathbf{k}'$ the summation goes over $m \neq m'$, and

$$H_j^\sigma = \frac{\beta}{V} \sum_{\mathbf{k}} \sum_m f_{\mathbf{k}m} s_{\mathbf{k}m\mathbf{k}m}^\sigma - \frac{\Delta\beta}{V} \sum_{\mathbf{k}} \sum_{m \neq m'} \frac{f_{\mathbf{k}m}(1-f_{\mathbf{k},m'})}{E_{\mathbf{k},m'} - E_{\mathbf{k}m}} (s_{\mathbf{k}m\mathbf{k}m'}^\sigma s_{\mathbf{k}m'\mathbf{k}m}^z + s_{\mathbf{k}m'\mathbf{k}m}^\sigma s_{\mathbf{k}m\mathbf{k}m'}^z). \quad (7.22)$$

To obtain the above expressions, I substituted the carrier-only part of Hamiltonian \mathcal{H}_0 (7.13) by the sum of P one-particle Hamiltonians h_0 from Eq. (7.14). I also used the formula $\langle \psi_{\mathbf{k}m} | h_0 | \psi_{\mathbf{k}'m'} \rangle = \delta_{\mathbf{k}\mathbf{k}'} (\delta_{mm'} E_{\mathbf{k}m} - \Delta s_{\mathbf{k}m\mathbf{k}'m'}^z)$, obtained from Hamiltonian h (7.14).

7.3 Interpretation of the effective Hamiltonian

Using the Löwdin perturbation-variational calculus, I have thus described the problem as a lattice spin system coupled by the effective exchange interaction, integrating out the carrier degrees of freedom. The physics of the carriers is embedded in the effective Hamiltonian \mathcal{H}^{eff} (7.20), and is responsible for the long-range nonlocal character of the mutual interactions between magnetic ions.

The first term of \mathcal{H}^{eff} contains the operator responsible for the mean-field generated by the carriers acting on the lattice ions (the first part in 7.22), plus the correction arising from the inter-band transitions. The latter can be associated with the Bloembergen–Rowland mechanism mentioned in Sec. 4.2.2. A small but worth noting result of the next section is that in the small oscillations approximation it cancels with the contribution from the second term.

The second term of \mathcal{H}^{eff} describes the effective long-range exchange interaction between the lattice ions. The nature of the interaction, mediated by the carrier between two ions, is reflected in the appearance of the squared β constant. The s – d exchange interaction characterised by the α constant is incorporated in the $s_{\mathbf{k}m\mathbf{k}'m'}^\sigma$ matrix elements via the P_{ex} operator. The fraction with the resonance denominator resulting from the perturbational approach dampens the influence of the distant energy bands, while the biggest contribution to the sum comes from the states in the vicinity of the Fermi level E_F . The denominator looks dangerous, as it may cause the fraction to diverge in the presence of the energy bands' crossings, which would make

my perturbation calculus invalid. However, the effective Hamiltonian for ions depends on the average of these factors, and will be shown (at least in the small oscillations approximation) immune to this problem in Sec. 7.4.

Contrary to the original RKKY range function (4.1), the formula (7.21) is anisotropic in space in the presence of the spin-orbit coupling, reflecting the symmetries of the crystal lattice. If, additionally, the bulk and structure inversion symmetries are broken (Sec. 5.4), it has an antisymmetric part in the form of the Dzyaloshinskii–Moriya interaction [195, 196],

$$\sum_{\sigma''} \sum_{jj'} iu_{jj'}^{\sigma''} \sum_{\sigma\sigma'} \epsilon_{\sigma''\sigma\sigma'} S_j^\sigma S_{j'}^{\sigma'}, \quad (7.23)$$

where $\epsilon_{\sigma''\sigma\sigma'}$ is the antisymmetric Levi-Civita symbol with $\epsilon_{+-z} = 1$, while \mathbf{u}_{ij} is a pseudovector and exists only in systems with broken inversion symmetry,

$$iu_{jj'}^{\sigma''} = \frac{1}{2} \sum_{\sigma\sigma'} \epsilon_{\sigma''\sigma\sigma'} H_{jj'}^{\sigma\sigma'}.$$

7.4 Small oscillations approximation

The system of coupled magnetic moments acts like that of harmonic oscillators, an analogy which is concretised mathematically by the Holstein-Primakoff bosonisation [197]:

$$S_j^+ = \sqrt{S} \sqrt{1 - \frac{a_j^\dagger a_j}{2S}} a_j, \quad S_j^- = \sqrt{S} a_j^\dagger \sqrt{1 - \frac{a_j^\dagger a_j}{2S}}, \quad S_j^z = S - a_j^\dagger a_j,$$

which replaces the spin operators with nonlinear functions of bosonic creation and annihilation operators a_j^\dagger and a_j . To investigate the dynamics of the groundstate and low-lying excitations of the effective Hamiltonian (7.20), I will use the small oscillations approximation and substitute these functions with their power expansions around the state of saturation magnetisation:

$$S_j^+ \approx \sqrt{S} a_j, \quad S_j^- \approx \sqrt{S} a_j^\dagger, \quad S_j^z = S - a_j^\dagger a_j, \quad (7.24)$$

leaving in the Hamiltonian only those terms which are quadratic in the creation and annihilation operators.

$$\begin{aligned}
\mathcal{H}^{\text{eff}} = & -\frac{\beta}{V} \times \\
& \sum_{j=1}^N \sum_{\mathbf{k}} \left(\sum_m f_{\mathbf{k}m} s_{\mathbf{k}m\mathbf{k}m}^z - 2\Delta \sum_{m \neq m'} \frac{f_{\mathbf{k}m}(1-f_{\mathbf{k},m'})}{E_{\mathbf{k},m'} - E_{\mathbf{k}m}} |s_{\mathbf{k}m\mathbf{k}m'}^z|^2 \right) a_j^\dagger a_j \\
& - \frac{S\beta^2}{V^2} \sum_{j,j'=1}^N \left(\sum_{\mathbf{k}\mathbf{k}'m m'} \frac{f_{\mathbf{k}m}(1-f_{\mathbf{k}'m'})}{E_{\mathbf{k}'m'} - E_{\mathbf{k}m}} e^{i(\mathbf{k}'-\mathbf{k}) \cdot (\mathbf{R}_j - \mathbf{R}_{j'})} |s_{\mathbf{k}m\mathbf{k}'m'}^z|^2 \right) \times \\
& (a_j^\dagger a_j + a_{j'}^\dagger a_{j'}) + \frac{S\beta^2}{V^2} \sum_{j=1}^N \sum_{j'=1}^N \sum_{\mathbf{k}\mathbf{k}'} \sum_{m m'} \frac{f_{\mathbf{k}m}(1-f_{\mathbf{k}'m'})}{E_{\mathbf{k}'m'} - E_{\mathbf{k}m}} e^{i(\mathbf{k}'-\mathbf{k}) \cdot (\mathbf{R}_j - \mathbf{R}_{j'})} \\
& \times (s_{\mathbf{k}m\mathbf{k}'m'}^+ a_j + s_{\mathbf{k}m\mathbf{k}'m'}^- a_{j'}^\dagger)^\dagger (s_{\mathbf{k}m\mathbf{k}'m'}^+ a_j + s_{\mathbf{k}m\mathbf{k}'m'}^- a_{j'}^\dagger) .
\end{aligned} \tag{7.25}$$

Within the small oscillations approximation, the linear and zeroth-order terms do not affect the excitation spectrum. This approximation works very well in the long-wave limit, $aq \ll \pi$, as the neglected magnon-magnon interactions are proportional to $(aq)^4$ [198].

First, let us take a closer look at the term

$$\frac{S\beta^2}{V^2} \sum_{j,j'=1}^N \left(\sum_{\mathbf{k}\mathbf{k}'} \sum_{m m'} \frac{f_{\mathbf{k}m}(1-f_{\mathbf{k}'m'})}{E_{\mathbf{k}'m'} - E_{\mathbf{k}m}} e^{i(\mathbf{k}'-\mathbf{k}) \cdot (\mathbf{R}_j - \mathbf{R}_{j'})} |s_{\mathbf{k}m\mathbf{k}'m'}^z|^2 \right) a_j^\dagger a_j .$$

Summation over j' gives $\sum_{j'=1}^N e^{i(\mathbf{k}'-\mathbf{k}) \cdot \mathbf{R}_{j'}} = N\delta_{\mathbf{k}\mathbf{k}'}$, which allows me to write the above term as

$$\frac{NS\beta^2}{V^2} \sum_{j=1}^N \left(\sum_{\mathbf{k}} \sum_{m m'} \frac{f_{\mathbf{k}m}(1-f_{\mathbf{k},m'})}{E_{\mathbf{k},m'} - E_{\mathbf{k}m}} |s_{\mathbf{k}m\mathbf{k}m'}^z|^2 \right) a_j^\dagger a_j .$$

The twin term with $a_{j'}^\dagger a_{j'}$ at the end is treated in the same fashion, after which I write (7.25) as

$$\begin{aligned}
\mathcal{H}^{\text{eff}} = & \\
& -\frac{\beta}{V} \sum_{j=1}^N \sum_{\mathbf{k}} \left(\sum_m f_{\mathbf{k}m} s_{\mathbf{k}m\mathbf{k}m}^z - 2\Delta \sum_{m \neq m'} \frac{f_{\mathbf{k}m}(1-f_{\mathbf{k},m'})}{E_{\mathbf{k},m'} - E_{\mathbf{k}m}} |s_{\mathbf{k}m\mathbf{k}m'}^z|^2 \right) a_j^\dagger a_j \\
& - \frac{2NS\beta^2}{V^2} \sum_{j=1}^N \left(\sum_{\mathbf{k}} \sum_{m m'} \frac{f_{\mathbf{k}m}(1-f_{\mathbf{k},m'})}{E_{\mathbf{k},m'} - E_{\mathbf{k}m}} |s_{\mathbf{k}m\mathbf{k}m'}^z|^2 \right) a_j^\dagger a_j \\
& + \frac{S\beta^2}{V^2} \sum_{j=1}^N \sum_{j'=1}^N \sum_{\mathbf{k}\mathbf{k}'} \sum_{m m'} \frac{f_{\mathbf{k}m}(1-f_{\mathbf{k}'m'})}{E_{\mathbf{k}'m'} - E_{\mathbf{k}m}} e^{i(\mathbf{k}'-\mathbf{k}) \cdot (\mathbf{R}_j - \mathbf{R}_{j'})} \\
& \times (s_{\mathbf{k}m\mathbf{k}'m'}^+ a_j + s_{\mathbf{k}m\mathbf{k}'m'}^- a_{j'}^\dagger)^\dagger (s_{\mathbf{k}m\mathbf{k}'m'}^+ a_j + s_{\mathbf{k}m\mathbf{k}'m'}^- a_{j'}^\dagger) .
\end{aligned}$$

Due to the equality $\Delta = NS\beta/V$, the terms with $|s_{\mathbf{k}m\mathbf{k}m'}^z|^2$ cancel and I get

$$\begin{aligned} \mathcal{H}^{\text{eff}} = & -\frac{\beta}{V} \left(\sum_{\mathbf{k}} \sum_m f_{\mathbf{k}m} s_{\mathbf{k}m\mathbf{k}m}^z \right) \sum_{j=1}^N a_j^\dagger a_j \\ & + \frac{S\beta^2}{V^2} \sum_{\mathbf{k}\mathbf{k}'} \sum_{mm'} \frac{f_{\mathbf{k}m}(1-f_{\mathbf{k}'m'})}{E_{\mathbf{k}'m'} - E_{\mathbf{k}m}} \\ & \times \left[\sum_{j=1}^N e^{i(\mathbf{k}'-\mathbf{k})\cdot\mathbf{R}_j} (s_{\mathbf{k}m\mathbf{k}'m'}^+ a_j + s_{\mathbf{k}m\mathbf{k}'m'}^- a_j^\dagger) \right] \\ & \times \left[\sum_{j'=1}^N e^{i(\mathbf{k}'-\mathbf{k})\cdot\mathbf{R}_{j'}} (s_{\mathbf{k}m\mathbf{k}'m'}^+ a_{j'} + s_{\mathbf{k}m\mathbf{k}'m'}^- a_{j'}^\dagger) \right]^\dagger. \end{aligned}$$

I can now proceed with the Fourier transform (invoking the virtual-crystal approximation), using the fact that $\sum_{j=1}^N a_j^\dagger a_j = \sum_{\mathbf{q}} a_{\mathbf{q}}^\dagger a_{\mathbf{q}}$:

$$\begin{aligned} \mathcal{H}^{\text{eff}} = & -\frac{\beta}{V} \left(\sum_{\mathbf{k}} \sum_m f_{\mathbf{k}m} s_{\mathbf{k}m\mathbf{k}m}^z \right) \sum_{\mathbf{q}} a_{\mathbf{q}}^\dagger a_{\mathbf{q}} + \frac{\Delta\beta}{V} \sum_{\mathbf{k}\mathbf{k}'} \sum_{mm'} \frac{f_{\mathbf{k}m}(1-f_{\mathbf{k}'m'})}{E_{\mathbf{k}'m'} - E_{\mathbf{k}m}} \\ & \times \left(s_{\mathbf{k}m\mathbf{k}'m'}^+ a_{\mathbf{k}'-\mathbf{k}} + s_{\mathbf{k}m\mathbf{k}'m'}^- a_{\mathbf{k}'-\mathbf{k}}^\dagger \right) \left(s_{\mathbf{k}m\mathbf{k}'m'}^+ a_{\mathbf{k}'-\mathbf{k}} + s_{\mathbf{k}m\mathbf{k}'m'}^- a_{\mathbf{k}'-\mathbf{k}}^\dagger \right)^\dagger. \end{aligned}$$

After simple algebraic transformations, including the symmetrisation of the sums over wavevectors, I arrive at the final form of the harmonic Hamiltonian,

$$\mathcal{H}^{\text{eff}} = \sum_{\mathbf{q}} \left[(\Xi - \chi_{\mathbf{q}}^{+-}) a_{\mathbf{q}}^\dagger a_{\mathbf{q}} - \frac{1}{2} \chi_{\mathbf{q}}^{++} a_{\mathbf{q}} a_{-\mathbf{q}} - \frac{1}{2} \chi_{\mathbf{q}}^{--} a_{\mathbf{q}}^\dagger a_{-\mathbf{q}}^\dagger \right]. \quad (7.26)$$

I call it the *interaction* representation as it describes the perturbation of the ground state by the isotropic Coulomb interaction (first term) and by the spin-orbit interaction, coupling modes of different \mathbf{q} (remaining terms). The spin susceptibility of the carriers is given by

$$\chi_{\mathbf{q}}^{\sigma\sigma'} = -\frac{nS\beta^2}{V} \sum_{\mathbf{k}} \sum_{mm'} \frac{f_{\mathbf{k}m} - f_{\mathbf{k}+\mathbf{q},m'}}{E_{\mathbf{k}m} - E_{\mathbf{k}+\mathbf{q},m'}} s_{\mathbf{k}m(\mathbf{k}+\mathbf{q})m'}^\sigma s_{(\mathbf{k}+\mathbf{q})m'\mathbf{k}m}^{\sigma'}, \quad (7.27)$$

where $n = N/V$ is the density of localised spins S in the sample volume V and $nS\beta = \Delta$. The presence of the energy denominator shows that $\chi_{\mathbf{q}}^{\sigma\sigma'}$ corresponds to the second-order part of the Hamiltonian (7.18). As promised in Sec. 7.3, the vanishing of the denominator is not harmful, due to the de l'Hospital rule.

The formula (7.27) implies that $\chi_{\mathbf{q}}^{++} = (\chi_{\mathbf{q}}^{--})^*$ is symmetric in \mathbf{q} . In the absence of the spin-orbit coupling the bands' spins become fully polarised,

which causes $\chi_{\mathbf{q}}^{++}$ to vanish, as $\langle \psi | s^+ | \psi' \rangle \langle \psi' | s^+ | \psi \rangle = 0$ for any choice of spinors $\psi, \psi' = |\uparrow\rangle, |\downarrow\rangle$. This is also true for non-zero spin-orbit coupling in the case when the valence bands are isotropic [43] and for the s -type bands in general, as for them the total angular momentum is equal to the spin and thus they are fully polarised even in the presence of spin-orbit interaction.

Because $\chi_{\mathbf{q}}^{+-}, \chi_{\mathbf{q}}^{-+} \in \mathcal{R}$ inherit the symmetry of the $\psi_{\mathbf{k}m}$ eigenstates, it can be expected to be symmetric with respect to \mathbf{q} for systems which preserve space inversion symmetry, like in the case analysed in Ref. [43], and otherwise for systems which do not. The \mathbf{q} -independent term describes the interaction of a single magnetic ion with a molecular field arising from the intraband spin polarisation of the carriers,

$$\Xi = -\frac{\beta}{V} \sum_{\mathbf{k}} \sum_m f_{\mathbf{k},m} s_{\mathbf{k}m\mathbf{k}m}^z . \quad (7.28)$$

The corresponding term reflecting the interband polarisation,

$$\Xi_{\text{so}} = \frac{nS\beta^2}{V} \sum_{\mathbf{k}} \sum_{m \neq m'} \frac{f_{\mathbf{k}m} - f_{\mathbf{k},m'}}{E_{\mathbf{k},m'} - E_{\mathbf{k}m}} |s_{\mathbf{k}m\mathbf{k}m'}^z|^2 , \quad (7.29)$$

arises from both $H_{jj'}^{\sigma\sigma'}$ (7.21) and the second part of H_j^σ coefficient (7.22), and cancels exactly in the full Hamiltonian \mathcal{H}^{eff} . As announced in the previous section, this shows that the Bloembergen–Rowland exchange, driven by virtual spin transitions between different bands, does not exist in the low-temperature limit covered by small oscillations approximation.

7.5 Summary

In Section 7.1 I have drawn a basic qualitative picture of ferromagnetism in (Ga,Mn)As, developing a set of mathematical tools for modelling statistical ensembles of non-interacting distinguishable spins. In particular, I provide a combinatorial formula for their sum of states for a given total magnetisation.

The main result of this chapter is the application of the proposed variation-perturbational Löwdin calculus to derive the effective Hamiltonian (7.26) for systems with carrier-mediated ferromagnetism. Within the small oscillations approximation, I have obtained the mean-field term and the spin susceptibility. Importantly, I have shown that the Bloembergen–Rowland mechanism, responsible for the interband polarisation, does not occur in this regime. The effective Hamiltonian is a starting point to the quantitative analysis of magnetic phenomena in the systems in question.

In the next chapter, I will calculate the Curie temperature and magnetocrystalline anisotropies in the $k \cdot p$ and tight-binding computational schemes outlined in Ch. 6.

Chapter 8

Curie temperature and uniaxial anisotropy in (Ga,Mn)As

The mean-field Curie temperature and uniaxial anisotropy field in (Ga,Mn)As, modelled by the 6-band $k \cdot p$ method within the virtual-crystal and mean-field approximations, were calculated by Dietl *et al.* [40]. In this chapter, I reconstruct these results and compare them to the outcomes of other computational schemes described in Ch. 6, namely the ones employing 8-band $k \cdot p$ and tight-binding ($spds^*$ and sps^*) band structure methods also within the virtual-crystal and mean-field approximations. Additionally, the results of this chapter will be useful as a check of the calibration of the employed computational schemes.

8.1 Mean-field Curie temperature

The ferromagnetism emerging below the characteristic value of the Curie temperature in dilute magnetic semiconductors is the most crucial property of these materials. The mean-field approximation allows for its reasonable overall description [40]. It reduces the problem of lattice spins coupled by the exchange interaction to that of noninteracting spins in the molecular field Ξ (7.28). Their magnetisation is described by the self-consistent equation,

$$M(T) = M(0) B_S \left(\frac{S\Xi(T)}{k_B T} \right), \quad (8.1)$$

where

$$B_S(x) = \frac{2S+1}{2S} \coth \left(\frac{2(S+1)x}{2S} \right) - \frac{1}{2S} \coth \left(\frac{x}{2S} \right).$$

The Brillouin function B_S describes the finite-temperature occupancy of the energy bands of the spin carriers, split into multiplets by the exchange field

of the lattice ions. It ignores the actual nature of thermal fluctuations and their correlations, and assumes that every spin fluctuates independently. Figure 8.1 presents the solution of the above self-consistent formula as compared to the experimental data for a typical (Ga,Mn)As system [199].

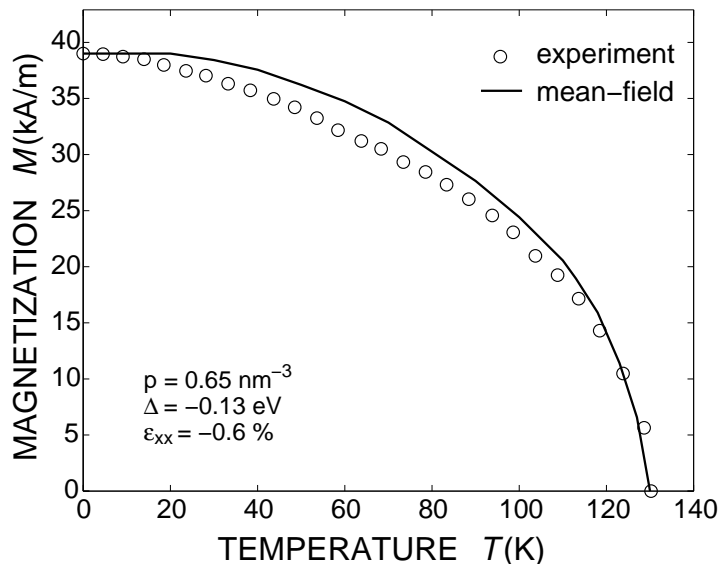


Figure 8.1: Temperature dependence of magnetisation for bulk (Ga,Mn)As obtained by solving the mean-field equation (8.1) (solid line). The experimental dependence for the sample from Ref. [199] is analysed in Sec. 9.7. The estimated values of the hole concentration p , spin splitting Δ and strain tensor ϵ_{xx} are indicated in the figure.

Linearisation of the $M(T)$ formula (8.1) leads to the mean-field Curie temperature expression (4.2). It shows that T_C is directly proportional to the density of carrier states, which suggests that it can be a good starting point for the comparison of the different computational schemes used in this thesis. As indicated in Ch. 6, the $k \cdot p$ and tight-binding approximations represent completely different approaches to the band structure modelling, from the mathematical way of constructing the Hamiltonian to its basis size. However, to account for the correct Curie temperature values, all these methods need to do is correctly describe the energy bands in which the hole carriers reside. Hence, a good benchmark test for the used computational schemes is to compare the T_C values they return.

Figure 8.2 presents the Curie temperatures calculated in different computational schemes as a function of the hole concentration p for three different Mn concentrations $x = 2\%$, 5% and 8% . The 6-band $k \cdot p$ and $spds^*$ tight-binding models, which are the most precise and tested methods in their respective classes, yield almost identical T_C values. The remaining 8-band $k \cdot p$ and sps^* tight-binding models exhibit some differences due to their parametrisation flaws. These results let us compare the ability of the em-

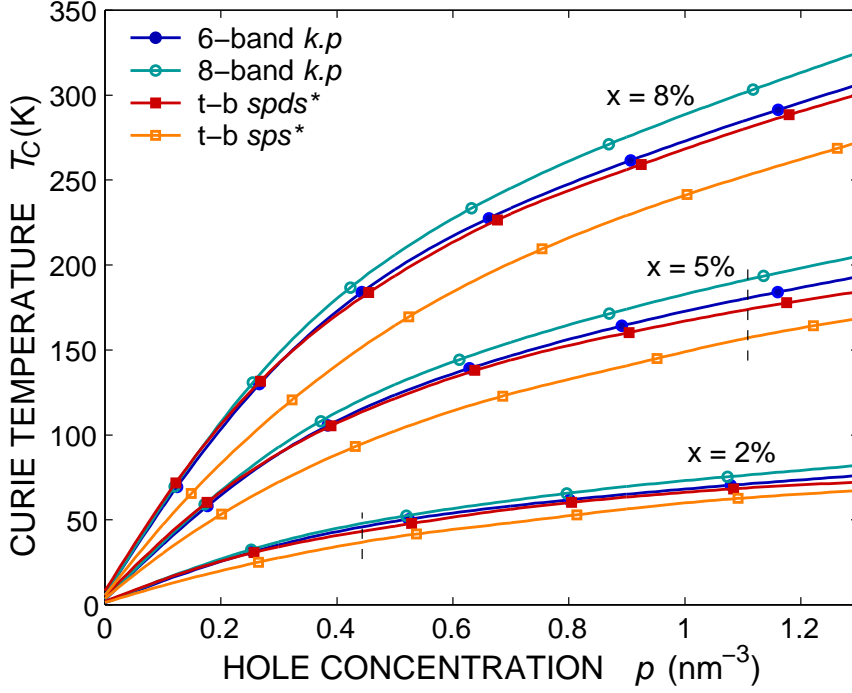


Figure 8.2: Computed magnitudes of the Curie temperature as a function of the hole concentration according to various band structure models for $\text{Ga}_{1-x}\text{Mn}_x\text{As}$ with the Mn content $x = 2\%$, 5% and 8% . Vertical lines indicate the maximal experimentally realisable hole densities for given x . On this and the following graphs, the numerical data were generated more densely than the markers, which are visual aids only.

ployed models to describe the properties of the six p -type bands occupied by hole carriers.

8.2 Uniaxial anisotropy field

Lattice spins in ferromagnetic (Ga,Mn)As below the Curie temperature, as described by the statistical model in Sec. 7.1, spontaneously polarise along some crystallographic direction. In this basic picture, involving the spherically symmetric two-parabolic-band model, this direction is chosen arbitrarily, the phenomenon called the spontaneous symmetry breaking. On the other hand, the advanced band structure models presented in Ch. 6 take into account the symmetry of the zincblende lattice within the procedure sketched in Ch. 5. These symmetries are passed on by the strong spin-orbit interaction to the system of spin carriers trapped in the crystal field, forming a rich energy landscape of magnetocrystalline anisotropy, which determines the direction of spontaneous magnetisation. (Substitutional Mn spins in (Ga,Mn)As treated within the RKKY or p - d Zener models as pure spins $S =$

$\frac{5}{2}$ with angular momentum $L = 0$ do not contribute to the anisotropy [40].)

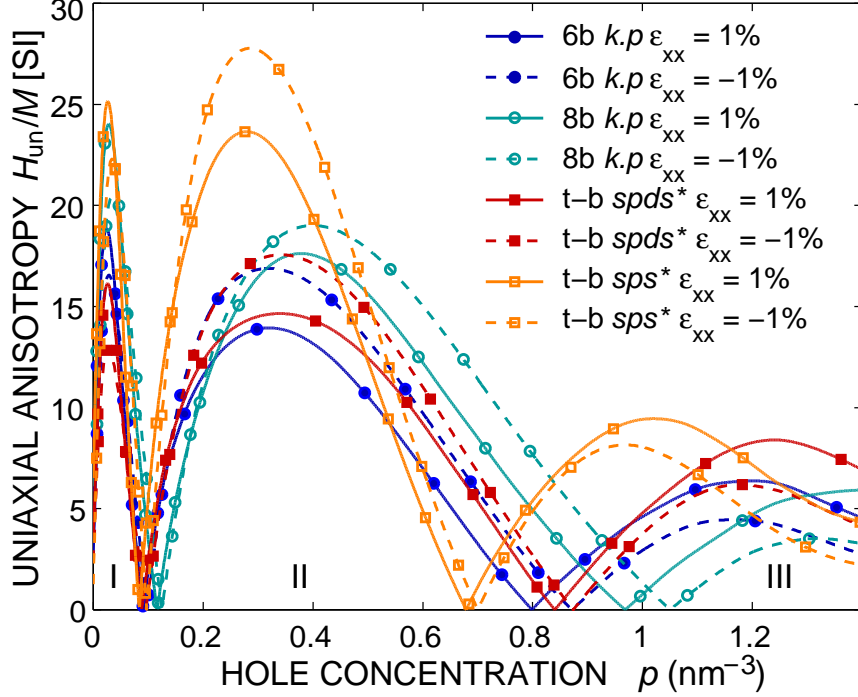


Figure 8.3: The amplitude of the uniaxial anisotropy field H_{un} (divided by saturation magnetisation, see Ref. [40]) for compressive ($\epsilon_{xx} = -1\%$) and tensile ($\epsilon_{xx} = 1\%$) biaxial strain in (Ga,Mn)As with spin splitting $\Delta = -0.15$ eV. The effect of shape anisotropy is neglected. In the central range of hole concentrations (II), the easy axis is in-plane and perpendicular to the plane for compressive and tensile strain, respectively, while the reorientation transition is expected in either low or high concentration regimes (I or III).

Since the magnetocrystalline anisotropy arises from the lattice symmetries, it should be well described already within the mean-field approximation. Indeed, the theory [40, 92] explains a number of experimental observations in (III,Mn)V systems [200–204].

The symmetry of the zincblende structure tells us that the magnetocrystalline anisotropy of bulk (Ga,Mn)As is cubic. However, the samples are grown epitaxially, so in practice one never deals with the pure bulk properties. The (Ga,Mn)As layers grown on substrates (most often [001]-oriented) are strained in the growth direction, due to the mismatch in the lattice constants, as described in Sec. 3.4. As mentioned in Sec. 5.5, this produces an additional uniaxial anisotropy perpendicular to the layer, which can be either tensile or compressively strained. The former results in an out-of-plane easy axis of the uniaxial anisotropy, while the latter leads to the complex anisotropy behaviour with the perpendicular-to-plane axis being easy or hard depending on the layer properties and experimental conditions. In par-

ticular, the out-of-plane easy axis encountered in layers with low Mn doping and at very low temperatures usually reorients into the in-plane direction at temperatures closer to T_C .

The evaluation of the magnitudes of uniaxial magnetic anisotropy field H_{un} provides a non-trivial comparison between the used computational schemes. Since magnetocrystalline anisotropies are driven by the presence of the spin-orbit interaction, the comparison of the H_{un} values shows how the different models deal with this relativistic property of (Ga,Mn)As.

I calculate the magnitude of H_{un} as proportional to the difference of the total carrier energy for the easy and hard magnetisation directions under 1% tensile or compressive strain [40]

$$\mu_0 H_{un} = |2 [E_c([001]) - E_c([100])] / M + \mu_0 M| .$$

As presented in Fig. 8.3, in a region of intermediate hole concentrations, the easy axis takes the [001] direction for tensile strain, while it is in the (001) plane for compressive strain. The situation is opposite for lower and higher hole concentrations. These results agree between the models, especially for the $spds^*$ tight-binding and the 6-band $k \cdot p$ calculations (the latter reconstructing the results of Ref. [40]), like in the case of the Curie temperature in the previous section. Consequently, all models correctly capture the uniaxial anisotropy trends, which means that they handle similarly well the spin-orbit splitting of the carrier bands.

8.3 Summary

The outcomes of this chapter are manifold. I have analysed two important characteristics of (Ga,Mn)As, the Curie temperature T_C and uniaxial anisotropy field H_{un} , within different computational schemes. I have reconstructed the known results of the 6-band $k \cdot p$ method [40] and compared them with the outcome of three other band structure models: the 8-band $k \cdot p$ and two tight-binding approximations, 40-orbital $spds^*$ and 20-orbital sps^* . The analysis of the obtained results served me as a benchmark to test the employed computational schemes. The 6-band $k \cdot p$ and $spds^*$ models, although based on completely different mathematical approximations, give consistent results. The remaining 8-band $k \cdot p$ and 20-orbital sps^* models differ slightly, but do not introduce any qualitative difference. The importance of this work will become more obvious in Ch. 10, which analyses the magnetotransport effects in (Ga,Mn)As.

It may seem surprising that the simplest model (6-band) agrees so well with the most complicated one (40-band). However, as already noticed, to model the above DMS characteristics it is enough to correctly describe the details of the carrier band structure, which are the six p -type bands

in the vicinity of the Γ point, including the spin-orbit coupling. As mentioned before, due to its empirical nature the 6-band $k \cdot p$ model does not provide an inferior description of these bands with respect to the more advanced models—it takes into account their coupling with higher bands, partly through its calibration to experimental data and partly through the perturbational calculus [41, 174], as described in Sec. 6.1. On the other hand, the 8-band $k \cdot p$ and 20-orbital sps^* models lack the robustness of the 6-band Kohn–Luttinger model and the detailed band structure of the 40-band tight-binding model [143, 171].

Finally, I have calculated the magnetisation vs. temperature curves within the mean-field approximation. As already mentioned, it does not work well at low temperatures, where the magnetisation of the system is reduced by spin waves. It predicts an exponential approach to zero-temperature saturation, $M(0) - M(T) \sim \exp(\Delta E/k_B T)$, while spin waves yield a power law approach, $M(0) - M(T) \sim T^{3/2}$, the well-known $T^{3/2}$ Bloch law [107]. In the next chapter, I will investigate spin waves and their effect on the $M(T)$ dependence and other properties of (Ga,Mn)As.

Chapter 9

Spin waves and exchange stiffness in (Ga,Mn)As

The $sp-d$ exchange interaction, which lies behind the mechanism of magnetic ordering in (Ga,Mn)As and many other dilute magnetic semiconductors, also affects the character of low-temperature excitations of spins in these systems. Called spin waves due to their wave-like nature, they contribute to both equilibrium (e.g. spontaneous magnetisation and Curie temperature) and nonequilibrium magnetic properties (ferromagnetic resonance and relaxation). In perfect ferromagnets, they form a continuum of delocalised states, which I will derive in the next section.

At the same time, this strong exchange interaction allows us to replace the atomic quantum-mechanical description of the system with the classical, continuous micromagnetic theory, where it appears in form of exchange stiffness constant \mathcal{A} [107]. Together with the magnetocrystalline anisotropy constant \mathcal{K} , they determine macroscopic properties of ferromagnets [198]. Then, \mathcal{A} can be understood as the amount of exchange energy associated with nonuniform distributions of local directions of magnetisation, while \mathcal{K} as the energy needed to change the total magnetisation direction with respect to the crystal axes, which usually involves the competing crystal-field and spin-orbit interactions. I will analyse these constants on the grounds of micromagnetic theory in Sec. 9.2.

While the main part of the exchange energy is isotropic, a consequence of its electrostatic origin, the relativistic spin-orbit coupling can create its small anisotropy, namely the dependence on the crystalline orientation of magnetisation. In Section 9.3, I will find the resulting relativistic correction to the exchange stiffness constant, the anisotropic exchange stiffness T , and suggest new physical effects it may induce.

In thin layers, where both the bulk inversion symmetry of the zincblende lattice and the inversion symmetry of the structure are broken, the spin-orbit coupling leads to many interesting effects related to the asymmetric Dzyalo-

shinskii–Moriya exchange. Some of them will be uncovered in Sec. 9.4, where I will show how they lead to a cycloidal spin arrangement and uniaxial in-plane anisotropy of diagonal directions in thin layers. The latter results in a surface-like anisotropy in thicker films.

Exciting a spin wave in an ordered system of spins costs some exchange energy proportional to \mathcal{A} . It can be provided in the form of thermal energy or of a microwave impulse, like in resonance experiments [205]. The spin waves of the thermal origin yield important contribution to the temperature dependence of magnetisation, described by the $T^{3/2}$ Bloch law. It will be discussed in Sec. 9.6, where I will show that the Bloch law is modified in the presence of magnetocrystalline anisotropies. I will also present a self-consistent method of calculating the spin-wave contribution to magnetisation in full temperature range, which remedies the flaws of the previous approach [44]. However, I will argue that spin waves do not lower the mean-field Curie temperature because of the thermal decoherence of the quantum spin system.

The spin-wave spectrum and the isotropic exchange stiffness in bulk (Ga,Mn)As were computed by König, Jungwirth and MacDonald [43], and by Brey and Gómez-Santos [206] within the p - d Zener model employing the 6-band $k \cdot p$ Hamiltonian [39, 40, 103], which neglects the inversion asymmetry specific to the zincblende lattice. It was found that the actual magnitude of the exchange stiffness is much greater when one takes into account the complex structure of the valence band, as compared to the case of a simple parabolic band [43, 206]. This, as well as the highly anisotropic Fermi surface, were shown to explain [206, 207] why the mean-field approximation [39] is so accurate in (Ga,Mn)As. It was also found that the values of exchange and anisotropy energies obtained within the same formalism describe quantitatively [208] the width of stripe domains in films with perpendicular magnetic anisotropy. More recently, Bouzerar [209] employed a self-consistent local random-phase approximation in order to evaluate the spectral density of spin-wave excitations in $\text{Ga}_{1-x}\text{Mn}_x\text{As}$. The magnitudes of spin-spin exchange range functions $J(r)$ were obtained from first principles computations within the local spin-density approximation (LSDA) and tight-binding linear muffin-tin orbital approach neglecting the spin-orbit interaction. The theory allows to treat disorder and thermal fluctuations, and shows that the calculated spectral density has well-defined maxima up to about one half of the relevant Debye wavevector $q_D = (24x/\pi)^{1/3}\pi/a$, where a is the lattice constant. This made it possible to determine the spin-wave dispersion $\omega(\mathbf{q})$ in the range $0 < q \lesssim q_D/2$, from which the magnitude of spin-wave stiffness was obtained [209].

Experimentally, Potashnik *et al.* [210] analysed the temperature dependence of magnetisation in a series of $\text{Ga}_{1-x}\text{Mn}_x\text{As}$ samples, which provided the values of spin-wave stiffness from the $T^{3/2}$ Bloch law. In later experiments, the stiffness was determined by examining spin precession modes

excited by optical pulses [211] and under ferromagnetic resonance conditions [212–214]. The values obtained for some films with thickness greater than 120 nm, either as-grown [211, 214] or annealed [211], are in good agreement with those predicted by Bouzerar [209]. However, the values for thinner films [211, 214] or another series of annealed samples [212, 213] were about three times smaller. Similarly small magnitudes of spin-wave stiffness were found by analysing the domain structure of annealed $\text{Ga}_{0.93}\text{Mn}_{0.07}\text{As}$ [199]. The experimental works [211–214] demonstrate that the spectral positions of spin-wave resonances are strongly affected by the character of spin pinning at the sample borders, mentioned in Sec. 9.4.1. The same effect is caused by magnetic anisotropy changes along the growth direction, particularly strong at the film interface and surface [214]. Therefore, theoretical predictions concerning spin-wave excitations in both thick and thin layers may provide a useful guide to better understanding of magnetisation dynamics in real samples.

To obtain quantitative results on spin waves and exchange stiffness in (Ga,Mn)As, its thin layers and bulk crystals, I will use the *spds*^{*} tight-binding computational scheme, described in Sec. 6.2. In Section 9.5, I will provide quantitative results on the spin-wave stiffness in form of the dimensionless parameter D_{nor} , and compare it to the results of the 6-band $k \cdot p$ model [43]. The dimensionless D_{nor} parameter will be employed in Sec. 9.7 to compare the theoretical results to related experimental findings [199, 210–214].

9.1 Microscopic picture of spin waves

In Section 7.2, I have used the Löwdin calculus to find the effective Hamiltonian of lattice ions interacting through hole carriers in a self-consistent way, written in the interaction representation of creation and annihilation operators. To calculate the dispersion dependence of its low lying energy states, spin waves, I need to transform the Hamiltonian to the *spin-wave representation*. To put it simply, I have to diagonalise it. For this purpose I will use the Bogoliubov transform, which I have adapted to systems with inversion symmetry breaking. The interaction and spin-wave pictures are associated with different sets of phenomenological parameters describing the macroscopic system, whose properties I will investigate later on.

The effective Hamiltonian for the lattice ions derived in Sec. 7.2 in the interaction picture has the following form:

$$\mathcal{H}^{\text{eff}} = \sum_{\mathbf{q}} \left[(\Xi - \chi_{\mathbf{q}}^{+-}) a_{\mathbf{q}}^{\dagger} a_{\mathbf{q}} - \frac{1}{2} \chi_{\mathbf{q}}^{++} a_{\mathbf{q}} a_{-\mathbf{q}} - \frac{1}{2} \chi_{\mathbf{q}}^{--} a_{\mathbf{q}}^{\dagger} a_{-\mathbf{q}}^{\dagger} \right].$$

It describes the spin system in terms of circularly polarised plane waves (the first term), which interact with each other and deform in time (the

remaining terms).

I want to obtain the dispersion relation of independent, stable magnons. For this purpose, I diagonalise \mathcal{H}^{eff} by the Bogoliubov transformation from $a_{\mathbf{q}}, a_{\mathbf{q}}^\dagger$ to $b_{\mathbf{q}}, b_{\mathbf{q}}^\dagger$ operators (which describe independent excitation modes), keeping in mind that I deal with the system which breaks the space inversion symmetry (see Sec. 5.4). Because \mathcal{H}^{eff} in the above form mixes states with opposite wavevectors, I write the sum over \mathbf{q} in an explicitly symmetrised form:

$$\begin{aligned} \mathcal{H}^{\text{eff}} = \frac{1}{2} \sum_{\mathbf{q}} & \left[(\Xi - \chi_{\mathbf{q}}^{+-}) a_{\mathbf{q}}^\dagger a_{\mathbf{q}} + (\Xi - \chi_{-\mathbf{q}}^{+-}) a_{-\mathbf{q}}^\dagger a_{-\mathbf{q}} \right. \\ & \left. - \frac{1}{2} (\chi_{\mathbf{q}}^{++} + \chi_{-\mathbf{q}}^{++}) a_{\mathbf{q}} a_{-\mathbf{q}} - \frac{1}{2} (\chi_{\mathbf{q}}^{--} + \chi_{-\mathbf{q}}^{--}) a_{\mathbf{q}}^\dagger a_{-\mathbf{q}}^\dagger \right]. \end{aligned} \quad (9.1)$$

The Bogoliubov transformation is given by the formula

$$a_{\mathbf{q}} = u_{\mathbf{q}} b_{\mathbf{q}} + v_{\mathbf{q}} b_{-\mathbf{q}}^\dagger, \quad u_{\mathbf{q}}, v_{\mathbf{q}} \in \mathbb{C}, \quad (9.2)$$

with the conditions

$$1 = |u_{\mathbf{q}}|^2 - |v_{\mathbf{q}}|^2, \quad 0 = u_{\mathbf{q}} v_{-\mathbf{q}} - v_{\mathbf{q}} u_{-\mathbf{q}} \quad (9.3)$$

ensuring the preservation of canonical commutation relations (equivalently, the invertibility of this transformation). Inserting this into (9.1), I obtain (neglecting the lower-order terms and making use of the properties of χ 's)

$$\begin{aligned} \mathcal{H}^{\text{eff}} = \frac{1}{2} \sum_{\mathbf{q}} & \left[(\Xi - \chi_{\mathbf{q}}^{+-}) (|u_{\mathbf{q}}|^2 b_{\mathbf{q}}^\dagger b_{\mathbf{q}} + |v_{\mathbf{q}}|^2 b_{-\mathbf{q}}^\dagger b_{-\mathbf{q}} + u_{\mathbf{q}}^* v_{\mathbf{q}} b_{\mathbf{q}}^\dagger b_{-\mathbf{q}}^\dagger + u_{\mathbf{q}} v_{\mathbf{q}}^* b_{\mathbf{q}} b_{-\mathbf{q}}) \right. \\ & + (\Xi - \chi_{-\mathbf{q}}^{+-}) (|u_{-\mathbf{q}}|^2 b_{-\mathbf{q}}^\dagger b_{-\mathbf{q}} + |v_{-\mathbf{q}}|^2 b_{\mathbf{q}}^\dagger b_{\mathbf{q}} + u_{-\mathbf{q}}^* v_{-\mathbf{q}} b_{-\mathbf{q}}^\dagger b_{\mathbf{q}}^\dagger + u_{-\mathbf{q}} v_{-\mathbf{q}}^* b_{\mathbf{q}} b_{-\mathbf{q}}) \\ & - \chi_{\mathbf{q}}^{++} (u_{\mathbf{q}} u_{-\mathbf{q}} b_{\mathbf{q}} b_{-\mathbf{q}} + u_{\mathbf{q}} v_{-\mathbf{q}} b_{\mathbf{q}}^\dagger b_{\mathbf{q}} + v_{\mathbf{q}} u_{-\mathbf{q}} b_{-\mathbf{q}}^\dagger b_{-\mathbf{q}} + v_{\mathbf{q}} v_{-\mathbf{q}} b_{\mathbf{q}}^\dagger b_{-\mathbf{q}}^\dagger) \\ & \left. - (\chi_{\mathbf{q}}^{++})^* (u_{\mathbf{q}}^* u_{-\mathbf{q}}^* b_{\mathbf{q}}^\dagger b_{-\mathbf{q}}^\dagger + u_{\mathbf{q}}^* v_{-\mathbf{q}}^* b_{\mathbf{q}}^\dagger b_{\mathbf{q}} + v_{\mathbf{q}}^* u_{-\mathbf{q}}^* b_{-\mathbf{q}}^\dagger b_{-\mathbf{q}} + v_{\mathbf{q}}^* v_{-\mathbf{q}}^* b_{\mathbf{q}} b_{-\mathbf{q}}) \right], \end{aligned} \quad (9.4)$$

which leads to the following complex equation for each \mathbf{q} :

$$(\Xi - \chi_{\mathbf{q}}^{+-}) u_{\mathbf{q}} v_{\mathbf{q}}^* + (\Xi - \chi_{-\mathbf{q}}^{+-}) u_{-\mathbf{q}} v_{-\mathbf{q}}^* - \chi_{\mathbf{q}}^{++} u_{\mathbf{q}} u_{-\mathbf{q}} - (\chi_{\mathbf{q}}^{++})^* v_{\mathbf{q}}^* v_{-\mathbf{q}}^* = 0. \quad (9.5)$$

Since all equations for u 's and v 's are invariant under the reflection of \mathbf{q} , I assume that $u_{\mathbf{q}} = u_{-\mathbf{q}}$ and $v_{\mathbf{q}} = v_{-\mathbf{q}}$. The standard parametrisation for $u_{\mathbf{q}}, v_{\mathbf{q}}$ consistent with the first condition (9.3) reads

$$u_{\mathbf{q}} = e^{i\mu_{\mathbf{q}}} \cosh \theta_{\mathbf{q}}, \quad v_{\mathbf{q}} = e^{i\nu_{\mathbf{q}}} \sinh \theta_{\mathbf{q}}.$$

Inserting it into (9.5) gives

$$\begin{aligned} 0 &= (2\Xi - \chi_{\mathbf{q}}^{+-} - \chi_{-\mathbf{q}}^{+-}) \cosh \theta_{\mathbf{q}} \sinh \theta_{\mathbf{q}} e^{i(\mu_{\mathbf{q}} - \nu_{\mathbf{q}})} \\ &\quad - \chi_{\mathbf{q}}^{++} \cosh^2 \theta_{\mathbf{q}} e^{2i\mu_{\mathbf{q}}} - (\chi_{\mathbf{q}}^{++})^* \sinh^2 \theta_{\mathbf{q}} e^{-2i\nu_{\mathbf{q}}} \\ &= (2\Xi - \chi_{\mathbf{q}}^{+-} - \chi_{-\mathbf{q}}^{+-}) \cosh \theta_{\mathbf{q}} \sinh \theta_{\mathbf{q}} \\ &\quad - \chi_{\mathbf{q}}^{++} \cosh^2 \theta_{\mathbf{q}} e^{i(\mu_{\mathbf{q}} + \nu_{\mathbf{q}})} - (\chi_{\mathbf{q}}^{++})^* \sinh^2 \theta_{\mathbf{q}} e^{-i(\mu_{\mathbf{q}} + \nu_{\mathbf{q}})}. \end{aligned}$$

There is no equation for $\mu_{\mathbf{q}} - \nu_{\mathbf{q}}$, so I assume it is zero. I can replace $\mu_{\mathbf{q}}$ by another unknown, $\mu'_{\mathbf{q}}$, defined by

$$\chi_{\mathbf{q}}^{++} e^{2i\mu_{\mathbf{q}}} = |\chi_{\mathbf{q}}^{++}| e^{2i\mu'_{\mathbf{q}}} ,$$

resulting in

$$(2\Xi - \chi_{\mathbf{q}}^{+-} - \chi_{-\mathbf{q}}^{+-}) \cosh \theta_{\mathbf{q}} \sinh \theta_{\mathbf{q}} = |\chi_{\mathbf{q}}^{++}| \left(\cosh^2 \theta_{\mathbf{q}} e^{2i\mu'_{\mathbf{q}}} + \sinh^2 \theta_{\mathbf{q}} e^{-2i\mu'_{\mathbf{q}}} \right)$$

or

$$\begin{aligned} (2\Xi - \chi_{\mathbf{q}}^{+-} - \chi_{-\mathbf{q}}^{+-}) \cosh \theta_{\mathbf{q}} \sinh \theta_{\mathbf{q}} = \\ |\chi_{\mathbf{q}}^{++}| \left(\cosh^2 \theta_{\mathbf{q}} + \sinh^2 \theta_{\mathbf{q}} \right) \cos 2\mu'_{\mathbf{q}} + i \sin 2\mu'_{\mathbf{q}} , \end{aligned}$$

which requires $\mu'_{\mathbf{q}} = 0$, leading to the equation

$$(2\Xi - \chi_{\mathbf{q}}^{+-} - \chi_{-\mathbf{q}}^{+-}) \cosh \theta_{\mathbf{q}} \sinh \theta_{\mathbf{q}} = |\chi_{\mathbf{q}}^{++}| (\cosh^2 \theta_{\mathbf{q}} + \sinh^2 \theta_{\mathbf{q}}) ,$$

hence

$$2\theta_{\mathbf{q}} = \operatorname{arctanh} \frac{|\chi_{\mathbf{q}}^{++}|}{\Xi - \frac{1}{2}(\chi_{\mathbf{q}}^{+-} + \chi_{-\mathbf{q}}^{+-})} , \quad (9.6)$$

with the solution non-existent when $\left| \frac{|\chi_{\mathbf{q}}^{++}|}{\Xi - \frac{1}{2}(\chi_{\mathbf{q}}^{+-} + \chi_{-\mathbf{q}}^{+-})} \right| > 1$. This particular¹ solution will turn out to be sufficient for my needs, as numerical calculations give $|\chi_{\mathbf{q}}^{++}| \ll |\Xi - \frac{1}{2}(\chi_{\mathbf{q}}^{+-} + \chi_{-\mathbf{q}}^{+-})|$.

Gathering all terms multiplying $b_{\mathbf{q}}^{\dagger} b_{\mathbf{q}}$ in (9.4), I obtain

$$\begin{aligned} & \frac{1}{2} \left[(\Xi - \chi_{\mathbf{q}}^{+-}) |u_{\mathbf{q}}|^2 + (\Xi - \chi_{-\mathbf{q}}^{+-}) |v_{-\mathbf{q}}|^2 - \chi_{\mathbf{q}}^{++} u_{\mathbf{q}} v_{-\mathbf{q}} - (\chi_{\mathbf{q}}^{++})^* u_{\mathbf{q}}^* v_{-\mathbf{q}}^* \right] \\ &= \frac{1}{2} \left[(\Xi - \chi_{\mathbf{q}}^{+-}) \cosh^2 \theta_{\mathbf{q}} + (\Xi - \chi_{-\mathbf{q}}^{+-}) \sinh^2 \theta_{\mathbf{q}} - 2|\chi_{\mathbf{q}}^{++}| \cosh \theta_{\mathbf{q}} \sinh \theta_{\mathbf{q}} \right] \\ &= \frac{1}{2} \left[\left(\Xi - \frac{\chi_{\mathbf{q}}^{+-} + \chi_{-\mathbf{q}}^{+-}}{2} \right) \cosh 2\theta_{\mathbf{q}} - \frac{\chi_{\mathbf{q}}^{+-} - \chi_{-\mathbf{q}}^{+-}}{2} - |\chi_{\mathbf{q}}^{++}| \sinh 2\theta_{\mathbf{q}} \right] . \end{aligned}$$

Using (9.6) and assuming that $\Xi - \frac{\chi_{\mathbf{q}}^{+-} + \chi_{-\mathbf{q}}^{+-}}{2} > 0$ (which is the case for my numerical calculations), I obtain the final form of the effective Hamiltonian in the *spin-wave representation*:

$$\mathcal{H}^{\text{eff}} = - \sum_{\mathbf{q}} \omega_{\mathbf{q}} b_{\mathbf{q}}^{\dagger} b_{\mathbf{q}} , \quad (9.7)$$

¹Other solutions may exist which do not fulfil the assumption that $u_{\mathbf{q}} = u_{-\mathbf{q}}$ and $v_{\mathbf{q}} = v_{-\mathbf{q}}$. However, for a finite number of degrees of freedom the representation of canonical commutation relations is unique up to a unitary transformation, which guarantees the uniqueness of the obtained dispersion relation. In general, a set of creation and annihilation operators diagonalising \mathcal{H}^{eff} must exist, but it does not necessarily need to be obtainable via a transformation of the form (9.2).

where excitation modes are spin waves with dispersion²

$$\omega_{\mathbf{q}} = \frac{\chi_{-\mathbf{q}}^{+-} - \chi_{\mathbf{q}}^{+-}}{2} + \sqrt{\frac{(2\Xi - \chi_{\mathbf{q}}^{+-} - \chi_{-\mathbf{q}}^{+-})^2}{4} - |\chi_{\mathbf{q}}^{++}|^2}. \quad (9.8)$$

In the case of $\chi_{\mathbf{q}}^{+-} = \chi_{-\mathbf{q}}^{+-}$, fulfilled for the systems invariant under space inversion, the above formula simplifies to the solution by König *et al.* [43],

$$\omega_{\mathbf{q}} = \sqrt{(\Xi - \chi_{\mathbf{q}}^{+-})^2 - |\chi_{\mathbf{q}}^{++}|^2}.$$

Furthermore, neglecting the spin-orbit coupling, when $\chi^{++} = 0$, Bogoliubov transformation is unnecessary, and the effective Hamiltonian is already diagonalised by $a_{\mathbf{q}}$, $a_{\mathbf{q}}^{\dagger}$ operators.

Apart from spin waves, which are the eigenstates of the stationary Hamiltonian \mathcal{H}^{eff} , dynamic excitations of different physical origin may occur (e.g. Stoner spin-flips). They transfer a single carrier across the Fermi level to the state excited by the energy $\hbar\omega = E_{\mathbf{k}m} - E_{\mathbf{k}+\mathbf{q},m'}$ (see the denominator of Eq. (7.27), and may lead to the spin waves' damping. In the presence of the spin-orbit coupling, they are likely to appear at very low energetic cost throughout the whole \mathbf{q} -vector range. On the other hand, well below the Curie temperature, substitutional and thermal disorder are characterised by a short correlation length ξ , which ensures a well-defined spin-wave excitation spectrum for $q < 2\pi/\xi$.

Figure 9.1 presents a typical spin-wave dispersion spectrum $\omega_{\mathbf{q}}$ (9.8) in bulk (Ga,Mn)As calculated in the *spds** tight-binding computational scheme. The hole concentration p equals 0.65 nm^{-3} and the spin splitting $\Delta = -0.13 \text{ eV}$ is applied along the easy axis \tilde{z} fixed to the [001] direction by the biaxial strain $\epsilon_{xx} = -0.6\%$ (see Sec. 8.2). The latter causes a small anisotropy between $\omega_{\mathbf{q}}$ for spin waves propagating in the [001] direction and in the (001) plane. Furthermore, due to the lack of inversion symmetry in the unit cell geometry (Sec. 5.4), $\chi_{\mathbf{q}}^{+-} \neq \chi_{-\mathbf{q}}^{+-}$ in general. This means that, contrary to the results of the 6-band $k \cdot p$ model [43], $\omega_{\mathbf{q}}$ can be asymmetric with respect to the sign of \mathbf{q} or Δ (Fig. 9.1, inset). This effect was studied experimentally and theoretically in the context of dielectric susceptibility in another zincblende crystal, InSb [215].

Figure 9.2 presents the spin-wave dispersion spectrum $\omega_{\mathbf{q}}$ in (Ga,Mn)As thin layer for $p = 0.3 \text{ nm}^{-3}$ and $\Delta = -0.1 \text{ eV}$ along the easy axis [110], which can be determined numerically e.g. by searching for the maximum of the mean-field energy term Ξ (7.28). The host crystal consists of two unstrained infinite monolayers (Ga, As, Ga, As) grown in the typical [001] direction. The qualitatively new effect, related to the inversion asymmetry of the layer structure, is a shift of the dispersion minimum to a non-zero \mathbf{q}_{min} value. This interesting finding will be thoroughly analysed in Sec. 9.3.

²The negative sign of the Hamiltonian (9.7) is a consequence of using the electronic convention to describe the carrier-ion system.

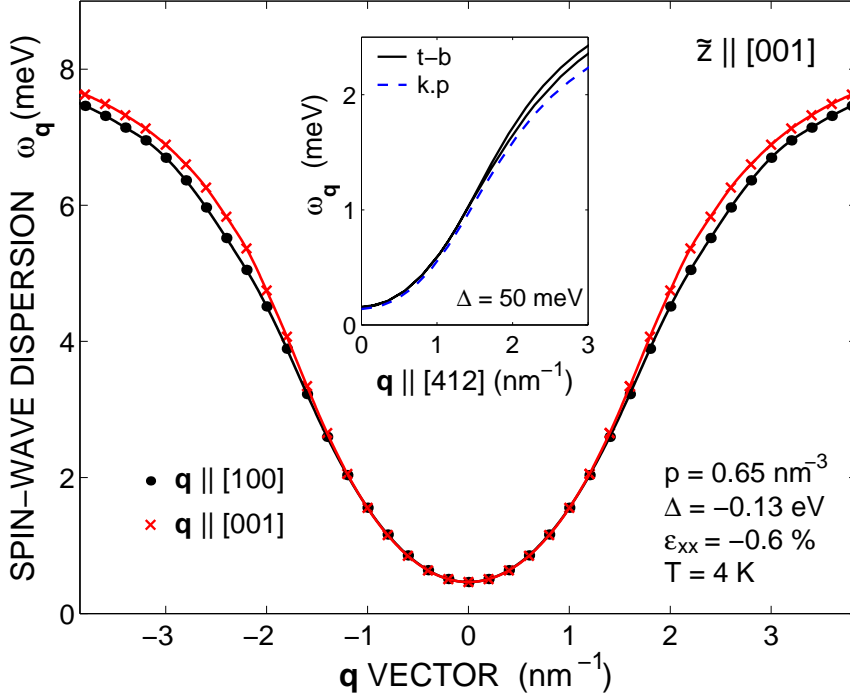


Figure 9.1: Dispersion dependence of spin waves propagating along [100] (equivalent to [010]) and [001] directions in bulk (Ga,Mn)As. Inset: the $\omega_{\mathbf{q}}$ asymmetry due to the bulk inversion asymmetry of GaAs lattice modelled by the *spds** tight-binding method, as compared to the 6-band *k* · *p* model preserving the symmetry. Lower and upper solid lines denote the [412] and the opposite $[4\bar{1}2]$ propagation direction.

According to the plots presented in Figs. 9.1 and 9.1, $\omega_{\mathbf{q}}$ for small \mathbf{q} -vectors can be described by the following general formula:

$$\omega_{\mathbf{q}} = D^{\mu\nu} q_{\mu} q_{\nu} - U^{\mu} q_{\mu} + \omega_0, \quad (9.9)$$

where indices $\mu, \nu = x, y, z$ denote spatial directions used in the Einstein sum convention. The \mathbf{D} and \mathbf{U} constants are, respectively, the spin-wave stiffness tensor and the Dzyaloshinskii–Moriya coefficient arising from the asymmetric exchange term (7.23) in the effective Hamiltonian (7.20). The ω_0 constant is the spin-wave gap created by magnetocrystalline anisotropies. The higher order terms arising from the bulk inversion asymmetry can be skipped as negligibly small for considered \mathbf{q} -vectors.

Alternatively, I can expand the \mathbf{q} -dependent terms in $\omega_{\mathbf{q}}$ given by the formula (9.8), considering their properties implied by Eq. (7.27), into

$$\chi_{\mathbf{q}}^{+-} \approx \frac{2g\mu_{\text{B}}}{M_s} (A^{\mu\nu} q_{\mu} q_{\nu} + \tilde{U}^{\mu} q_{\mu}) + \chi_{\mathbf{q}=0}^{+-} \quad (9.10)$$

and

$$\chi_{\mathbf{q}}^{++} \approx \frac{2g\mu_{\text{B}}}{M_s} T_{++}^{\mu\nu} q_{\mu} q_{\nu} + \chi_{\mathbf{q}=0}^{++}, \quad (9.11)$$

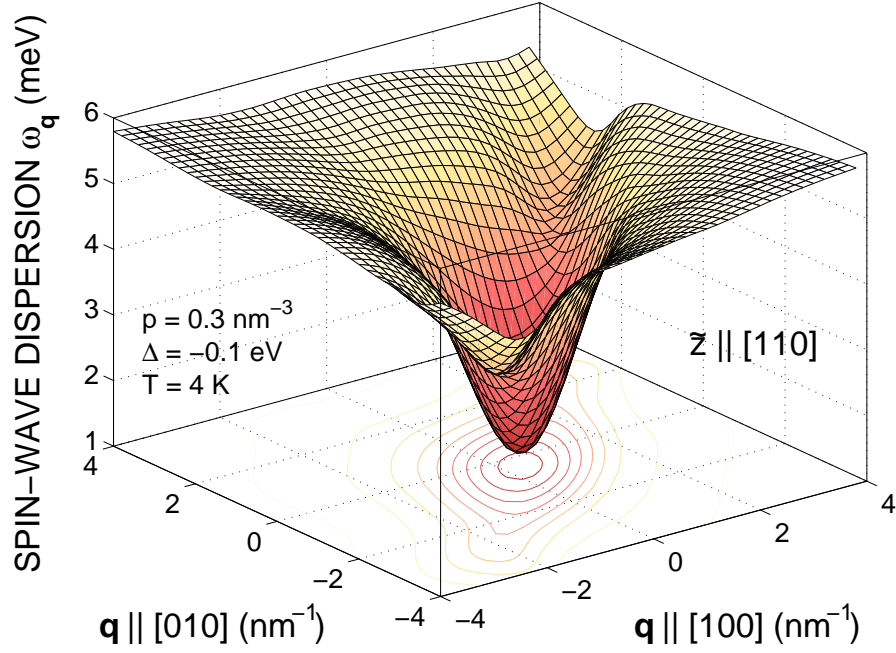


Figure 9.2: Dispersion dependence of spin waves in two (Ga,Mn)As monolayers. The minimum shift of in the $[1\bar{1}0]$ direction to $\mathbf{q}_{\text{min}} = (0.43, -0.43) \text{ nm}^{-1}$ can be observed (in the contour plot).

where $M_s = g\mu_B nS$ is the saturation magnetisation of the spin system. By inserting the above expansions back into the $\omega_{\mathbf{q}}$ formula (9.8), and comparing it to the $\omega_{\mathbf{q}}$ expansion (9.9), I obtain that, up to quadratic terms, the spin-wave stiffness depends only on the $\chi_{\mathbf{q}}^{+-}$ term. Hence,

$$\mathbf{D} = \frac{2g\mu_B}{M_s} \mathbf{A} , \quad (9.12)$$

while

$$\mathbf{U} = \frac{2g\mu_B}{M_s} \tilde{\mathbf{U}} .$$

The above constants are the subject of micromagnetics, which I will investigate in the next section. It ignores the quantum nature of the atomic matter and uses classical physics in the limit of a continuous medium.

9.2 Micromagnetic theory

The atomic-scale effects investigated in the previous section lead to the wave-like behaviour of the spin system. In micromagnetics, these spins are replaced by classical vectors with their slow-varying direction $\mathbf{n}(\mathbf{r})$ described

by the free energy functional:

$$E[\mathbf{n}(\mathbf{r})] = \int \left[\sum_{j=1}^{\infty} \mathcal{K}_j^\mu n_\mu^{2j} + \mathcal{A}_{\alpha\beta}^{\mu\nu} \partial_\mu n^\alpha \partial_\nu n^\beta + U^\mu \epsilon_{\alpha\beta} n^\alpha \partial_\mu n^\beta \right] d^3\mathbf{r}, \quad (9.13)$$

where indices $\mu, \nu = x, y, z$ and $\alpha, \beta = \tilde{x}, \tilde{y}$ denote spatial and magnetisation directions, respectively, and $\epsilon_{\alpha\beta}$ is the antisymmetric Levi-Civita symbol. The first term describes the anisotropy energy, which depends on the orientation of the magnetisation with respect to the easy axis \tilde{z} . Consecutive orders of the magnetocrystalline anisotropy tensor \mathcal{K} in principal-axis representation are numbered by j . The next term is the symmetric exchange energy, where \mathcal{A} is the exchange stiffness tensor, with $\mathcal{A}_{\alpha\beta}^{\mu\nu} = \mathcal{A}_{\beta\alpha}^{\nu\mu}$. The antisymmetric part of exchange is expressed by the last, Dzyaloshinskii–Moriya term. Since I describe the magnetisation fluctuations around the easy axis, I do not include the derivatives of $n^{\tilde{z}}$ in the sum, as they are of higher order.

The exchange stiffness \mathcal{A} can be split into two parts. The first one is isotropic in the magnetisation direction, but can bear the anisotropy of the exchange interaction in space (e.g. caused by biaxial strain),

$$A^{\mu\nu} = \frac{1}{2} (\mathcal{A}_{xx}^{\mu\nu} + \mathcal{A}_{yy}^{\mu\nu}) . \quad (9.14)$$

The remaining part is anisotropic with respect to the magnetisation direction,

$$T_{\alpha\beta}^{\mu\nu} = \mathcal{A}_{\alpha\beta}^{\mu\nu} - A^{\mu\nu} \delta_{\alpha\beta} . \quad (9.15)$$

I define indices $\sigma, \sigma' = +, -$, referring to corresponding spin components, so that $n^\pm = (n^{\tilde{x}} \pm i n^{\tilde{y}})/\sqrt{2}$ and $\mathcal{A}_{\alpha\beta}^{\mu\nu} \partial_\mu n^\alpha \partial_\nu n^\beta = \mathcal{A}_{\sigma\sigma'}^{\mu\nu} \partial_\mu n^\sigma \partial_\nu n^{\sigma'}$. It follows from the tensors' definitions that $(T_{++}^{\mu\nu})^* = T_{--}^{\mu\nu}$ and $T_{+-}^{\mu\nu} = 0$. I shall use the new notation to rewrite the exchange energy, including the Dzyaloshinskii–Moriya term, in the following form:

$$E_{\text{ex}} = \int \left[2A^\mu \partial_\mu n^+ \partial_\mu n^- + T_{\sigma\sigma'}^{\mu\nu} \partial_\mu n^\sigma \partial_\nu n^{\sigma'} + iU^\mu (n^+ \partial_\mu n^- - n^- \partial_\mu n^+) \right] d^3\mathbf{r} . \quad (9.16)$$

In analogy to the microscopic approach, I can transform the exchange energy functional to the reciprocal space,

$$E_{\text{ex}} = \frac{g\mu_B}{M_s} \sum_{\mathbf{q}} \left[\left(2A^\mu q_\mu^2 + \tilde{U}^\mu q_\mu \right) a(\mathbf{q})^\dagger a(\mathbf{q}) + T_{++}^{\mu\nu} q_\mu q_\nu a(\mathbf{q})^\dagger a(-\mathbf{q})^\dagger + T_{--}^{\mu\nu} q_\mu q_\nu a(\mathbf{q}) a(-\mathbf{q}) \right] . \quad (9.17)$$

I compare the above result to the effective Hamiltonian (7.26) in the interaction representation. It becomes clear that \mathbf{A} together with \mathbf{U} correspond to

the coefficients of the q -dependent terms in the $\chi_{\mathbf{q}}^{+-}$ expansion (9.10), while \mathbf{T} corresponds to the coefficient of the $\chi_{\mathbf{q}}^{++}$ expansion (9.11). Furthermore, I can identify the components of the above form with different physical mechanisms governing the spins' behaviour. The term involving \mathbf{A} describes the energy of a circularly polarised spin wave, as it arises from the isotropic part of exchange interaction. Hence, I shall call it the *isotropic* exchange stiffness tensor. The two terms involving \mathbf{T} account for the anisotropic exchange, as I have chosen in Eq. (9.15), induced by the spin-orbit coupling. Hence, I shall call it the *relativistic* exchange stiffness tensor. Its non-zero elements imply that the tilting of an individual spin from the easy axis \tilde{z} to different directions has different energetic cost. As a consequence, the polarisation of the spin wave deforms and acquires an elliptical shape. The linear term characterised by the $\tilde{\mathbf{U}}$ vector represents the minimum shift of the spin-wave dispersion, which has been observed in thin (Ga,Mn)As layers (Fig. 9.2), and can be associated with the asymmetric exchange of Dzyaloshinskii-Moriya (7.23). The energy ω_0 in Eq. (9.9) is related to the anisotropy constant \mathcal{K} in the full free energy functional (9.13).

In the next sections, I will calculate the above tensors for the bulk (Ga,Mn)As from Fig. 9.1 and two monolayers from Fig. 9.2.

9.3 Bulk (Ga,Mn)As

The dispersion spectrum of spin waves propagating in bulk (Ga,Mn)As along two main crystal axes, $[100] \parallel x$ (equivalent to $[010]$) and $[001] \parallel z$, is presented in Fig. 9.1. The simulated system is biaxially strained, $\epsilon_{xx} = -0.6\%$, with the hole concentration $p = 0.65 \text{ nm}^{-3}$ and spin splitting $\Delta = -0.13 \text{ eV}$ along the easy axis $\tilde{z} \parallel [001]$. To calculate the exchange stiffness tensors, I fit the coefficients of the $\chi_{\mathbf{q}}^{+-}$ and $\chi_{\mathbf{q}}^{++}$ expansions in Eqs. (9.10) and (9.11) on ca 1 nm^{-1} edge cube (or square) in \mathbf{q} -space, centred around zero. The obtained tensors describe the energy of spin waves polarised in the plane perpendicular to the easy axis \tilde{z} . If they propagate in this plane, I call them longitudinal waves. Transverse spin waves propagate along \tilde{z} .

The energy cost of exciting a circularly polarised wave is given by the exchange stiffness tensor

$$\mathbf{A} = \begin{pmatrix} 1.32 & 0 & 0 \\ 0 & 1.32 & 0 \\ 0 & 0 & 1.28 \end{pmatrix} \text{meV nm}^{-1}. \quad (9.18)$$

It is expressed by a diagonal form with eigenvectors pointing along crystal axes, as the magnetisation in the spins' ground state is uniform. The difference between its elements reflects the anisotropy of the exchange interaction in space (between the xy plane and the growth direction z) caused by the biaxial strain.

In the presence of the spin-orbit coupling, the circular polarisation can deform into an ellipse. This polarisation anisotropy is described by the relativistic \mathbf{T}_{++} tensor, which depends on the mutual orientation of magnetisation and spin-wave propagation directions. In the system discussed here, with the easy axis \tilde{z} along the spatial z direction, it takes the following form:

$$\mathbf{T}_{++} = \begin{pmatrix} 0.020 & -0.035 i & 0 \\ -0.035 i & -0.020 & 0 \\ 0 & 0 & 0 \end{pmatrix} \text{meV nm}^{-1}. \quad (9.19)$$

Its zero diagonal component means that the polarisation of transverse spin waves is circular, while the non-zero elements indicate that longitudinal spin waves have elliptical polarisation, with the shorter axis of the ellipse rotated to the \mathbf{q} direction. The resulting polarisations are illustrated in Fig. 9.3 (a).

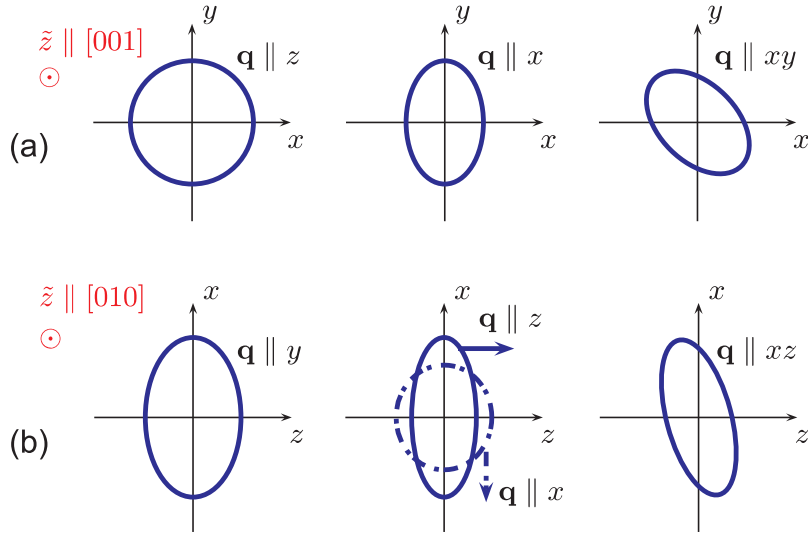


Figure 9.3: Spin-wave polarisation (exaggerated for clarity), namely a shape traced out in a fixed plane by the spin vector rotating around the magnetisation easy axis \tilde{z} , in (a) the bulk (Ga,Mn)As from Fig. 9.1 with $\tilde{z} \parallel [001]$ and (b) after changing \tilde{z} to $[010]$.

For an arbitrary propagation direction, the shape of the spin-wave polarisation can be calculated from the following polarisation matrix:

$$\mathbf{p} = \begin{pmatrix} p_{\tilde{x}\tilde{x}} & p_{\tilde{x}\tilde{y}} \\ p_{\tilde{y}\tilde{x}} & p_{\tilde{y}\tilde{y}} \end{pmatrix}, \quad (9.20)$$

where $p_{\alpha\beta} = \mathcal{A}_{\alpha\beta}^{\mu\nu} q_\mu q_\nu$, or in more detail

$$\begin{aligned} p_{\tilde{x}\tilde{x}} &= \mathbf{q} (\mathbf{A} + \Re \mathbf{e} \mathbf{T}_{++}) \mathbf{q}^T + \chi_0^{+-} + \Re \chi_0^{++} - \Xi , \\ p_{\tilde{y}\tilde{y}} &= \mathbf{q} (\mathbf{A} - \Re \mathbf{e} \mathbf{T}_{++}) \mathbf{q}^T + \chi_0^{+-} - \Re \chi_0^{++} - \Xi , \\ p_{\tilde{x}\tilde{y}} &= p_{\tilde{y}\tilde{x}} = -\Im \mathbf{m} \mathbf{q} \mathbf{T}^{++} \mathbf{q}^T - \Im \chi_0^{++} . \end{aligned}$$

The ellipse is the solution of the equation

$$n^\alpha n^\beta p_{\alpha\beta} = \text{const} ,$$

where n^α and n^β are the in-plane components of the magnetisation unit vector \mathbf{n} . The ratio of the lengths of its longer and shorter main axes, a and b , can be derived from the eigenvalues of the polarisation matrix (9.20) as

$$\frac{a}{b} = \sqrt{\frac{p_{\tilde{x}\tilde{x}} + p_{\tilde{y}\tilde{y}} + \sqrt{(p_{\tilde{x}\tilde{x}} - p_{\tilde{y}\tilde{y}})^2 + 4p_{\tilde{x}\tilde{y}}^2}}{p_{\tilde{x}\tilde{x}} + p_{\tilde{y}\tilde{y}} - \sqrt{(p_{\tilde{x}\tilde{x}} - p_{\tilde{y}\tilde{y}})^2 + 4p_{\tilde{x}\tilde{y}}^2}}} .$$

Kinetically, a longitudinal elliptical spin wave can be viewed as a circular one, which experiences the Lorentz contraction in the direction of motion, $b = a\sqrt{1 - v^2/c^2}$, travelling with the velocity v , where c is the speed of light. Figure 9.4 presents this *spin-wave relativistic velocity* in the relevant range of \mathbf{q} vectors along [100] and [110] directions.³

As already mentioned, \mathbf{T} is induced by the spin-orbit coupling, which connects the symmetries of the lattice with spins. Thus, similarly to magnetocrystalline anisotropies, it depends on the magnetisation direction with respect to the crystal axes. The \mathbf{T} tensor calculated in the analysed (Ga,Mn)As system with the easy axis \tilde{z} changed to the [010] direction would acquire the following form:

$$\mathbf{T}_{++} = \begin{pmatrix} -0.018 & 0 & 0.034 i \\ 0 & -0.033 & 0 \\ 0.034 i & 0 & 0.007 \end{pmatrix} \text{meV nm}^{-1} ,$$

which reveals its dependence on the biaxial strain. (An appropriate rearrangement of the matrix elements gives the \mathbf{T}_{++} tensor for \tilde{z} along [100].) Now the longitudinal spin waves propagate in the $\tilde{x}\tilde{y} \parallel (010)$ plane and experience the ‘‘Lorentz contraction’’ as described above, while the transverse waves propagate along the new easy axis \tilde{z} . Their polarisations are additionally deformed by the potential of the strained crystal. The latter

³This kinetic analogy does not mean that the velocity of the considered spin wave equals v . Rather, it says that the crystal environment creates the conditions equivalent to the situation in which the spin wave is accelerated to the velocity v , and experiences the Lorentz contraction. The analogy demonstrates the magnitude of relativistic effects in the considered systems.

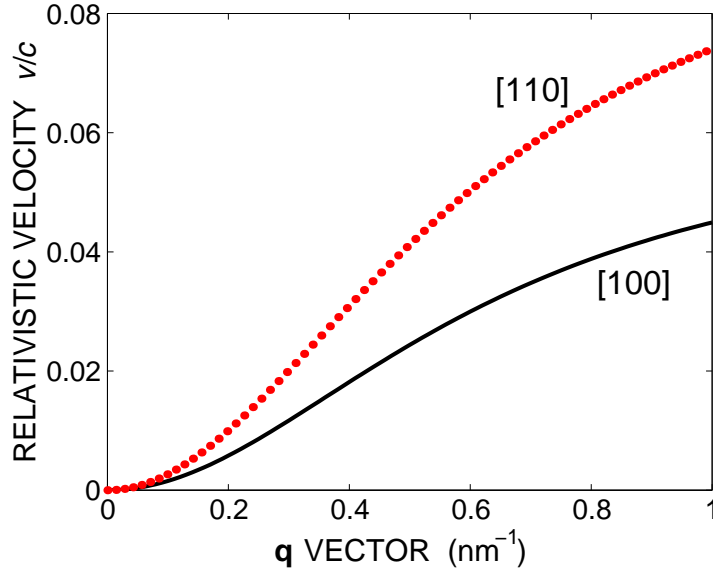


Figure 9.4: Relativistic velocity of spin waves propagating in two crystallographic directions: [110] (dotted line) and [100] (solid line), as a function of the \mathbf{q} -vector magnitude.

is stretched equally in the [100] and [010] directions and compressed in the [001] direction, and so are the polarisations. The magnitude of their deformations is given by the \mathbf{q} -independent terms of the polarisation matrix \mathbf{p} (9.20). Figure 9.3 (b) is illustrative of this effect.

Technically, the relativistic exchange might lead to macroscopic anisotropies in the system, if they did not average out for spin waves propagating in different directions. However, one can imagine a weak anisotropy arising from the described phenomena in asymmetrically shaped samples, where the largest number of similarly polarised modes can exist along the longest dimension. It would then be a possible explanation of the weak uniaxial anisotropy of the [100] and [010] crystal axes observed in some (Ga,Mn)As samples [216].

9.4 Thin (Ga,Mn)As layers

9.4.1 Cycloidal spin structure in (Ga,Mn)As layers

In thin layers of (Ga,Mn)As (Fig. 9.2), the minimum shift of the spin-wave dispersion to a non-zero \mathbf{q}_{\min} value can be observed, which was not present in bulk. It is a hallmark of the Dzyaloshinskii–Moriya asymmetric exchange (7.23), arising from structure inversion symmetry breaking. The mechanism of this interaction is demonstrated in my numerical simulations for the two monolayers of (Ga,Mn)As from Fig. 9.2. I calculate the exchange

stiffness tensors in a similar manner as in the previous section.

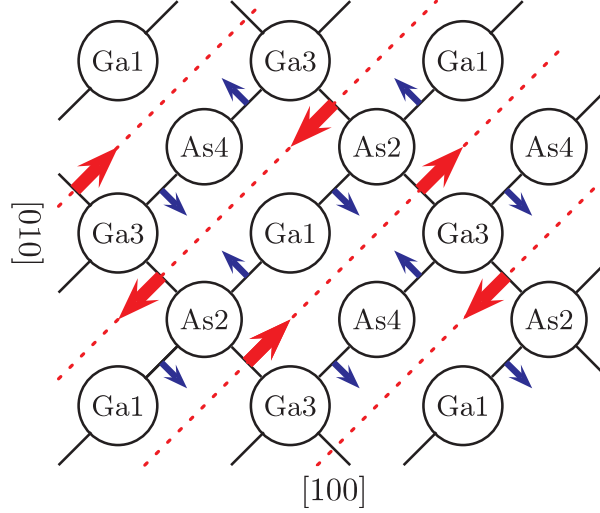


Figure 9.5: Two monolayers of GaAs. The Ga and As sites are numbered by their elevation in the growth direction $[001]$: 1's are situated at $(\cdot, \cdot, 0)$, 2 at $(\cdot, \cdot, \frac{1}{4}a)$, 3 at $(\cdot, \cdot, \frac{1}{2}a)$ and 4 at $(\cdot, \cdot, \frac{3}{4}a)$. The magnetic Mn ions are introduced within the virtual crystal and mean-field approximations, creating a uniform effective magnetic field. The strongest interactions between the nearest neighbours are marked by solid bonds. The created solid lines define mirror planes in the zincblende crystal, (110) and $(1\bar{1}0)$. Since the analysed structure has two-dimensional periodicity, the carrier momenta in the growth direction are quantised and spin waves propagate in-plane only. Red and blue arrows indicate the direction of the Dzyaloshinskii–Moriya vectors \mathbf{u}_{ij} .

The structure of the modelled lattice is shown in Fig. 9.5. Thanks to the lack of inversion symmetry at the midpoint of each Ga–As bond, the exchange interaction of Dzyaloshinskii–Moriya is allowed, $\mathbf{u}_{jj'} \cdot \mathbf{S}_j \times \mathbf{S}_{j'}$. According to Moriya's rules [196], the \mathbf{u}_{ij} vector of each atom pair, indicated by an arrow at each bond, is perpendicular to their mirror plane. Its sense is always the same when we go from Ga to As atom. Since in my theoretical approach, outlined in Sec. 9.1, I have used the Holstein-Primakoff transformation to describe spin waves as small fluctuations around the magnetisation direction \tilde{z} , only the $u_{jj'}^{\tilde{z}}$ terms contribute to the spin-wave dispersion relation. For the above reasons, I expect the maximum effect of the Dzyaloshinskii–Moriya interaction in systems magnetised along the \mathbf{u} vectors, i.e. perpendicular to $[110]$ or $[1\bar{1}0]$. First, I consider the magnetisation \tilde{z} set along the $[110]$ direction and a spin wave propagating perpendicular to it, $\mathbf{q} \parallel [1\bar{1}0]$. The dotted line is the wavefront, along which all spins must be in phase. Along this wavefront, the constant \mathbf{u} vector (big arrows) tilts the spins perpendicular to itself and to each other to minimise the energy of the Dzyaloshinskii–Moriya interaction. The $\mathbf{u}_{jj'}$ vector is a function of the

distance between the spins, $\mathbf{R}_j - \mathbf{R}_{j'}$. Hence, when we move from one spin pair to another in a regular lattice structure, their chirality $\mathbf{S}_j \times \mathbf{S}_{j'}$ minimising the energy is constant in magnitude and antiparallel to $\mathbf{u}_{jj'}$. Therefore, each spin will be rotated with respect to its neighbours by a constant angle around a constant axis. The rotation direction is parallel or antiparallel to the spin-wave propagation direction \mathbf{q} , depending on whether $\mathbf{u}_{jj'}$ is parallel or antiparallel to \hat{z} . In this way, a cycloidal structure with a period λ forms in the spin system. Since the modulation occurs along the $[\bar{1}\bar{1}0]$ direction, this is where I observe the dispersion minimum shift by $q_{\min} = 2\pi/\lambda$ (Fig. 9.2). For the magnetisation \hat{z} pointing along the $[\bar{1}\bar{1}0]$ direction, the \mathbf{u} vectors (small arrows) cancel out when looking along this direction, and no frustrated structure of lower energy can arise. Since the Dzyaloshinskii–Moriya interaction operates in the sample plane, neither shall we observe its hallmarks when \hat{z} is perpendicular to this plane.

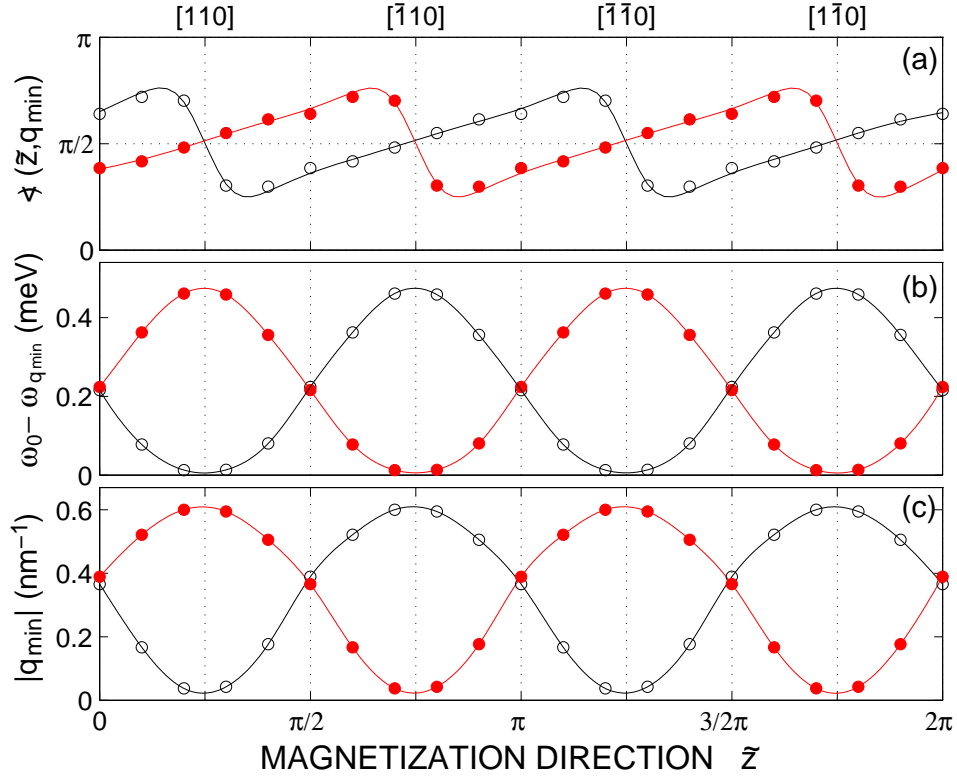


Figure 9.6: Parameters of the minimum shift \mathbf{q}_{\min} in two (Ga,Mn)As monolayers from Fig. 9.2 as a function of the magnetisation direction \hat{z} for the analysed system (full circles) and for its mirror-reflection (open circles). a) The direction of the \mathbf{q}_{\min} vector with respect to \hat{z} , b) energy gain $\omega_0 - \omega_{\mathbf{q}_{\min}}$, c) magnitude of the minimum shift \mathbf{q}_{\min} .

For the quantitative analysis of the described effects, I fit the spin-wave

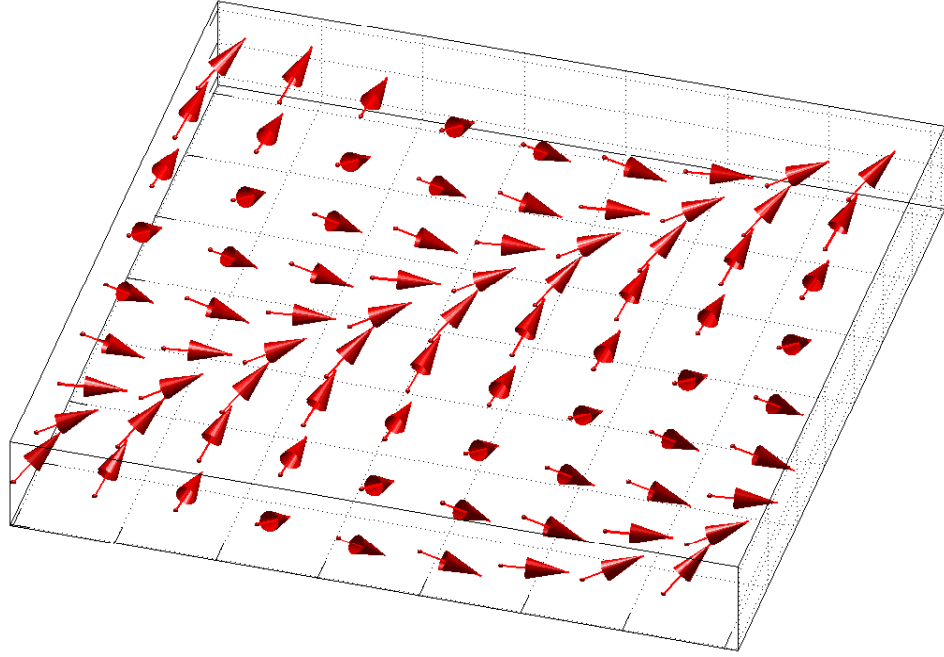


Figure 9.7: Cycloidal spin structure in the magnetisation ground state of the sample with the $[110]$ easy axis from Fig. 9.5.

dispersion presented in Fig. 9.2 with the form (9.9). In Fig. 9.6 (full circles) I sweep the magnetisation \tilde{z} in the sample plane (001) and report the obtained angle between \tilde{z} and \mathbf{q}_{\min} together with the energy gain $\omega_0 - \omega_{\mathbf{q}_{\min}}$ due to the Dzyaloshinskii–Moriya interaction, and the magnitude of \mathbf{q}_{\min} . From simple algebra I have $\mathbf{q}_{\min} = -\frac{1}{2}\mathbf{D}^{-1}\mathbf{U}$ and $\omega_0 - \omega_{\mathbf{q}_{\min}} = \mathbf{q}_{\min}^T \mathbf{D} \mathbf{q}_{\min}$. As expected, the energy gain is the largest when \tilde{z} and \mathbf{q}_{\min} are perpendicular to each other, for $\tilde{z} \parallel [110]$, and drops to zero for $\tilde{z} \parallel [1\bar{1}0]$ (Fig. 9.6 a,b). The first arrangement is accompanied by the strongest frustration of the spin system, $q_{\min} = 0.6 \text{ nm}^{-1}$ (Fig. 9.6 c), resulting in the spin cycloid with period $\lambda = 10 \text{ nm}$. In the other arrangement, no spin frustration arises and the collinear spin order is preserved. This behaviour accounts for an in-plane anisotropy with the easy and hard axes along the $[110]$ and $[1\bar{1}0]$ directions, respectively. It is easy to notice that if we mirror-reflect the sample (or equivalently, move the bottom Ga1 layer to the top Ga5 position), the two axes switch— $[110]$ will become the hard axis and $[1\bar{1}0]$ the easy axis (Fig. 9.6, open circles). Consequently, the sign of \mathbf{q}_{\min} and the orientation of the spin cycloid will change.

In the above reasoning, it is important to remember that we deal with the hole-mediated ferromagnetism. While the magnetic lattice ions substitute only Ga sites and would seem oblivious to the inversion asymmetry

of the Ga–As pairs, the carriers interact with all surrounding atoms. As a consequence, the system of magnetic ions coupled by the sp – d exchange is sensitive to all symmetry properties of the crystal.

The cycloidal spin structure in the magnetisation ground state of the sample with the $[110]$ easy axis from Fig. 9.5 is presented in Fig. 9.7. The described anisotropy arises from the net Dzyaloshinskii–Moriya interaction. Although it is a surface effect, it should not be confused with the surface anisotropy, which does not occur in the zincblende (001) surface—the $[110]$ and $[\bar{1}\bar{1}0]$ crystallographic directions I am interested in are equivalent here. Thus, a similar cycloidal spin structure observed on the surface of layers of manganese on a tungsten (110) substrate [217], where the Dzyaloshinskii–Moriya interaction stems from the anisotropy of the $[100]$ and $[\bar{1}\bar{1}0]$ directions, is of a *different* nature than the effect reported here.

On the other hand, the termination of the lattice at the surface (or internal interfaces) leads to pinning effects, which can strongly influence the behaviour of the spin system. Such effects and their consequences for the FMR spectra in multilayer heterostructures were investigated by Professor Henryk Puzskarski *et al.* (e.g. [218] and references therein). They pointed out that in addition to the bulk spin-wave modes, there can exist surface “acoustic” and “optic” modes. These can also lead to spin frustration, as I will demonstrate with the numerical simulation based on the mentioned theory.

The system is divided in layers numbered with indices $l = 0, \dots, L - 1$, the values 0 and $L - 1$ corresponding respectively to the bottom and top sample surfaces. Localised spins interact with an effective field $\mathbf{H}_l^{\text{eff}}$, in this case associated with strong magnetocrystalline anisotropies, and with their neighbours via the exchange interaction characterised by a constant J . The Hamiltonian reads

$$\mathcal{H} = -2 \sum_{(l,j;l+g,j')} J \hat{\mathbf{S}}_{l,j} \cdot \hat{\mathbf{S}}_{l+g,j'} - g\mu_B \sum_{l,j} \mathbf{H}_l^{\text{eff}} \cdot \hat{\mathbf{S}}_{l+g,j} \quad (9.21)$$

I assume that the spin is quantised along the direction of the magnetic field, and is homogeneous across every layer due to the minimisation of the exchange interaction and the influence of the effective field. A surface anisotropy field K^{surf} responsible for the pinning effects acts on the external surfaces. Hence, for $L = 1, \dots, L - 2$ we have $\mathbf{H}_l^{\text{eff}} = \mathbf{H}^{\text{eff}}$, while for $l = 0, L - 1$ we have $\mathbf{H}_l^{\text{eff}} = \mathbf{H}^{\text{eff}} + \mathbf{K}^{\text{surf}}$.

In two dimensions, the system geometry can be parametrised using an angle ϕ , as in Fig. 9.8. In this coordinates,

$$\mathbf{S}_l = S[\cos \phi_l, \sin \phi_l], \quad \mathbf{H}^{\text{eff}} = [H_x^{\text{eff}}, H_y^{\text{eff}}], \quad \mathbf{K}_k^{\text{surf}} = [K_{k,x}^{\text{surf}}, K_{k,y}^{\text{surf}}].$$

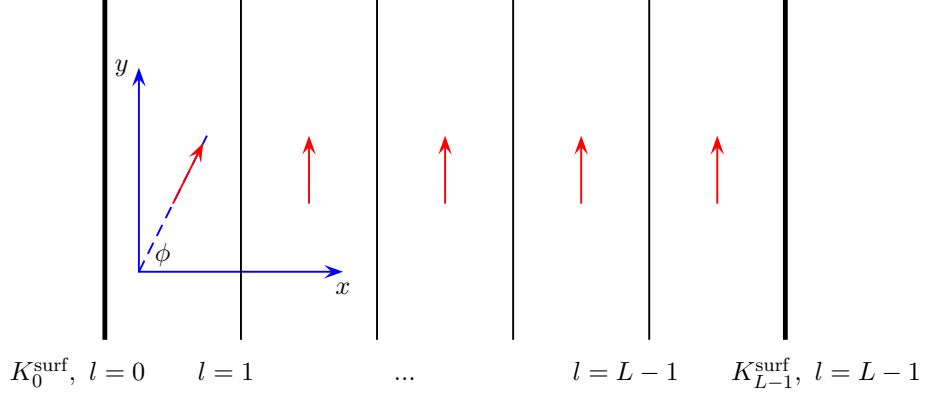


Figure 9.8: Parametrisation of a spin in a layer.

I can thus write the mean energy of Hamiltonian (9.21),

$$E[\{\mathbf{S}_l\}] = -2J \sum_{l=1}^{L-1} \mathbf{S}_{l-1} \cdot \mathbf{S}_l - \sum_{l=0}^{L-1} \mathbf{S}_l \cdot \left(\mathbf{H}^{\text{eff}} + \delta_{l,0} \mathbf{K}_0^{\text{surf}} + \delta_{l,L-1} \mathbf{K}_1^{\text{surf}} \right) ,$$

as

$$\begin{aligned} E[\{\phi_l\}] &= -2JS^2 \sum_{l=1}^{L-1} (\cos \phi_{l-1} \cos \phi_l + \sin \phi_{l-1} \sin \phi_l) \\ &\quad - S \sum_{l=0}^{L-1} \left(H_x^{\text{eff}} \cos \phi_l + H_y^{\text{eff}} \sin \phi_l \right) + S \left(K_{0,x}^{\text{surf}} \cos \phi_0 + K_{0,y}^{\text{surf}} \sin \phi_0 \right) \\ &\quad + S \left(K_{L-1,x}^{\text{surf}} \cos \phi_{L-1} + K_{L-1,y}^{\text{surf}} \sin \phi_{L-1} \right) . \end{aligned}$$

I minimise the functional $E[\{\phi_l\}]$ using a genetic algorithms program [219] for given J , \mathbf{H}^{eff} , $\mathbf{K}_0^{\text{surf}}$ and $\mathbf{K}_{L-1}^{\text{surf}}$ (the initial values of $\{\phi_l\}$ angles have been selected randomly). Figure 9.9 presents the outcome of my simulations for three different situations. As one would expect, spins coupled by the exchange mechanism are uniformly polarised along a random direction, while switching the effective anisotropy field fixes this direction to its easy axis. This situation can be associated with Fig. 9.9 (1). Things become interesting when the surface anisotropy on the outer layers is involved. Then, the system achieves equilibrium spreading the spins into fans throughout the thickness of the sample, as illustrated in Fig. 9.9 (2,3).

In the presence of the Dzyaloshinskii-Moriya interaction, the described spin pinning on the surface would be locally determined by the cycloidal spin structure, and thus probably lead to an extremely complicated, inextricable resonance spectrum.

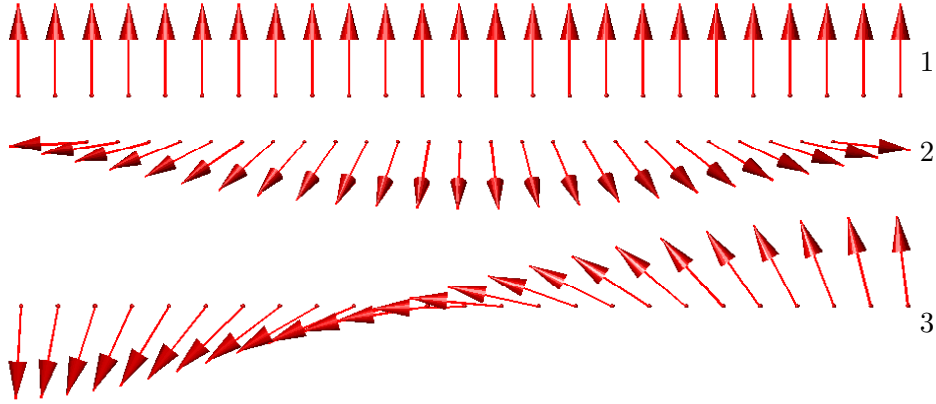


Figure 9.9: Ground-state spin structures in thin layers: 1. collinear spin order in the absence of the surface anisotropy; fan-like spin arrangements: 2. with top and bottom surface anisotropy vectors perpendicular to the layer, pointing in opposite directions, and 3. with surface anisotropy vectors parallel to the layer, pointing in opposite directions. For anisotropy vectors in the same direction the fan-like structure vanishes.

9.4.2 Stiffness tensors in layers

As I have shown in the previous section, the Dzyaloshinskii–Moriya interaction in thin (Ga,Mn)As layers leads to the frustration of spins in the ground state. While in bulk (Ga,Mn)As the diagonal form of tensor \mathbf{A} (9.18) depicts the uniform ground state magnetisation, the exchange stiffness tensors in thin layers reveal a spin cycloid oriented along one of the mirror planes:

$$\mathbf{A} = \begin{pmatrix} 0.93 & -0.28 \\ -0.28 & 0.93 \end{pmatrix} \text{meV nm}^{-1},$$

$$\mathbf{T} = \begin{pmatrix} 0.09 - 0.01i & 0.05 + 0.005i \\ 0.05 + 0.005i & 0.09 + 0.006i \end{pmatrix} \text{meV nm}^{-1}.$$

Their eigenvectors point along the highest symmetry axes, $[110]$ and $[1\bar{1}0]$. This effect is equivalent to applying strain along one of these directions, which would account for a magnetoelastic anisotropy, like the one in biaxially strained samples. However, contrary to the case of a uniformly strained sample, all effects related to the Dzyaloshinskii–Moriya interaction vanish in the bulk limit.

The \mathbf{A} , \mathbf{T} and \mathbf{U} constants let us think of the magnetic system in terms of the interactions by which it is governed, as described by the Hamiltonian (7.26) in the interaction representation. Alternatively, if we want to deal with independent stationary magnons (with already deformed polarisation), represented by the Hamiltonian (9.7), we calculate the spin-wave stiffness \mathbf{D} , related to \mathbf{A} by the formula (9.12). The difference between these

two pictures is especially apparent at finite temperatures, where the length of the magnetisation vector, $M(T)$, decreases and Eq. (9.12) becomes

$$\mathbf{D}(T) = \frac{2g\mu_B}{M(T)} \mathbf{A}(T) . \quad (9.22)$$

The higher the temperature, the stronger we have to tilt the magnetisation vector in order to excite the quantum of spin waves (a magnon). Hence, $\mathbf{A}(T)$ decreases with temperature faster than $\mathbf{D}(T)$.

9.5 Normalised spin-wave stiffness

This section discusses the relation between the spin-wave stiffness and the Curie temperature, based on which the normalised spin-wave stiffness parameter D_{nor} can be defined. Depending only weakly on the hole density p and spin splitting Δ , it makes a convenient tool for experimentalists to estimate the spin-wave stiffness values D given the Curie temperature and the magnetisation of the sample. I provide quantitative numerical results on D_{nor} for bulk (Ga,Mn)As obtained in the *spds** tight-binding computational scheme (see Sec. I), and compare them to the outcome of the previously employed 6-band $k \cdot p$ model [43]. I also clarify that the surprisingly large magnitude of D in these systems results from the p -like character of the periodic part of Bloch function.

The standard relation between the spin-wave stiffness D and the Curie temperature T_C in a cubic crystal, which is often used in the literature on the topic, reads

$$D = \frac{k_B T_C r_{\text{nn}}^2}{2(S+1)} , \quad (9.23)$$

where r_{nn} is the nearest neighbour distance [107]. Derived for short-range interactions, it is interesting to find out how it is modified when considering the actual nature of the spin-spin exchange. This question has a number of implications. For instance, both carrier relaxation time, which is limited by magnon scattering, and the quantitative accuracy of the mean-field approximation grow with D/T_C , as the density of spin waves at given temperature T diminishes when D increases. It is worth noting that a simple adaption of this formula to (Ga,Mn)As by replacing r_{nn} with $(xN_0)^{-1/3}$ resulted in an overestimation of the p - d exchange integral by an order of magnitude [211].

Allowing for spatially modulated structures, the magnetic ordering temperature T_C for a carrier-controlled ferromagnet is given by a solution of the mean-field equation [65, 220],

$$\beta^2 \chi(\mathbf{q}, T) \chi_S(\mathbf{q}, T) = 1 , \quad (9.24)$$

where χ and χ_S are the carrier and lattice ion spin susceptibilities. In the simple case of a parabolic band they are proportional to the Pauli and Curie-Weiss magnetic susceptibilities, respectively.

First, I consider the two-band model of carriers residing in a simple parabolic band, where all that is left of the \mathcal{A} tensor of Eq. (9.13) is the scalar isotropic exchange stiffness A . According to the previous section, it is related to the quadratic coefficient of the expansion $\chi(q) \approx \chi_0 + nS\beta^2 C q^2$, by $D = nS\beta^2 C = 2A/nS$. Additionally, I assume that the ground state of the system corresponds to the uniform ferromagnetic ordering, $\mathbf{q} = 0$, and take $\chi_S(\mathbf{q}, T)$ in the Curie form,

$$\chi_S(\mathbf{q}, T) = \frac{nS(S+1)}{3k_B T}. \quad (9.25)$$

Using Eqs. (9.24) and (9.25), I obtain

$$D = \frac{3k_B T_C C(T \rightarrow 0)}{(S+1)\chi(0, T = T_C)}.$$

If the values of both spin splitting Δ at $T \rightarrow 0$ and $k_B T_C$ are much smaller than the Fermi energy E_F , the carrier susceptibility is given by

$$\chi(q) = \frac{1}{4}\rho(E_F) F\left(\frac{q}{2k_F}\right). \quad (9.26)$$

The total density of states at $E_F = \hbar^2 k_F^2 / (2m^*)$ is $\rho(E_F) = m^* k_F / (\pi \hbar)^2$ and

$$\begin{aligned} F\left(\frac{q}{2k_F}\right) &= \frac{1}{2} + \frac{k_F}{2q} \left(1 - \frac{q^2}{4k_F^2}\right) \log \left| \frac{2k_F + q}{2k_F - q} \right| \\ &= 1 - \frac{q^2}{12k_F^2} - O\left(\frac{q^4}{k_F^4}\right) \end{aligned} \quad (9.27)$$

is the Lindhard function. I obtain from these equations

$$D = \frac{k_B T_C}{4(S+1)k_F^2}. \quad (9.28)$$

We see that, in agreement with the notion that magnetic stiffness increases with the range of the spin-spin interaction, r_{nn} in Eq. (9.23) is replaced by $1/(k_F \sqrt{2})$ in Eq. (9.28), which scales with the range of the carrier-mediated interactions. Indeed, according to the RKKY theory [42], the magnitude of the ferromagnetic exchange integral decays at small spin-spin distances r as $1/(rk_F)$ and reaches the first zero at $r \approx 2.2/k_F$.

Since in semiconductors $1/k_F \gg a_0$, the above formulae imply that D/T_C is rather large in systems with carrier-controlled ferromagnetism. A question arises as to how the ratio D/T_C would be modified, if the complexities of the valence band were taken into account.

As already noticed by König *et al.* [43], the values of exchange stiffness for (Ga,Mn)As are greater in the 6-band model with a spin-orbit coupling than in the case of a simple parabolic band. As argued by these authors,

due to the multiplicity of the valence bands, the Fermi level for a given carrier concentration is much lower than in the two-band model, and hence both carrier polarisation and exchange stiffness are greater [43]. On the other hand, Brey and Gómez-Santos [206] assign large values of D to higher magnitudes of T_C in the multi-band model.

To check these suggestions I plot in Fig. 9.10 the values of dimensionless parameter

$$D_{\text{nor}} = \frac{4(S+1)k_F^2 D}{k_B T_C},$$

for various hole concentrations p and $k_F = (3\pi^2 p)^{1/3}$. The ratio D/T_C for

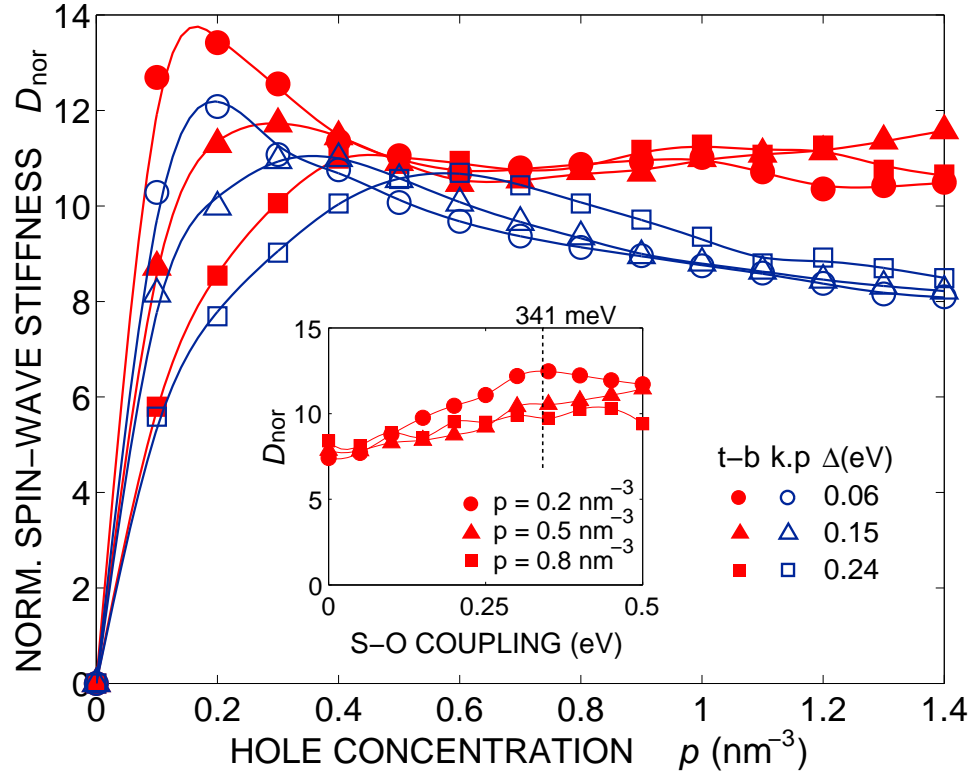


Figure 9.10: Normalised spin-wave stiffness D_{nor} in bulk (Ga,Mn)As as a function of the hole concentration p and the spin-orbit coupling (inset; the observed value of the spin-orbit coupling is indicated by dotted line) for different spin splittings Δ . Filled and empty markers indicate the results of the $spds^*$ tight-binding and the 6-band $k \cdot p$ model, respectively.

bulk (Ga,Mn)As is computed using the $spds^*$ tight-binding (Sec. 6.2) and the previously employed [43] 6-band $k \cdot p$ model of the semiconductor band structure. Guided by the results of the two band model, one could expect $D_{\text{nor}} \lesssim 1$ in the limit of small spin polarisations, $\Delta \ll |E_F|$. In contrast to these expectations, D_{nor} is of the order of 11 and, moreover, weakly depen-

dent on the polarisation, altered here by changing the hole concentration and the spin-orbit splitting. Furthermore, the experimentally observed biaxial strain magnitudes have only slight effect on the stiffness tensor (see Fig. 9.1 and Eq. (9.18) [43]. This indicates that the single parameter D_{nor} can serve to estimate the magnitudes of D and A if only the Mn magnetisation M and hole concentration p are known.

Knowing that neither the spin-orbit coupling nor the multiplicity of carrier bands can explain the large spin-wave stiffness, I turn my attention to the matrix elements $\langle u_{\mathbf{k}m} | \hat{s}^\sigma | u_{\mathbf{k}+\mathbf{q},m'} \rangle$ in the spin susceptibility of holes (7.27). Neglecting the spin-orbit coupling, $u_{\mathbf{k}m}$ is a product of the spin part s_m and the real spatial part $w_{\mathbf{k}m}$. Thus, I can write

$$\langle u_{\mathbf{k}m} | \hat{s}^\sigma | u_{\mathbf{k}+\mathbf{q},m'} \rangle = \pm \frac{1}{\sqrt{2}} (1 - \langle s_m | s_{m'} \rangle) \langle w_{\mathbf{k}m} | w_{\mathbf{k}+\mathbf{q},m'} \rangle$$

for $\sigma = +, -$. In the parabolic two-band model with its carrier wavefunctions described by plane waves $\psi_{\mathbf{k}m}(\mathbf{r}) = s_m e^{i\mathbf{k}\cdot\mathbf{r}}$, the periodic part $u_{\mathbf{k}m} = s_m$. Hence $\langle s_m | s_{m'} \rangle = \delta_{mm'}$ and $w_{\mathbf{k}m} = 1$, and $F(\mathbf{q}) = \chi(\mathbf{q})/\chi(0)$ simplifies to the Lindhard function (9.27). More realistic models take into account the periodic lattice potential, which mixes different atomic orbitals and leads to the \mathbf{k} -dependent modulation of $u_{\mathbf{k}m}$. (The eventual composition of hole states in the *spds** tight-binding model is presented in Fig. 9.11 a–c.)

9.6 Spin waves' contribution to magnetisation

In this section, I address the problem of the applicability of the mean-field approximation, analysed in Sec. 8.1, to the description of temperature dependence of magnetisation in the investigated systems. It is a known fact that the critical fluctuations in the presence of long-range exchange interactions leads to the same Curie temperature as the mean-field models [187]. On the other hand, several papers [44, 221, 222] discuss how spin waves can change the magnetisation vs. temperature dependence and the Curie transition point. König *et al.* [44] proposed a self-consistent method for calculating this effect and provided analytical results within the 4-band $k \cdot p$ method. However, the model is based on crude approximations (incorrect constraint on the number of spin waves in each mode, $\leq 2S$, put to increase the numerical efficiency) and phenomenological assumptions (the spin-wave spectrum is independent of the q -vector). I propose a self-consistent model which takes into account the correct number of spin-wave excitations and, additionally, thermal depolarisation of spins. However, I argue that spin waves do not lower the mean-field T_C due to thermal decoherence of quantum spin system.

The mean-field approximation employed in the presented model allows for a reasonable overall description of ferromagnetism in the analysed sys-

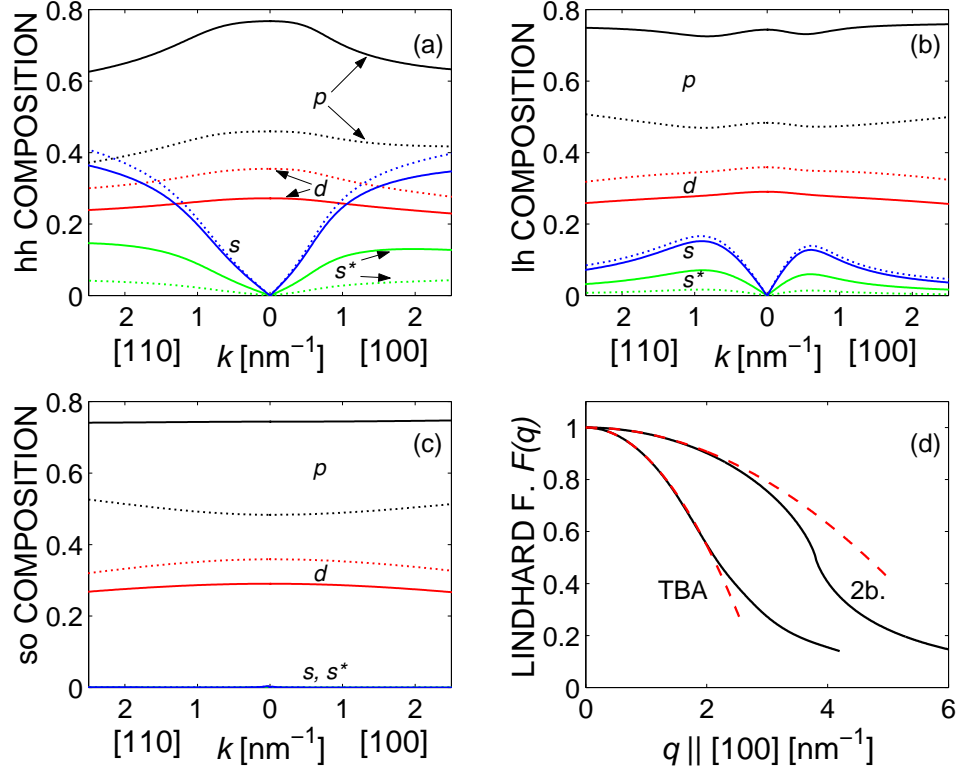


Figure 9.11: Atomic composition of heavy, light and spin-orbit split-off hole bands (a, b and c panels) as a function of the k -vector. It is given by the norms of projections of the carrier state on atomic s , p , d or s^* orbitals of As or Ga atoms (solid and dotted lines). Panel d presents the Lindhard function $F(q)$ calculated in the tight-binding model ($p = 0.65 \text{ nm}^{-3}$ and $\Delta = -0.13 \text{ eV}$, with the spin-orbit coupling set to zero) and in the parabolic band model with the same Fermi energy $E_F = -0.27 \text{ eV}$. Dashed lines are their square form fits.

tems. It reduces the problem of lattice spins coupled by the exchange interaction to that of noninteracting spins in the molecular field Ξ (7.28). Their magnetisation is described by the self-consistent equation (8.1).

As already mentioned, the Brillouin function B_S ignores the actual nature of thermal fluctuations and their correlations, and assumes that every spin fluctuates independently, which in my theory corresponds to the high- q limit of spin-wave excitations (see Fig. 9.1). At low temperatures, however, the long-wavelength magnons of much lower energies can exist. Since each of them carries a magnetic moment μ_B , they yield a strong contribution to the temperature dependence of magnetisation [107, 223],

$$M(T) = M(0) \left(1 - (NS)^{-1} \sum_{\mathbf{q}} \langle n_{\mathbf{q}} \rangle_T \right), \quad (9.29)$$

where $\langle n_{\mathbf{q}} \rangle_T$ is the thermal average of spin-wave excitations in each mode.

The latter can be modelled by the Bose-Einstein distribution, $\langle n_{\mathbf{q}} \rangle_T = 1/(\exp(\omega_{\mathbf{q}}/k_B T) - 1)$, as spin waves are bosons. Then, replacing the summation in Eq. (9.29) by an integral and putting $\omega_{\mathbf{q}} \approx Dq^2$, one obtains the well known $T^{3/2}$ Bloch law [198]

$$\int d\mathbf{q} \langle n_{\mathbf{q}} \rangle_T = \zeta_{3/2} \pi^{3/2} \left(\frac{k_B T}{D} \right)^{3/2}, \quad (9.30)$$

where $\zeta_{3/2} \approx 2.612$ is the Riemann zeta function.

Remembering about the spin-wave gap created by magnetic anisotropy, which allows for ferromagnetism in low dimensional systems despite the Mermin–Wagner theorem [224], I have $\omega_{\mathbf{q}} \approx \omega_0 + Dq^2$. (We neglect the Dzyaloshinskii-Moriya coefficient, which vanishes in bulk limit.) In that case, the above law is modified to

$$\int d\mathbf{q} \langle n_{\mathbf{q}} \rangle_T = \text{Li}_{3/2}(e^{-\omega_0/k_B T}) \pi^{3/2} \left(\frac{k_B T}{D} \right)^{3/2}, \quad (9.31)$$

where $\text{Li}_{3/2}(e^{-\omega_0/k_B T})$ is de Jonqui ere’s function. A similar formula was used to investigate $M(T)$ in amorphous alloys [225].

Furthermore, the Bose-Einstein statistics allows for the unlimited number of spin waves in each mode (as already mentioned, K onig *et al.* [43] assume that there can be only $2S$ spin waves of each \mathbf{q} , which is too strict). In fact, their total number cannot be larger than $2NS$, corresponding to complete magnetisation reversal. I handle this by introducing a fictious mode with zero energy, which is “occupied” by the spin waves which have not been excited in reality. In this way I can treat the problem with classic Bose-Einstein condensate methods [191]: the total number of bosons occupying all modes is always $2NS$, their zero-energy mode constitutes the “condensate” phase, while the excited spin waves constitute the “thermal cloud”. The total number of spin waves in the limit of infinite crystal volume is therefore given by

$$\min \left(\sum_{\mathbf{q} \leq \mathbf{q}_D} \frac{e^{-\omega_{\mathbf{q}}/k_B T}}{1 - e^{-\omega_{\mathbf{q}}/k_B T}}, 2NS \right).$$

Additionally, while at zero temperature the system is described by a pure state Ψ_0 , where exciting a spin wave costs the energy

$$\omega_{\mathbf{q}}^0 = \langle b_{\mathbf{q}}^\dagger \Psi_0 | \mathcal{H}^{\text{eff}} | b_{\mathbf{q}}^\dagger \Psi_0 \rangle - \langle \Psi_0 | \mathcal{H}^{\text{eff}} | \Psi_0 \rangle,$$

at non-zero temperatures it is described by a mixture of pure states Ψ_n with a certain number of spins flipped by one-particle thermal excitations, $\sum_n p_n |\Psi_n\rangle \langle \Psi_n|$. Thus, its magnetisation drops to $M(T)$ according to the

mean-field Brillouin function (8.1). The energy cost of exciting a spin wave is now given by

$$\omega_{\mathbf{q}}^T = \sum_n p_n \left[\langle b_{\mathbf{q}}^\dagger \Psi_n | \mathcal{H}^{\text{eff}} | b_{\mathbf{q}}^\dagger \Psi_n \rangle - \langle \Psi_n | \mathcal{H}^{\text{eff}} | \Psi_n \rangle \right] .$$

Since the spin-wave dispersion $\omega_{\mathbf{q}}$ (9.8) depends on temperature T almost exclusively via the spin splitting Δ and is approximately proportional to it, I can estimate the above expression by

$$\omega_{\mathbf{q}}^0 \sum_n p_n \frac{M_n}{M(0)} = \omega_{\mathbf{q}}^0 \frac{M(T)}{M(0)} = \omega_{\mathbf{q}}^0 \frac{\Delta(T)}{\Delta(0)} ,$$

where M_n is the magnetisation in the state Ψ_n . Spin waves are thus perturbations of the thermal state of lattice spins and not of the ground state, which I can model just by replacing $M(0)$ with $M(T)$ (or Δ with $\Delta(T)$) in the dispersion relation $\omega_{\mathbf{q}}$. They additionally lower the magnetisation to $M'(T)$. Remaining in the limit of small oscillation approximation, I obtain the following set of equations:

$$\begin{aligned} M(T) &= M(0) B_S \left(\frac{S \Xi(\Delta'(T))}{k_B T} \right) , \\ M'(T) &= M(T) \\ &\quad - \min \left(\frac{M(0)}{NS} \sum_{\mathbf{q} \leq \mathbf{q}_D} \frac{e^{\xi_{\mathbf{q}}}}{1 - e^{\xi_{\mathbf{q}}}}, 2M(T) \right) , \end{aligned} \tag{9.32}$$

where $\xi_{\mathbf{q}} = -\omega_{\mathbf{q}}(\Delta(T), T)/k_B T$. The spin splitting $\Delta(T)$ is induced by the mean field of the lattice spins described by the first equation, while $\Delta'(T)$ additionally takes into account their depolarisation due to spin waves.

Figure 9.12 presents the temperature dependence of magnetisation as described by the above methods for the bulk (Ga,Mn)As from Fig. 9.1. The $T^{3/2}$ Bloch law and its modified version apply to low temperatures only. It can be seen that the values of D determined neglecting the anisotropy gap would be overestimated. The “spin-wave condensate” includes the magnon contribution to magnetisation in the whole temperature range, and leads to significantly lower Curie temperature than in the mean-field model. This method uses the correct bound for the number of spin-wave excitations. It also naively attempts to solve the problem of the well-known shortcomings of the spin-wave theory [226] introduced by the Holstein-Primakoff transformation (7.24), as it includes thermal disorder by depolarising the lattice spins with temperature. However, quantum-mechanical intuition suggests that the spin waves should vanish completely at higher temperatures. Non-zero temperature leads to the loss of information about the system: pure states are replaced by mixed states, namely the thermal states $e^{-\beta H} / \text{Tr } e^{-\beta H}$, and

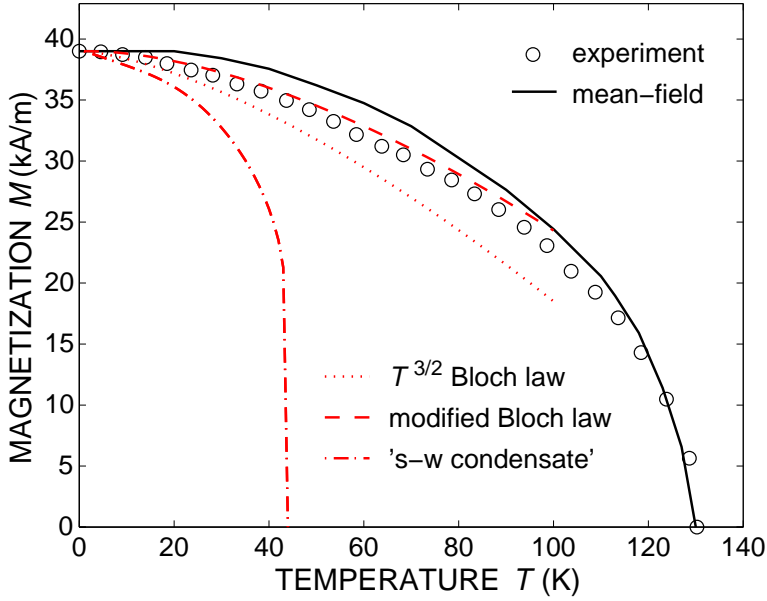


Figure 9.12: Temperature dependence of magnetisation for bulk (Ga,Mn)As from Fig. 9.1, calculated within the mean-field model (8.1), $T^{3/2}$ Bloch law (9.29) and its modified version (9.31), and the “spin-wave condensate” (9.32). The experimental dependence for the sample from Ref. [199] is analysed in Sec. 9.7.

the quantum correlation of spins vanishes. This can be reflected in the p - d Hamiltonian by replacing $\beta \sum_{i,j} \mathbf{s}_i \cdot \mathbf{S}_j$ with $\beta \sum_{i,j} \langle s_i^z \rangle \langle S_j^z \rangle = \Xi \sum_j \langle S_j^z \rangle$, which is simply the mean-field model. Similarly, in the vicinity of the Curie transition, where the problem of critical fluctuations arises, the mean-field models of systems with long-range exchange interactions are known to work very well [187].

The next section provides further insight into the applicability of the presented models by comparing their results to experiment.

9.7 Comparison to experiment

Gourdon *et al.* [199] carried out a detailed analysis of the magnetic domain structure and magnetic properties of an annealed $\text{Ga}_{0.93}\text{Mn}_{0.07}\text{As}$ layer of 50 nm thickness with a perpendicular magnetic easy axis and the Curie temperature of 130 K. Two employed experimental methods yielded an upper and lower limit of the isotropic exchange stiffness A as a function of temperature T . As found by these authors from examining the domain-wall velocity, the higher values of $A(T)$, determined from the lamellar domain width, are reliable.

I model the sample in the tight-binding computational scheme for bulk (Ga,Mn)As (see Sec. 6.2). In order to determine the material param-

ters for numerical simulations, I start by estimating the effective Mn content x_{eff} from the measured low-temperature spontaneous magnetisation $M(T \rightarrow 0) = 39 \text{ kA/m}$. Taking into account the hole contribution, $M_c \approx -5 \text{ kA/m}$ [227], implies the magnetisation of the Mn spins $M_s = 44 \text{ kA/m}$. This value corresponds to the effective Mn content $x_{\text{eff}} = 4.3\%$ and the spin splitting $\Delta = -0.13 \text{ eV}$. No direct measurements of the hole concentration are available for this sample, so I estimate its magnitude from the effective and total Mn content, x_{eff} and $x = 7\%$. Assuming that interstitial Mn donors had survived the annealing process and formed antiferromagnetic pairs with the substitutional Mn acceptors [228, 229], I obtain $p = (3x_{\text{eff}}/2 - x/2)N_0 = 0.65 \text{ nm}^{-3}$ [230].

From Fig. 9.10, for the given value of p and Δ , I find $D_{\text{nor}} \approx 10.5$, which gives the spin-wave stiffness $D = 1.1 \text{ meV nm}^2$ ($A = 0.21 \text{ pJ/m}$) at $T \rightarrow 0 \text{ K}$. Knowing this, I can calculate the temperature dependence of magnetisation according to Sec. 9.6 (Fig. 9.12). In the mean-field picture (solid lines), the magnetisation of lattice spins M_s is described by the Brillouin function (8.1). The magnitude of hole magnetisation $|M_c|$ decreases with temperature proportionally to M_s , according to Eq. (7.28). The resulting magnetisation $M(T)$ is compared to the experimental curve (circles). I obtain a good agreement with the measured data, especially near the Curie transition, and $T_C = 127 \text{ K}$. At low temperatures, I plot the outcomes of the $T^{3/2}$ Bloch law (9.30) and its modified version (9.31) employing the calculated spin-wave stiffness value D (dotted lines). The modified Bloch law, adjusted to include the spin-wave gap, gives very good agreement with the experimental dependence, which indicates that in this regime the spin-wave excitations are solely responsible for demagnetisation. Near the Curie transition, I reconstruct the measured Curie temperature and magnetisation values with the Brillouin function, which suggests that the temperature destroys the spin-wave coherence and recalls the mean-field picture.

To reconstruct the $A(T)$ trend obtained from the magnitudes of lamellar domain width [199], I again make use of the fact that the susceptibility $\chi_{\mathbf{q}}^{+-}$ (7.27) depends on temperature almost exclusively via spin splitting. Thus, and according to the formula (9.22), the exchange stiffness scales with temperature as $\Delta(T)^2$ [208]. I use the experimentally determined $M(T)$ and the calculated $A(T \rightarrow 0) = 0.21 \text{ pJ/m}$ to estimate the exchange stiffness values for the remaining temperatures as $A(T) = A(0)M(T)/M(0)$. As shown in Fig. 9.13, this procedure correctly reproduces the experimental $A(T)$ trend. However, the same value of $A(T \rightarrow 0)$, which has been shown to successfully describe the experimental $M(T)$ dependence with the modified Bloch law, is twice as large as the exchange stiffness constant determined from the measured lamellar domain width.

The same group of researchers investigated the $(\text{Ga,Mn})\text{As}_{1-y}\text{P}_y$ layers, where a few percent of As sites was substituted by phosphorus [231]. This helped them to realise the high quality (with low number of compensational

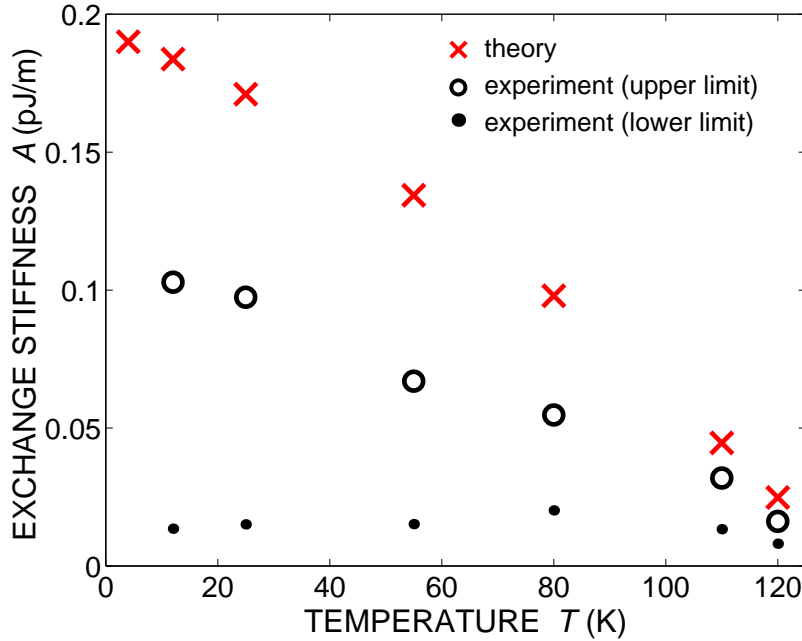


Figure 9.13: Theoretical reconstruction of experimental data on exchange stiffness A as a function of temperature T obtained in Ref. [199] from the analysis of the lamellar domain width in $\text{Ga}_{0.93}\text{Mn}_{0.07}\text{As}$.

defects and regular crystalline structure) samples grown on a GaAs buffer with the out-of-plane easy axis orientation. I reconstruct their results for a $\text{Ga}_{0.896}\text{Mn}_{0.104}\text{As}_{0.93}\text{P}_{0.07}$ sample. According to the measured saturation magnetisation $M_s = 53.5 \text{ kA/m}$; assuming that the hole contribution lowers this value by ca 10%, I estimate the spin-splitting $\Delta = 0.17 \text{ eV}$. This gives the hole concentration $p = 0.5 \text{ nm}^{-3}$ for the measured value of $T_C = 159 \text{ K}$. In a similar way as for the sample in Fig. 9.13 I calculate $A(T)$. The very good agreement of the theory with experimental results, presented in Fig. 9.14, shows that the main obstacle in modeling stiffness constant in related materials arises from the presence of interstitial and antisite defects.

Potashnik *et al.* [210] evaluated the isotropic exchange constant J for the set of optimally annealed (Ga,Mn)As layers with varying Mn content. The values derived from the temperature dependence of magnetisation, using the standard Bloch law, and from the Curie temperature within the three-dimensional Heisenberg model [198], were similar.

The theoretical reconstruction of the experiment by the $spds^*$ tight-binding model of bulk (Ga,Mn)As is demonstrated in Fig. 9.15. To obtain the presented results, I have estimated the effective Mn content x_{eff} from the measured low-temperature magnetisation $M(T \rightarrow 0)$, and then increased it by about 10% to include the hole contribution [227]. Assuming that annealing removed all interstitials and each remaining substitutional Mn produces

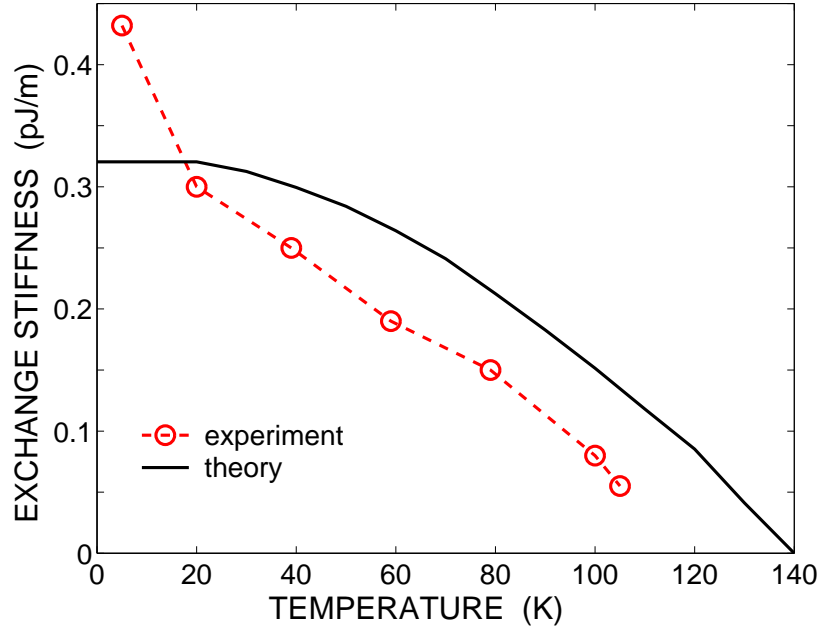


Figure 9.14: Theoretical reconstruction of experimental data on exchange stiffness A as a function of temperature T obtained in Ref. [231] from the analysis of the lamellar domain width in $(\text{Ga,Mn})\text{As}_{1-y}\text{P}_y$.

one hole carrier, the hole density $p = x_{\text{eff}} N_0$. For the obtained values of p and x_{eff} I have calculated the mean-field Curie temperatures T_C and the exchange constant $J = D(x_{\text{eff}} N_0)^{2/3}/2S$ assuming that Mn ions form a cubic lattice. It should be noted that this form is equivalent up to a few percent to that employed in Ref. [210]: $J = D(4\pi x N_0/24)^{2/3}/2S$, where x is the total Mn content.⁴ Since for the samples with low Mn content the theoretical values of T_C are much lower than the experimental ones, I conclude that the corresponding estimates of J (indicated by empty circles) are not reliable. In this regime of low Mn and hole concentrations a polaron model might (Sec. 4.2.6) a priori be considered to better describe the ferromagnetic state. On the other hand, I reconstruct the Curie temperatures for samples with $x_{\text{eff}} > 2.5\%$ (filled circles), but this time the theoretical values of J are much smaller than the experimental ones. This discrepancy points to the importance of the anisotropy-induced energy gap in the spin-wave spectrum. As illustrated in Fig. 9.15 (inset) for the sample with $x_{\text{eff}} = 3.3\%$, fitting the experimental $M(T)$ curves with the standard Bloch law neglecting the gap leads to higher values of J than those expected theoretically. At the same time, the modified Bloch law (9.31) employing the theoretical exchange constant $J = 0.12 \text{ meV nm}^2$ reconstructs the analysed $M(T)$ trend. It should

⁴N. Samarth, private communication.

be noticed that it perfectly describes the mild slope of the low-temperature $M(T)$, contrary to the standard Bloch law [210]. Similarly to the case of the Gourdon *et al.* experiment [199], the mean-field model works very well at higher temperatures.

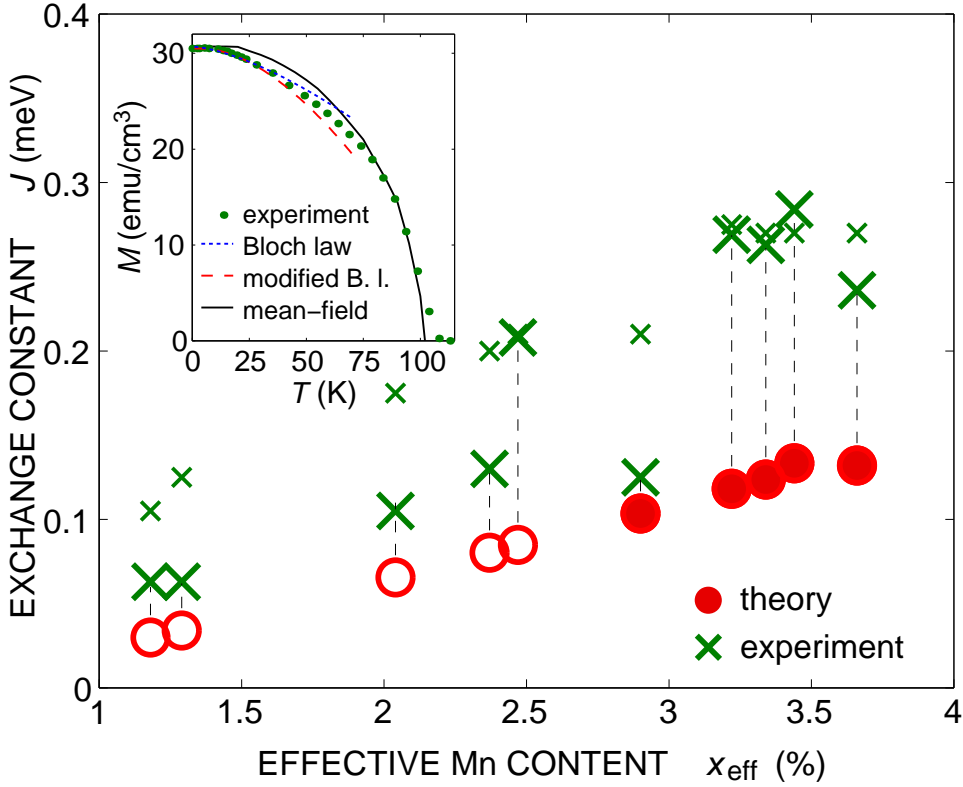


Figure 9.15: Theoretical reconstruction of experimental data on exchange constant J for samples with varying effective Mn content x_{eff} , as determined from the temperature dependence of magnetisation using the $T^{3/2}$ Bloch law (large crosses) and from the Curie temperature (small crosses) in Ref. [210]. Empty circles indicate the region where the experimental T_C exceeds the theoretical predictions. Inset: experimental temperature dependence of magnetisation for the sample with $x_{\text{eff}} = 3.3\%$ fit by the standard Bloch law with $J = 0.26$ meV (Ref. [210]), the modified Bloch law (9.31) with the theoretically obtained $J = 0.12$ meV and by the mean-field Brillouin function.

In a series of experiments, the spin-wave stiffness was determined by examining spin precession modes excited by optical pulses [211] and under ferromagnetic resonance conditions [212–214]. According to these works, the experimental findings are strongly affected by gradients of magnetic anisotropy, presumably associated with carrier depletion at the surface and interface, which also affect the character of spin pinning. I also note that no influence of the magnetic field on the hole spins, visible as a deviation of the Landé factor from the value $g = 2$ [227], was taken into account in

the employed Landau-Lifshitz equations. With these reservations I show in Fig. 9.16 the experimentally evaluated values of D plotted as a function of the nominal Mn concentration x for various as-grown and annealed samples of $\text{Ga}_{1-x}\text{Mn}_x\text{As}$. These findings are compared to the results of *ab initio* computations [209] (dashed line) and my theory for the hole concentration $p = xN_0$ and $p = 0.3xN_0$ (solid lines). When comparing theoretical and experimental results, one should take into account that the actual Mn concentration x_{eff} is smaller than x , particularly in as-grown samples. As seen, the presented theory describes properly the order of magnitude of the spin-wave stiffness D but cannot account for a rather large dispersion in the experimental data.

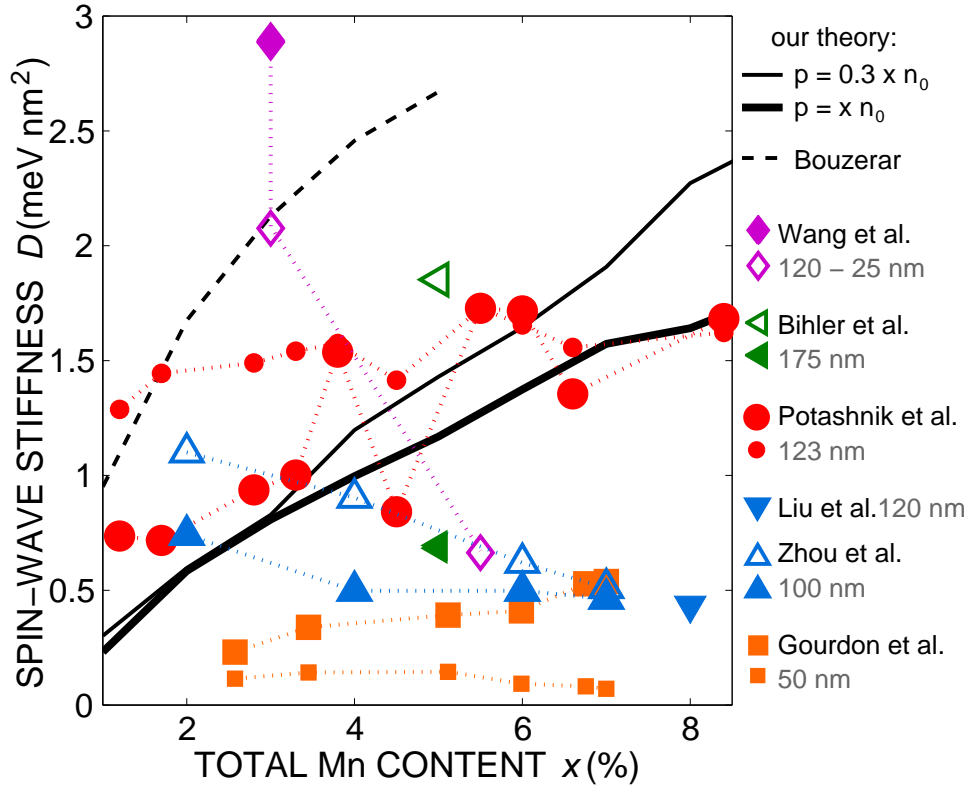


Figure 9.16: Compilation of theoretical results (lines), obtained with no adjustable parameters, and experimental data (markers) on the spin-wave stiffness D as a function of the nominal Mn concentration x in $\text{Ga}_{1-x}\text{Mn}_x\text{As}$. Solid symbols denote annealed as well as etched and hydrogenated samples (Ref. [214]). Empty symbols denote as-grown samples. The value $g = 2$ was used to convert D in magnetic units (T nm^2) to energy units (meV nm^2).

In thin (Ga,Mn)As layers, described in Sec. 9.4, the Dzyaloshinskii–Moriya interaction can be observed in form of a spin-wave dispersion minimum shift. It leads to the formation of a cycloidal spin structure and

uniaxial in-plane anisotropy of the $[110]$ and $[1\bar{1}0]$ directions, with the easy axis determined by the sample geometry. Both these phenomena have been a subject of considerable interest in recent years [126, 204, 232–234]. While the long-period spin structures have not been hitherto observed, the uniaxial anisotropy is commonly present in $(\text{Ga},\text{Mn})\text{As}$ [92, 230]. However, it was shown by gradual etching [126] or by investigating different samples [234] to be insensitive to the layer thickness. This is not the case for the anisotropy caused by the Dzyaloshinskii–Moriya interaction, which is a surface effect and vanishes with increasing layer thickness. To test my predictions of the cycloidal spin structure, one should pick very thin high-quality samples grown in the $[001]$ direction, which additionally excludes the anisotropy of the surface, with the easy axis along one of the in-plane diagonal directions. It could be then observed e.g. under a magnetic force microscope or by neutron scattering. The sample should be probed along the $[110]$ and $[1\bar{1}0]$ directions to find the long-period modulation of magnetisation only along the one perpendicular to the easy axis.

9.8 Summary

I have investigated spin waves and exchange stiffness in thin layers and bulk crystals of ferromagnetic $(\text{Ga},\text{Mn})\text{As}$ described by the *spds** tight-binding computational scheme. The results of this model remain in very good agreement with the 6-band $k \cdot p$ approach. Using the proposed variation-perturbational calculus, I have described the analysed systems and their spin-wave excitations. Their properties have been expressed by the phenomenological parameters of micromagnetic theory. The strength of ferromagnetic order described by the isotropic exchange stiffness has been found to be significantly amplified by the p -like character of carrier wavefunctions, as compared to the simple parabolic band model. Furthermore, I have encountered various effects reflecting the tendency of the spin-orbit interaction to pervade every aspect of carrier dynamics. They produce the relativistic corrections to spin-waves given by the anisotropic exchange stiffness tensor and the asymmetric Dzyaloshinskii–Moriya coefficient. The latter accounts for the cycloidal spin arrangement and the accompanying uniaxial in-plane anisotropy of diagonal ($[110]/[1\bar{1}0]$) directions in thin layers, which can result in a surface-like anisotropy in thicker films. Quantitative results on the stiffness constant have been provided in form of a normalised parameter, which assumes the value $D_{\text{nor}} \approx 11$ over a wide range of Mn and hole concentrations in $(\text{Ga},\text{Mn})\text{As}$. They agree with the previous $k \cdot p$ calculations [43, 206] but predict significantly smaller values of spin-wave stiffness than those resulting from *ab initio* computations [209].

The above theories have been applied to analyse the related experimental data on the stiffness parameter and the temperature dependence of mag-

netisation. The basic theoretical model has not managed to reconstruct all stiffness values obtained by various experimental methods. On the other hand, in all cases I have reconstructed the entire range of magnetisation dependence on temperature. At low temperatures, it can be understood within the the modified Bloch law employing the values of spin-wave stiffness calculated by my model. At higher temperatures, the mean-field theory becomes justifiable owing to thermal decoherence and the long-range character of spin-spin interactions. At the same time, I have reproduced only partially the stiffness values obtained from analysing precession modes in (Ga,Mn)As thin films. The presented results may allow to separate bulk and surface effects, as well as bring to light the pinning phenomena and the role of inhomogeneities in experiments examining precession modes in slabs of carrier-controlled ferromagnetic semiconductors.

Until now I have been investigating the phenomena related to the magnetic properties of dilute magnetic semiconductors, like the behaviour of magnetization with temperature, magnetocrystalline anisotropies, Curie temperature and spin waves. In all cases I have noticed no significant differences between their values calculated using the discussed computational schemes. As it has been already explained, this stems from the fact that these phenomena are governed by the physics of the six p -type carrier bands from the vicinity of the Γ point, which are described similarly well by all the models. For this reason, I call them the *static* properties. In the next chapter I will turn to the transport properties of (Ga,Mn)As and show that their nature goes beyond the current picture. They will be called the *dynamic* properties.

Chapter 10

Anomalous Hall effect in ferromagnetic (Ga,Mn)As

The anomalous Hall effect was first observed in ferromagnets by Edwin Hall himself [235, 236]. In 1879, he made the momentous discovery that, when a conductor with a current is placed in a magnetic field, the Lorentz force acting on the electrons directs them towards one side of the conductor. This was followed next year by the observation that the “pressing electricity” effect, as Hall called it, was ten times larger in ferromagnetic iron, thus earning itself the name of the anomalous Hall effect. The first discovery provided a simple and elegant tool to measure carrier concentration in non-magnetic semiconductors. For this role, the ordinary Hall effect was often considered one of the most important solid-state transport experiments [237]. The dependence of its stronger cousin on the material properties of a ferromagnetic conductor is more complex, and after a century still remains a challenge for the theoreticians and experimentalists alike. One of the reasons the AHE has been such a hard nut to crack is that, at its core, it involves concepts from topology and geometry that have been formulated only in recent times, such as the Berry phase [238] and topological defects. On the other hand, many theoretical constructions which had previously been considered relevant mainly in high-energy physics, such as non-commuting coordinates and magnetic monopoles, became measurable in experiments on the anomalous Hall effect [45, 239–241]. Recently, the interest in AHE has been revived by the development of dilute magnetic semiconductors, in which this effect is hoped to bring about the means of spin-polarised current control and magnetisation characterisation.

In non-magnetic conductors, the Hall resistivity ρ_{xy} increases linearly with applied magnetic field H_z , as expected from the Lorentz force. In ferromagnets, however, ρ_{xy} first grows steeply with weak H_z , but later saturates at a value which is nearly independent of H_z . In Fe, Co and Ni this value has been observed to be roughly proportional to the magnetisation

M_z [242] and has a weak anisotropy with respect to the orientation of the magnetisation direction, corresponding to the weak magnetic anisotropy of these elements [243]. A short time thereafter, an empirical relation between ρ_{xy} , H_z and M_z

$$\rho_{xy} = R_0 H_z + R_a M_z , \quad (10.1)$$

applicable over a wide range of external magnetic fields, has been established experimentally [244, 245]. The second term represents the AHE. Unlike R_0 , which is inversely proportional to the carrier density n , R_a depends subtly on material-specific parameters, in particular on the longitudinal resistivity $\rho_{xx} \equiv \rho$. It is generally assumed that the relation between ρ_{xy} and ρ is of the power law form,

$$\rho_{xy} \sim \rho^\gamma , \quad (10.2)$$

with γ between 1 and 2, depending on the mechanism governing the AHE.

In 1954, Karplus and Luttinger proposed a theory for the AHE which later turned out to be a crucial step in understanding this problem [246]. They showed that when an external electric field is applied to a crystal, the electrons' group velocity acquires an additional term (called "Karplus–Luttinger anomalous velocity") perpendicular to the electric field, which can therefore contribute to Hall effects. In a ferromagnetic conductor, the sum of the anomalous velocity over all occupied bands can be non-zero, and thus modify the measured Hall conductivity σ_{xy} . Because this contribution to σ_{xy} originates exclusively from the band structure and largely ignores scattering, it has been named the intrinsic AHE. Inverting the conductivity tensor, we obtain the contribution to $\rho_{xy} \approx \sigma_{xy}/\sigma_{xx}^2$, hence proportional to ρ^2 . The anomalous velocity is a function of the lattice Hamiltonian only and relates to the changes in the phase of Bloch state wavepackets when they evolve under the electric field [247–249]. Quite unusually, the intrinsic anomalous Hall conductivity does not concern the changing of the occupations of Bloch bands by scattering on impurities. Rather, it results from the interband coherence [250, 251] caused by the universal tendency of physical systems to progressively increase the indeterminacy of their state. The Karplus–Luttinger mechanism anticipated by several decades the modern topological theory of the Berry phase, which was found to provide an ample description of the intrinsic AHE [249, 252].

The Karplus–Luttinger theory of the AHE was criticised mainly for neglecting the effect of scattering on impurities. The competing semi-classical theories by Smit and Berger focused instead on the influence of disorder scattering. According to Smit, the main source of the anomalous Hall current was asymmetric (*skew*) scattering on impurities caused by the spin-orbit interaction, which predicted $\rho_{xy} \sim \rho$ ($\gamma = 1$) [253, 254]. On the other hand, Berger argued that the AHE arises mainly from the *side-jump* experienced by carriers upon scattering on spin-orbit coupled impurities [255]. This mechanism could be related to the intrinsic one by viewing the side-jump

as the consequence of the Karplus–Luttinger mechanism acting when the carrier was under the influence of the electric field of the impurity. The side-jump AHE current is proportional to the product of the side-jump per scattering event and the scattering rate. Recently, it was expressed in a neat analytical form and included in calculations [256]. Puzzlingly, the side-jump current is independent of the impurity density and the strength of scattering potential, leading to ρ_{xy} being proportional to ρ^2 as in the case of anomalous velocity mechanism.

Apart from the three above contributions to the AHE, higher-order effects in the scattering amplitude were predicted [257–261]. However, it is the intrinsic mechanism that is believed to play the key role in the Hall effect of these materials [45, 262–267]. It provides information on the hitherto inaccessible aspects of the band structure topology in the presence of various spin-orbit interactions, and for this reason has been of interest for spintronics researchers.

A surprisingly universal empirical power-law relation between ρ_{xy} and ρ , with $\gamma = 1.6$, has been found to be obeyed by a number of bulk ferromagnetic semiconductors on the lower side of their conductivity values, where Anderson–Mott quantum localisation effects should be important [268]. This value, which is consistent with the anomalous (in $3d$ transition metals and their oxides) [237] and ordinary Hall effect scaling laws in the hopping conduction regime, has been recovered theoretically by fitting the impurity potential strength and scattering lifetime [267]. However, the power-law relation breaks down completely in low-dimensional structures [37].

Karplus–Luttinger’s theory of the intrinsic AHE is complete and well-founded in quantum mechanics, but fails to provide a simple picture of this effect. It describes the AHE in terms of the off-diagonal elements of the density matrix and of the velocity operator, which are not gauge-independent on their own and only their product gives finally a gauge-independent current. In 1959, Adams and Blount proposed a more intuitive, semiclassical theory of intrinsic AHE which solves this issue [269].

The straightforward semiclassical approach, based on constructing a wavepacket from states of the same band, may not work in the presence of the electric field. Since the latter mixes states from different bands, a part of the initially free wavepacket starts to oscillate fast with frequencies $\omega \sim E_{n\mathbf{k}} - E_{n'\mathbf{k}}$ relative to the rest of it. Such a wavepacket could not be considered a classical object because it would be composed of parts with strongly different oscillation frequencies.

Adams and Blount suggested that the solution to this problem lies in constructing the packet from a different set of Bloch states, in which the off-diagonal matrix elements of the electric field, considered as a periodic field added to the Hamiltonian, are zero [269]. To linear order in $\mathcal{E} = \mathcal{E}_x \mathbf{n}_x$,

the periodic parts of the modified Bloch states have the form

$$u'_{n\mathbf{k}} = u_{n\mathbf{k}} - ie\mathcal{E}_x \sum_{n' \neq n} \frac{\langle u_{n'\mathbf{k}} | \frac{\partial u_{n\mathbf{k}}}{\partial k_x} \rangle}{E_{n\mathbf{k}} - E_{n'\mathbf{k}}} u_{n'\mathbf{k}} .$$

At $t = 0$ we can prepare a wavepacket from them, centred around \mathbf{k}_c in the reciprocal space,

$$\Psi'_{n\mathbf{k}_c}(\mathbf{r}, t = 0) = \int d^3\mathbf{k} a(\mathbf{k}) e^{i\mathbf{k}\cdot\mathbf{r}} u'_{n\mathbf{k}}(\mathbf{r}) ,$$

which does not have the problem with vastly different oscillation frequencies in external electric field. Let us now calculate the velocity of this wavepacket perpendicular to the field direction (i.e. in y). Let the full Hamiltonian be $H = H_0 - e\mathcal{E}_x x$. The wavepacket evolves according to the formula

$$\Psi'_{n\mathbf{k}_c}(\mathbf{r}, t) = e^{-iHt/\hbar} \Psi'_{n\mathbf{k}_c}(\mathbf{r}, 0) ,$$

which leads to the transverse velocity being equal to (see also [270])

$$\begin{aligned} v_y &= \frac{d}{dt} \langle \Psi'_{n\mathbf{k}_c}(\mathbf{r}, t) | y | \Psi'_{n\mathbf{k}_c}(\mathbf{r}, t) \rangle \\ &= \left\langle u'_{n\mathbf{k}_c} \left| \frac{1}{i\hbar} \left[i \frac{\partial}{\partial k_y}, H_0 \right] \right| u'_{n\mathbf{k}_c} \right\rangle \\ &= \frac{1}{\hbar} \frac{\partial E_{n\mathbf{k}}}{\partial k_y} \Big|_{\mathbf{k}_c} + \frac{ie}{\hbar} \mathcal{E}_x \left(\left\langle \frac{\partial u_{n\mathbf{k}}}{\partial k_y} \left| \frac{\partial u_{n\mathbf{k}}}{\partial k_x} \right\rangle - \left\langle \frac{\partial u_{n\mathbf{k}}}{\partial k_x} \left| \frac{\partial u_{n\mathbf{k}}}{\partial k_y} \right\rangle \right) \Big|_{\mathbf{k}_c} \right. \\ &= \frac{1}{\hbar} \frac{\partial E_{n\mathbf{k}_c}}{\partial k_y} - \frac{e}{\hbar} \mathcal{E}_x \Omega^z(n, \mathbf{k}_c) , \end{aligned}$$

where

$$\Omega^z(n, \mathbf{k}_c) = 2 \Im \left\langle \frac{\partial u_{n\mathbf{k}_c}}{\partial k_y} \left| \frac{\partial u_{n\mathbf{k}_c}}{\partial k_x} \right\rangle \right. \quad (10.3)$$

is the z component of Berry curvature [238] of the n -th unmodified band, and the \mathbf{k}_c subscript indicates that the relevant quantity is calculated for the centre of the wavepacket. This leads to the formula for the intrinsic anomalous Hall conductivity

$$\sigma_{xy} = -\frac{e^2}{V\hbar} \langle \Omega_z^n \rangle = -\frac{e^2}{V\hbar} \sum_{\mathbf{k}, n} f_{n\mathbf{k}} \Omega^z(n, \mathbf{k}) , \quad (10.4)$$

where e is the electron charge and $f_{n,\mathbf{k}}$ is the Fermi-Dirac distribution associated with the band n and wavevector \mathbf{k} .

The above semiclassical approach, taking into account the complete geometrical Bloch state description, leads to an intuitive picture of the origin and mechanism of the intrinsic anomalous Hall effect in ferromagnetic semiconductors. It applies to the weak scattering regime, where it was

proved to be formally equivalent to more systematic quantum-mechanical techniques [250]. In this framework, the anomalous Hall conductivity was calculated for the p - d Zener model [39] by Jungwirth *et al.* [45]. The model neglects the spin-orbit induced Bychkov–Rashba (linear in k), unless the lifetime is spin dependent, and Dresselhaus (k^3) terms. While the former, together with all terms linear in k , does not generate the spin current [271], the latter does [272], which has not been hitherto studied in (Ga,Mn)As and related ferromagnets.

In this chapter, I will investigate the intrinsic anomalous Hall effect in (Ga,Mn)As within all computational schemes described in Ch. 6. The comparison of the outcomes of these models will reveal qualitative differences in the Berry curvatures and the anomalous Hall conductivities. In particular, the Dresselhaus spin splitting, arising from the inversion asymmetry of the zincblende lattice, can change the sign of the AHE conductivity, which was not observed in the previously employed 6-band $k \cdot p$ model [45]. I will provide the physical interpretation of my findings and discuss their experimental implications.

10.1 Theoretical approach

I investigate AHE in a Hall sample of ferromagnetic (Ga,Mn)As with the electric field $\mathcal{E} \parallel \hat{x}$ and the magnetic field applied along the $[00\bar{1}]$ direction. This setup yields the anomalous conductivity given by the formula (10.4). Then, the positive values of σ_{xy} mean that the anomalous Hall voltage has the same sign as in the ordinary Hall effect.

The Berry curvature in (10.4) can be expressed by the equation (10.3), or by the equivalent Kubo formula (derived by differentiating the Schrödinger equation over \mathbf{k} , which makes sense in the finite-dimensional Hilbert space used in numerical calculations)

$$\Omega_z(n, \mathbf{k}) = 2 \Im \sum_{n' \neq n} \frac{c_{nn'}^y c_{n'n}^x}{(E_{n\mathbf{k}} - E_{n'\mathbf{k}})^2}, \quad (10.5)$$

where $\mathbf{c}_{nn'} = \langle u_{n\mathbf{k}} | \partial_{\mathbf{k}} \hat{H}_{\mathbf{k}} | u_{n'\mathbf{k}} \rangle$, and $u_{n\mathbf{k}}$ are the periodic parts of the Bloch states with energies $E_{n\mathbf{k}}$.

The $\Omega_z(n, \mathbf{k})$ formula (10.3) may carry large error even when we describe the Bloch wavefunctions quite accurately, because it involves their derivatives. For instance, in the 6-band $k \cdot p$ model [40, 103], I obtain an almost perfect description of the p -type bands around the Γ point, but their derivatives in general include significant contributions from the states outside this space. On the other hand, the sum in (10.5) goes over all bands, not just the hole p -type ones. Even the detailed description of these bands only is, therefore, not sufficient to calculate the Berry curvature accurately. The

model used must also have enough room to allow for the inversion symmetry breaking, an important property of (Ga,Mn)As lattice [142].

For the above reasons, one can expect the multiband tight-binding models of the host band structure to be the most appropriate for the description of the Berry curvature. They automatically take into account the lack of inversion symmetry, as they distinguish Ga and As atoms. Contrary to the perturbative $k \cdot p$ methods, they properly describe the Bloch states away from the centre of the Brillouin zone, which makes them better suited to high hole concentrations. Hence, I will use the $spds^*$ and sps^* tight-binding computational schemes described in Sec. 6.2. The impact of the inversion symmetry breaking on the Berry curvature will be additionally tested in the 8-band $k \cdot p$ model with the Dresselhaus term included, as described in Sec. 6.1. The dispersion relations of the top of the valence band calculated by the above methods have been compared in Fig. 6.3 on p. 76. There is very good agreement between the most popular 6-band $k \cdot p$ and the most detailed $spds^*$ tight-binding models, as well as the 8-band $k \cdot p$ approach, while the results obtained within sps^* parametrisation differ slightly.

In both $k \cdot p$ and tight-binding models, I have been able to compute the derivatives of the Hamiltonian matrix in (10.5) analytically, which significantly improves the accuracy of numerical results. Formula (10.3) is equally suitable for numerical computation, if we overcome the problems created by the wavefunction phase gauge freedom, which is cancelled analytically, but not numerically. One should simply fix the phases of the relevant wavefunctions by dividing each of them by the phase factor of its first non-zero basis coefficient.

10.2 Berry curvature

In Chapters 8 and 9, I have characterised the mean-field Curie temperature, uniaxial anisotropy and spin waves in (Ga,Mn)As. Their common feature is that they depend on the properties of the carrier p -type bands only, and hence the 6-band $k \cdot p$ model is sufficient to describe them correctly. The details of the other bands' structure, in particular the Dresselhaus spin splitting, do not influence their values. This can be explained by the fact that all these quantities are determined by the properties of carriers at equilibrium, free from any external disturbance. For this reason I call them the *static* quantities. In marked contrast, the derivatives and interband elements in the Berry curvature formulas, (10.3) and (10.5), express the *dynamic* character (related to the carrier drift caused by electric field) of the AHE and lead to qualitative differences between the models. Below I demonstrate the effect of the bulk inversion asymmetry on the Berry curvature and consequently on the anomalous conductivity trends.

The 6-band $k \cdot p$ model describes the diamond lattice structure. Since

the Kohn–Luttinger Hamiltonian it uses is invariant under space inversion, which is unitary, I have $\Omega(-\mathbf{k}) = \Omega(\mathbf{k})$. On the other hand, the antiunitarity of time reversal operator leads to $\Omega(-\mathbf{k}) = -\Omega(\mathbf{k})$ in the presence of the corresponding symmetry. Thus, the Berry curvature in this model is always symmetric and vanishes in the absence of magnetic fields, as presented in Fig. 10.1a, and no spin current flows.

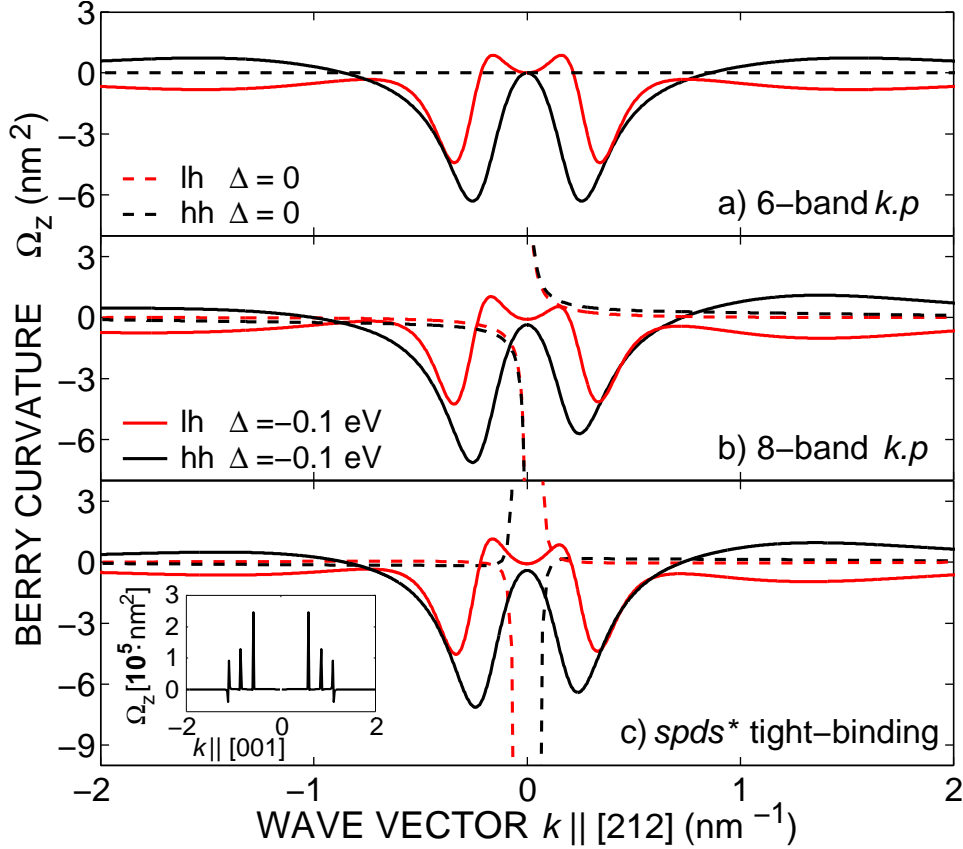


Figure 10.1: Berry curvature of majority heavy and light hole bands in (Ga,Mn)As calculated using a) the 6-band $k \cdot p$, b) 8-band $k \cdot p$ and c) $spds^*$ tight-binding model, with and without the spin splitting Δ . Inset: Divergences in the Berry curvature.

The 8-band $k \cdot p$ model contains, in addition, the s -type conduction band with the Dresselhaus spin splitting included by the use of Löwdin perturbation calculus [171, 175]. It results from the inversion symmetry breaking in the zincblende structure [142] and thus, in the presence of the time-reversal symmetry, leads to non-vanishing antisymmetric Berry curvatures (Fig. 10.1b). Then, the related k^3 energy term in the conduction band spectrum accounts for a non-zero spin current within the intrinsic spin Hall effect [272]. When the magnetic field is on, the significant asymmetry of the curvatures can still be observed.

The multiband tight-binding methods give us the detailed band parametrisations and introduce realistic symmetries of the crystal lattice in a natural way. Figure 10.1c presents the Berry curvatures obtained using the *spds** parametrisation. Their symmetry is similar to the 8-band *k.p* model, but the shape differs (especially for $\Delta = 0$), highlighting the sensitivity of the spin topological effects to the subtleties of the band structure.

An interesting effect is the formation of so-called diabolic points corresponding to the energy bands' crossings, best visible for $\Omega_z(\mathbf{k})$ in the $\mathbf{k} \parallel [001]$ direction (Fig. 10.1c, inset). A commonly held view is that it is them which are the source of the anomalous Hall conductivity. Even though the degeneracies of states in the *k*-space do produce a nontrivial Berry potential, it is easy to show that their contributions to σ_{xy} vanish for $T \rightarrow 0$ K. The coefficients $c_{nn'}^{x_i}$ in (10.5) are the matrix elements of Hermitian operators $\partial_{k_{x_i}} \hat{H}_{\mathbf{k}}$, hence $c_{nn'}^{x_i} = (c_{n'n}^{x_i})^*$. The conductivity is thus proportional to the sum

$$2 \Im \sum_{\mathbf{k}} \sum_{n < n'} \frac{c_{nn'}^y c_{n'n}^x}{(E_{n\mathbf{k}} - E_{n'\mathbf{k}})^2} (f_{n\mathbf{k}} - f_{n'\mathbf{k}}) . \quad (10.6)$$

For $E_{n\mathbf{k}} \neq E_{n'\mathbf{k}}$, a component of the above sum with given (\mathbf{k}, n, n') has a non-zero contribution to σ_{xy} only if $f_{n\mathbf{k}} \neq f_{n'\mathbf{k}}$, which for $T \rightarrow 0$ happens when one state is above and another below the Fermi level E_F . (Exploiting this observation in numerical computations ensures fast convergence of calculated integrals.) The component corresponding to the bands' crossing is thus zero, since $f_{n\mathbf{k}} = f_{n'\mathbf{k}}$ in a neighbourhood of the diabolic point. For a diabolic point lying exactly at the Fermi level, the same follows from the fact that the crossing bands are always on the same side of E_F in a neighbourhood of the diabolic point (which is always true for investigated systems, in which the Fermi level does not touch the borders of the Brillouin zone). Hence, for $T \rightarrow 0$ the diabolic points have no singular contribution to the anomalous Hall conductivity, which I also have confirmed numerically for finite temperatures. It is clearly seen from (10.3) and (10.5) that the Berry curvature arises from the spin-orbit interaction. This is because Hamiltonians without the spin-orbit coupling operator have real representations for all \mathbf{k} . One can then choose $u_{n\mathbf{k}}$ which are entirely real for all \mathbf{k} and do not produce the Berry curvature. By the introduction of the spin-orbit coupling, the Hamiltonian becomes complex, causing the Berry curvature to arise. Yet, the diabolic points manifest themselves, when passing the Fermi level, as kinks in the conductivity (marked with an arrow in Fig. 10.2).

10.3 Anomalous Hall conductivity

The qualitative difference of the Berry curvature between the models takes an effect on the anomalous Hall conductivity trends. The values of σ_{xy} in

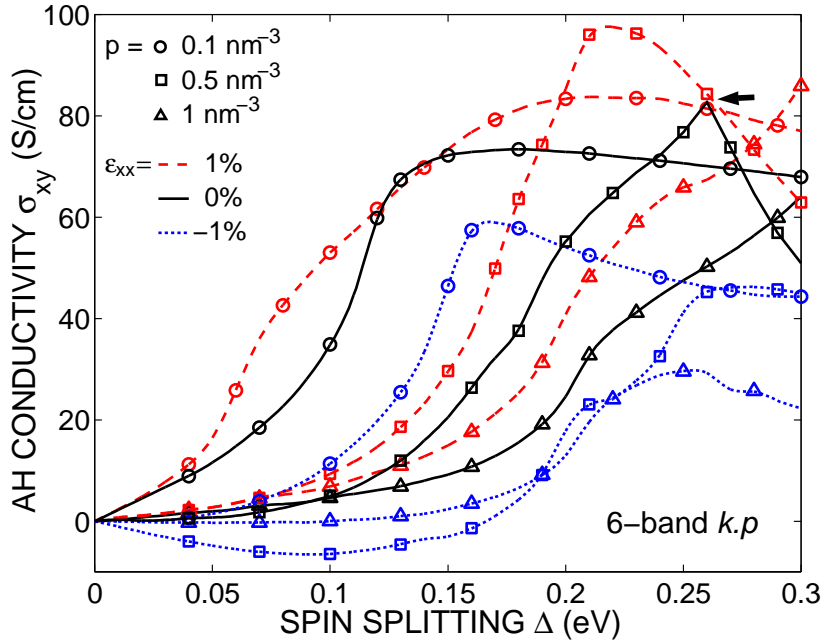


Figure 10.2: Anomalous Hall conductivity σ_{xy} vs. spin splitting Δ for different hole concentrations p and biaxial strain ϵ_{xx} in the 6-band $k \cdot p$ model. The hallmark of the diabolic point for unstrained $p = 0.5 \text{ nm}^{-3}$ curve is marked with an arrow. Numerical errors are ca 0.5%.

the $k \cdot p$ and tight-binding approaches, computed for various hole concentrations p as a function of the valence band splitting Δ , are presented in Figs. 10.2-10.6. The results obtained within the particular models remain in good agreement throughout the whole range of Δ values only for low hole concentrations, $p < 0.3 \text{ nm}^{-3}$. For higher carrier densities, differences in the σ_{xy} values become significant, particularly for small and intermediate spin splittings. Remarkably, I obtain a negative sign of σ_{xy} within the 8-band and tight-binding models (Figs. 10.3-10.6) in this range: the higher the hole concentration, the wider the range of Δ for which the negative sign persists. This is the effect of the Dresselhaus splitting which increases with k , while for increasing hole concentrations the states with high k -vectors become occupied and contribute to the conductivity. However, strong enough spin splitting destroys the negative sign. This shows a dramatic and so far unnoticed influence of the Dresselhaus term on the AHE in hole-controlled ferromagnetic semiconductors.

It has been suggested in Ref. [273] that the influence of disorder on the intrinsic AHE can be phenomenologically modelled by substituting one of the energy differences in (10.5) with $E_{n\mathbf{k}} - E_{n'\mathbf{k}} + i\hbar\Gamma$. The phenomenological underlay of this method has been mentioned in Sec. 5.1. The scattering-induced broadening of bands in (Ga,Mn)As at the localisation boundary,

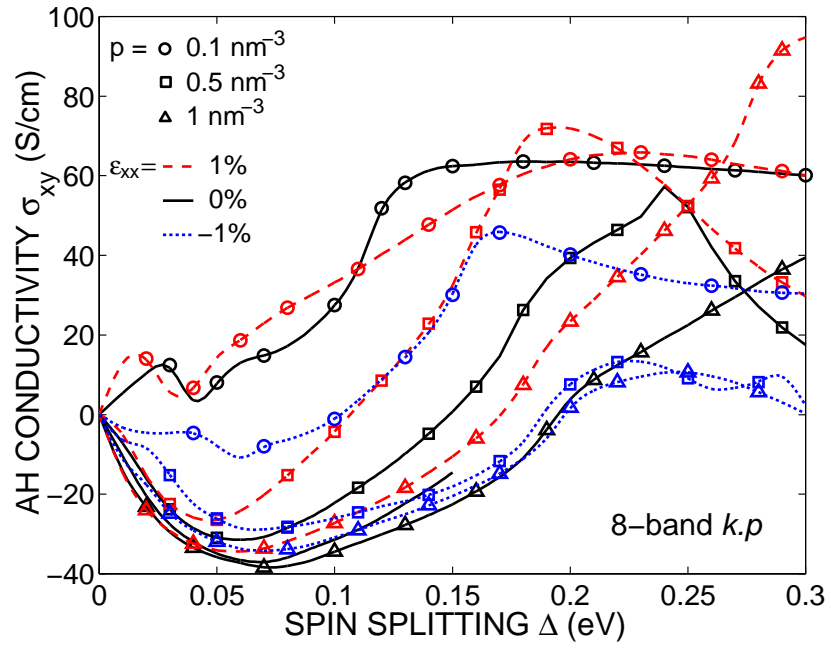


Figure 10.3: Anomalous Hall conductivity σ_{xy} vs. spin splitting Δ for different hole concentrations p and biaxial strain ϵ_{xx} in the 8-band $k \cdot p$ model.

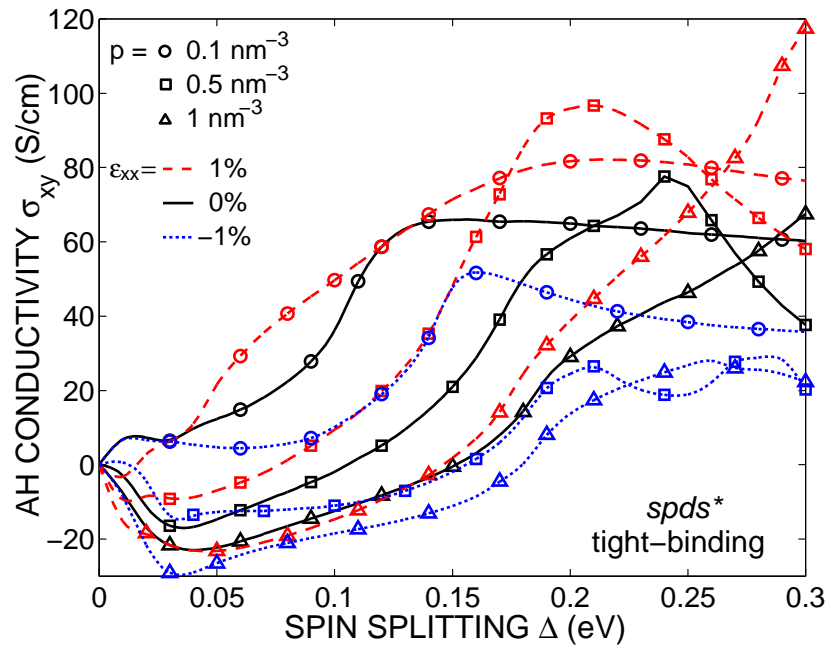


Figure 10.4: Anomalous Hall conductivity σ_{xy} vs. spin splitting Δ for different hole concentrations p and biaxial strain ϵ_{xx} in the $spds^*$ tight-binding model.

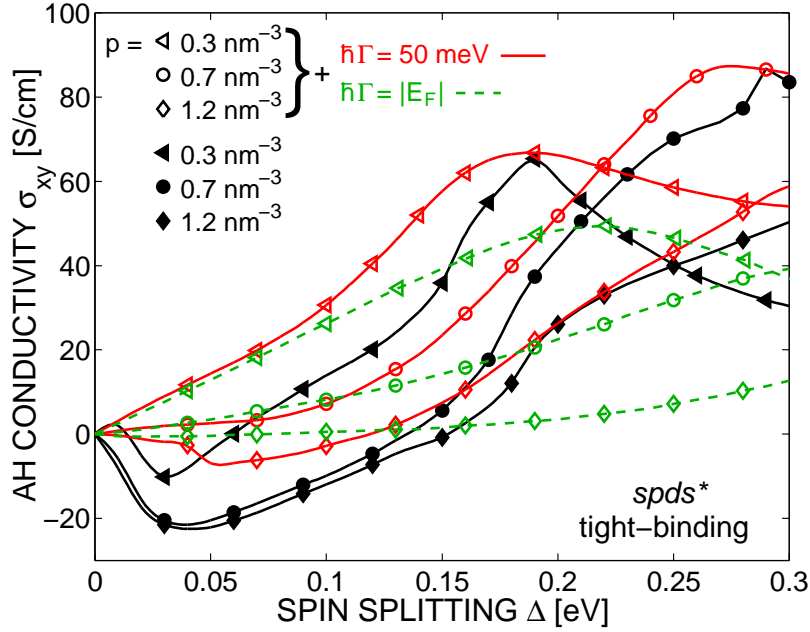


Figure 10.5: Anomalous Hall conductivity σ_{xy} vs. spin splitting Δ for different hole concentrations p in the $spds^*$ tight-binding model. The scattering-induced energy level broadening $\hbar\Gamma$ equal to 50 meV and $|E_F|$ is included.

$\hbar\Gamma$, is presumably of the same order as the magnitude of the Fermi energy $|E_F|$ [274]. It washes out the Dresselhaus splitting and reduces the magnitude of its negative contribution to σ_{xy} , as shown in Fig. 10.5. However, this approach is not without its own problems: the energy level broadening is but a part of equal-rank “extrinsic” terms in the Kubo-Středa formalism [250], and its magnitude is typically too large to treat its effect on the AHE perturbatively.

The sensitivity of the AHE to the details of the band structure suggests that it can be influenced by the biaxial strain. Figures 10.2–10.6 contain the results on the anomalous Hall conductivity in tensile and compressively strained (Ga,Mn)As samples, $\epsilon_{xx} = 1\%$ and $\epsilon_{xx} = -1\%$. The σ_{xy} values tend to increase in the first case and decrease in the latter in all models. As seen, small negative values are found already within the 6-band $k \cdot p$ model for the tensile strain.

Additionally, I checked that despite the overall sensitivity, the effect of the temperature parameter in the Fermi-Dirac function on σ_{xy} for a fixed value of spin splitting is negligibly small.

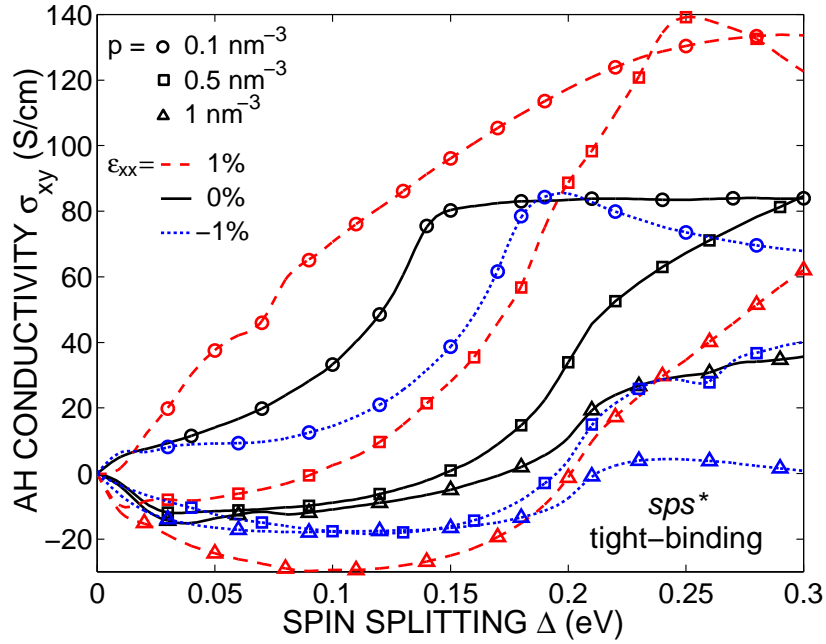


Figure 10.6: Anomalous Hall conductivity vs. spin splitting for different hole concentrations p and biaxial strain ϵ_{xx} in the sps^* tight-binding model.

10.4 Comparison to experiment

10.4.1 Bulk (Ga,Mn)As

Figure 10.7 compares the theoretical and experimental results [273, 275] on the anomalous Hall conductivity for the set of annealed samples with nominal Mn concentration x , hole concentration p and biaxial strain ϵ_{xx} . The calculations of the $k \cdot p$ and tight-binding models corresponding to the experimental parameters do not fit the measured points. The new detailed theories, which include the inversion asymmetry of the GaAs lattice, predict a negative sign of σ_{xy} for low Mn content x . At the same time, all the models predict the σ_{xy} values larger than in the experiment for high Mn content. They are nevertheless significantly lowered by the—strong in this regime—biaxial strain, as shown by the comparison with zero strain calculations for sps^* tight-binding model (diamonds).

The much smaller than theoretical values of σ_{xy} for samples with high Mn content may be connected to the presence of Mn interstitials [228], which do not form magnetic moments. The ones which survived the annealing process, as suggested by the measured hole densities, compensate one substitutional Mn spin each. As a result, the effective Mn concentration is lower than the total Mn content used in the calculations, which typically leads to lower σ_{xy} values. This effect cannot explain the qualitative difference be-

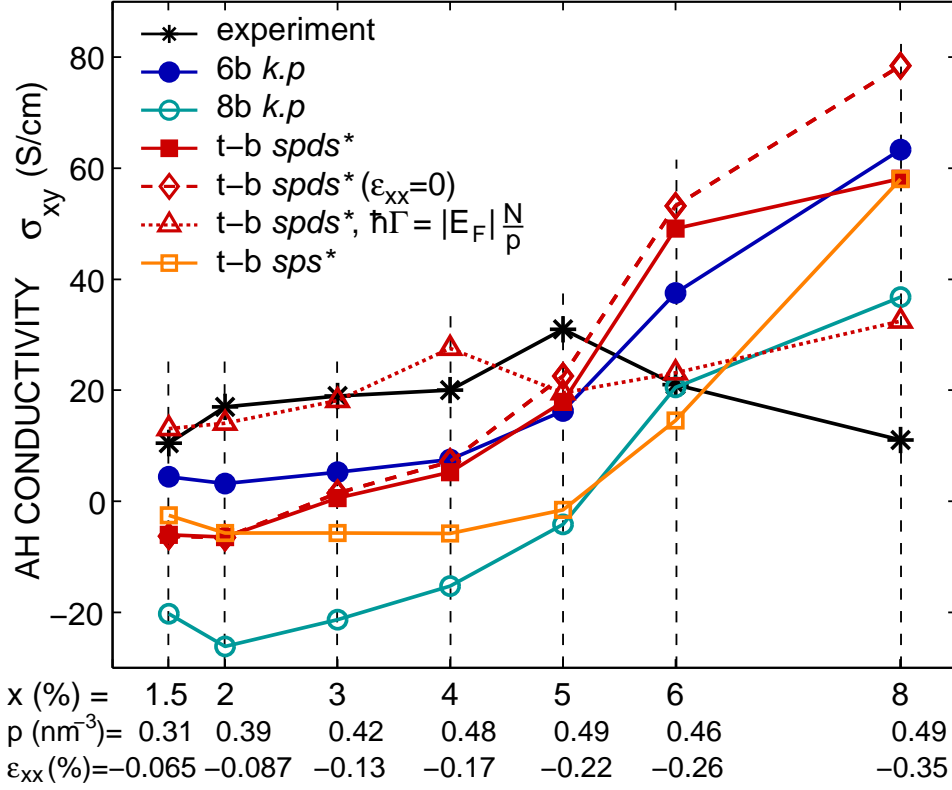


Figure 10.7: Reconstruction of the experimental [273] anomalous Hall conductivities for nominal Mn concentration x , hole concentration p and strain ϵ_{xx} , using different theoretical models.

tween the new theories and experiment at low Mn concentrations. However, some experimental data suggest that the negative σ_{xy} can be found under conditions indicated by the present computations [276].

Additionally, the energy levels' lifetime broadening [273], as a part of scattering effects derived within the Kubo-Středa formalism, is taken into account in the $spds^*$ model (triangles). The broadening $\hbar\Gamma$ is taken to be the ratio of the total Mn concentration $n = 4x/a_0^3$ and hole concentration p , times the magnitude of Fermi energy, $|E_F|$. As mentioned before (Fig. 10.5 and related text), it is done in a rather phenomenological way, but nevertheless leads to much better agreement with the experimental data.

10.4.2 Thin layers of (Ga,Mn)As

While the AHE in thick films behaves analogously to the bulk samples, an entirely different picture of it emerges from measurements in thin layers (with thicknesses of the order of few nm) [37]. As shown in Fig. 10.8, for such layers the scaling law $\sigma_{xy} \sim \sigma_{xx}^{1.6}$ breaks down completely. In particular,

the negative AHE conductivity is observed in a part of the samples. In the

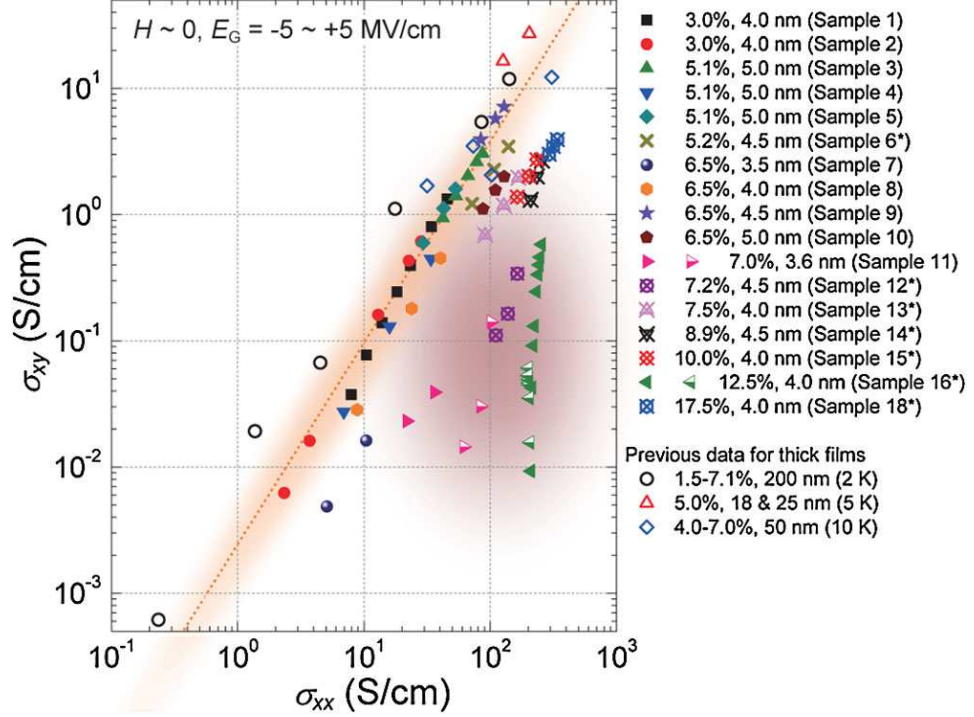


Figure 10.8: Relation between Hall and longitudinal conductivities at various values of gate electric fields E_G at 10 K (30 K for sample 1) for metal-insulator-semiconductor structures (MIS) of $\text{Ga}_{1-x}\text{Mn}_x\text{As}$ [37]. The legend shows the values of the Mn content x , channel thickness t , as well as the sample number. The half-filled symbols denote the absolute value of negative σ_{xy} , while the open symbols (circles, triangles up, and diamonds) denote the data for thick films. The dotted line plots the dependence $\sigma_{xy} \sim \sigma_{xx}^\gamma$, $\gamma = 1.6$. (Source: Ref. [37])

course of my collaboration with Professor Hideo Ohno's group at Tohoku University, I analysed the experimental data on $(\text{Ga},\text{Mn})\text{As}$ thin layers [37]. All calculations have been performed using the tight-binding Hamiltonian. Despite taking into account the spin-orbit coupling and the inversion symmetry breaking, it was not possible to recover the observed values of σ_{xy} . Nevertheless, several mechanisms may explain the discrepancy.

As can be seen in Fig. 10.9, the gate electric field does not affect significantly the temperature dependence of the Hall resistance R_{yx} . However, the presence of two interfaces can be expected to exhibit structure inversion asymmetry in the layers, leading to the lowering of the point symmetry from D_{2d} to C_{2v} and the Bychkov–Rashba spin-orbit interaction (see Sec. 5.4.2). In order to explain the observed data, the structure asymmetry contribution to R_{yx} should be negative and its amplitude should dominate the bulk terms at sufficiently high magnetisation values. However, the measurements of the

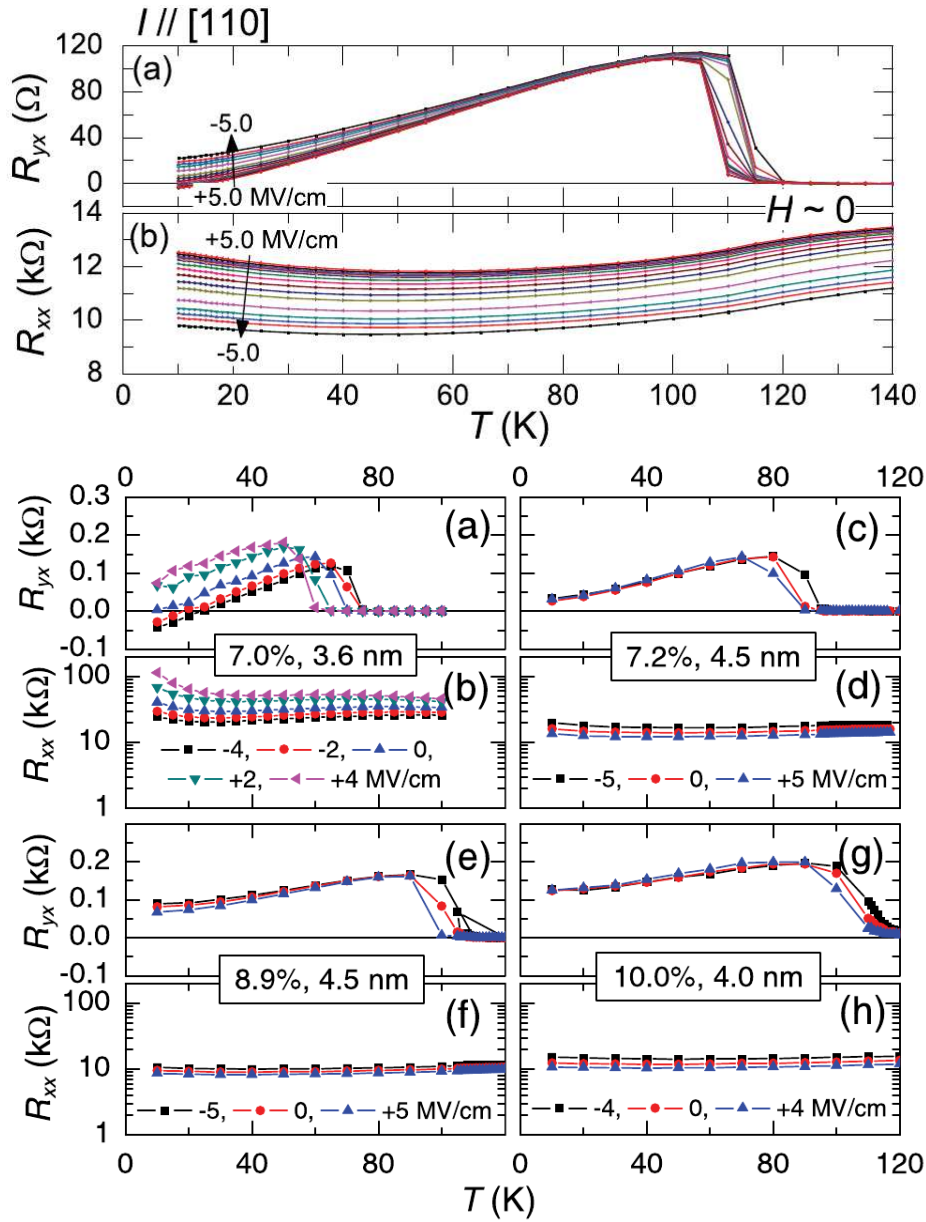


Figure 10.9: Hall R_{yx} and longitudinal R_{xx} sheet resistances at various values of the gate electric fields in thin layer structures showing a strong temperature dependence of R_{yx} . (Source: Ref. [37])

in-plane anisotropy of the conductivity tensor, shown in Fig. 10.10, did not prove that the symmetry is lowered to C_{2v} . Nevertheless, it is possible that the structural asymmetry was masked by an accidental degeneracy, e.g. due to the compensation of asymmetry in the values of the density of states and

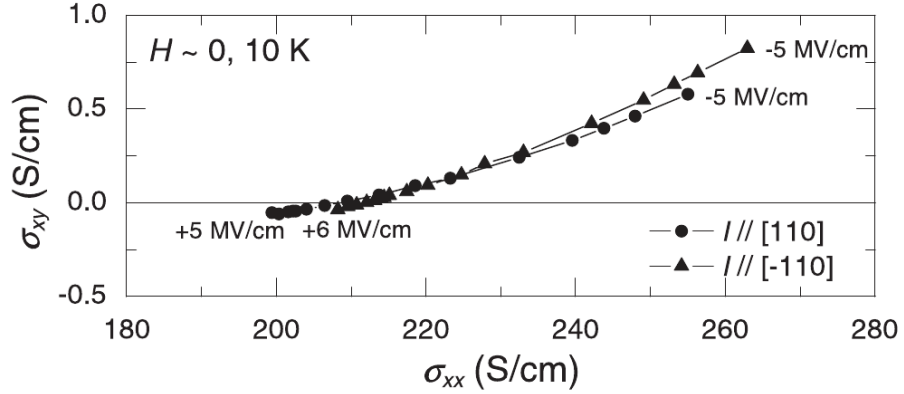


Figure 10.10: Hall conductivity vs. conductivity for 4-nm thick $\text{Ga}_{0.875}\text{Mn}_{0.125}\text{As}$ channels oriented along $[110]$ and $[\bar{1}10]$ in-plane crystallographic orientations. Similar values of Hall and longitudinal conductance were observed in both cases. (Source: Ref. [37])

relaxation time.

Another possibility is that the spatial confinement in the transverse direction changes significantly the topology of the Fermi surface introducing, in particular, a number of additional band crossings. This scenario may explain why the negative sign of σ_{xy} is observed for different signs of the gate potential in different structures (Fig. 10.9).

One should note that the empirical scaling found for thick films as well as for thin layers with low conductance cannot be explained by the intrinsic mechanisms of the AHE, as the corresponding theory predicts a decrease of σ_{xy} with both hole density and scattering time (see Refs. [45, 264, 273] and Sec. 10.3) in a wide range of relevant hole concentrations and spin splittings. This suggests that the physics of AHE is dominated by the proximity to the Anderson–Mott localisation boundary [134, 277]. So far the influence of quantum interference effects on the anomalous Hall conductance has been studied considering the side-jump and skew-scattering terms within the single-particle theory [278]. The data summarised in Fig. 10.8 call for the extension of the theory towards the intrinsic AHE with the effects of disorder on the interference of carrier-carrier scattering amplitudes taken into account.

10.5 Summary

I have compared four models of the (Ga,Mn)As band structure with regards to their impact on the Berry curvature and the intrinsic anomalous Hall effect. I considered the 8-band $k \cdot p$ and two tight-binding ($spds^*$ and sps^*) parametrisations, and compared their results with the previously employed

6-band $k \cdot p$ approach. While the static quantities, such as the Curie temperature, magnetocrystalline anisotropy field and spin waves, do not depend significantly on the model used, the anomalous Hall effect exhibits qualitative dependence on the details of the band structure beyond the six hole bands. In particular, the inversion asymmetry of the zincblende lattice producing the Dresselhaus spin splitting of the Γ_6 conduction band leads to the negative anomalous conductivity sign. Despite using the more detailed models of the band structure, I have not obtained the agreement with the experimental results on bulk crystals of (Ga,Mn)As—indeed, moved away from it. Moreover, I have failed to reproduce the experimental data on thin layers. This is possibly a symptom of the intrinsic AHE theory being insufficient to describe the observed phenomena. Additional mechanisms which merit a detailed investigation include scattering, localisation, and—in thin layers—confinement effects.

Chapter 11

Summary and outlook

11.1 Summary of thesis work

In my dissertation work, I have investigated the family of (III,Mn)V alloys as future spintronic materials, focusing on (Ga,Mn)As, their textbook example. Thanks to the intrinsically large spin-orbit coupling in the III–V host, these materials are perfect candidates for the device which can realise the full potential of spintronics—a CPU and a hard drive in one. However, introducing Mn atoms into this familiar ground turns it into a true welter of interactions, phases and regimes. It drew me into theoretical and computational studies of an extensive array of topics: magnetic anisotropies, the Curie temperature (Ch. 8, Ref. [46]), spin waves (Ch. 9, Ref. [47]), as well as the anomalous Hall effect and the electric-field control of ferromagnetism in these systems (Ch. 10, Refs. [37, 46]).

In the first chapters, I have presented the theoretical and experimental background to my investigations: the nature of dilute magnetic semiconductors and (Ga,Mn)As in particular (Ch. 3), the physics of its ferromagnetic order (Ch. 4) and its band structure (Ch. 5). To model (Ga,Mn)As numerically, I developed a modularised, object-oriented library (described in Appendix A) employing envelope-function $k \cdot p$ and multiorbital tight-binding computational schemes (Ch. 6). It allows for the quantitative description of most magnetic and transport properties accessible to experiment. I have used it to analyse the following problems.

In Chapter 9 I have investigated the physics of spin waves and the macroscopic spin-wave stiffness parameter, which determines the properties of magnetic domains. They are crucial for investigating such effects as the magnetic-field and current-induced domain-wall motion [35], as well as their applications in spintronic devices (e.g. racetrack memories or domain-wall logic circuits [17, 38]). Furthermore, the growing interest in this topic is brought about by the rapid development of a new field of physics called magnonics [279]. It promises multifunctional devices based on magnonic

crystals, which provide full control of spin waves, like photonic crystals already do for light.

To model spin waves in (III,Mn)V thin layers and bulk crystals, I developed a simple analytical method for a self-consistent description of coupled many-particle systems, called the Löwdin variation-perturbational calculus [41, 47, 122], described in Sec. 7.2. It is an extension of the RKKY theory, which is self-consistent (takes into account the dynamics of free carriers) and can accommodate any band structure (of any number of bands, with the spin-orbit coupling and the values of spin-splitting up to those encountered in (III,Mn)V ferromagnets). I extended the theory of spin waves to systems with broken space inversion symmetry, provided their definition at high temperatures, and showed how they lower the Curie temperature. I also analysed the stiffness parameter and defined its relativistic counterpart arising from the spin-orbit interaction, which may be responsible for some of the rich diversity of magnetic anisotropies observed in these materials [92]. However, the thorough comparison to experiment suggests that factors such as spin pinning or Mn and hole concentration gradients should be taken into account.

In the thin layers of (Ga,Mn)As, I predicted the cycloidal spin structure in the magnetisation groundstate, resulting from the Dzyaloshinskii-Moriya interaction. I showed that it can produce an in-plane uniaxial anisotropy of the diagonal directions on the film surface. This new kind of magnetic anisotropy relates to the common but so far unexplained experimental observation [126]. The non-trivial physics of the surface could improve the predictions of bulk structure models and help interpret many inexplicable experimental data. Moreover, it would lead to various new topological phenomena and bring about additional spintronic functionalities of ferromagnetic semiconductors. The above results have been published in Ref. [47].

The strong spin-orbit coupling in (III,Mn)V materials provides a handle for the electron spin. A remarkable demonstration of this fact are the spin and anomalous Hall effects investigated in Ch. 10. Over one hundred years of studies on the AHE revealed that it can be induced by multiple mechanisms, the main ones being the intrinsic one, skew scattering and side jump, as outlined in Sec. 10.1. While novel experiments on cold atoms in artificial magnetic field or cavity quantum electrodynamics offer the possibility to investigate some of these phenomena separately [280, 281], in ferromagnetic semiconductors we have to consider all three of them simultaneously. My studies, published in Ref. [46], revealed the spectacular sensitivity of the intrinsic AHE to the details of the full band structure, in particular the Dresselhaus spin splitting of the conduction band. Furthermore, the joint experimental and theoretical work on the anomalous Hall effect in field-effect transistors of (Ga,Mn)As [37], which I was part of, revealed new and unanticipated aspects of the AHE, which we have attributed to localisation and confinement effects. To obtain their quantitative description, I have

initiated theoretical and numerical studies on the AHE in thin layers.

11.2 Open problems

My work made me familiar with a wide spectrum of effects related to exchange interactions, spin-orbit coupling, dimensionality and topology of real and reciprocal spaces. Eventually, it pitted me against challenging questions about the role of disorder and correlations in the physics of electrons in solids. They permeate its almost every aspect [192, 282] and lead to critical behaviours, which retain their importance even beyond the condensed matter: from ultracold atomic gases in random optical lattice potentials to frustrated insulating magnets, high-temperature superconductors and heavy fermions, all the way to classical systems (light, acoustic and seismic waves) [283–285] or even financial mathematics [286–288]. Much effort has been spent on understanding them, and the resulting concepts and ideas form an important part of modern theoretical physics [289]. They are far from being complete, especially—as shown by recent novel experiments [290–292]—in the context of diluted magnetic semiconductors. In these materials, disorder leads to the breakdown of the classical Drude conductance theory and to metal-insulator transition [293], which forces us to think beyond the standard Landau Fermi-liquid approach. Consequently, we can no longer safely model the ferromagnetism as spatially homogeneous, but have to consider the dependence of magnetic interactions on a complex landscape of electron wavefunctions from both sides of the mobility edge, formed by their quantum interference in the disordered lattice. At the same time, the rare large events in the fat-tailed distributions of the local density of states mean that the behaviour of the system cannot be fully described by its average properties. In other words, we cannot rely on the mean-field theory alone.

Because of the technological importance of dilute magnetic semiconductors and the fascinating theoretical and computational challenges in their modelling, we need to study them further, applying more advanced theoretical methods describing strong correlations, disorder and spatial fluctuations, in particular the Dynamic Mean-Field Theory (DMFT) in conjunction with Local Density Approximation (or, possibly, less computationally demanding band structure methods) [294]. Recent studies based on this approach made considerable improvements in the description of these materials [295–298]. The DMFT turns a lattice model into a quantum impurity problem in a self-consistent medium, treating all energy scales of local interactions on equal footing. Solving this impurity problem in disordered, strongly correlated systems requires the use of helper methods, such as Numerical Renormalisation Group [299], Density Matrix Renormalisation Group [300], Quantum Monte Carlo [301] or exact diagonalisation [302, 303]. In the

form of statistical DMFT (statDMFT), it can also describe the Anderson localisation and other consequences of disorder. This method consists in calculating the geometrical average of the local density of states (LDOS) and feeding it back to the self-consistent DMFT equations [303]. The geometrical, instead of arithmetic, averaging gives the *typical* value of LDOS even when its distribution has wide tails, as it does when the system is at a critical point and the electron wavefunctions become multifractal [304]. We are thus able to recover the localisation caused by disorder, recognise the corresponding critical point and obtain full distribution functions of other physical quantities [282]. Furthermore, the rare region effects in the vicinity of the Anderson transition are likely to be stronger and more complex in systems with long-range interactions. To take this into account, one would combine statDMFT with the Dynamical Cluster Approximation, an extension of DMFT in which, instead of a single site, a cluster of them interacts with the dynamical mean-field [305–307]. Alternatively, the Functional Renormalisation Group [308] can be employed for this purpose, additionally allowing a direct investigation of the multifractal nature of metal-insulator transition. This method does not use the mean-field approximation at all, and accounts fully for spatial fluctuations. However, in its current form it is limited to weak disorder and interactions. With the help of all these tools we could investigate the impact of rare large effects on the physics of dilute magnetic semiconductors and their experimental implications.

The studies of disorder, localisation and rare large events bring us to such hot topics as heavy fermions, Dirac fermions and graphene [309], topological insulators and integer/spin quantum Hall effect [310, 311], ultracold atoms [312], cavity QED [313] and finally the exotic nature of high temperature superconducting (HTS) materials [314–317], which are now making inroads in wide-scale commercial applications [318]. Since they share a common background with the semiconductor physics discussed above [192], the tools developed for the latter should be applicable to them as well. The cross-fertilisation among these fields of research would certainly be a rich source of scientific discoveries.

Appendix A

Numerical implementation

A.1 Code structure

To perform the required numerical calculations, I wrote an object-oriented C library.¹ The $k \cdot p$ Hamiltonians were handled fully inside my library, while a part of the tight-binding model implementation made use of the Fortran code by Vogl and Strahberger [163] (employed previously in the studies of spin transport properties in modulated (Ga,Mn)As structures and extended by Oszwałdowski *et al.* [164, 165]). I utilised several numerical libraries: Cuba and TOMS (optionally) for adaptive integration, and LAPACK for matrix diagonalisation [319–321]. Figure A.1 shows the structure of the library, its dependencies and client programs.

The main interface provided by the library is the `ham_struct` structure (defined in module `hamiltonian`), which contains customizable references to functions calculating the Hamiltonian matrix and its derivative for given \mathbf{k} vector. The reference to it is provided to structures `spinwave_calculator` (in module `spinwaves`) and `berry_calculator` (in module `berry`), which are used by the client programs to compute:

- integrands used to calculate $E_{\mathbf{q}}^{++}$ and $E_{\mathbf{q}}^{+-}$,
- Berry curvature for given band and \mathbf{k} vector,
- integrand used to calculate AHE conductivity.

`ham_struct` is thus an abstract interface to the \mathbf{k} -dependent Hamiltonian. Modules `sixband` and `kane` provide the full implementation of the two $k \cdot p$ Hamiltonians described in Section 6.1, while the module `tightbinding` uses the Fortran code by Vogl and Strahberger to provide the tight-binding model. Additionally, the module `fourband` implements the Dietl 6×6 Hamiltonian in the limit of infinite spin-orbit splitting; it was used for testing, as in this limit one can calculate the band energies analytically.

¹Object-orientation is an aspect of the program design, not a language feature.

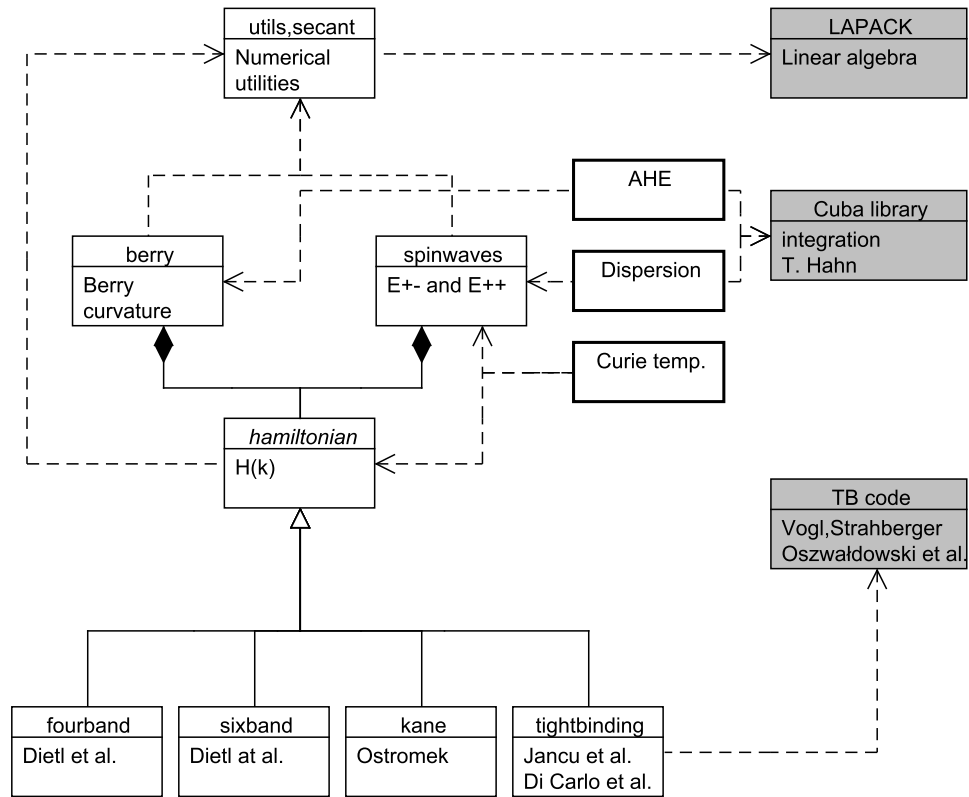


Figure A.1: Relations between software components (some smaller modules omitted for clarity). Straight lines with triangles indicate implementation of an abstract interface (in italics), lines with black diamonds – composition and dashed arrows – functional dependence. Light grey boxes denote external dependencies and boxes with bold borders – client programs used to generate the final results.

A.2 Computational problems

The most computationally intensive numerical tasks I faced were the efficient calculation of Hamiltonian matrices and their derivatives, their diagonalisation and the integration of various quantities over the part of or the whole Brillouin zone.

The derivatives of the Hamiltonian matrix over \mathbf{k} were calculated analytically without using finite-difference approximations, which turned out to be a significant enhancement of accuracy and performance.

The matrix diagonalisation was performed with the help of ZHEEVD routine from LAPACK, which uses a divide-and-conquer algorithm [322].

Integration over the reciprocal space was performed using adaptive quadratures in cartesian or spherical/polar coordinates, depending on the problem. The domain of integration was defined by the three reciprocal basis

vectors \mathbf{b}_1 , \mathbf{b}_2 and \mathbf{b}_3 :

$$\int f(\mathbf{k})d^3k := \mathbf{b}_1 \cdot (\mathbf{b}_2 \times \mathbf{b}_3) \int_{-1/2}^{1/2} dc_1 \int_{-1/2}^{1/2} dc_2 \int_{-1/2}^{1/2} dc_3 f\left(\sum_{i=1}^3 c_i \mathbf{b}_i\right), \quad (\text{A.1})$$

and the integrated functions were always functions of the Hamiltonian and its derivatives at \mathbf{k} ,

$$f(\mathbf{k}) \equiv f[H(\mathbf{k}), \partial H(\mathbf{k})] .$$

In the case of tight-binding Hamiltonian, definition (A.1) is equivalent to integrating over the Brillouin zone, due to the periodicity of Hamiltonian (6.6). This equivalence is lost when using the $k \cdot p$ method, but the difference between two domains can be neglected in this case, as the $k \cdot p$ method I used is valid in the neighbourhood of $\mathbf{k} = (0, 0, 0)$ point only (i.e. for small hole concentrations).

Additional routines calculate the Fermi energy for a given hole concentration p and spin splitting Δ . To minimise the computational cost, I have used a discrete cubic grid in the reciprocal space, consisting of $10^5 - 10^7$ points. The value of hole concentration is converted into a number n of holes occupying the grid using the formula

$$n = p \frac{8\pi^3}{v},$$

where v is the volume of a single grid cell. Next, the eigenvalues of the Hamiltonian from all grid sites are sorted and the n -th highest one is returned as the Fermi energy.

The self-consistent equation for the average magnetisation has been solved using the secant algorithm², which proved to be more stable in this case than Brent. Integrals of functions depending on the spin wave $\omega_{\mathbf{q}}$ dispersion values were approximated by sums over very sparse grids (less than 100 points), due to the large computational cost of calculating $\omega_{\mathbf{q}}$.

²The oldest known one-dimensional root-finding method, with 3000 years of history [323].

Appendix B

Acronyms and symbols

AHE	anomalous Hall effect
BMP	bound magnetic polaron
CPU	central processing unit
DMFT	dynamic mean field theory
DMS	dilute magnetic semiconductors
DOS	density of states
DRAM	dynamic random access memory
FET (spin-FET)	field-effect transistor
FFT	fast Fourier transform
GMR	giant magnetoresistance
HTS	high-temperature superconductors
IR	infra-red
IT	internet technologies
LCAO	linear combination of atomic orbitals
LDA	local density approximation
LDOS	local density of states
LED	light emitting diode
MBE	molecular-beam epitaxy
MOS	metal-oxide-semiconductor
MRAM	magnetic random access memory
QED	quantum electrodynamics
RKKY	theory Rudderman-Kittel-Kasyua-Yoshida theory
SQUID	superconducting quantum interference device
SRAM	static random access memory
TB	tight-binding
TMR	tunelling magnetoresistance
a	(Ga,Mn)As unstrained lattice constant
a_0	GaAs unstrained lattice constant
$\mathbf{a}_1, \mathbf{a}_2, \mathbf{a}_3$	primitive vectors of the real lattice

a_{str} strained lattice constant
 a^* Bohr radius
 \mathcal{A} exchange stiffness tensor
 \mathbf{A} isotropic part of the exchange stiffness tensor
 A_F correction factor for carrier-carrier interactions in the p - d Zener model
 α s - d exchange integral
 $\mathbf{b}_1, \mathbf{b}_2, \mathbf{b}_3$ primitive vectors of the reciprocal lattice
 \mathcal{B} first Brillouin zone
 β p - d exchange integral
 B_S Brillouin function
 c speed of light in vacuum
 Ξ intraband carrier spin polarisation
 Ξ_{so} interband carrier spin polarisation
 \mathbf{D} spin-wave stiffness tensor
 D_{nor} normalised spin-wave stiffness
 Δ spin splitting
 Δ_{so} spin-orbit splitting
 $\epsilon_{\mu\nu}$ strain tensor component
 E energy
 \mathcal{E} electric field
 E_c total carrier energy
 E_F Fermi energy
 E_g band gap
 $E_{\mathbf{k}m}$ energy of the Bloch wavefunction with wavevector \mathbf{k} in the m -th band
 f Fermi-Dirac distribution
 $F(q/2k_F)$ Lindhard function
 F_c, F_S carrier and ion free energy
 g Landé factor
 \mathbf{G} reciprocal lattice vector
 Γ highest symmetry point in the Brillouin zone of the fcc lattice or the carrier multiparticle state in the Löwdin calculus (where Γ_0 is the lowest eigenstate)
 $\hbar\Gamma$ disorder-induced broadening of energy bands
 H magnetic field
 H_{un} uniaxial anisotropy field
 \mathcal{H} Hamiltonian
 $\mathcal{H}(\mathbf{k})$ \mathbf{k} -dependent Hamiltonian acting on $u(\mathbf{r})$ only
 \hbar Planck constant divided by 2π
 J exchange function ($J(r)$ RKKY exchange)
 \mathbf{k}, \mathbf{q} wavevector
 k_F Fermi vector
 k_B Boltzmann constant
 \mathcal{K} magnetocrystalline anisotropy vector
 L orbital momentum

$\text{Li}_{3/2}$ de Jonqui re's function
 Λ, Λ^* real and reciprocal lattices
 m_0 free electron rest mass
 m^* electron effective mass
 M magnetisation
 M_s saturation magnetisation
 μ_0 vacuum permeability
 μ_B Bohr magneton
 $\langle n_{\mathbf{q}} \rangle_T$ thermal average of spin-wave excitations in a mode \mathbf{q}
 N number of localised ions' spins in a sample
 N_0 number of cation sites in an elementary cell
 O_h diamond point group (octahedral symmetry)
 O_h^7 space group of a diamond structure
 P number of carriers in a sample
 P_{ex} (defined in Secs. 6.1.2 and 6.2.2) , $P_{s,p}^{\text{Ga,As}}$ projection operators
 p hole concentration (or the p orbital symbol)
 \hat{p} momentum operator
 q_D Debye vector
 \mathbf{q}_{min} dispersion minimum shift
 r distance
 $r_{\text{nn}'}$ distance between the nearest Mn spins
 R_0 Hall constant
 R_a anomalous Hall constant
 R_{yx} Hall resistance
 ρ_{xy} Hall resistivity
 ρ_{xx}, ρ longitudinal resistivity
 s carrier spin
 s, l, j, m_s, m_l, m_j spin, orbital and total angular momentum quantum numbers and their secondary quantum numbers (projections on the quantisation axis)
 S spin of the lattice ion
 \mathcal{S} entropy
 $\hat{\sigma}$ vector of Pauli matrices
 σ_{xy} Hall conductivity
 σ_{xx} longitudinal conductivity
 T temperature
 \mathbf{T} anisotropic part of the exchange stiffness tensor
 T_C Curie temperature
 T_{AF} correction from antiferromagnetic superexchange to T_C in the p - d Zener model
 T_d zincblende point group (tetrahedral symmetry)
 T_d^2 space group of a zincblende structure
 $u(\mathbf{r})$ periodic part of the Bloch function
 \mathbf{u}_{ij} Dzyaloshinskii-Moriya exchange constant

\mathbf{U} Dzyaloshinskii-Moriya vector
 V crystal volume
 $V(\mathbf{r})$ lattice potential
 $\omega_{\mathbf{q}}$ spin-wave frequency ($\omega_{\mathbf{q}}^T$ at temperature T and $\omega_{\mathbf{q}}^0$ at 0 K)
 Ω unit cell volume or sum of states in Ch. 7
 Ω_z Berry curvature
 x, x_{tot} total concentration of Mn in the sample
 x_{eff} effective concentration of Mn (contributing to magnetisation)
 x_{a} concentration of antisite Mn
 x_{i} concentration of interstitial Mn
 x_{sub} concentration of substitutional Mn_{Ga}
 $\chi_s, \chi_{\mathbf{q}}$ carrier spin susceptibility
 $\psi_{\mathbf{k}m}(\mathbf{r})$ Bloch wavefunction
 Z partition function
 $\zeta_{3/2}$ Riemann zeta function

Appendix C

Odpowiedzi dla Recenzentów

Recenzja prof. dra hab. Piotra Bogusławskiego

Pani Werpachowska zaznacza tu, że dzięki symetrii blendy cynkowej sumowania po strefie Brillouina można było ograniczyć do 1/48 strefy. Wyda się to błędne: nieprzywiedlna część strefy Brillouina to 1/24 część strefy, i można spodziewać się błędów czy niedokładności wynikających z tego założenia. (1/48-ą część strefy należy używać w strukturze diamentu, z symetrią inwersji).

Dziękuję za wychwycenie błędu w tekście pracy, powinno być napisane 1/24. Ważnym elementem mojej pracy była analiza wpływu braku symetrii inwersji struktury blendy cynkowej na fizykę badanego materiału. Takiego wpływu nie zaobserwowałabym redukując obszar całkowania do 1/48 strefy. Ponadto procedury numeryczne testowałam całkując po całej strefie.

W rozdziale 6 przedstawione są dwa podejścia do obliczeń struktury pasmowej GaMnAs. Pierwszym jest metoda kp, w wersji 6-cio i 8-mio pasmowej (czyli odpowiednio podejście Kohna-Luttingera i Kane'a). Autorka nie podała związku stałych takich jak A' , P_0 czy B z elementami macierzowymi w bazie użytej w rachunkach.

Poniżej wyprowadzam brakujące wzory, posługując się notacją z prac [171, 175].

Hamiltonian Kane'a jest zapisany w bazie będącej iloczynem tensorowym stanów przestrzennych S (należącego do reprezentacji nieprzywiedlnej Γ_1 pojedynczej grupy T_d w notacji Kostera [171]) oraz X, Y, Z (należących do reprezentacji Γ_5) i spinowych $|\uparrow\rangle, |\downarrow\rangle$. Zmodyfikowane parametry Luttingera, użyte w hamiltonianie Kane'a, są dane wzorami

$$\gamma_1 = -\frac{2m_0}{3\hbar^2}(L' + 2M) - 1 \quad \gamma_2 = -\frac{m_0}{3\hbar^2}(L' - M) \quad \gamma_3 = -\frac{m_0}{3\hbar^2}N'$$

gdzie

$$\begin{aligned}
L' &= F' + 2G & M &= H_1 + H_2 \\
M &= H_1 + H_2 & N' &= F' - G + H_1 - H_2 \\
F' &= \frac{\hbar^2}{m_0^2} \sum_{nj} \frac{|\langle X | p_x | n\Gamma_{1j} \rangle|^2}{E_v - E_{n,\Gamma_1}} & G &= \frac{\hbar^2}{2m_0^2} \sum_{nj} \frac{|\langle X | p_x | n\Gamma_{3j} \rangle|^2}{E_v - E_{n,\Gamma_3}} \\
H_1 &= \frac{\hbar^2}{2m_0^2} \sum_{nj} \frac{|\langle X | p_x | n\Gamma_{5j} \rangle|^2}{E_v - E_{n,\Gamma_5}} & H_2 &= \frac{\hbar^2}{2m_0^2} \sum_{nj} \frac{|\langle X | p_x | n\Gamma_{4j} \rangle|^2}{E_v - E_{n,\Gamma_4}}
\end{aligned}$$

gdzie sumy po nj oznaczają sumy po stanach $n\Gamma_{k,j}$ należących do odpowiednich reprezentacji Γ_k pojedynczej grupy T_d i uwzględnionych perturbacyjnie w hamiltonianie Kane'a [171]. E_c i $E_{v'} = E_v - \Delta_{\text{SO}}/3$ są odpowiednio energiami punktu Γ dla pasma przewodnictwa i pasma walencyjnego, zaś Δ_{SO} oznacza rozszczepienie spin-orbitalne w punkcie Γ . Funkcje bazowe S , X , Y i Z związane są z bazą hamiltonianu Kane'a (zob. str. 65) w następujący sposób:

$$\begin{aligned}
S|\uparrow\rangle &= u_2 \\
X|\uparrow\rangle &= \frac{i}{\sqrt{6}} (\sqrt{2}u_7 - \sqrt{3}u_4 - u_6) \\
Y|\uparrow\rangle &= -\frac{1}{\sqrt{6}} (\sqrt{2}u_7 + \sqrt{3}u_4 - u_6) \\
Z|\uparrow\rangle &= \frac{i}{\sqrt{3}} (u_8 - \sqrt{2}u_3)
\end{aligned}$$

Dodatkowe parametry hamiltonianu Kane'a są dane wzorami

$$\begin{aligned}
A' &= \frac{\hbar^2}{m_0^2} \sum_{nj} \frac{|\langle S | p_x | n\Gamma_{5j} \rangle|^2}{E_c - E_{n,\Gamma_5}} & B &= 2 \frac{\hbar^2}{m_0^2} \sum_{nj} \frac{\langle S | p_x | n\Gamma_{5j} \rangle \langle n\Gamma_{5j} | p_x | Z \rangle}{(E_c + E_v)/2 - E_{n,\Gamma_5}} \\
P_0 &= -i \frac{\hbar}{m_0} \langle S | p_x | X \rangle
\end{aligned}$$

Hamiltonian Kohna-Luttingera różni się od hamiltonianu Kane'a brakiem stanów bazowych $S|\uparrow\rangle$ i $S|\downarrow\rangle$, co prowadzi do pojawienia się dodatkowych członów w jego parametrach, opisujących perturbacyjnie sprzężenie ze stanem S . Użyte w nim standardowe parametry Luttingera są dane wzorami

$$\gamma_1^l = -\frac{2m_0}{3\hbar^2}(L + 2M) - 1 \quad \gamma_2^l = -\frac{m_0}{3\hbar^2}(L - M) \quad \gamma_3^l = -\frac{m_0}{3\hbar^2}N$$

gdzie

$$\begin{aligned}
L &= F + 2G \\
N &= F - G + H_1 - H_2 & F &= F' + \frac{P_0^2}{E_{v'} - E_c}
\end{aligned}$$

Funkcje bazowe X , Y i Z związane są z bazą hamiltonianu Kohna-Luttingera (zob. str. 63) w następujący sposób:

$$\begin{aligned} X|\uparrow\rangle &= \frac{1}{\sqrt{2}} \left(u_1 - \sqrt{3}u_3 + i\sqrt{6}u_6 \right) \\ Y|\uparrow\rangle &= -\frac{i}{\sqrt{2}} \left(u_1 + \sqrt{3}u_3 - i\sqrt{6}u_6 \right) \\ Z|\uparrow\rangle &= \frac{i}{\sqrt{3}} \left(\sqrt{2}u_2 - iu_5 \right) \end{aligned}$$

Autorka nie wspomina tu także o problemie pasma domieszkowego indukowanego obecnością Mn w GaMnAs. Problem ten jest oczywiście kontrowersyjny, lecz powinien zostać tu zasygnalizowany.

Problem pasma domieszkowego i innych alternatywnych opisów bogatej fizyki (Ga,Mn)As starałam się zasygnalizować w rozdziale 4.3 “Magnetic regimes in (Ga,Mn)As”, bardzo skrótowym jak na tak obszerny temat. W swojej pracy skupiłam się zaledwie na reżimie metalicznym.

W standardowym podejściu opisanym np. w cytowanej książce Bira i Pikusa, w członach opisujących sprzężenie z wyższymi pasmami w drugim rzędzie mianownik energetyczny jest różnicą energii stanów jednocząstkowych, a nie energii całkowitych stanów wielocząstkowych użytych przez autorkę.

W swoich obliczeniach wyszłam od abstrakcyjnego ujęcia rachunku Löwdina: jego główną ideą jest redukcja bazy hamiltonianu do ograniczonego zbioru stanów (klasa A) poprzez uwzględnienie przejść pomiędzy stanami z klasy A a nadmiarowymi stanami (klasa B) jako zaburzenia [193]. W podejściu opisanym przez Bira i Pikusa, którego używa się na przykład do wyprowadzenia hamiltonianu Kane’a, rozpatrujemy hamiltonian jednocząstkowy i za nadmiarowe uznajemy stany z wyższych pasm. Moim celem było wyjście poza model pola średniego poprzez uwzględnienie wyższego rzędu sprzężenia dziur z manganami, w którym dziury są wzbudzone ponad poziom Fermiego zmieniając zarówno pasma, jak i wektory falowe. Dlatego nadmiarowe były nie stany z określonych pasm, ale wielocząstkowe stany wzbudzone dziur. W mianowniku pojawia się zatem różnica energii stanów wielocząstkowych $E_{\Gamma_0} - E_{\Gamma''}$, która w toku obliczeń (w przybliżeniu jednoelektronowym) sprowadza się do różnicy energii stanów jednocząstkowych $E_{\mathbf{k}m} - E_{\mathbf{k}'m'}$.

Rysunek 8.1 pokazuje, że temperaturowa zależność magnetyzacji jest dobrze opisana modelem pola średniego, niestety autorka nie specyfikuje wartości parametrów i modelu użytego w obliczeniach.

Zależność $M(T)$ została obliczona z funkcji Brillouina (równ. 8.1), dla

której wartość pola średniego Ξ wyznaczyłam na podstawie zmierzonej [199] magnetyzacji nasycenia, $M(T = 0)$.

Recenzja prof. dra hab. Henryka Puzkarskiego

Uwaga odnośnie obliczeń fal spinowych w cienkich warstwach.

W obliczeniach fal spinowych w cienkich warstwach wykorzystałam rachunek dla próbek objętościowych, kładąc $q_z = 0$. W ten sposób uwzględniłam tylko mod zerowy na kierunku prostopadłym do warstwy (mod jednorodny na kierunku z). Wówczas wydawało mi się to słuszne, ponieważ rozpatrywałam niefizycznie cienkie warstwy, chcąc zaprezentować jedynie nowe zjawiska, jakie możemy w takich strukturach zaobserwować (ze wzgl. na możliwości obliczeniowe, maksymalna grubość warstwy jaką symulowałam to zaledwie 12 monowarstw, a więc znacznie mniej niż grubość typowej cienkiej próbki). Te nowe zjawiska, takie jak struktura spiralna i związane z nią przesunięcie minimum dyspersji fal spinowych, nie powinny zagiąć po uwzględnieniu wyższych modów. Natomiast pełny rachunek jest niewątpliwie konieczny dla poprawnego ilościowego opisu fal spinowych w cienkich warstwach. W mojej pracy dane doświadczalne o sztywności fal spinowych porównałam jedynie z wynikami teoretycznymi dla struktur objętościowych. Wyniki dla cienkich warstw z uwzględnieniem powyższej wskazówki prawdopodobnie lepiej odtworzą dane doświadczalne. Niestety, nie będzie to miało wpływu na wyniki z części pracy o anomalnym efekcie Halla, gdzie nie rozumiemy danych doświadczalnych dla cienkich warstw, a moja praca jedynie wykluczyła pewne teorie, nie dostarczając pozytywnej interpretacji tych danych.

Chciałabym podziękować Recenzentom za ich czas i uwagę poświęcone mojej pracy oraz za wartościowe uwagi, które wytyczają dalszy kierunek badań.

Bibliography

- [1] Overclocking record: “duck overclocking on EVGA P55 - CPU frequency world record!”. http://www.youtube.com/watch?v=c0fHN_MV8yc, Sep 10, 2010.
- [2] J. Leake and R. Woods. Revealed: the environmental impact of Google searches. *The Times*, Jan 11 2009.
- [3] P. K. Pachauri and A. Reisinger, editors. *IPCC Fourth Assessment Report: Climate Change 2007 (AR4)*. Cambridge University Press, Cambridge, UK and New York, NY, USA, 1997.
- [4] IBM’s annual list of five innovations set to change our lives in the next five years. <http://www.gizmag.com>, Dec 28, 2010.
- [5] W. Kleemann. Switching magnetism with electric fields. *Physics*, 2:105, Dec 2009.
- [6] A. M. Steane and E. G. Rieffel. Beyond bits: The future of quantum information processing. *Computer*, 33:38–45, 2000.
- [7] R. P. Feynman. Simulating physics with computers. *Int. J. Theor. Phys.*, 21:467, 1982.
- [8] K. Temme, T. J. Osborne, K. G. Vollbrecht, D. Poulin, and F. Verstraete. Quantum metropolis sampling. *Nature*, 471(7336):87–90, 2011.
- [9] Quantum computing demo announcement. <http://dwave.wordpress.com>, Jan 19, 2007.
- [10] The Orion quantum computer anti-hype FAQ by Scott Aaronson. <http://www.scottaaronson.com/blog/?p=198>, Feb 9, 2007.
- [11] M. N. Baibich, J. M. Broto, A. Fert, F. Nguyen Van Dau, F. Petroff, P. Etienne, G. Creuzet, A. Friederich, and J. Chazelas. Giant magnetoresistance of (001)Fe/(001)Cr magnetic superlattices. *Phys. Rev. Lett.*, 61(21):2472–2475, Nov 1988.

- [12] G. Binasch, P. Grünberg, F. Saurenbach, and W. Zinn. Enhanced magnetoresistance in layered magnetic structures with antiferromagnetic interlayer exchange. *Phys. Rev. B*, 39(7):4828–4830, Mar 1989.
- [13] D. D. Awschalom and M. E. Flatte. Challenges for semiconductor spintronics. *Nat. Phys.*, 3:153, 2007.
- [14] Mram-info: Mram tech news and resources. <http://www.mram-info.com>.
- [15] Search MRAM at <http://www.freescale.com>.
- [16] M. Julliere. Tunneling between ferromagnetic films. *Phys. Lett. A*, 54(3):225 – 226, 1975.
- [17] S. S. P. Parkin, M. Hayashi, and L. Thomas. Magnetic domain-wall racetrack memory. *Science*, 320:190, 2008.
- [18] J. C. Slonczewski. Current-driven excitation of magnetic multilayers. *J. Magn. Magn. Mater.*, 159(1-2):L1 – L7, 1996.
- [19] L. Berger. Emission of spin waves by a magnetic multilayer traversed by a current. *Phys. Rev. B*, 54(13):9353, Oct 1996.
- [20] M. Flatte. Spintronics. *IEEE Trans. Elec. Dev.*, 54:907, 2007.
- [21] S. Datta and B. Das. Electronic analog of the electro-optic modulator. *Appl. Phys. Lett.*, 56:665, 1990.
- [22] S. Bandyopadhyay and M. Cahay. Reexamination of some spintronic field-effect device concepts. *Appl. Phys. Lett.*, 85:1433, 2004.
- [23] R. Pela and L. Teles. Spin transistors vs. conventional transistors: What are the benefits? *J. Supercond. Nov. Magn.*, 23:61–64, 2010.
- [24] J. Wunderlich, B.-G. Park, A. C. Irvine, L. P. Zarbo, E. Rozkotova, P. Nemeč, V. Novak, J. Sinova, and T. Jungwirth. Spin Hall effect transistor. *Science*, 330(6012):1801–1804, 2010.
- [25] D. Kahng. Electric field controlled semiconductor device. *U. S. Patent No. 3,102,230*, 1960.
- [26] J. A. Halderman, S. D. Schoen, N. Heninger, W. Clarkson, W. Paul, J. A. Calandrino, A. J. Feldman, J. Appelbaum, and E. W. Felten. Lest we remember: Cold boot attacks on encryption keys. <http://citp.princeton.edu/memory>.
- [27] X. Wang and Y. Chen. Spintronic memristor devices and application. In *Design, Automation & Test in Europe Conference and Exhibition*, March 2010. Seagate Technology.

- [28] T. Dietl. A ten-year perspective on dilute magnetic semiconductors and oxides. *Nature Mat.*, 9:965, 2010.
- [29] A. Zunger, S. Lany, and H. Raebiger. The quest for dilute ferromagnetism in semiconductors: Guides and misguides by theory. *Physics*, 3:53, Jun 2010.
- [30] P. W. Anderson. Random-phase approximation in the theory of superconductivity. *Phys. Rev.*, 112(6):1900–1916, Dec 1958.
- [31] P. W. Higgs. Broken symmetries and the masses of gauge bosons. *Phys. Rev. Lett.*, 13(16):508–509, Oct 1964.
- [32] F. Wilczek. *Fractional statistics and anyon superconductivity*. World Scientific, 1990.
- [33] O. Tchernyshyov. Parity and time-reversal anomaly in a semiconductor. *Phys. Rev. B*, 62(24):16751–16755, Dec 2000.
- [34] N. Metropolis, A. W. Rosenbluth, M. N. Rosenbluth, A. H. Teller, and E. Teller. Equation of state calculations by fast computing machines. *J. Chem. Phys.*, 21:1087–1092, June 1953.
- [35] M. Yamanouchi, D. Chiba, F. Matsukura, and H. Ohno. Current-induced domain-wall switching in a ferromagnetic semiconductor structure. *Nature*, 428:539, 2004.
- [36] H. Ohno, D. Chiba, F. Matsukura, T. Omiya, E. Abe, T. Dietl, T. Ohno, and K. Ohtani. Electric-field control of ferromagnetism. *Nature*, 408:944, 2000.
- [37] D. Chiba, A. Werpachowska, M. Endo, Y. Nishitani, F. Matsukura, T. Dietl, and H. Ohno. Anomalous Hall effect in field-effect structures of (Ga,Mn)As. *Phys. Rev. Lett.*, 104(10):106601, Mar 2010.
- [38] D. A. Allwood, G. Xiong, C. C. Faulkner, D. Atkinson, D. Petit, and R. P. Cowburn. Magnetic domain-wall logic. *Science*, 309:1688, 2005.
- [39] T. Dietl, H. Ohno, F. Matsukura, J. Cibert, and D. Ferrand. Zener model description of ferromagnetism in zinc-blende magnetic semiconductors. *Science*, 287:1019, 2000.
- [40] T. Dietl, H. Ohno, and F. Matsukura. Hole-mediated ferromagnetism in tetrahedrally coordinated semiconductors. *Phys. Rev. B*, 63(19):195205, Apr 2001.
- [41] P.O. Löwdin. A note on the quantum-mechanical perturbation theory. *J. Chem. Phys.*, 19:1396–1401, 1951.

- [42] M. A. Ruderman and C. Kittel. Indirect exchange coupling of nuclear magnetic moments by conduction electrons. *Phys. Rev.*, 96(1):99, Oct 1954.
- [43] J. König, T. Jungwirth, and A. H. MacDonald. Theory of magnetic properties and spin-wave dispersion for ferromagnetic (Ga,Mn)As. *Phys. Rev. B*, 64:184423, 2001.
- [44] J. König, H.-H. Lin, and A. H. MacDonald. Theory of diluted magnetic semiconductor ferromagnetism. *Phys. Rev. Lett.*, 84(24):5628–5631, Jun 2000.
- [45] T. Jungwirth, Q. Niu, and A. H. MacDonald. Anomalous Hall effect in ferromagnetic semiconductors. *Phys. Rev. Lett.*, 88:207208, 2002.
- [46] A. Werpachowska and T. Dietl. Effect of inversion asymmetry on the intrinsic anomalous Hall effect in ferromagnetic (Ga,Mn)As. *Phys. Rev. B*, 81(15):155205, Apr 2010.
- [47] A. Werpachowska and T. Dietl. Theory of spin waves in ferromagnetic (Ga,Mn)As. *Phys. Rev. B*, 82:085204, 2010.
- [48] I. Tsubokawa. On the magnetic properties of a CrBr₃ single crystal. *Journal of the Physical Society of Japan*, 15(9):1664–1668, 1960.
- [49] B. T. Matthias, R. M. Bozorth, and J. H. Van Vleck. Ferromagnetic interaction in EuO. *Phys. Rev. Lett.*, 7(5):160–161, Sep 1961.
- [50] T. Kasuya and A. Yanase. Anomalous transport phenomena in Eu-chalcogenide alloys. *Rev. Mod. Phys.*, 40(4):684–696, Oct 1968.
- [51] A. Mauger and C. Godart. The magnetic, optical, and transport properties of representatives of a class of magnetic semiconductors: The europium chalcogenides. *Phys. Rep.*, 141:51, 1986.
- [52] G. Busch, B. Magyar, and P. Wachter. Optical absorption of some ferro- and antiferromagnetic spinels, containing Cr³⁺-ions. *Phys. Lett.*, 23(7):438–440, 1966.
- [53] R. B. Woolsey and R. M. White. Electron-magnon interaction in ferromagnetic semiconductors. *Phys. Rev. B*, 1:4474–4486, 1970.
- [54] J. Schoenes and P. Wachter. Exchange optics in Gd-doped EuO. *Phys. Rev. B*, 9(7):3097–3105, Apr 1974.
- [55] W. Nolting. Theory of ferromagnetic semiconductors. *Phys. Stat. Sol. (b)*, 96:11, 1979.

- [56] H. Ohno and F. Matsukura. A ferromagnetic III-V semiconductor: (Ga,Mn)As. *Solid State Comm.*, 117(3):179 – 186, 2001.
- [57] J. K. Furdyna. Diluted magnetic semiconductors. *J. Appl. Phys.*, 64:R29, 1988.
- [58] R.R. Gałazka. Physics of semiconductors. In B. L. H. Wilson, editor, *Proc 14th International Conference on the physics of semiconductors*, volume 133. Edinburgh, 1978.
- [59] S. Von Molnar and S. Methfessel. Giant negative magnetoresistance in ferromagnetic $\text{Eu}_{1-x}\text{Gd}_x\text{Se}$. *J. Appl. Phys.*, 38:959, 1967.
- [60] A. Haury, A. Wasiela, A. Arnoult, J. Cibert, S. Tatarenko, T. Dietl, and Y. Merle d’Aubigné. Observation of a ferromagnetic transition induced by two-dimensional hole gas in modulation-doped cdmnte quantum wells. *Phys. Rev. Lett.*, 79(3):511–514, Jul 1997.
- [61] T. Story, R. R. Gałazka, R. B. Frankel, and P. A. Wolff. Carrier-concentration-induced ferromagnetism in PbSnMnTe. *Phys. Rev. Lett.*, 56(7):777–779, Feb 1986.
- [62] Y. Fukuma, H. Asada, J. Miyashita, N. Nishimura, , and T. Koyanagi. Magnetic properties of IV–VI compound GeTe based diluted magnetic semiconductors. *J. Appl. Phys.*, 93:7667, 2003.
- [63] H. Munekata. Optical phenomena in magnetic semiconductors. *Concepts in Spin Electronics*, 1:1, 2006.
- [64] H. Munekata, H. Ohno, S. von Molnar, A. Segmüller, L. L. Chang, and L. Esaki. Diluted magnetic III–V semiconductors. *Phys. Rev. Lett.*, 63(17):1849–1852, Oct 1989.
- [65] F. Matsukura, H. Ohno, and T. Dietl. chapter 1 III-V ferromagnetic semiconductors. In K.H.J. Buschow, editor, *III-V Ferromagnetic Semiconductors*, volume 14 of *Handbook of Magnetic Materials*. Elsevier, 2002.
- [66] H. Munekata, H. Ohno, R. R. Ruf, R. J. Gambino, and L. L. Chang. P-type diluted magnetic III–V semiconductors. *J. Cryst. Growth*, 111(1-4):1011, 1991.
- [67] T. Dietl and H. Ohno. Ferromagnetic III-V and II-VI semiconductors. *MRS Bulletin*, 28:714, 2003.
- [68] H. Ohno, H. Munekata, T. Penney, S. von Molnár, and L. L. Chang. Magnetotransport properties of p-type (In,Mn)As diluted magnetic III–V semiconductors. *Phys. Rev. Lett.*, 68(17):2664–2667, Apr 1992.

- [69] H. Munekata, A. Zaslavsky, P. Fumagalli, and R. J. Gambino. Preparation of (In,Mn)As/(Ga,Al)Sb magnetic semiconductor heterostructures and their ferromagnetic characteristics. *Appl. Phys. Lett.*, 63:2929, 1993.
- [70] H. Ohno, A. Shen, F. Matsukura, A. Oiwa, A. Endo, S. Katsumoto, and Y. Iye. (Ga,Mn)As: A new diluted magnetic semiconductor based on GaAs. *Appl. Phys. Lett.*, 69:363, 1996.
- [71] S. Sharma, R. Bajpai, and B.P. Chandra. Photoplastic effect in polycarbonate using tensile deformation. *J. Appl. Pol. Science*, 90(10):2703–2707, 2003.
- [72] K. Sato, L. Bergqvist, J. Kudrnovský, P. H. Dederichs, O. Eriksson, I. Turek, B. Sanyal, G. Bouzerar, H. Katayama-Yoshida, V. A. Dinh, T. Fukushima, H. Kizaki, and R. Zeller. First-principles theory of dilute magnetic semiconductors. *Rev. Mod. Phys.*, 82(2):1633–1690, May 2010.
- [73] P. Bogusławski and J. Bernholc. Fermi-level effects on the electronic structure and magnetic couplings in (Ga,Mn)N. *Phys. Rev. B*, 72(11):115208, Sep 2005.
- [74] O. Volnianska and P. Bogusławski. Magnetism of solids resulting from spin polarization of p orbitals. *J. Phys.: Cond. Mat.*, 22(7):073202, 2010.
- [75] G. Arlt and P. Quadflieg. Piezoelectricity in III-V compounds with a phenomenological analysis of the piezoelectric effect. *Phys. Stat. Sol.*, 25:323, 1968.
- [76] P. Y. Yu and M. Cardona. *Fundamentals of Semiconductors: Physics and Materials Properties*. Springer, 2005.
- [77] U. Rossler. Nonparabolicity and warping in the conduction band of GaAs. *Sol. Stat. Comm.*, 49(10):943 – 947, 1984.
- [78] B. Zhu and Y.-C. Chang. Inversion asymmetry, hole mixing, and enhanced Pockels effect in quantum wells and superlattices. *Phys. Rev. B*, 50(16):11932–11948, Oct 1994.
- [79] D. Kitchen, A. Richardella, and A. Yazdani. Spatial structure of a single Mn impurity state on GaAs (110) surface. *J. Supercond.*, 18:23–28, 2005.
- [80] J. Schneider, U. Kaufmann, W. Wilkening, M. Baeumler, and F. Köhl. Electronic structure of the neutral manganese acceptor in gallium arsenide. *Phys. Rev. Lett.*, 59(2):240, Jul 1987.

- [81] R. A. Chapman and W. G. Hutchinson. Photoexcitation and photoionization of neutral manganese acceptors in gallium arsenide. *Phys. Rev. Lett.*, 18(12):443, 1967.
- [82] M. Linnarsson, E. Janzén, B. Monemar, M. Kleverman, and A. Thilderkvist. Electronic structure of the GaAs:Mn_{Ga} center. *Phys. Rev. B*, 55(11):6938, Mar 1997.
- [83] K. Ando, T. Hayashi, M. Tanaka, and A. Twardowski. Magneto-optic effect of the ferromagnetic diluted magnetic semiconductor Ga_{1-x}Mn_xAs. *J. Appl. Phys.*, 83:6548, 1998.
- [84] J. Okabayashi, T. Mizokawa, D. D. Sarma, A. Fujimori, T. Slupinski, A. Oiwa, and H. Munekata. Electronic structure of In_{1-x}Mn_xAs studied by photoemission spectroscopy: Comparison with Ga_{1-x}Mn_xAs. *Phys. Rev. B*, 65(16):161203, Apr 2002.
- [85] J. Szczytko, A. Twardowski, K. Świątek, M. Palczewska, M. Tanaka, T. Hayashi, and K. Ando. Mn impurity in Ga_{1-x}Mn_xAs epilayers. *Phys. Rev. B*, 60(11):8304–8308, Sep 1999.
- [86] Y. Sasaki, X. Liu, J. K. Furdyna, M. Palczewska, J. Szczytko, and A. Twardowski. Ferromagnetic resonance in GaMnAs. *J. Appl. Phys.*, 91:7484, 2002.
- [87] M. Marder. *Condensed Matter Physics*. Wiley, New York, 2000.
- [88] T. Jungwirth, J. Sinova, J. Mašek, J. Kučera, and A. H. MacDonald. Theory of ferromagnetic (III,Mn)V semiconductors. *Rev. Mod. Phys.*, 78(3):809, 2006.
- [89] J. Masek, I. Turek, J. Kudrnovsky, F. Maca, and V. Drchal. Compositional dependence of the formation energies of substitutional and interstitial mn in partially compensated (Ga,Mn)As. *Acta Phys. Pol. A*, 105:637, 2004.
- [90] T. Jungwirth, K. Y. Wang, J. Mašek, K. W. Edmonds, J. König, J. Sinova, M. Polini, N. A. Goncharuk, A. H. MacDonald, M. Sawicki, A. W. Rushforth, R. P. Campion, L. X. Zhao, C. T. Foxon, and B. L. Gallagher. Prospects for high temperature ferromagnetism in (Ga,Mn)As semiconductors. *Phys. Rev. B*, 72(16):165204, Oct 2005.
- [91] A. M. Yakunin, A. Yu. Silov, P. M. Koenraad, J.-M. Tang, M. E. Flatté, W. Van Roy, J. De Boeck, and J. H. Wolter. Spatial structure of Mn-Mn acceptor pairs in GaAs. *Phys. Rev. Lett.*, 95(25):256402, Dec 2005.

- [92] J. Zemen, J. Kučera, K. Olejník, and T. Jungwirth. Magnetocrystalline anisotropies in (Ga,Mn)As: Systematic theoretical study and comparison with experiment. *Phys. Rev. B*, 80:155203, Oct 2009.
- [93] M. Jaczynski, J. Kossut, and R. R. Galazka. Influence of exchange interaction on the quantum transport phenomena in $\text{Hg}_{1-x}\text{Mn}_x\text{Te}$. *Phys. Stat. Sol. B*, 88:73–85, 1978.
- [94] Y.-J. Zhao, W. T. Geng, A. J. Freeman, and B. Delley. Structural, electronic, and magnetic properties of α - and β -MnAs: LDA and GGA investigations. *Phys. Rev. B*, 65(11):113202, Feb 2002.
- [95] J. Sadowski and J. Z. Domagala. Influence of defects on the lattice constant of GaMnAs. *Phys. Rev. B*, 69(7):075206, Feb 2004.
- [96] X. Liu, A. Prasad, J. Nishio, E. R. Weber, Z. Liliental-Weber, and W. Walukiewicz. Native point defects in low-temperature-grown GaAs. *Appl. Phys. Lett.*, 67:279, 1995.
- [97] H. Ohno. Properties of ferromagnetic iii-v semiconductors. *J. Magn. Magn. Mater.*, 200(1-3):110 – 129, 1999.
- [98] T. E. M. Staab, R. M. Nieminen, J. Gebauer, R. Krause-Rehberg, M. Luysberg, M. Haugk, and Th. Frauenheim. Do arsenic interstitials really exist in As-rich GaAs? *Phys. Rev. Lett.*, 87(4):045504, Jul 2001.
- [99] P. A. Korzhavyi, I. A. Abrikosov, E. A. Smirnova, L. Bergqvist, P. Mohn, R. Mathieu, P. Svedlindh, J. Sadowski, E. I. Isaev, Yu. Kh. Vekilov, and O. Eriksson. Defect-induced magnetic structure in $\text{Ga}_{1-x}\text{Mn}_x\text{As}$. *Phys. Rev. Lett.*, 88(18):187202, Apr 2002.
- [100] A. Shen, H. Ohno, F. Matsukura, Y. Sugawara, N. Akiba, T. Kuroiwa, A. Oiwa, A. Endo, S. Katsumoto, and Y. Iye. Epitaxy of (Ga,Mn)As, a new diluted magnetic semiconductor based on GaAs. *J. Cryst. Growth*, 175-176(Part 2):1069 – 1074, 1997. Molecular Beam Epitaxy 1996.
- [101] C. Kittel. *Introduction to Solid State Physics*. John Wiley & Sons, Inc., New York, 6th edition, 1986.
- [102] J. Wenisch. *Ferromagnetic (Ga,Mn)As Layers and Nanostructures: Control of Magnetic Anisotropy by Strain Engineering*. PhD dissertation, Julius-Maximilians-Universität Würzburg, Fakultät für Physik und Astronomie, 2008.
- [103] M. Abolfath, T. Jungwirth, J. Brum, and A. H. MacDonald. Theory of magnetic anisotropy in $\text{III}_{1-x}\text{Mn}_x\text{V}$ ferromagnets. *Phys. Rev. B*, 63(5):054418, Jan 2001.

- [104] J. Wenisch, L. Ebel, C. Gould, G. Schmidt, L.W. Molenkamp, and K. Brunner. Epitaxial GaMnAs layers and nanostructures with anisotropy in structural and magnetic properties. *J. Cryst. Growth*, 301-302:638 – 641, 2007. 14th International Conference on Molecular Beam Epitaxy - MBE XIV.
- [105] M. V. Berry and J. M. Robbins. Indistinguishability for quantum particles: spin, statistics and the geometric phase. *Proc. R. Soc. Lond. A*, 453(1963):1771–1790, 1997.
- [106] W. Li. Essay Electron spin: Theory and applications, May 23, 2009.
- [107] R. Skomski. *Simple Models of Magnetism*. Oxford New York, 2008.
- [108] T. Dietl. (diluted) magnetic semiconductor. volume 3B of *Handbook on Semiconductors*, page 1251. North-Holland, Amsterdam, 1994.
- [109] S. A. Crooker, J. J. Baumberg, F. Flack, N. Samarth, and D. D. Awschalom. Terahertz spin precession and coherent transfer of angular momenta in magnetic quantum wells. *Phys. Rev. Lett.*, 77(13):2814–2817, Sep 1996.
- [110] A. Bonanni. Ferromagnetic nitride-based semiconductors doped with transition metals and rare earths. *Semicond. Sci. Tech.*, 22(9):R41, 2007.
- [111] R. M. White. *Quantum Theory of Magnetism*. New York, McGraw-Hill, 1970.
- [112] P. W. Anderson. Antiferromagnetism. Theory of superexchange interaction. *Phys. Rev.*, 79(2):350–356, Jul 1950.
- [113] T. Shinjo. *Nanomagnetism and spintronics*. Elsevier, 2009.
- [114] J.B. Goodenough. An interpretation of the magnetic properties of the perovskite-type mixed crystals $\text{La}_{1-x}\text{Sr}_x\text{CoO}_3$. *J. Phys. Chem. Solids*, 6:287, 1958.
- [115] J. Kanamori. Superexchange interaction and symmetry properties of electron orbitals. *J. Phys. Chem. Solids*, 10(2-3):87–98, July 1959.
- [116] N. Bloembergen and T. J. Rowland. Nuclear spin exchange in solids: Tl^{203} and Tl^{205} magnetic resonance in thallium and thallic oxide. *Phys. Rev.*, 97(6):1679–1698, Mar 1955.
- [117] P. Kacman. Spin interactions in diluted magnetic semiconductors and magnetic semiconductor structures. *Semiconductor Science and Technology*, 16(4):R25, 2001.

- [118] C. Zener. Interaction between the d -shells in the transition metals. II. Ferromagnetic compounds of manganese with perovskite structure. *Phys. Rev.*, 82(3):403–405, May 1951.
- [119] A. Bonanni and T. Dietl. A story of high-temperature ferromagnetism in semiconductors. *Chem. Soc. Rev.*, 39:528, 2010.
- [120] D. C. Mattis. *Theory of Magnetism*. Harper and Row, New York, 1965.
- [121] R. Skomski, J. Zhou, J. Zhang, and D. J. Sellmyer. Indirect exchange in dilute magnetic semiconductors. *J. Appl. Phys.*, 99:08D504, 2006.
- [122] A. Werpachowska and Z. Wilamowski. RKKY coupling in diluted magnetic semiconductors. *Mat. Sci.-PL*, 24(3):675, 2006.
- [123] C. Zener. Interaction between the d shells in the transition metals. *Phys. Rev.*, 81(3):440–444, Feb 1951.
- [124] J.M. Luttinger and W. Kohn. Motion of electrons and holes in perturbed periodic fields. *Phys. Rev.*, 97:869, 1955.
- [125] B. Beschoten, P. A. Crowell, I. Malajovich, D. D. Awschalom, F. Matsukura, A. Shen, and H. Ohno. Magnetic circular dichroism studies of carrier-induced ferromagnetism in $\text{Ga}_{1-x}\text{Mn}_x\text{As}$. *Phys. Rev. Lett.*, 83(15):3073–3076, Oct 1999.
- [126] M. Sawicki, K.-Y. Wang, K. W. Edmonds, R. P. Campion, C. R. Staddon, N. R. S. Farley, C. T. Foxon, E. Papis, E. Kamińska, A. Piotrowska, T. Dietl, and B. L. Gallagher. In-plane uniaxial anisotropy rotations in (Ga,Mn)As thin films. *Phys. Rev. B*, 71(12):121302, Mar 2005.
- [127] E. Abrahams, P. W. Anderson, D. C. Licciardello, and T. V. Ramakrishnan. Scaling theory of localization: Absence of quantum diffusion in two dimensions. *Phys. Rev. Lett.*, 42(10):673–676, Mar 1979.
- [128] A. Kaminski and S. Das Sarma. Polaron percolation in diluted magnetic semiconductors. *Phys. Rev. Lett.*, 88(24):247202, May 2002.
- [129] M. Berciu and R. N. Bhatt. Effects of disorder on ferromagnetism in diluted magnetic semiconductors. *Phys. Rev. Lett.*, 87(10):107203, Aug 2001.
- [130] A. C. Durst, R. N. Bhatt, and P. A. Wolff. Bound magnetic polaron interactions in insulating doped diluted magnetic semiconductors. *Phys. Rev. B*, 65(23):235205, Jun 2002.

- [131] E. A. Pashitskii and S. M. Ryabchenko. Magnetic ordering in semiconductors with magnetic impurities. *Sov. Phys. Solid State*, 21:322, 1979.
- [132] R. P. Campion, K. W. Edmonds, L. X. Zhao, K. Y. Wang, C. T. Foxon, B. L. Gallagher, and C. R. Staddon. The growth of GaMnAs films by molecular beam epitaxy using arsenic dimers. *J. Cryst. Growth*, 251:311, 2003.
- [133] Y. Ohno, D. K. Young, B. Beschoten, F. Matsukura, H. Ohno, and D. D. Awschalom. Electrical spin injection in a ferromagnetic semiconductor heterostructure. *Nature*, 402:790, 1999.
- [134] T. Dietl. Interplay between carrier localization and magnetism in diluted magnetic and ferromagnetic semiconductors. *J. Phys. Soc. Jap.*, 77(3):031005, 2008.
- [135] C. P. Moca, B. L. Sheu, N. Samarth, P. Schiffer, B. Janko, and G. Zarand. Scaling theory of magnetoresistance and carrier localization in $\text{Ga}_{1-x}\text{Mn}_x\text{As}$. *Phys. Rev. Lett.*, 102(13):137203, Apr 2009.
- [136] D. Awschalom and N. Samarth. Spintronics without magnetism. *Physics*, 2:50, Jun 2009.
- [137] Y. K. Kato, R. C. Myers, A. C. Gossard, and D. D. Awschalom. Current-induced spin polarization in strained semiconductors. *Phys. Rev. Lett.*, 93(17):176601, Oct 2004.
- [138] Y. Kato, R. C. Myers, A. C. Gossard, and D. D. Awschalom. Coherent spin manipulation without magnetic fields in strained semiconductors. *Nature*, 427(6969):50–53, January 2004.
- [139] Y. K. Kato, R. C. Myers, A. C. Gossard, and D. D. Awschalom. Observation of the Spin Hall Effect in Semiconductors. *Science*, 306(5703):1910–1913, December 2004.
- [140] N. Levy, S. A. Burke, K. L. Meaker, M. Panlasigui, A. Zettl, F. Guinea, A. H. Castro Neto, and M. F. Crommie. Strain-Induced Pseudo-Magnetic Fields Greater Than 300 Tesla in Graphene Nanobubbles. *Science*, 329(5991):544–547, 2010.
- [141] A. P. Horsfield and A. M. Bratkovsky. Ab initio tight binding. *J. of Phys.: Cond. Mat.*, 12(2):R1, 2000.
- [142] G. Dresselhaus. Spin-orbit coupling effects in zinc blende structures. *Phys. Rev.*, 100(2):580–586, Oct 1955.

- [143] J. Jancu, R. Scholz, F. Beltram, and F. Bassani. Empirical *spds** tight-binding calculation for cubic semiconductors: General method and material parameters. *Phys. Rev. B*, 57(11):6493–6507, Mar 1998.
- [144] A. S. Davydov. *Quantum Mechanics*. Pergamon, Oxford, 1965.
- [145] H. A. Kramers. *Proc. Acad. Sci. Amsterdam*, 33:959, 1930.
- [146] E. P. Wigner. Über die Operation der Zeitumkehr in der Quantenmechanik. *Nachr. Ges. Wiss. Gottingen*, 31:546, 1932.
- [147] R. H. Parmenter. Symmetry properties of the energy bands of the zinc blende structure. *Phys. Rev.*, 100(2):573–579, Oct 1955.
- [148] M. P. Surh, M.-F. Li, and S. G. Louie. Spin-orbit splitting of GaAs and InSb bands near Γ . *Phys. Rev. B*, 43(5):4286–4294, Feb 1991.
- [149] Yu. A. Bychkov and E. I. Rashba. Oscillatory effects and the magnetic susceptibility of carriers in inversion layers. *J. Phys. C: Sol. Stat. Phys.*, 17(33):6039, 1984.
- [150] Yu. A. Bychkov and E. I. Rashba. Properties of a 2D electron gas with lifted spectral degeneracy. *Nachr. Ges. Wiss. Gottingen*, 39:78, 1984.
- [151] S. Adachi. *Properties of Group-IV, III-V and II-VI Semiconductors*. John Wiley & Sons Ltd., England, 2005.
- [152] W. Zawadzki and P. Pfeffer. Spin splitting of subband energies due to inversion asymmetry in semiconductor heterostructures. *Semicond. Sci. Technol.*, 19:R1, 2004.
- [153] J. Fabian, A. Matos-Abiague, C. Ertler, P. Stano, and Igor Zutic. Semiconductor spintronics. *Acta Physica Slovaca*, 57:565, 2007.
- [154] D. D. Awschalom, D. Loss, and N. Samarth. *Semiconductor Spintronics and Quantum Computation*. Springer-Verlag, Berlin, 2002.
- [155] D. Z.-Y. Ting and X. Cartoixa. Resonant interband tunneling spin filter. *Appl. Phys. Lett.*, 81:4198, 2002.
- [156] J. Schliemann, J. C. Egues, and D. Loss. Nonballistic spin-field-effect transistor. *Phys. Rev. Lett.*, 90(14):146801, Apr 2003.
- [157] M. Poggio. *Spin Interactions Between Conduction Electrons and Local Moments in Semiconductor Quantum Wells*. PhD dissertation, University of California, Santa Barbara, 2005.

- [158] J. Okabayashi, A. Kimura, O. Rader, T. Mizokawa, A. Fujimori, T. Hayashi, and M. Tanaka. Core-level photoemission study of $\text{Ga}_{1-x}\text{Mn}_x\text{As}$. *Phys. Rev. B*, 58(8):R4211–R4214, Aug 1998.
- [159] G. M. Dalpian and S.-H. Wei. Electron-mediated ferromagnetism and negative $s - d$ exchange splitting in semiconductors. *Phys. Rev. B*, 73(24):245204, Jun 2006.
- [160] R. C. Myers, M. Poggio, N. P. Stern, A. C. Gossard, and D. D. Awschalom. Antiferromagnetic $s - d$ exchange coupling in gamnas. *Phys. Rev. Lett.*, 95(1):017204, Jun 2005.
- [161] M. Poggio, R. C. Myers, N. P. Stern, A. C. Gossard, and D. D. Awschalom. Structural, electrical, and magneto-optical characterization of paramagnetic gamnas quantum wells. *Phys. Rev. B*, 72(23):235313, Dec 2005.
- [162] C. Śliwa and T. Dietl. Electron-hole contribution to the apparent s - d exchange interaction in III-V diluted magnetic semiconductors. *Phys. Rev. B*, 78:165205, 2008.
- [163] C. Strahberger and P. Vogl. Model of room-temperature resonant-tunneling current in metal/insulator and insulator/insulator heterostructures. *Phys. Rev. B*, 62(11):7289–7297, Sep 2000.
- [164] R. Oszwałdowski, J. A. Majewski, and T. Dietl. Influence of band structure effects on domain-wall resistance in diluted ferromagnetic semiconductors. *Phys. Rev. B*, 74(15):153310, 2006.
- [165] P. Sankowski, P. Kacman, J. A. Majewski, and T. Dietl. Spin-dependent tunneling in modulated structures of $(\text{Ga},\text{Mn})\text{As}$. *Phys. Rev. B*, 75(4):045306, 2007.
- [166] G. L. Bir and G. E. Pikus. *Symmetry and Strain-Induced Effects in Semiconductors*. Wiley, New York, 1974.
- [167] F. Seitz. The theoretical constitution of metallic lithium. *Phys. Rev.*, 47(5):400–412, March 1935.
- [168] E. O. Kane. Band structure of indium antimonide. *J. Phys. Chem. Solids*, 1:249, 1957.
- [169] M. Cardona and F. H. Pollak. Energy-band structure of germanium and silicon: The $k \cdot p$ method. *Phys. Rev.*, 142:530–543, 1966.
- [170] R. Soline, F. Aniel, and G. Fishman. Energy-band structure of Ge, Si, and GaAs: A thirty-band $k \cdot p$ method. *Phys. Rev. B*, 74:235204, 2004.

- [171] T. E. Ostromek. Evaluation of matrix elements of the 8x8 k.p Hamiltonian with k-dependent spin-orbit contributions for the zinc-blende structure of GaAs. *Phys. Rev. B*, 54(20):14467, 1996.
- [172] A. Marnetto, M. Penna, F. Bertazzi, E. Bellotti, and M. Goano. Ab initio and full-zone k.p computations of the electronic structure of wurtzite BeO. In *Numerical Simulation of Optoelectronic Devices, 2008. NUSOD '08. International Conference on*, 2008.
- [173] I. J. Robertson and M. C. Payne. k -point sampling and the $k \cdot p$ method in pseudopotential total energy calculations. *J. Phys.: Cond. Mat.*, 2:9837, 1990.
- [174] W. W. Chow and S. M. Koch. *Semiconductor-laser fundamentals: physics of the gain materials*. Springer, 1999.
- [175] T. B. Bahder. Eight-band $k.p$ model of strained zinc-blende crystals. *Phys. Rev. B*, 41:11992, 1990.
- [176] J. Okabayashi, A. Kimura, O. Rader, Mizokawa T., A. Fujimori, and T. Hayashi. Electronic structure of $\text{Ga}_{1-x}\text{Mn}_x\text{As}$ studied by angle-resolved photoemission spectroscopy. *Physica E*, 10:192, 2001.
- [177] L. Bhusal, A. Alemu, and A. Freundlich. Band alignments and quantum confinement in (111) GaAsN/InAs strain-balanced nanostructures. *Nanotechnology*, 15(4):S245–S249, 2004.
- [178] C. M. Goringe, D. R. Bowler, and E. Hernández. Tight-binding modelling of materials. *Rep. Prog. Phys.*, 60:1447–1512, 1997.
- [179] J. C. Slater and G. F. Koster. Simplified LCAO method for the periodic potential problem. *Phys. Rev.*, 94(6):1498–1524, 1954.
- [180] P.-O. Löwdin. On the non-orthogonality problem connected with the use of atomic wave functions in the theory of molecules and crystals. *J. Chem. Phys.*, 18:365, 1950.
- [181] R. Werpachowski. On the approximation of real powers of sparse, infinite, bounded and Hermitian matrices. *Lin. Alg. Appl.*, 428:316–323, 2008.
- [182] P. Vogl, H. P. Hjalmarson, and J. D. Dow. A semi-empirical tight-binding theory of the electronic structure of semiconductors. *J. Phys. Chem. Solids*, 44:365, 1983.
- [183] A. Di Carlo and P. Lugli. Valley mixing in resonant tunnelling diodes with applied hydrostatic pressure. *Semicond. Sci. Technol.*, 10:1673–1679, 1995.

- [184] D. J. Chadi. Spin-orbit splitting in crystalline and compositionally disordered semiconductors. *Phys. Rev. B*, 16(2):790–796, 1977.
- [185] W. A. Harrison. *Electronic structure and the properties of solids: The physics of the chemical bond*. Freeman, San Francisco, 1980.
- [186] F. Matsukura, H. Ohno, A. Shen, and Y. Sugawara. Transport properties and origin of ferromagnetism in (Ga,Mn)As. *Phys. Rev. B*, 57(4):R2037–R2040, Jan 1998.
- [187] J. J. Binney, A. J. Fisher, and Newman M. E. J. *The Theory of Critical Phenomena*. Oxford University Press, 1992.
- [188] A. Werpachowska. Exact and approximate methods of calculating the sum of states for classical non-interacting particles occupying a finite number of modes. *arXiv*, Feb 2011.
- [189] L. D. Landau. Theory of phase transformations. I. *Phys. Z. Sowjetunion*, 11:26, 1937.
- [190] L. D. Landau. Theory of phase transformations. II. *Phys. Z. Sowjetunion*, 11:545, 1937.
- [191] K. Huang. *Statistical mechanics*. Wiley, New York, 1987.
- [192] T. Vojta. Rare region effects at classical, quantum, and nonequilibrium phase transitions. *J. Phys. A: Math. Gen.*, 39:R143, 2006.
- [193] J. M. Thijssen. *Computational Physics*. Cambridge University Press, 2007.
- [194] C. H. Ziener, S. Glutsch, and F. Bechstedt. RKKY interaction in semiconductors: Effects of magnetic field and screening. *Phys. Rev. B*, 70(7):075205, Aug 2004.
- [195] I. E. Dzyaloshinskii. A thermodynamic theory of “weak” ferromagnetism of antiferromagnetics. *J. Phys. Chem. Solids*, 4:241, 1958.
- [196] T. Moriya. Anisotropic superexchange interaction and weak ferromagnetism. *Phys. Rev.*, 120(1):91–98, Oct 1960.
- [197] T. Holstein and H. Primakoff. Field dependence of the intrinsic domain magnetization of a ferromagnet. *Phys. Rev.*, 58(12):1098–1113, Dec 1940.
- [198] C. Kittel. *Quantum Theory of Solids*. Wiley, 1987.

- [199] C. Gourdon, A. Dourlat, V. Jeudy, K. Khazen, H. J. von Bardeleben, L. Thevenard, and A. Lemaître. Determination of the micromagnetic parameters in (Ga,Mn)As using domain theory. *Phys. Rev. B*, 76(24):241301, 2007.
- [200] X. Liu, W. L. Lim, L. V. Titova, T. Wojtowicz, M. Kutrowski, K. J. Yee, M. Dobrowolska, J. K. Furdyna, S. J. Potashnik, M. B. Stone, P. Schiffer, I. Vurgaftman, and J. R. Meyer. External control of the direction of magnetization in ferromagnetic InMnAs/GaSb heterostructures. *Physica E*, 20:370, 2004.
- [201] X. Liu, Y. Sasaki, and J. K. Furdyna. Ferromagnetic resonance in $\text{Ga}_{1-x}\text{Mn}_x\text{As}$: Effects of magnetic anisotropy. *Phys. Rev. B*, 67(20):205204, May 2003.
- [202] S. C. Masmanidis, H. X. Tang, E. B. Myers, Mo Li, K. De Greve, G. Vermeulen, W. Van Roy, and M. L. Roukes. Nanomechanical measurement of magnetostriction and magnetic anisotropy in (Ga,Mn)As. *Phys. Rev. Lett.*, 95(18):187206, Oct 2005.
- [203] H. Ohno, F. Matsukura, A. Shen, Y. Sugawara, A. Oiwa, A. Endo, S. Katsumoto, and Y. Iye. Spin splitting of subband energies due to inversion asymmetry in semiconductor heterostructures. *Proc. 23rd Int. Conf. Phys. Semicond.*, page 405, Singapore 1996.
- [204] M. Sawicki, F. Matsukura, A. Idziaszek, T. Dietl, G. M. Schott, C. Ruester, C. Gould, G. Karczewski, G. Schmidt, and L. W. Molenkamp. Temperature dependent magnetic anisotropy in (Ga,Mn)As layers. *Phys. Rev. B*, 70(24):245325, Dec 2004.
- [205] M. Farle. Ferromagnetic resonance of ultrathin metallic layers. *Rep. Prog. Phys.*, 61(7):755, 1998.
- [206] L. Brey and G. Gómez-Santos. Magnetic properties of GaMnAs from an effective Heisenberg hamiltonian. *Phys. Rev. B*, 68:115206, Sep 2003.
- [207] C. Timm and A. H. MacDonald. Anisotropic exchange interactions in III-V diluted magnetic semiconductors. *Phys. Rev. B*, 71(15):155206, 2005.
- [208] T. Dietl, J. König, and A. H. MacDonald. Magnetic domains in III-V magnetic semiconductors. *Phys. Rev. B*, 64(24):241201, Nov 2001.
- [209] G. Bouzerar. Magnetic spin excitations in diluted ferromagnetic systems: The case of $\text{Ga}_{1-x}\text{Mn}_x\text{As}$. *Europhys. Lett.*, 79(5):57007, 2007.

- [210] S. J. Potashnik, K. C. Ku, R. Mahendiran, S. H. Chun, R. F. Wang, N. Samarth, and P. Schiffer. Saturated ferromagnetism and magnetization deficit in optimally annealed $\text{Ga}_{1-x}\text{Mn}_x\text{As}$ epilayers. *Phys. Rev. B*, 66(1):012408, Jul 2002.
- [211] D. M. Wang, Y. H. Ren, X. Liu, J. K. Furdyna, M. Grimsditch, and R. Merlin. Light-induced magnetic precession in (Ga,Mn)As slabs: Hybrid standing-wave Damon-Eshbach modes. *Phys. Rev. B*, 75(23):233308, 2007.
- [212] Y.-Y. Zhou, Y.-J. Cho, Z. Ge, X. Liu, M. Dobrowolska, and J. K. Furdyna. Magnetic anisotropy, spin pinning and exchange constants of (Ga,Mn)As films. *IEEE Trans. Magn.*, 43:3019, 2007.
- [213] X. Liu, Y. Y. Zhou, and J. K. Furdyna. Angular dependence of spin-wave resonances and surface spin pinning in ferromagnetic (Ga,Mn)As films. *Phys. Rev. B*, 75:195220, 2007.
- [214] C. Bihler, W. Schoch, W. Limmer, S. T. B. Goennenwein, and M. S. Brandt. Spin-wave resonances and surface spin pinning in $\text{Ga}_{1-x}\text{Mn}_x\text{As}$ thin films. *Phys. Rev. B*, 79(4):045205, Jan 2009.
- [215] Y.-F. Chen, M. Dobrowolska, J. K. Furdyna, and S. Rodriguez. Interference of electric-dipole and magnetic-dipole interactions in conduction-electron-spin resonance in InSb. *Phys. Rev. B*, 32(2):890–902, Jul 1985.
- [216] K. Pappert, S. Humpfner, J. Wensch, K. Brunner, C. Gould, G. Schmidt, and L. W. Molenkamp. Transport characterization of the magnetic anisotropy of (Ga,Mn)As. *Appl. Phys. Lett.*, 90(6):062109, 2007.
- [217] M. Bode, M. Heide, K. von Bergmann, P. Ferriani, S. Heinze, G. Bihlmayer, A. Kubetzka, O. Pietzsch, S. Blügel, and R. Wiesendanger. Chiral magnetic order at surfaces driven by inversion asymmetry. *Nature*, 447(7141):190–193, 2007.
- [218] S. Mamica and H. Puzskarski. Interface-localized mode in bilayer film ferromagnetic resonance spectrum. *Horizons in World Physics*, 244:1, 2004.
- [219] Z. Michalewicz and C. Z. Janikow. GENOCOP: A genetic algorithm for numerical optimization problems with linear constraints. *Communications of the ACM*, 39(12es):175–201, 1996.
- [220] T. Dietl, J. Cibert, D. Ferrand, and Y. Merle d’Aubigné. Carrier-mediated ferromagnetic interactions in structures of magnetic semiconductors. *Materials Sci. Engin.*, 63:103, 1999.

- [221] H. B. Callen. Green function theory of ferromagnetism. *Phys. Rev.*, 130(3):890–898, May 1963.
- [222] M.-F. Yang, S.-J. Sun, and M.-C. Chang. Comment on “Theory of diluted magnetic semiconductor ferromagnetism”. *Phys. Rev. Lett.*, 86(24):5636, Jun 2001.
- [223] F. Bloch. *Z. Phys.*, 61:206, 1930.
- [224] N. D. Mermin and H. Wagner. Absence of ferromagnetism or antiferromagnetism in one- or two-dimensional isotropic Heisenberg models. *Phys. Rev. Lett.*, 17(22):1133–1136, Nov 1966.
- [225] E. M. Jackson, S. B. Liao, S. M. Bhagat, and M. A. Manheimer. Field-induced parameters of re-entrant magnets and concentrated spin glasses. *J. Magn. Magn. Mater.*, 80(2-3):229 – 240, 1989.
- [226] A. Aharoni. *Introduction to the Theory of Ferromagnetism*. Oxford University Press, 2001.
- [227] C. Śliwa and T. Dietl. Magnitude and crystalline anisotropy of hole magnetization in (Ga,Mn)As. *Phys. Rev. B*, 74(24):245215, 2006.
- [228] J. Blinowski and P. Kacman. Spin interactions of interstitial Mn ions in ferromagnetic GaMnAs. *Phys. Rev. B*, 67(12):121204, Mar 2003.
- [229] K. W. Edmonds, P. Boguslawski, K. Y. Wang, R. P. Campion, S. N. Novikov, N. R. S. Farley, B. L. Gallagher, C. T. Foxon, M. Sawicki, T. Dietl, M. Buongiorno Nardelli, and J. Bernholc. Mn interstitial diffusion in (Ga,Mn)As. *Phys. Rev. Lett.*, 92(3):037201, Jan 2004.
- [230] W. Stefanowicz, C. Śliwa, P. Aleshkevych, T. Dietl, M. Döppe, U. Wurstbauer, W. Wegscheider, D. Weiss, and M. Sawicki. Magnetic anisotropy of epitaxial (Ga,Mn)As on (113)*a* GaAs. *Phys. Rev. B*, 81(15):155203, Apr 2010.
- [231] S. Haghgoo, M. Cubukcu, H. J. von Bardeleben, L. Thevenard, A. Lemaître, and C. Gourdon. Exchange constant and domain wall width in (Ga,Mn)(As,P) films with self-organization of magnetic domains. *Phys. Rev. B*, 82(4):041301, Jul 2010.
- [232] T. G. Rappoport, P. Redliński, X. Liu, G. Zaránd, J. K. Furdyna, and B. Jankó. Anomalous behavior of spin-wave resonances in $\text{Ga}_{1-x}\text{Mn}_x\text{As}$ thin films. *Phys. Rev. B*, 69(12):125213, Mar 2004.
- [233] G. Zaránd and B. Jankó. $\text{Ga}_{1-x}\text{Mn}_x\text{As}$: A frustrated ferromagnet. *Phys. Rev. Lett.*, 89(4):047201, Jul 2002.

- [234] U. Welp, V. K. Vlasko-Vlasov, A. Menzel, H. D. You, X. Liu, J. K. Furdyna, and T. Wojtowicz. Uniaxial in-plane magnetic anisotropy of $\text{Ga}_{1-x}\text{Mn}_x\text{As}$. *Appl. Phys. Lett.*, 85:260, 2004.
- [235] E. H. Hall. *Philos. Mag.*, 10:301, 1880.
- [236] E. H. Hall. *Philos. Mag.*, 12:157, 1881.
- [237] N. Nagaosa, J. Sinova, S. Onoda, A. H. MacDonald, and N. P. Ong. Anomalous Hall effect. *Rev. Mod. Phys.*, 82:1539, 2010.
- [238] M. V. Berry. Quantal phase factors accompanying adiabatic changes. *Proc. Roy. Soc. of London*, 392:45–57, 1984.
- [239] Z. Fang, N. Nagaosa, K. S. Takahashi, A. Asamitsu, R. Mathieu, T. Ogasawara, H. Yamada, Y. Kawasaki, Y. Tokura, and K. Terakura. The anomalous Hall effect and magnetic monopoles in momentum space. *Science*, 302:92, 2003.
- [240] S. H. Chun, M. B. Salamon, Y. Lyanda-Geller, P. M. Goldbart, and P. D. Han. Magnetotransport in manganites and the role of quantal phases: Theory and experiment. *Phys. Rev. Lett.*, 84:757, 2000.
- [241] Y. Yao, L. Kleinman, A. H. MacDonald, J. Sinova, T. Jungwirth, D. Wang, E. Wang, and Q. Niu. First principles calculation of anomalous Hall conductivity in ferromagnetic bcc Fe. *Phys. Rev. Lett.*, 92:037204, 2004.
- [242] A. Kundt. *Wied. Ann.*, 49:257, 1893.
- [243] W. L. Webster. The Hall effect in single crystals of iron. *Proc. Cambridge Phil. Soc.*, 23:800, 1925.
- [244] E. M. Pugh. Hall effect and the magnetic properties of some ferromagnetic materials. *Phys. Rev.*, 36:1503, 1930.
- [245] E. M. Pugh and T. W. Lippert. Hall e.m.f. and intensity of magnetization. *Phys. Rev.*, 42:709, 1932.
- [246] R. Karplus and J. M. Luttinger. Hall effect in ferromagnets. *Phys. Rev.*, 95:1154, 1954.
- [247] A. Bohm, A. Mostafazadeh, H. Koizumi, Q. Niu, and J. Zwanziger. *The geometric phase in quantum systems*. Springer, Berlin, 2003.
- [248] M. Chang and Q. Niu. Berry phase, hyperorbits, and the Hofstadter spectrum: Semiclassical dynamics in magnetic Bloch bands. *Phys. Rev. B*, 53:7010, 1996.

- [249] G. Sundaram and Q. Niu. Wave-packet dynamics in slowly perturbed crystals: Gradient corrections and Berry-phase effects. *Phys. Rev. B*, 59:14915, 1999.
- [250] N. A. Sinitsyn. Semiclassical theories of the anomalous Hall effect. *J. Phys.: Cond. Matt.*, 20(2):023201, 2008.
- [251] S. Onoda, N. Sugimoto, and N. Nagaosa. Quantum transport theory of anomalous electric, thermoelectric, and thermal Hall effects in ferromagnets. *Phys. Rev. B*, 77:165103, 2008.
- [252] F. D. M. Haldane. Berry curvature on the Fermi surface: Anomalous Hall effect as a topological Fermi-liquid property. *Phys. Rev. Lett.*, 93:206602, 2004.
- [253] J. Smit. The spontaneous Hall effect in ferromagnetics I. *Physica*, 21:877, 1955.
- [254] J. Smit. The spontaneous Hall effect in ferromagnetics. II. *Physica*, 24:39, 1958.
- [255] L. Berger. Side-jump mechanism for the Hall effect of ferromagnets. *Phys. Rev. B*, 2:4559, 1970.
- [256] A. A. Kovalev, J. Sinova, and Y. Tserkovnyak. Anomalous Hall effect in disordered multiband metals. *Phys. Rev. Lett.*, 105:036601, 2010.
- [257] N. F. Mott and H. S. W. Massey. *The theory of atomic collisions*. Clarendon Press, Oxford, 1965.
- [258] M. I. Dyakonov and V. I. Perel. Current-induced spin orientation of electrons in semiconductors. *Phys. Lett. A*, 35:459, 1971.
- [259] M. I. Dyakonov and A. V. Khaetskii. *Z. Eksp. Teor. Fiz.*, 84:1843, 1984.
- [260] M. I. Dyakonov. Magnetoresistance due to edge spin accumulation. *Phys. Rev. Lett.*, 99(12):126601, 2007.
- [261] D. A. Abanin, A. V. Shytov, L. S. Levitov, and B. I. Halperin. Nonlocal charge transport mediated by spin diffusion in the spin Hall effect regime. *Phys. Rev. B*, 79:035304, 2009.
- [262] P. Matl, N. P. Ong, Y. F. Yan, Y. Q. Li, D. Studebaker, T. Baum, and G. Doubinia. Hall effect of the colossal magnetoresistance manganite $\text{La}_{1-x}\text{Ca}_x\text{MnO}_3$. *Phys. Rev. B*, 57:10248, 1998.
- [263] Y. Taguchi, Y. Oohara, H. Yoshizawa, N. Nagaosa, and Y. Tokura. Spin chirality, Berry phase, and anomalous Hall effect in a frustrated ferromagnet. *Science*, 291:2573, 2001.

- [264] T. Dietl, F. Matsukura, H. Ohno, J. Cibert, and D. Ferrand. Hall effect and magnetoresistance in p -type ferromagnetic semiconductors. In I. Vagner, editor, *Recent Trends in Theory of Physical Phenomena in High Magnetic Fields*, page 197. Kluwer, Dordrecht, 2003.
- [265] W.-L. Lee, S. Watauchi, V. L. Miller, R. J. Cava, and N. P. Ong. Dissipationless anomalous Hall current in the ferromagnetic spinel $\text{CuCr}_2\text{Se}_{4-x}\text{Br}_x$. *Science*, 303:1647, 2004.
- [266] W.-L. Lee, S. Watauchi, V. L. Miller, R. J. Cava, and N. P. Ong. Anomalous Hall heat current and Nernst effect in the $\text{CuCr}_2\text{Se}_{4-x}\text{Br}_x$ ferromagnet. *Phys. Rev. Lett.*, 93:226601, 2004.
- [267] S. Onoda, N. Sugimoto, and N. Nagaosa. Intrinsic versus extrinsic anomalous Hall effect in ferromagnets. *Phys. Rev. Lett.*, 97(12):126602, Sep 2006.
- [268] T. Fukumura, H. Toyosaki, K. Ueno, M. Nakano, T. Yamasaki, and M. Kawasaki. A scaling relation of anomalous Hall effect in ferromagnetic semiconductors and metals. *Jpn. J. Appl. Phys.*, 46:L642, 2007.
- [269] E. N. Adams and E. I. Blount. Energy bands in the presence of an external force field - II : Anomalous velocities. *J. Phys. Chem. Solids*, 10:286, 1959.
- [270] D. Culcer, Y. Yao, and Q. Niu. Coherent wave-packet evolution in coupled bands. *Phys. Rev. B*, 72:085110, 2005.
- [271] E. I. Rashba. Sum rules for spin Hall conductivity cancellation. *Phys. Rev. B*, 70(20):201309, Nov 2004.
- [272] A. G. Mal'shukov and K. A. Chao. Spin Hall conductivity of a disordered two-dimensional electron gas with Dresselhaus spin-orbit interaction. *Phys. Rev. B*, 71:121308, 2005.
- [273] T. Jungwirth, J. Sinova, K. Y. Wang, K. W. Edmonds, R. P. Campion, B. L. Gallagher, C. T. Foxon, Q. Niu, and A. H. MacDonald. DC-transport properties of ferromagnetic (Ga,Mn)As semiconductors. *Appl. Phys. Lett.*, 83(2):320–322, 2003.
- [274] T. Jungwirth, B. L. Gallagher, and J. Wunderlich. Transport properties of ferromagnetic semiconductors. In T. Dietl, editor, *Spintronics, Semiconductors and Semimetals*, volume 82, pages 135–205. Elsevier, Amsterdam, 2008.

- [275] K. Y. Wang, K. W. Edmonds, R. P. Campion, L. X. Zhao, C. T. Foxon, and B. L. Gallagher. Anisotropic magnetoresistance and magnetic anisotropy in high-quality (Ga,Mn)As films. *Phys. Rev. B*, 72(8):085201, Aug 2005.
- [276] D. Ruzmetov, J. Scherschligt, David V. Baxter, T. Wojtowicz, X. Liu, Y. Sasaki, J. K. Furdyna, K. M. Yu, and W. Walukiewicz. High-temperature Hall effect in $\text{Ga}_{1-x}\text{Mn}_x\text{As}$. *Phys. Rev. B*, 69(15):155207, Apr 2004.
- [277] D. Belitz and T. R. Kirkpatrick. The Anderson-Mott transition. *Rev. Mod. Phys.*, 66(2):261–380, Apr 1994.
- [278] V. K. Dugaev, A. Crépieux, and P. Bruno. Localization corrections to the anomalous Hall effect in a ferromagnet. *Phys. Rev. B*, 64(10):104411, Aug 2001.
- [279] S. Neusser and D. Grundler. Magnonics: Spin waves on the nanoscale. *Adv. Mater.*, 21:2927, 2009.
- [280] C. Zhang. Spin-orbit coupling and perpendicular Zeeman field for fermionic cold atoms: Observation of the intrinsic anomalous Hall effect. *Phys. Rev. A*, 82:021607, 2010.
- [281] J. Larson. Analog of the spin-orbit-induced anomalous Hall effect with quantized radiation. *Phys. Rev. A*, 81:051803, 2010.
- [282] E. Miranda and V. Dobrosavljevic. Disorder-driven non-Fermi liquid behaviour of correlated electrons. *Rep. Prog. Phys.*, 68:2337, 2005.
- [283] J. Billy, V. Josse, Z. Zuo, A. Bernard, B. Hambrecht, P. Lugan, D. Clement, L. Sanchez-Palencia, P. Bouyer, and A. Aspect. Direct observation of anderson localization of matter waves in a controlled disorder. *Nature*, 453:891, 2008.
- [284] G. R. Stewart. Non-fermi-liquid behavior in d - and f -electron metals. *Rev. Mod. Phys.*, 73:797, 2001.
- [285] H. Hu, A. Strybulevych, J. H. Page, S. E. Skipetrov, and B. A. van Tiggelen. Localization of ultrasound in a three-dimensional elastic network. *Nature*, 4:945, 2008.
- [286] J. Gatheral. *The volatility surface. A practitioner's guide*. Wiley, 2006.
- [287] B. Bobey. From default correlation to implied hazard rate densities. *SSRN*, April 2008.
- [288] P. Jorion and G. Zhang. Credit contagion from counterparty risk. *SSRN*, Dec 2008.

- [289] E. W. Montroll and M. F. Shlesinger. Maximum entropy formalism, fractals, scaling phenomena, and $1/f$ noise: A tale of tails. *J. Stat. Phys.*, 32:209, 1983.
- [290] A. Richardella, P. Roushan, S. Mack, B. Zhou, D. A. Huse, D. D. Awschalom, and A. Yazdani. Visualizing critical correlations near the metal-insulator transition in $\text{Ga}_{1-x}\text{Mn}_x\text{As}$. *Science*, 327:665, 2010.
- [291] M. Sawicki, D. Chiba, A. Korbecka, Y. Nishitani, J. Majewski, F. Matsukura, T. Dietl, and H. Ohno. Experimental probing of the interplay between ferromagnetism and localization in $(\text{Ga}, \text{Mn})\text{As}$. *Nat. Phys.*, 6:22, 2010.
- [292] A. P. Li, J. Shen, J. R. Thompson, and H. H. Weitering. Ferromagnetic percolation in $\text{Mn}_x\text{Ge}_{1-x}$ dilute magnetic semiconductor. *Appl. Phys. Lett.*, 86:152507, 2005.
- [293] P. W. Anderson. Absence of diffusion in certain random lattices. *Phys. Rev.*, 109:1492, 1958.
- [294] H. Karsten, I.A. Nekrasov, G. Keller, V. Eyert, N. Blumer, A.K. McMahan, R.T. Scalettar, T. Pruschke, V.I. Anisimov, and D. Vollhardt. The LDA+DMFT approach to materials with strong electronic correlations in “Quantum simulations of complex many-body systems: From theory to algorithms, Lecture notes”, J. Grotendorst, D. Marx, A. Muramatsu (Eds.). NIC Series, Vol. 10:175, 2002.
- [295] A. Chattopadhyay, S. Das Sarma, and A. J. Millis. Transition temperature of ferromagnetic semiconductors: A dynamical mean field study. *Phys. Rev. Lett.*, 87:227202, 2001.
- [296] L. Craco, M. S. Laad, and E. Müller-Hartmann. Ab initio description of the diluted magnetic semiconductor $\text{Ga}_{1-x}\text{Mn}_x\text{As}$: Ferromagnetism, electronic structure, and optical response. *Phys. Rev. B*, 68:233310, 2003.
- [297] K. Aryanpour, J. Moreno, M. Jarrell, and R. S. Fishman. Magnetism in semiconductors: A dynamical mean-field study of ferromagnetism in $\text{Ga}_{1-x}\text{Mn}_x\text{As}$. *Phys. Rev. B*, 72:045343, 2005.
- [298] F. Popescu, C. Şen, and E. Dagotto. Dynamical mean-field study of the ferromagnetic transition temperature of a two-band model for colossal magnetoresistance materials. *Phys. Rev. B*, 73:180404, 2006.
- [299] R. Bulla, T.A. Costi, and T. Pruschke. Numerical renormalization group method for quantum impurity systems. *Rev. Mod. Phys.*, 80:395, 2008.

- [300] D. J. Garcia, K. Hallberg, and M. J. Rozenberg. Dynamical mean field theory with the density matrix renormalization group. *Phys. Rev. Lett.*, 93:246403, 2004.
- [301] J. E. Hirsch and R. M. Fye. Monte Carlo method for magnetic impurities in metals. *Phys. Rev. Lett.*, 56:2521, 1986.
- [302] A. Georges, G. Kotliar, W. Krauth, and M.J. Rozenberg. Dynamical mean-field theory of strongly correlated fermion systems and the limit of infinite dimensions. *Rev. Mod. Phys.*, 68:13, 1996.
- [303] D. Vollhardt. Dynamical mean-field theory of electronic correlations in models and materials (to be published in “Lectures on the physics of strongly correlated systems XIV”. *AIP Conf. Proc.*, 2010.
- [304] A. D. Mirlin, F. Evers, I. V. Gornyi, and P. M. Ostrovsky. Anderson transitions: Criticality, symmetries, and topologies. *Int. J. Mod. Phys. B*, 24:1577, 2010.
- [305] M. Jarrell and H. R. Krishnamurthy. Systematic and causal corrections to the coherent potential approximation. *Phys. Rev. B*, 63:125102, 2001.
- [306] T. Maier, M. Jarrell, T. Pruschke, and M. H. Hettler. Quantum cluster theories. *Rev. Mod. Phys.*, 77:1027, 2005.
- [307] U. Yu, A.-M. Nili, K. Mielson, B. Moritz, J. Moreno, and M. Jarrell. Nonlocal effects on magnetism in the diluted magnetic semiconductor $\text{Ga}_{1-x}\text{Mn}_x\text{As}$. *Phys. Rev. Lett.*, 104:037201, 2010.
- [308] M. S. Foster, S. Ryu, and A. W. W. Ludwig. Termination of typical wave-function multifractal spectra at the Anderson metal-insulator transition: Field theory description using the functional renormalization group. *Phys. Rev. B*, 80:075101, 2009.
- [309] V. M. Pereira, J. M. B. Lopes dos Santos, and A. H. Castro Neto. Modeling disorder in graphene. *Phys. Rev. B*, 77:115109, 2008.
- [310] C. L. Kane and E. J. Mele. Z_2 topological order and the quantum spin Hall effect. *Phys. Rev. Lett.*, 95:146802, 2005.
- [311] B. A. Bernevig, T. L. Hughes, and S.-C. Zhang. Quantum spin Hall effect and topological phase transition in HgTe quantum wells. *Science*, 314:1757, 2006.
- [312] A. Aspect and M. Inguscio. Anderson localization of ultracold atoms. *Phys. Today*, 62:30, 2009.

- [313] L. Sapienza, H. Thyrrerstrup, S. Stobbe, P.D. Garcia, S. Smolka, and P. Lodahl. Cavity quantum electrodynamics with anderson-localized modes. *Science*, 327:1352, 2010.
- [314] H. Takagi, B. Batlogg, H. L. Kao, J. Kwo, R. J. Cava, J. J. Krajewski, and W. F. Peck. Systematic evolution of temperature-dependent resistivity in $\text{La}_{2-x}\text{Sr}_x\text{CuO}_4$. *Phys. Rev. Lett.*, 69:2975, 1992.
- [315] F. C. Chou, N. R. Belk, M. A. Kastner, R. J. Birgeneau, and Amnon Aharony. Spin-glass behavior in $\text{La}_{1.96}\text{Sr}_{0.04}\text{CuO}_4$. *Phys. Rev. Lett.*, 75:2204, 1995.
- [316] T. J. Liu, J. Hu, B. Qian, D. Fobes, Z. Q.Mao, W. Bao, M. Reehuis, S. A. J. Kimber, K. Prokes, S. Matas, D. N. Argyriou, A. Hiess, A. Rotaru, H. Pham, L. Spinu, Y. Qiu, V. Thampy, A. T. Savici, J. A. Rodriguez, and C. Broholm. From $(\pi,0)$ magnetic order to superconductivity with (π,π) magnetic resonance in $\text{Fe}_{1.02}\text{Te}_{1-x}\text{Se}_x$. *Nature Mat.*, 9:716, 2010.
- [317] C. Panagopoulos and V. Dobrosavljevic. Self-generated electronic heterogeneity and quantum glassiness in the high-temperature superconductors. *Phys. Rev. B*, 72:014536, 2005.
- [318] J. Millton. Superconductors come of age. *Nature*, October 2010.
- [319] T. Hahn. CUBA—a library for multidimensional numerical integration. *Comput. Phys. Commun.*, 168:78–95, 2005.
- [320] P. Favati, G. Lotti, and F. Romani. Algorithm 691: Improving QUADPACK automatic integration routines. *ACM Transactions on Mathematical Software*, 17(2):218–232, June 1991.
- [321] E. Anderson, Z. Bai, C. Bischof, S. Blackford, J. Demmel, J. Dongarra, J. Du Croz, A. Greenbaum, S. Hammarling, A. McKenney, and D. Sorensen. *LAPACK Users' Guide*. Society for Industrial and Applied Mathematics, Philadelphia, PA, third edition, 1999.
- [322] Divide-and-conquer eigenvalue algorithm. <http://en.wikipedia.org>.
- [323] J. Papakonstantinou. The historical development of the secant method in 1-D. Paper presented at the annual meeting of the Mathematical Association of America, 2007.